Extrinsic Quantum Centers in Silicon for Nanophotonics and Quantum Applications

Dissertation

von M.Sc. Tobias Herzig

geboren am 30.01.1987 in Weissenfels

Gewidmet meinen Kindern, Aura und Tito,

sowie dem Mond meines Lebens.

"Ich fürchte," sagte Goldmund, "es wird mir nie gelingen, mir von deiner Denkwelt, wo man ohne Vorstellungen denkt, einen Begriff zu machen."

"O doch, sofort wird dir das gelingen. Höre zu: der Denker versucht das Wesen der Welt durch die Logik zu erkennen und darzustellen. Er weiß, daß unser Verstand und sein Werkzeug, die Logik, unvollkommene Instrumente sind ebenso wie ein kluger Künstler recht wohl weiß, daß sein Pinsel oder Meißel niemals vollkommen das strahlende Wesen eines Engels oder Heiligen wird ausdrücken können. Dennoch versuchen es beide, der Denker wie der Künstler, auf ihre Weise. Sie können und dürfen nicht anders. Denn indem ein Mensch mit den ihm von Natur gegebenen Gaben sich zu verwirklichen sucht, tut er das Höchste und einzig Sinnvolle, was er kann."

- Hermann Hesse, Narziss und Goldmund

Bibliografische Beschreibung

Herzig, Tobias
Extrinsic Quantum Centers in Silicon for Nanophotonics and Quantum Applicatons
Universität Leipzig, Dissertation
193 S.[1], 345 Lit.[2], 78 Abb.[3], 4 Tab.[4]

Referat

Quantenzentren in Kristallgittern spielen als sogenannte Festkörper-Qubits eine entscheidende Rolle für die Entwicklung der zweiten Quantenrevolution. Das G-Zentrum in Silizium kann hierfür einen wesentlichen Beitrag leisten, da es sich CMOS-kompatibel und damit skalierbar herstellen lässt, es eine scharfe Nullphononenlinie im Bereich der optischen Telekommunikation besitzt und ODMR-aktiv ist. Dies macht es zu einem geeigneten Kandidaten für die Entwicklung photonischer Mikrochips, auf denen Quantentechnologien und Lichtwellenleitung durch eine Spin-Photon-Schnittstelle miteinander verknüpft werden, um somit alle Kriterien zum Aufbau eines Quantennetzwerkes zu erfüllen. In der vorliegenden Arbeit werden G-Zentren durch niederenergetische und räumlich-selektive Ionen-Implantation hergestellt und mittels Photolumineszenz-Spektroskopie und Magnetresonanzmessungen auf ihre optischen und quantenphysikalischen Eigenschaften untersucht. Anhand umfangreicher temperaturabhängiger Ensemble-Messungen in reinem Silizium werden offene Fragen zum Sättigungsverhalten, der Rekombinationsdynamik und der Verschiebung bzw. Verbreiterung der Nullphononenlinie geklärt und die ersten Zerfallszeit-Messungen des angeregten Zustandes des Defektes vorgestellt. Durch die Verwendung von SOI-Proben in Kombination mit niederenergetischer Ionen-Implantation wird weiterhin die erste, jemals in Silizium isolierte Einzelphotonenquelle hergestellt und durch zahlreiche Polarisations- und Korrelationsmessungen als solche identifiziert. Durch die Einzelphotonenmessung erfolgt zusätzlich eine erste Abschätzung der Quanteneffizienz der G-Zentren und die Messung der Lebensdauer des isolierten angeregten Zustandes. Um den Quantenzustand der G-Zentren mittels Mikrowellenfeld manipulieren und sowohl optische als auch elektronisch auslesen zu können, wird ein experimenteller Aufbau beschrieben, mit dem die magnetische Resonanz der G-Zentren in einer SOI-Probe temperaturabhängig bis in den kryogenen Bereich detektiert werden kann. Nach den ersten manuellen Testmessungen wird der Versuchsaufbau durch neue Steuergeräte und eine Automatisierung weiter optimiert, um damit umfangreiche Messungen bei $T = 40\,\mathrm{K}$ und Raumtemperatur durchzuführen. Dabei wird eine mikrowellenabhängige Manipulation der Photolumineszenz der G-Zentren beobachtet, welche mit dem detektierten Photostrom korreliert ist. Die Manipulation der Photolumineszenz wird hauptsächlich auf eine Veränderung der Ladungsträgerdichte aufgrund anderer spinabhängiger Rekombinationszentren zurückgeführt, welche sich an den Grenzflächen des SOI-Schichtstapels bilden. Ideen, um den Einfluss der G-Zentren durch Unterdrückung der anderen Rekombinationszentren zu erhöhen, werden diskutiert.

---

[1]... S. (Seitenzahl insgesamt)
[2]... Lit. (Anzahl der im Literaturverzeichnis ausgewiesenen Literaturangaben)
[3]... Abb. (Anzahl der im Abbildungsverzeichnis ausgewiesenen Abbildungen)
[4]... Tab. (Anzahl der im Tabellenverzeichnis ausgewiesenen Tabellen)

Abstract

Quantum centers in crystal lattices can form so-called solid-state qubits that play a crucial role for the progress of the second quantum revolution. The G center in silicon can make a significant contribution to this, since it can be fabricated in a CMOS compatible and thus scalable way, it has a sharp zero-phonon line in the optical telecommunication range, and it is ODMR active. This makes it a suitable candidate for the development of photonic microchips, where quantum technologies and optical waveguides are linked by a spin-photon interface, thus fulfilling all the criteria to build a quantum network. In the present work, G centers are fabricated by low-energy and spatially-selective ion implantation and their optical and quantum physical properties are investigated by photoluminescence spectroscopy and magnetic resonance measurements. Using extensive temperature-dependent ensemble measurements in pure silicon, open questions on saturation behavior, recombination dynamics, and zero-phonon line shift as well as broadening are clarified, and the first decay time measurements of the excited state of this defect are presented. By using SOI samples in combination with low-energy ion implantation, the first single-photon source ever isolated in silicon is further fabricated and identified as such by extensive polarization and correlation measurements. The single-photon measurement additionally provides a first estimation of the quantum efficiency of the G centers and the measurement of the lifetime of the isolated excited state. In order to manipulate the quantum state of the G centers by means of a microwave field and to enable an optical as well as an electronical readout, an experimental setup is designed and assembled that allows the temperature-dependent detection of magnetic resonances of G centers in a SOI sample down to the cryogenic range. After the first manual test measurements, the experimental setup is further optimized by new control devices and process automation to allow extensive measurements at $T = 40\,\mathrm{K}$ and room temperature. A microwave-dependent manipulation of the photoluminescence of the G centers is observed, which is correlated with the detected photocurrent. The manipulation of the photoluminescence is mainly attributed to a change in the charge carrier density due to other spin-dependent recombination centers that form at the interfaces of the SOI layer stack. Ideas to increase the influence of the G centers by suppressing the other recombination centers are discussed.

Zusammenfassung der Dissertation

Extrinsische Quantenzentren in Silizium für Nanophotonik und Quantenanwendungen

der Fakultät für Physik und Geowissenschaften der Universität Leipzig

eingereicht von

M. Sc. Tobias Herzig

angefertigt am

Felix-Bloch-Institut für Festkörperphysik / Abteilung Angewandte Quantensysteme

November 2021

Quantenzentren in Kristallgittern spielen als sogenannte Festkörper-Qubits eine entscheidende Rolle für die Entwicklung der zweiten Quantenrevolution. Das G-Zentrum in Silizium kann hierzu einen wesentlichen Beitrag leisten, da es sich CMOS-kompatibel und damit skalierbar herstellen lässt, eine scharfe Nullphononenlinie im Bereich der optischen Telekommunikation besitzt und ODMR-aktiv ist. Da sich Silizium trotz seiner indirekten Bandlücke, welche lichtemittierende Übergänge unwahrscheinlich macht, gut für optische Anwendungen eignet und dabei hochrein, temperaturstabil und in großen Mengen kostengünstig produzieren lässt, gelten G-Zentren in Silizium als aussichtsreiche Kandidaten für die Entwicklung photonischer Mikrochips. In diesen werden Quantentechnologien und Lichtwellenleitung durch eine Spin-Photon-Schnittstelle miteinander verknüpft, womit alle Kriterien zum Aufbau eines weitreichenden Quantennetzwerkes erfüllt wären. Trotz langjähriger Erforschung und zahlreicher Vorteile dieser Punktdefekte fehlt es aktuell noch an grundlegenden Kenntnissen über deren elektronische und optische Eigenschaften. Ebenso war vor dieser Arbeit unbekannt, ob sich in der schmalen Bandlücke von Silizium überhaupt isolierte Zustände erzeugen lassen, welche die Herstellung von Einzelphotonenquellen im Siliziumkristall erlauben. Und obwohl G-Zentren zu den ersten Festkörper-Qubits gehörten, die mittels ODMR-Messungen untersucht wurden, ist die deterministische Manipulation und elektronische bzw. optische Auslese unzureichend entwickelt. Um das volle Potential von G-Zentren auszuschöpfen, hat sich deshalb ein internationales Projekt gebildet, in dessen Rahmen diese Arbeit entstanden ist und in welchem sowohl die Eigenschaften dieser Defekte intensiv untersucht, als auch deren Herstellung und Verwertung optimiert werden sollen. G-Zentren sind bistabile Defekte, welche aus zwei Kohlenstoff-Atomen bestehen, die über ein interstitielles Si-Atom miteinander verbunden sind. In dieser Arbeit werden sie durch räumlich-selektive ^{12}C- und ^{1}H-Implantation in verschiedenen Schichten von SOI-Waferchips erzeugt und anschließend mittels PL-Spektroskopie sowie Autokorrelations- und Magnetresonanzmessungen auf ihre optischen und quantenphysikalischen Eigenschaften untersucht. Die wichtigsten Ergebnisse daraus werden im Folgenden kurz zusammengefasst.

- Temperaturabhängige PL-Messungen im Bereich von $T = 5 - 110\,\mathrm{K}$ zeigen eine Rotverschiebung der ZPL-Energie bei gleichzeitiger Linienverbreiterung mit steigender Temperatur. Die Rotverschiebung von $E_0^{\mathrm{ens}} = 969.6\,\mathrm{meV}$ um $\Delta E = -2.4\,\mathrm{meV}$ weicht dabei von der Verkleinerung der Silizium-Bandlücke ab. Die Ursache wird hauptsäch-

lich auf Nullpunktfluktuationen der Elektron-Phononen-Wechselwirkung bei niedrigen Energien zurückgeführt. Die Linienverbreiterung von $\Gamma_0^{\mathrm{ens}} = 0.3\,\mathrm{meV}$ auf $\Gamma^{\mathrm{ens}} = 4.2\,\mathrm{meV}$ wird sowohl auf eine inhomogene Verbreiterung durch die Ensemble-Messung, als auch eine homogene, phononenassistierte Verbreiterung zurückgeführt, welche hauptsächlich mit der TA(X)-Phononenmode und der wachsenden Wahrscheinlichkeit für Phononenabsorption bei steigenden Temperaturen in Verbindung steht.

- Aus der Temperaturabhängigkeit der PL-Intensität und der gemessenen Lebensdauer von G-Zentren im Ensemble ($\tau_0^{\mathrm{ens}} = 5.9\,\mathrm{ns}$) wurde die Aktivierungsenergie jeweils zu $E_{\mathrm{A}}^{(1)} = 41\,\mathrm{meV}$ bzw. $E_{\mathrm{A}}^{(2)} = 39\,\mathrm{meV}$ bestimmt. Aus den ähnlichen Aktivierungsenergien und den strahlenden bzw. nicht-strahlenden Rekombinationsraten wurde geschlussfolgert, dass die strahlende Zerfallszeit temperaturunabhängig ist und die Abnahme der Zerfallszeit und PL-Intensität mit steigenden Temperaturen durch die gesteigerte Wahrscheinlichkeit nicht-strahlender Prozesse hervorgerufen wird.

- Durch Ionen-Implantation und Autokorrelationsmessungen wurden die ersten jemals in Silizium isolierten und optisch aktiven Punktdefekte (Einzelphotonenquellen) mit $g^{(2)}(0) \approx 0.3$, das heißt einem deutlichen Antibunching, hergestellt und nachgewiesen.

- Messwerte von $g^{(2)}(\tau) > 1$ deuten auf einen metastabilen Triplett-Zustand hin, welcher eine nicht-strahlende Relaxation vom angeregten Zustand ermöglicht.

- Spektrale und zeitaufgelöste PL-Messungen an 29 individuellen, einzelnen G-Zentren zeigen Schwankungen der ZPL-Energie mit $\langle E_{\mathrm{ZPL}}^{\mathrm{sin}} \rangle = 976.3\,\mathrm{meV}$ und der Zerfallsdauer mit $\langle \tau_{\mathrm{e}}^{\mathrm{sin}} \rangle = 35.8\,\mathrm{ns}$, welche auf lokale Spannungen und das veränderte Umfeld zurückgeführt werden. Durch Polarisationsmessungen wurden vier Ausrichtungen des optischen Dipols identifiziert, welche jeweils um einen Winkel von $\approx 45°$ zueinander versetzt sind und dabei um $\alpha = 10°$ von der [110] bzw. [1$\bar{1}$0] Kristallachse abweichen.

- Zeitaufgelöste PL-Messungen einzelner G-Zentren zeigen eine hohe und stabile PL-Intensität ohne Blinken und Bleaching, welche auch nach mehreren Temperaturzyklen zwischen $10 - 300\,\mathrm{K}$ bestehen bleibt. Aus der Berechnung der Wahrscheinlichkeit, ein Photon pro optischer Anregung zu detektieren und der Transmission des PL-Spektrometers sowie der Abschätzung der eingesammelten Photonen wurde schließlich die untere Grenze der Quanteneffizienz von G-Zentren zu $\eta_{\mathrm{QE}} \gtrsim 50\,\%$ bestimmt.

- Es wurde ein experimenteller Aufbau für ODMR und PDMR bei kryogenen Temperaturen entworfen. Erste Testmessungen haben gezeigt, dass sich sowohl die PL als auch der Photostrom der angeregten G-Zentren bei definierten Frequenzen eines Mikrowellenfeldes verändern.

- Der Quantenzustand der G-Zentren wurde nicht direkt, sondern indirekt beeinflusst. Die Erklärung für die gemessene Frequenzabhängigkeit der PL und des Photostromes liegt in der Anregung zahlreicher spinabhängiger Rekombinationszentren, welche in großer Menge an den Si/SiO$_2$-Grenzflächen der SOI-Probe auftreten. Diese Zentren verändern die Anzahl und Mobilität freier Ladungsträger und sorgen für Übergänge von Elektronen in das Leitungsband. Dadurch nimmt der Photostrom in Abhängigkeit von der angelegten Polarität zu oder ab, sodass weniger Ladungsträger für die Rekombination im G-Zentrum zur Verfügung stehen.

Auflistung der Zusammenarbeiten und Fremdbeiträge

- Flash-Annealing der Proben in Kapitel 4 - 6 durch Abdennacer Benali und Mario Khoury unter der Leitung von Marco Abbarchi am Institut Matériaux Microélectronique Nanosciences de Provence (IM2NP) der Aix-Marseille Université

- Photolumineszenz-Spektroskopie und Einzelphotonendetektion bzw. Autokorrelationsmessungen sowie deren Auswertung in Kapitel 4 und 5 durch Clement Beaufils, Walid Redjem, Emmanuel Rousseau, Alrik Durand, Isabelle Robert-Philip, Bernard Gil, Vincent Jacques und Anaïs Dréau unter der Leitung von Guillaume Cassabois am Laboratoire Charles Coulomb (L2C) der Université de Montpellier

- Kohlenstoff-Implantationen in Kapitel 4 und 5 durch Andrej Kuznetsov vom Department of Physics der University of Oslo

- numerische Simulationen in Kapitel 5 durch Damien Caliste und Pascal Pochet aus der Abteilung Modeling and Exploration of Materials Laboratory (MEM) und Jean-Michel Gérard aus der Abteilung Quantum Photonics, Electronics and Engineering Laboratory (PHELIQS) der Université Grenoble Alpes

- SOI-Materialbeschaffung der Proben aus Kapitel 4 - 6 durch Marco Abbarchi (IM2NP, Marseille) und Jean-Michel Gérard (PHELIQS, Grenoble)

- Hilfe bei der Programmierung der Steuersoftware und dem experimentellen Aufbau für die ODMR- und PDMR-Messungen in Kapitel 6 durch Evgeny Krüger aus der Abteilung Halbleiterphysik (HLP) und Robert Staacke aus der Abteilung Angewandte Quantensysteme (AQS) der Universität Leipzig

- Hilfe bei der Beschaffung von Messinstrumenten durch Gert Klotzsche (Spectrum Analyzer) aus der Abteilung Magnetische Resonanz komplexer Quantenfestkörper (MQF) der Universität Leipzig und Gopalakrishnan Balasubramanian (Mikrowellengenerator, Labornetzteil) vom Leibniz-Institut für Oberflächenmodifizierung (IOM)

Contents

List of Figures

List of Tables

Abbreviations

3LS 3-level system

AAO anodic aluminum oxide

amp amplifier

ANR Agence Nationale de la Recherche

AOM acousto-optic modulator

APD avalanche photodiodes

AQS Applied Quantum Systems

BCM adiabatic bond charge model

BEM bound exciton model

BN boron nitride

BS beam splitter

CB conduction band

CCD charge-coupled device sensor

cf. confer, compare

CLSM confocal laser scanning microscope

CMOS complementary metal-oxide semiconductor

Cs Cesium

CVD chemical vapour deposition

CW continuous wave

Cz Czochralski

DB dangling bond states

DFG Deutsche Forschungsgemeinschaft

DFT Density functional theory

DL	Dislocation loops
DLTS	deep-level transient spectroscopy
DNP	dynamic nuclear polarization
DOS	density of states
DTE	defect-trapped excitons
DWF	Debye-Waller factor
e	electrons
EBL	electron-beam lithography
EDMR	electrically detected magnetic resonance
EL	electroluminescence
e.g.	exempli gratia, for example
EPR	electron paramagnetic resonance
FBI	Felix Bloch Institute for Solid State Physics
FC	faraday cup
fcc	face-centered cubic
FinFET	fin-field-effect transistor
FWHM	full width at half maximum
FWM	Four-wave mixing
FZ	float-zone
GaAs	gallium arsenide
GaN	gallium nitride
GHZ	Greenberger–Horne–Zeilinger
GND	ground
h	holes
HBT	Hanbury Brown-Twiss
hcp	hexagonal close-packed
He	helium
HMDS	hexamethyldisilizanes
HF	high-frequency

HV	high-voltage
IC	integrated circuits
ICP	inductively coupled plasma
i.e.	id est, that is
IM2NP	Institut Matériaux Microélectronique et Nanosciences de Provence
InGaAs	indium gallium arsenide
IR	infrared
IRS	infrared absorption spectroscopy
ISC	intersystem crossing
KLM	Knill-Laflamme-Milburn
KSM	Kaplan-Solomon-Mott
L2C	Laboratoire Charles Coulomb
LA	longitudinal acoustic
LED	light-emitting diodes
LO	longitudinal optical
LOQC	linear optical quantum computing
LVM	local vibrational mode
MBPT	many-body perturbation theory
MBE	molecular beam epitaxy
MM	movable mirror
MOSFET	metal-oxide-semiconductor field-effect transistor
MW	microwave
NC	nanocrystals
NV	nitrogen-vacancy
ODMR	optically detected magnetic resonance
PBS	polarizing beam splitter
PCB	printed circuit board
PDMR	photocurrent detected magnetic resonance
PIXE	proton-induced x-ray emission

PL	photoluminescence
PLE	photoluminescence excitation
PMMA	polymethylmetacrylate
PSB	phonon sideband
PSE	periodic system of elements
PVD	physical vapor deposition
QC	quantum computer
QET	quantum enabling technology
QKD	quantum key distribution
RBS	Rutherford backscattering
RC	resistance-capacitance
RF	radio frequency
RIE	reactive ion etching
RT	room temperature
RTP	rapid thermal processing
SDH	spin-dependent hopping
SDR	spin-dependent recombination
SE	secondary electron
Si	silicon
SiC	silicon carbide
SiO$_2$	silicon dioxide
SM	steering mirror
SNICS	source of negative iony by cesium sputtering
SNR	signal-to-noise ratio
SOI	silicon on insulator
SPDC	spontaneous parametric down-conversion
SPM	Self-phase modulation
SPS	Single-photon sources
SRH	Shockley-Read-Hall

SRIM	stopping and range of ions in matter
SRS	Stimulated Raman scattering
SQUID	superconducting quantum interference devices
STD	shallow thermal donor
STIM	scanning transmission ion microscopy
TA	transversal acoustic
TCSPC	time-correlated single-photon counting
TEM	transmission electron microscopy
THG	Third-harmonic generation
TO	transversal optical
TPA	two-photon absorption
TS	tail state
TSR	time-resolved measurement of spin-dependent recombination
VB	valence band
XPM	Cross-phase modulation
ZFL	zero-field line
ZFS	zero-field splitting
ZPL	zero-phonon line

Introduction and motivation

1.1 Demand for silicon photonics and quantum technologies

The world as we know it today would not have been possible without the development of microelectronic integrated circuits (IC). Fabrication of semiconductor technologies, first and foremost based on silicon (Si), led to a technological revolution in the mid-20th century, thats rapid development we now encounter in all areas of life in the form of computers, smart devices and everyday objects. In this context, silicon has established itself as a semiconducting base material in production because it is an inexpensive, widely available and temperature-stable raw material that can be manufactured with extremely high purity. Accordingly, production facilities worldwide have specialized in processing this material to meet the huge demand for microchips. Today, complementary metal-oxide semiconductor (CMOS) technology allows the production of up to 50000 microchips simultaneously on a single round 8-inch silicon wafer. The ever-increasing demand for more powerful technologies and corresponding advances in production has led to structures on microchips that become more and more compact and smaller. This is reflected in the empirically determined Moore's Law [1], which is formulated as, among other things, the integration density of transistors doubles every 18 to 24 months as depicted in Fig. 1.1. At the time of writing, a 2 nm chip technology with a gate length of 12 nm has been announced by IBM. The shrinking structure sizes allow on the one hand a higher integration density and on the other hand higher clock frequencies, thus more computing operations per second. However, there are natural, physical limits to this development of increasing the performance of devices through more compact structures, which is the reason why Moore's Law will begin to stagnate in the near future. The increasingly densely packed conducting paths create the so-called interconnect bottleneck problem. The signal propagation speed in the conducting paths is limited by the resistance-capacitance (RC) constant of circuits and their inductance, since parasitic capacities increase with smaller structures [2]. In addition to the physical limits, however, economic factors also play a role, since the production effort and thus the costs in manufacturing increase with smaller structures.

  Since the problems just described were foreseeable, technologies were developed to counteract the impending stagnation of performance. Thus, at the beginning of the 2000s, microchips began to be commercialized which were extended in the vertical direction by, for example, wire bonding or interconnects between the ICs ("3D-IC or 3D packaging"). Although this theoretically allows a higher yield, the higher complexity also increases the risk of defects on the chip. At about the same time, transistor design was extended in the vertical direction ("fin-field-effect transistor (FinFET)"). This design allows gate structure sizes of ≤ 10 nm, much faster switching times and smaller leakage currents, but does not solve the problem of parasitic capacitances. Another method to stop the stagnation of
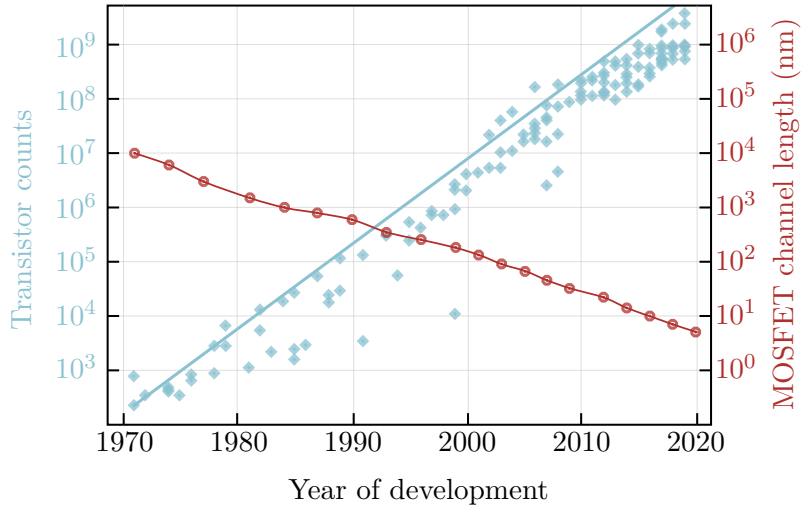
Figure 1.1   Representation of Moore's law. Blue dots represent the number of transistors on different microchip technologies. The blue line shows the calculated development of the integration density when the number of transistors doubles every two years. The red dots represent the progression of the metal-oxide-semiconductor field-effect transistor (MOSFET) channel length (distance between source and drain of the transistor). The red line is just a guide to the eye. Graphic adapted from [3], values taken from [4].

Moore's law is to use wide-bandgap semiconductors such as boron nitride (BN), gallium nitride (GaN), or silicon carbide (SiC). Due to the larger bandgap, these materials can be used to develop electronic devices that can operate at higher voltages, frequencies and temperatures. However, the industrial production of wide-bandgap materials is hampered by higher costs, lack of development tools and additional production steps. Since the problems just presented are due to the electronic nature of the devices, new technologies that are more or less independent of electronics are in the focus of future developments. The solution to this lies in the integration of photonic devices into microelectronic circuits.

Optical waveguides have long been used for efficient data transfer over long distances. To reduce losses at the interfaces between waveguides and power conductors, they are now also implemented at short "rack-to-rack" distances. The next step is therefore now to enable on-chip communication through nanoscale optical sources, circuits and detectors to encode and transmit data around the chip [5]. Although silicon was considered unsuitable for optical applications due to its indirect bandgap, the variety of non-linear optical effects (see Sec. 2.3.2), strong optical confinement, and CMOS compatible fabrication of microscopic photonic structures has led to a variety of high-performance optical devices [6]. Such devices are based on silicon on insulator (SOI) wafers, in which a thin silicon layer is separated from the bulk Si by a layer of insulating silicon dioxide (SiO_2). Due to the large difference in refractive indices ($n_{air} = 1$, $n_{Si} = 3.48$, $n_{SiO_2} = 1.44$) and high optical transmission in the infrared (IR) wavelength range (Fig. 1.2), IR light can be optimally affected and guided over long distances without loss in this material. This enables the construction of a huge, efficient optical communication network in which highly integrated multifunctional devices perform optical and electronic operations on a single, inexpensive microchip, and information can be exchanged between different chips and computers ultra-fast and energy-efficiently, i.e. in an environmentally friendly manner [7].
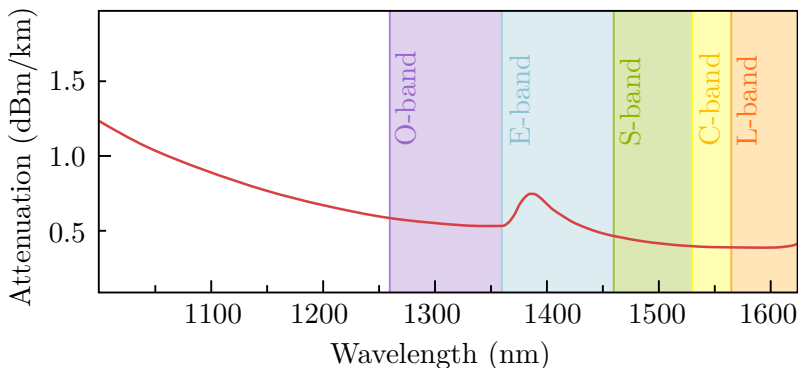
Figure 1.2 Wavelength-dependent transmission loss of silicon. Silicon is transparent for infrared light, making this bandwidth suitable for long-distance communication and optoelectronical chip integration. The different bandwidths of optical telecommunication are highlighted. Graph adapted from [8].

Despite the increasing power and efficiency of modern computers and microchips, there are tasks that cannot be solved in a meaningful way even with the most powerful classical technologies. Even the precise modeling of traffic networks, small molecular structures and weather phenomena, or seemingly simple optimization problems (e.g. the Traveling Salesman Problem) quickly become so complex that a classical computer, even if the data transmission was performed through optical waveguides, would need thousands of years to solve these tasks. Thus, to solve such ubiquitous problems in the future, a completely new class of technologies based on the non-classical principles of quantum mechanics will be needed.

Quantum technologies like lasers, light-emitting diodes (LED) or also IC microchips date back to the first quantum revolution in the middle of the 20th century. Nowadays, we encounter these technologies everywhere in our everyday life, so that they have become normality for us. The situation is still different with the technologies of the second quantum revolution, which are regarded however as key technologies with a broad application field (for example medicine, material research, artificial intelligence, environmental protection, navigation, traffic, communication, and so on) and as important link in a broadly conceived value chain [9]. Here phenomena of quantum mechanics will be made utilized, which can hardly be explained with classical conceptions. Purely quantum physical effects such as superposition, entanglement, the quantization of quantum states or Heisenberg's uncertainty principle allow the development of sensors with ultra-fine sensitivity, the construction of a quantum computer (QC) that can solve problems within minutes for which modern, classical computers need thousands of years [10] or enable the completely tap-proof transmission of information. These quantum technologies ultimately rely on the production, control and measurement of the states of so-called quantum bits (qubits). Qubits are quantum mechanical 2-level systems (e.g. spin up/down), which can be realized in different ways. Currently, qubits based on superconducting quantum interference devices (SQUID) and ions in ion traps are the most advanced, but other physical systems such as single photons [11], topological insulators [12] or quantum dots [13] can also be used for the production of qubits. Although the superiority of quantum computers was shown by Google in 2019 by a computation with 53 SQUID qubits [10], no fully-controlled quantum register was

achieved here. Currently, quantum computers with over 100 qubits already exist, but they suffer from random errors caused by decoherence and and inefficient measurements. Thus, to the best knowledge of the author, the current records for fully-controlled qubit gates are 10 SQUID qubits [14,15], 10 photonic qubits [16], and 20 trapped ion qubits [17,18]. However, to build reliable quantum computers, the number of qubits must be further increased. On the one hand, the computing power is exponentially enhanced with each additional qubit, and on the other hand, additional qubits are needed for quantum error correction to compensate computational errors which are caused by quantum noise or decoherence. Therefore, quantum computers will need several thousand qubits before they can perform useful operations like modelling of chemical systems [19].

To realize quantum technologies with qubits, they must meet certain criteria. Thus, for the construction of a quantum computer, the following rules, known as DiVincenzo criteria, must be fulfilled [20]:

- a scalable physical system with well characterized qubits

- the ability to initialize the state of the qubits to a simple fiducial state, such as $|000...\rangle$

- long relevant decoherence times, much longer than the gate operation time

- a "universal" set of quantum gates

- a qubit-specific measurement capability

And in addition to building a quantum network:

- the ability to interconvert stationary and flying qubits

- the ability to faithfully transmit flying qubits between specified locations

While the previously mentioned qubit types meet some of these criteria, there is a large technical cost associated with them. For example, SQUID qubits require extremely low temperatures in the millikelvin range to maintain superconducting properties [21] and the conversion to flying qubits is difficult. Qubits made of trapped ions, on the other hand, must be trapped by superimposed electromagnetic fields and additionally cooled by laser cooling [22], which involves enormous technical and economic effort. Photonic qubits, on the other hand, are excellent flying qubits, but can only be entangled with each other at great expense, since photons hardly interact with each other [23]. Even though there has been progress in miniaturizing SQUID and trapped ion qubits [24], scalable fabrication of qubits, which would allow economic production of qubits and quantum computers, is not within reach with these systems.

Another way to create qubits lies in exploiting the spin properties of impurities in crystals. These so-called quantum centers are referred to as solid-state qubits and offer several advantages over the other currently established technologies. For example, they can be produced in microchips by CMOS compatible methods, in which they are subsequently integrated in a fixed and non-volatile manner. This means that no large, costly and high-maintenance devices are needed to stabilize the qubits, enabling scalable as well as low-cost fabrication and operation. In addition, various solid-state qubits exist, some of which can even be operated at room temperature (RT). As quantum centers, they act as light-matter interfaces, since the spin properties of the embedded ions can be manipulated, emitting characteristic single photons that contains quantum information, which in turn can be manipulated and

readout using e.g. optically detected magnetic resonance (ODMR). Thus, one has scalable well characterized qubits as well as flying qubits in one system. However, in order to utilize them, the defects must be incorporated into the crystal with high accuracy ($< 25\,\text{nm}$) and in isolation from each other [25] to minimize the interactions of the nuclei and allow the generation of single photons. Nowadays, ion implantation techniques are under development for this purpose [26], with which the concentration and depth of the defects can be controlled and that, depending on the requirements, also allow implantations with spatial nanometer resolution [27]. Single-photon sources (SPS) generated by ion implantation have already been experimentally verified on well-known ODMR-active defects such as the nitrogen-vacancy (NV) centers in diamond (wavelength $\lambda_{\text{ZPL}} = 637\,\text{nm}$) [28, 29] or SiV centers in silicon carbide ($\lambda_{\text{ZPL}} = 850 - 1200\,\text{nm}$) [30, 31]. Also in silicon, ODMR-active quantum centers have already been ascertained. These so-called G centers in silicon are the subject of this work and exhibit most properties that predestine them for the scalable and economical fabrication of quantum technologies and the construction of a quantum communication network.

The G center is a defect in silicon, which consists of the combination of two carbon atoms with one silicon interstitial atom between them. It is considered as a bistable defect since it can occur in two different configurations (A- and B-form) within the crystal. While no photons are emitted in the A-form, the B-form produces a sharp and intense zero-phonon line (ZPL), which has a wavelength of $\lambda_{\text{ZPL}} \approx 1280\,\text{nm}$ and thus lies in the O-band of optical telecommunications (see Sec. 2.4). Although its PL strongly decreases at temperatures above $T > 50\,\text{K}$, it can still be measured at the common temperature of liquid nitrogen ($77\,\text{K}$) [32, 33]. Quantum technologies based on G centers in silicon can rely on an extensive manufacturing infrastructure, since the fabrication of these centers is fully CMOS compatible and SOI technology also enables the development of nanophotonic circuits. Together with the ODMR activity of these centers [34, 35], the construction of a purely silicon-based quantum network could thus be realized. However, further developments are needed for this. Although there have been extensive optical and electron paramagnetic resonance (EPR) measurements of these centers in the past, in which the energetic structure of these quantum centers has been investigated [36–38], a precise understanding of the recombination dynamics and measurements of the lifetime of this defect is still lacking. Likewise, it is still unclear whether optically active single defects can be fabricated at all in the narrow bandgap of silicon ($E_{\text{g}} \approx 1.1\,\text{eV}$) whose electronic states are sufficiently isolated from the valence and conduction bands to enable a silicon-based single-photon source [39]. Accordingly, it has not yet been possible to make any statements about the quantum efficiency of these centers. In addition to these purely physical questions that still exist about G centers, there is also still a lack of optimized techniques to control, manipulate, and select the quantum state of G centers. Thus, following the developments for NV centers in diamond [40–42], ODMR and PDMR techniques at G centers could be further developed. Similarly, the proper parameters for the design of photonic micro-resonators that can be used to control the spontaneous emission rate of the centers via Purcell effect need to be investigated. These advances would help in the development of on-demand SPS and lasing in silicon [43, 44], paving the way for silicon-based photonic on-chip quantum technologies.

1.2 Description and aim of the project

The present work was carried out within an international project (ULYSSES - Quantum and classical light emitters in silicon: Impurities and complex defects for nanophotonics), that was funded by the ANR (ANR-15-CE24-0027) and DFG (project no.: 286945677). The project can be divided into three areas according to the participating institutes:

Sample fabrication (IM2NP - Aix-Marseille Université, France)

- growth of Si, SOI and Si_xGe_{1-x} alloys

- manufacturing of photonic structures with electron-beam lithography (EBL) and etching processes

G center creation (AQS/FBI - Universität Leipzig, Germany)

- carbon implantation and doping

- defect generation with high-energy or spatially-selective irradiation (e.g. H, He, Si)

Spectroscopic investigations (L2C - Université de Montpellier, France)

- IR photoluminescence spectrocopy

- IR single-photon measurement

For individual tasks, further collaborations were also entered with various european partners. An overview of the participating institutes is shown in Fig. 1.3. The main goal of the project was to fabricate point defects in silicon and silicon-based photonic structures that can be used as bright as well as single-photon sources. The direct generation of light in the silicon crystal would allow the fabrication of optoelectronic devices, that could circumvent e.g. the interconnect bottleneck problem. Likewise, in combination with fiber optic cables, information could be transported over long distances with low loss and without delays at the interfaces between the electronic circuit and the fiber. The many advantages that silicon photonics can provide for today's technologies led to many new developments in this field and a great deal of interest on both the scientific and commercial sides. As a result, techniques such as Raman scattering or quantum confined structures have now made it possible to implement LEDs and lasers directly in silicon. G centers could further spur this development by combining the high intensity and narrow emission of the ZPL with photonic structures to produce efficient and low cost LEDs and lasers in the bandwidth of optical telecommunications.

While silicon photonics is now well established and considered a major leap forward in development, solid-state quantum technologies based on silicon are still largely unexplored. One reason for this is again the narrow indirect bandgap of silicon, which is considered unsuitable for isolating individual quantum states. Thus, it is currently uncertain whether single-photon sources, which are needed for applications such as quantum computing, quantum sensing or quantum cryptography, can be generated in silicon at all. Moreover, despite the great potential, many aspects of G centers are still uncertain. Thus, at the beginning of this work, a clear understanding of the emission mechanism (photon emission statistics, recombination dynamics) of the G center as well as a concrete and reproducible blueprint
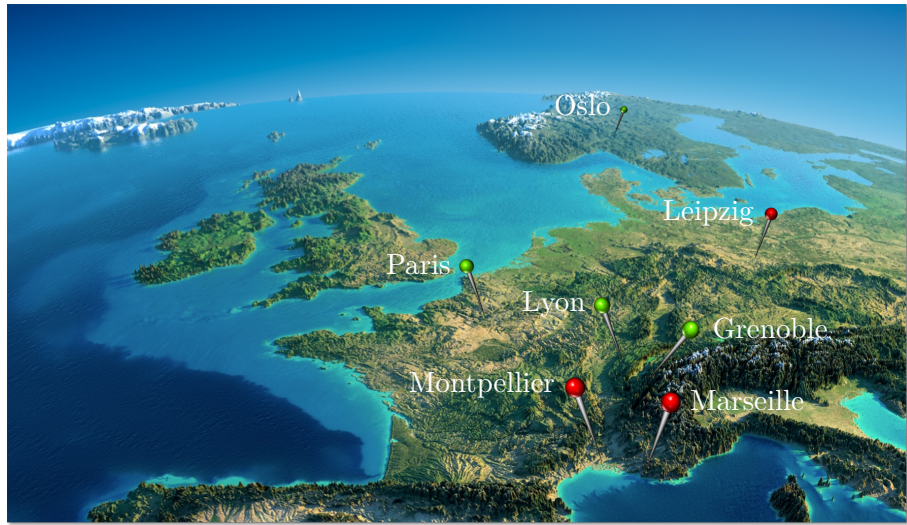
Figure 1.3   Locations of the different project partners. The red pins indicate main partners and the green pins show contributors. Grenoble (Department of Physics, IRIG, Université Grenoble Alpes and CEA, Grenoble, France), Lyon (Institut des Nanotechnologies de Lyon-INL, Ecole Centrale de Lyon, Ecully, France) and Paris (Laboratoire Pierre Aigrain, Ecole Normale Supérieure, Université Paris Diderot, France) were mainly involved for the fabrication and study of photonic structures, while Oslo (Department of Physics, University of Oslo, Norway) assisted us in the implantations. Picture taken from [45].

for the fabrication of advanced photonic devices to control the optical properties of these emitters was missing. Accordingly, the second goal within the project is to investigate the recombination mechanisms, to demonstrate the suitability of G centers as potential candidates for single-photon sources in silicon, and to optimize photonic structures for G center emission. Such a light-matter interface in combination with silicon photonic devices would be an enormously important step for an economical development of new quantum technologies and an important contribution to the second quantum revolution.

1.3 Outline

This introduction is followed by Ch. 2 about the solid-state and optical properties of silicon. It will explain how its crystal and band structure affect the optical and electronic properties and how these can be influenced by doping and defects. Building on this, ways in which light can be generated in silicon will be described before the core topic of this thesis, namely G centers as light-emitting point defects in silicon, is examined in more detail. Ch. 3 then describes important aspects of modern solid-state quantum technologies, ranging from methods to fabricate quantum centers using ion implantation devices, to the measurement of quantum properties by PL spectroscopy and single-photon detection, and the theoretical basis for quantum optics and statistics. The chapter ends with a brief insight into how quantum computers can be realized from solid-state qubits with different technological schemes.

These preliminary theoretical considerations are followed by the results section, which is divided into three chapters. Ch. 4 deals with the first joint publication of the project, in

which already known optical properties of an ensemble of G centers were verified in more detail and supplemented by new findings, e.g. the decay time of the defect. Ch. 5 then presents another joint work in which, for the first time ever, a single-photon source in silicon (in the form of single G centers) was detected. The properties of these SPS are discussed in more detail, and the results are used to make the first estimate of the quantum efficiency of G centers. Following the developments of NV centers in diamond, a setup for optical and electronic manipulation and readout of the quantum states of G centers (ODMR and PDMR) is presented in Ch. 6. For this purpose, the complex experimental setup is first described in detail and the first test measurements are presented. By further optimizing the measurement process, more accurate automated measurements are then presented and the resulting findings are evaluated. The thesis ends in Ch. 7 with a summary of the results and an outlook on the future of silicon-based quantum technologies.

Solid-state and optical properties of silicon

Introduction

In the following chapter, the crystallographic properties of silicon, that are important for this thesis, and their significance for the development of semiconductor technology are first described and discussed. A brief overview of crystal defects is followed by a section on the optical properties of silicon and various methods of generating light in this indirect semiconductor. Various light-emitting defects are presented, before the chapter ends with a detailed description of the optical and structural properties of G centers and the current state of research.

2.1 Crystal properties

2.1.1 Structure

Silicon crystallizes in a diamond structure with a diatomic base and the lattice constant $a_0 = 5.34\,$Å. The lattice, as shown in Fig. 2.1, consists of two face-centered cubic (fcc) Bravais lattices whose origin is shifted along the diagonal of the cubic cell by a quarter of its length. With four complete atoms inside the unit cell, six half atoms on its outer faces and eight 1/8 atoms on the vertices, there are eight Si atoms in each unit cell. Together with the size of the unit cell, the density of single-crystal silicon can be calculated to be $2.33\,$g/cm^3 or $4.995 \times 10^{22}\,$atoms/cm^3. Silicon belongs to the cubic space group 227 ($Fd\bar{3}m$) or to the cubic hexakisoctahedral point group 32 (Schoenflies symbol O_h^7, Hermann-Mauguin symbol $m\bar{3}m$). Thus, it has 6x 2-fold rotational symmetry, 4x 3-fold rotational symmetry, 3x 4-fold rotational symmetry, 9 planes with mirror symmetry and inversion symmetry [46, 47].

The formation of sp^3 hybrid orbitals due to the overlap of the s- and p-bands in the crystal gives rise to the tetragonal bonding between atoms characteristic of the diamond structure. The angle spanned by three adjacent silicon crystal atoms is 109.5° and the bond distance between two atoms is $d = 2.35\,$Å.

2.1.2 Lattice vibrations

The atomic nuclei of a crystal lattice perform oscillations which have a direct influence on various properties of the solid, such as dielectricity or inelastic light scattering. Based on laws of classical mechanics, a linear, homogeneous system of equations can be developed to

(a)   (b)   (c)
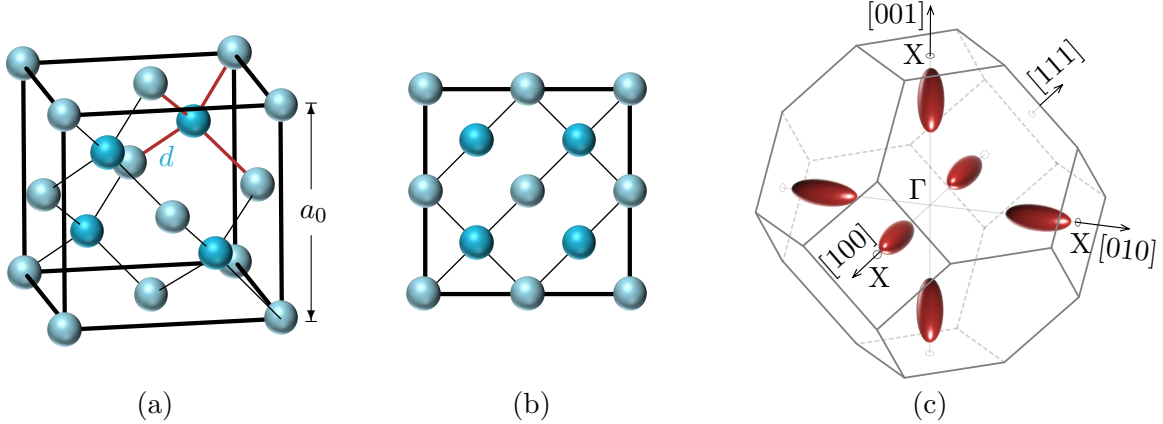
Figure 2.1   Lattice structure of silicon. (a) shows the unit cell of the silicon crystal with fcc Bravais lattice. The red bonds represent the tetrahedral structure to the nearest neighbors in the silicon lattice. **(b)** Projection of the atomic structure on a cube face in the silicon unit cell. The fcc structure is formed by two similar cubic lattices (different shades of blue) displaced along the body diagonal by $1/4$ of the total length. **(c)** Following the fcc structure, the first Brillouin zone is a rhombic dodecahedron. The ellipsoids shown along the $\Gamma \to X$ axes are the valleys of constant energy (minima of the conduction band) [48].

describe the crystal dynamics for a periodic lattice with n'-atomic base:

$$- \omega^2 A_{\alpha i}(\mathbf{k}) + \sum_{\beta, j} D_{\alpha i}^{\beta j}(\mathbf{k}) A_{\beta j}(\mathbf{k}) = 0 \tag{2.1}$$

where ω corresponds to the frequency and A to the amplitude of the core vibration and $\mathbf{k}$ is its wave vector. $D_{\alpha i}^{\beta j}(\mathbf{k})$ further forms the so-called dynamical matrix, which depends on the masses involved, their coupling constants and the corresponding distances [47]. This equation system has non-trivial solutions only if the corresponding coefficient determinant vanishes, that is:

$$\det \left(D_{\alpha i}^{\beta j}(\mathbf{k}) - \omega^2 \mathbf{1} \right) = 0. \tag{2.2}$$

For the so-called dispersion relation $\omega(\mathbf{k})$ there are $n = D \times n'$ solutions, where D corresponds to the dimensionality of the crystal system with n'-atomic base. With a diatomic base, as in the silicon lattice, one obtains for the dispersion relation

$$\omega^2 = f \left(\frac{1}{M_1} + \frac{1}{M_2} \right) \pm f \left[\left(\frac{1}{M_1} + \frac{1}{M_2} \right)^2 - \frac{4}{M_1 M_2} \sin^2 \left(\frac{ka}{2} \right) \right]^{1/2} \tag{2.3}$$

forming two dispersion branches $\omega_+(k)$ and $\omega_-(k)$ for this system, where f is the coupling constant between adjacent planes, M_1 and M_2 are the respective atomic masses of the diatomic base, the wavenumber $k = |\mathbf{k}| = \frac{2\pi}{\lambda}$ is the magnitude of the wave vector and a is the atomic plane distance. While the masses in the frequency band ω_- oscillate in phase (as in acoustic waves), the atoms in the frequency band ω_+ move in phase opposition, whereby electric dipole moments can occur, which affect the optical behavior of the crystal. Accordingly, the frequency band ω_- is called the acoustic branch and ω_+ the optical branch. Depending on the direction of vibration of the atoms to the direction of propagation of the wave, the branches are additionally differentiated between transversal and longitudinal. For a three-dimensional silicon lattice, $n = 3n' = 6$ dispersion branches should occur
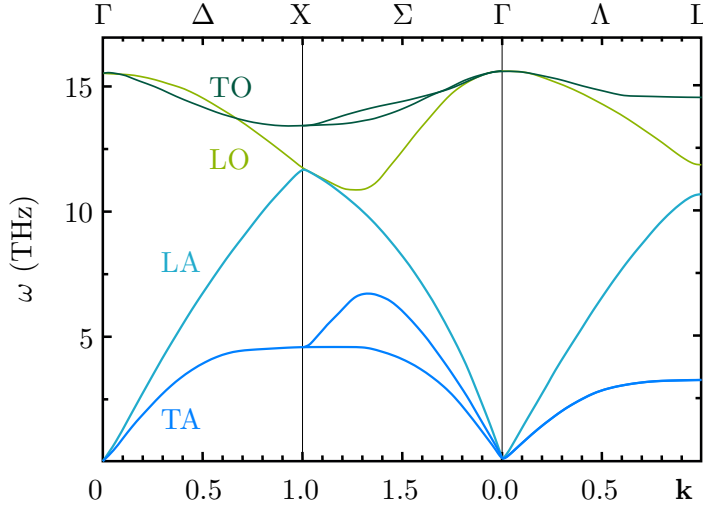
Figure 2.2 Phonon dispersion of bulk silicon calculated with a BCM. The four different dispersion branches from longitudinal acoustic (LA), transversal acoustic (TA), longitudinal optical (LO) and transversal optical (TO) phonons are distinguished by color. Adapted from [49].

accordingly. However, due to the degeneracy of the transversal branches along the [100] and the [111] directions, only four different branches are measured here (see Fig. 2.2) [47].

2.1.3 Debye-Waller factor

The Debye-Waller factor (DWF) is an important parameter in the investigation of temperature-dependent scattering processes in crystals and accordingly appears in the evaluation in Ch. 4 and Ch. 5. It describes the decrease (or attenuation, respectively) of the intensity of diffraction reflections with increasing temperature due to the thermal motion of the crystal atoms. According to [47] the elastic scattering intensity is given by

$$I = I_0 \cdot e^{-\frac{1}{3}G^2 \langle u^2(t) \rangle} = I_0 \cdot \Theta(T) \tag{2.4}$$

where the exponential factor represents the DWF Θ, which contains the reciprocal lattice vector G and the temperature-dependent vibrational amplitude of the atoms u, which is defined by

$$\langle E \rangle = \frac{1}{2}M\omega^2 \langle u^2 \rangle = \frac{3}{2}k_B T \tag{2.5}$$

The DWF can be represented by means of a Taylor expansion in a power series whose zero-order (constant) term corresponds to elastic zero-phonon processes and consequently represents the fraction of the ZPL in the total PL signal intensity [50]. Considering linear electron-phonon interactions and assuming that the total phonon density of states can be approximated by a single phonon mode of energy $\Lambda = \hbar\nu$, the DWF can be represented as

$$\Theta(T) = e^{-\xi^2 \coth(\Lambda/2k_B T)}, \tag{2.6}$$

where ξ describes the linear electron-phonon coupling strength [51].

2.1.4 Energy bands

The valence band (VB) of silicon has a maximum at the Γ point of the Brillouin zone. The conduction band (CB), on the other hand, has an absolute minimum far from this
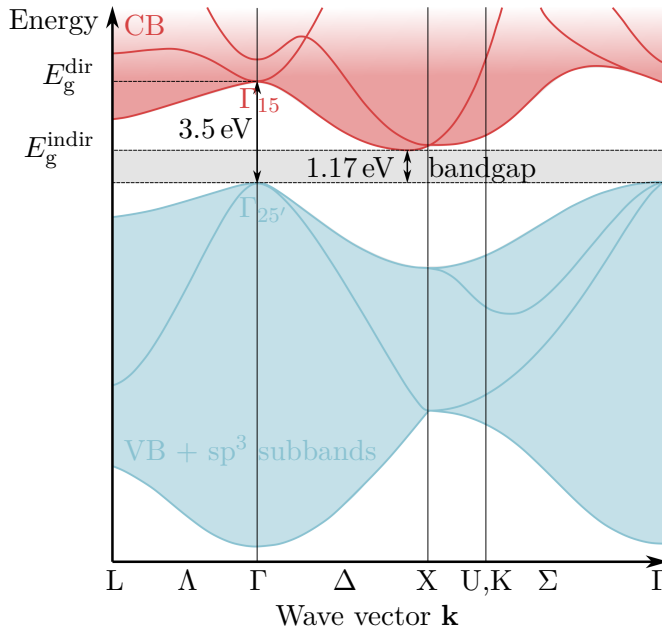
Figure 2.3 Band structure of pure silicon. Valence band (blue) and conduction band (red) are separated by an indirect bandgap with an energy of $E_g^{indir} = 1.17\,\text{eV}$. The direct transition at the Γ position has an energy of $E_g^{dir} = 3.5\,\text{eV}$.

symmetry point near the X point along the $\langle 001 \rangle$ direction, resulting in an indirect bandgap as depicted in Fig. 2.3. In total, the conduction band minimum lies at six equivalent Δ points on the $\Gamma - X$ lines. In the vicinity (called the valley) of every such point the band spectrum is quadratic in $\mathbf{k}$ and build ellipsoids of constant energy (see Fig. 2.1) [48], that depend on the effective masses of the electrons. Symmetry considerations result in different effective masses m^* for electrons in the longitudinal x-direction ($m_l^* = 0.916\,m_0$) and in the transversal y- and z-directions ($m_t^* = 0.19\,m_0$). While the direct transition from $\Gamma_{25'}$ to Γ_{15} has an energy difference of $E_g^{dir} = 3.5\,\text{eV}$, the indirect bandgap energy between CB minimum and VB maximum at $T = 0\,\text{K}$ is $E_g^{indir} = 1.17\,\text{eV}$. However, electronic transitions between these extrema only take place with a change of the wave vector to maintain the total momentum of the system. If silicon is irradiated with photons (wave vector $\mathbf{k}_\gamma$) whose energy $E = \hbar\omega$ is greater than its bandgap, they are absorbed and electrons are excited from the valence band into the conduction band. For such a transition, both the energy and momentum conservation must hold:

$$E_g = \hbar\omega(\mathbf{k}_\gamma) \pm \hbar\Omega(\mathbf{k}) \tag{2.7}$$

$$\hbar\Delta\mathbf{k} = \hbar\mathbf{k}_\gamma \pm \hbar\mathbf{k} \tag{2.8}$$

$\Delta\mathbf{k}$ corresponds to the wave vector difference of the involved states in the valence and conduction bands. Since photons have very small wave vectors $k_\gamma = \omega/c$, Δk is also small for transitions only involving photons. However, this only takes place in direct semiconductors, where the transition from the valence band maximum to the conduction band minimum is quasi-vertical. In indirect semiconductors such as silicon, where Δk is larger, additional excitations, e.g. by phonons, must take place. Since their momentum $|\mathbf{k}|$ is much larger

than that of photons ($|\mathbf{k}_\gamma|$), but their energy $\hbar\Omega$ is significantly smaller, the photon provides the energy and the phonon the necessary momentum during an interband transition [47].

2.2 Defects and doping in silicon

A perfect crystal without deviations in the lattice structure does not exist in reality. In real crystals, a large number of structural disorder defects exist that can significantly affect the optical and electronic properties of the solid (see Fig. 2.4). Some of these defects are unintentional, as they have negative effects on the functionality of electronic devices. Others, however, show promising properties for novel technologies. Accordingly, "defect engineering" has emerged as a new discipline through which quantum physical and photonic devices can be developed that are more powerful and efficient than their electronic counterparts.

2.2.1 Intrinsic and extrinsic point defects

Point defects are zero-dimensional, atomic disorders of the otherwise uniform and regular crystal lattice. They can be distinguished into intrinsic point defects, which arise only from displacements of the crystal atoms, and extrinsic point defects, in which foreign atoms are involved in the defect. In both cases, the formation of vacancies (i.e. missing atoms on lattice sites) and interstitials (additional intrinsic or foreign atoms on interstitial sites) can occur. For crystals with a polyatomic base, the atoms of the respective sublattices must be taken into account. A pair of two vacancies, each originating from a cation or anion sublattice site, are electrically neutral and are called Schottky defects. In contrast, a so-called Frenkel defect occurs when a lattice atom is shifted to an interstitial site and is neutralized by a vacancy of the same lattice. If foreign atoms are incorporated into the crystal lattice by, for example, ion implantation or chemical and physical growth processes, they are also referred to as substitutional (on lattice site) or interstitial (on interstitial site) foreign atoms. In general, interstitial defects are more likely to form in open lattices of semiconductor crystals (e.g. diamond or silicon) than in very densely packed ones (e.g. metals). In the wide gaps between the crystal atoms of semiconductors, small atoms such as hydrogen, boron, carbon, nitrogen or oxygen preferentially accumulate, while larger atoms tend to occupy substitutional lattice sites [47].

2.2.2 Line, area and volume defects

A linear arrangement of several, correlated point defects leads to higher-dimensional defects, which can be one-, two- or three-dimensional according to their structure and lead to different interfacial energies. One-dimensional line defects result from the displacement of single, limited lattice lines (dislocation line) by the lattice constant a_0 and the stress-compensating deformation of the surrounding lattice, so that one side is compressed (increased pressure) and the other side is stretched (lower pressure). The direction of the dislocation is described by the so-called Burgers vector $\vec{b}$. If this is perpendicular to the dislocation line, it is called an edge dislocation. If, on the other hand, it runs parallel to the dislocation line, a screw dislocation occurs. The dislocation density in high-purity silicon crystals is approximately $1 \times 10^2\,\mathrm{cm}^{-2}$ and can attain up to $1 \times 10^{12}\,\mathrm{cm}^{-2}$ in the case of strongly deformed metals [47].
Two-dimensional surface defects form at interfaces between regions of different physical
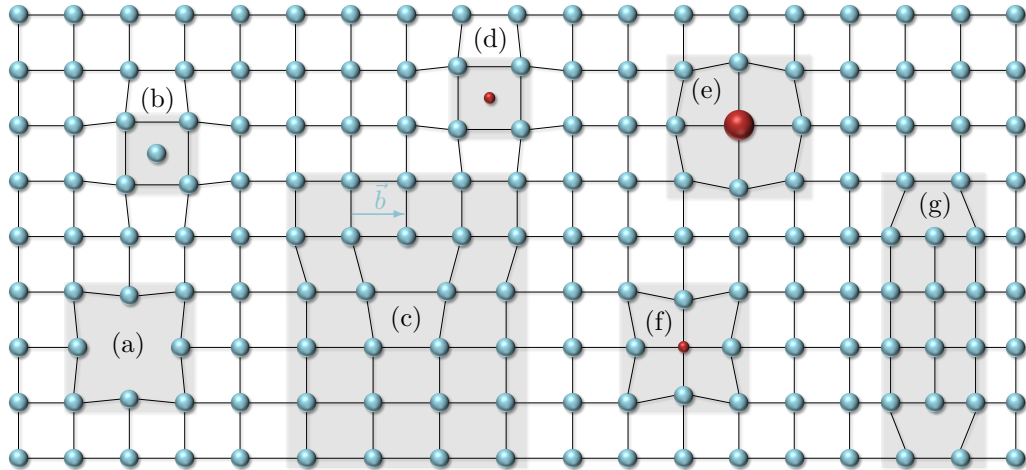
Figure 2.4 Different defects in a two-dimensional crystal lattice illustration. (a) vacancy, **(b)** self-interstitial, **(c)** edge dislocation with vertical Burgers vector, **(d)** interstitial impurity, **(e)** large substitutional impurity, **(f)** small substitutional impurity **(g)** extrinsic dislocation loop. The distortions of the surrounding crystal atoms are only exemplary here, since in nature both the size and the charge of the atoms involved determine whether the surrounding lattice moves towards the defect or away from the defect. Adapted from [52].

and chemical properties. For example, the surface of a crystal can be viewed as an interface between the crystal lattice and a gaseous or liquid phase, where unsaturated dangling bonds form or other impurities (e.g. oxygen or phosphorus) aggregate (see Ch. 6). If single-crystalline regions of different orientations or compositions meet within a solid, the interfaces are called grain boundaries in the first case and two-phase interfaces in the second case (e.g. in SOI material). The different properties of the various phases lead to lattice distortions at the interfaces and thus to anisotropic surface tensions. Furthermore, dislocations can occur between surfaces, that are stacked on each other ("stacking faults"). These dislocations also occur perfectly periodically in nature (preferably with alternating fcc-hexagonal close-packed (hcp) or α-wurtzite and β-wurtzite packing, respectively), from which it can be concluded that they have an energetically favorable shape. The resulting new crystal structures may also have useful properties and accordingly play a role in technological applications.

Three-dimensional volume defects can be divided into four classes according to their size and effect [53]. Again, there are desirable defects like precipitates (size $< 1\,\mu$m) and dispersants (size $1 - 100\,\mu$m), which are used for targeted variation of electronic and mechanical properties, but also undesirable defects (inclusions and voids/pores with both microscopic and macroscopic sizes), which are detrimental to microelectronic devices and mechanical stability.

2.2.3 Doping

Depending on the purity of semiconducting materials, they tend to be insulating or conducting ("intrinsic conductivity"). Silicon can be produced with the highest purity, having an impurity concentration of about $1 \times 10^{12}\,\mathrm{cm}^{-3}$ or a carrier concentration of $n_i = 1.5 \times 10^{10}\,\mathrm{cm}^{-3}$. By introducing impurities into a semiconductor ("doping"), additional free charge carriers can be generated in the crystal and thus influence the conductivity.
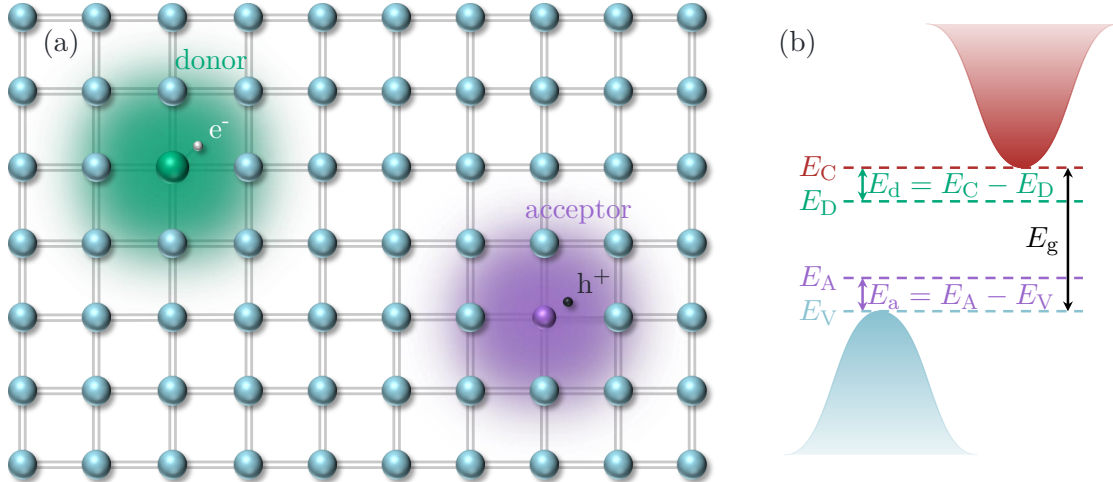
Figure 2.5   Effect of doping on the bandgap of a semiconductor. (a) In the regular silicon crystal lattice, all covalent bonds (double lines) are saturated. By introducing dopants into the semiconductor, weakly bound electrons or holes are created, which are promoted to the conduction band or valence band by a low ionization energy of $E_d \sim E_a \sim 30\,\text{meV}$ in silicon **(b)**, thus increasing the conductivity of the semiconductor [47].

Elements for doping, which provide additional electrons (e) for the conduction band, are called donors and mostly come from the V. main group of the periodic system of elements (PSE) (mainly phosphorus and arsenic with a total of five valence electrons), while elements which create additional holes (h) in the valence band are called acceptors and come from the III. main group of the PSE (mainly boron with three valence electrons). These three or five valence electrons fill the tetrahedral covalent bonds of the tetravalent crystal atoms in silicon, leaving either an excess electron or a hole at tbe defect. In this process, additional energy levels are formed in the bandgap which are located either near the conduction (donor) or valence band edge (acceptor), respectively. This results in a low (thermal) energy expenditure (ionization energy $E_d \simeq E_a \simeq 30\,\text{meV}$) needed to release the charge carriers from the dopant, thus increasing the conductivity (Fig. 2.5).

2.3 Luminescence from silicon

2.3.1 Optical properties of bulk silicon

The optical properties of a semiconductor can be derived from the electronic ones. The imaginary part of the dielectric function is related to the absorption coefficient α of the material and the real part to the dielectric constant ε. By measuring the dependence of the absorption coefficient α on the photon energy $E = h\nu$, it is possible to determine whether the semiconductor has a direct [54]

$$\alpha \approx A \cdot \sqrt{h\nu - E_g} \tag{2.9}$$

or indirect [55]

$$\alpha \propto \frac{(h\nu - E_g + E_P)^2}{\exp\left(\frac{E_P}{k_B T}\right) - 1} + \frac{(h\nu - E_g - E_P)^2}{1 - \exp\left(-\frac{E_P}{k_B T}\right)} \tag{2.10}$$

bandgap, where A is a frequency-independent constant, h is Planck's constant, ν is the frequency of the photons, E_g is the bandgap energy, k_B is the Boltzmann's constant, T is the temperature and E_P is the energy of the phonon involved in the transition. Thus, one obtains a linear relationship between α^2 and $h\nu$ for direct bandgaps, and a linear relationship between $\alpha^{1/2}$ and $h\nu$ for indirect bandgaps.

Since electrons in direct semiconductors like gallium arsenide (GaAs) can be very easily excited into the CB, the radiative recombination rate is very high (order of $2 \times 10^7\,\text{s}^{-1}$) and the lifetime is correspondingly short (nanoseconds). In untreated indirect semiconductors, on the other hand, the probability of recombination is much lower (order of $1 \times 10^2\,\text{s}^{-1}$) and the lifetime of the excited state is in the range of milliseconds due to the necessary additional momentum from a phonon. The internal quantum efficiency of electronic grade silicon is therefore in the order of $\eta_\text{int} \approx 10^{-6}$ [57]. If one wants to extract light efficiently from silicon, the probability of recombination must be increased accordingly, e.g. by either manipulating the phonon wave vector **k** or the band structure. In addition to the indirect bandgap, other competing electron-hole recombination processes also contribute to the poor luminescence efficiency (Fig. 2.6), as they further reduce the radiative recombination rate. The internal quantum efficiency of a semiconductor can be expressed via [56]

Figure 2.6 Recombination paths in silicon. Due to the indirect bandgap of silicon, radiative e-h recombinations have a long lifetime (in the order of milliseconds), resulting in a low probability. Since the non-radiative recombination lifetime τ_NR of other recombination processes is in the range of a few ns [56], most excited e-h pairs recombine non-radiatively. Adapted from [57].

$$\eta_\text{int} = \frac{\Gamma_\text{r}}{\Gamma_\text{r} + \Gamma_\text{nr}} = \frac{\tau_\text{nr}}{\tau_\text{r} + \tau_\text{nr}} \tag{2.11}$$

where $\Gamma_\text{r} = \tau_\text{r}^{-1}$ is the decay rate of the radiative transition and τ_r describes its lifetime, whereas τ_nr is the lifetime of the recombination processes that take place without the formation of a photon. The total non-radiative recombination rate is the sum of all different non-radiative processes and can be calculated with

$$\frac{1}{\tau_\text{nr}} = \sum_i \frac{1}{\tau_\text{nr,i}} \tag{2.12}$$

and is of the order of microseconds for silicon. According to Eq. (2.11), τ_r must be significantly shorter than τ_{nr} to achieve high radiative efficiency. Competing non-radiative recombination processes are shown in Fig. 2.6 and include:

- **free carrier absorption** - direct excitation of charge carriers into the same energy band, where they are free to move

- **Auger recombination** - energy from a e-h recombination is given to an electron in the CB, where it loses its energy to thermal vibrations

- **Shockley-Read-Hall (SRH) recombination** - non-radiative interband transistion via localized energy states in the bandgap caused by dopants and defects

- **surface recombination** - dangling bonds on the crystal surface act as traps for recombination centers

Thus, bulk Si has a very low quantum efficiency and is therefore rather unsuitable as a basis for light-emitting components. However, there are processes that increase the recombination rate of radiative transitions or suppress the non-radiative transitions. Some of these will be briefly described below.

2.3.2 Non-linear effects in silicon

Although silicon appears unsuitable for optical applications due to its indirect bandgap, various non-linear optical processes can take place in a silicon crystal by which light can not only be generated but also detected and processed [6]. Non-linearities in silicon arise from the interaction of the electric field component of an electromagnetic wave with the outer electrons of the crystal atoms. These electrons resonate with the incident wave, resulting in a dipole oscillation $\vec{P}(\vec{E})$ of the atom. The relationship between the generated polarization $\vec{P}(t)$ and the electric field $\vec{E}(t)$ of the wave can be explained via the Taylor series

$$\vec{P}(t) = \varepsilon_0 \cdot (\underbrace{\chi^{(1)}\vec{E}(t)}_{\substack{\text{linear} \\ \text{polarization} \\ \text{vector}}} + \underbrace{\chi^{(2)}\vec{E}^2(t) + \chi^{(3)}\vec{E}^3(t) + ...}_{\substack{\text{non}-\text{linear} \\ \text{optical effects}}}) \qquad (2.13)$$

where ε_0 is the vacuum permittivity and $\chi^{(i)}$ is the optical susceptibility ith-order. This formula is the approximate solution of an inhomogeneous differential equation derived from Maxwell's equations and solved by Green's functions. The susceptibilities $\chi^{(i)}$ are tensors of rank $(i+1)$ and determine [6]

- whether the relation between wave and polarization is linear or non-linear.

- whether the electric field causes a phase shift

- whether there is absorption or amplification of the incident field, and

- whether waves of a different frequency are generated.

$\chi(1)$ **processes**

The first-order susceptibility of Eq. (2.13) describes the excitation of a dipole with free or bound electrons by a single photon and the associated change in the refractive index. $\chi^{(1)}$ is a complex number whose real part is related to the real part of the refractive index of the crystal and whose imaginary part describes an attenuation or amplification. Hendrik Antoon Lorentz and Paul Drude developed a model that describes the proportion of bound and free electrons in the susceptibility. According to the Lorentz model, the change in the

refractive index in bound states is particularly strong in the vicinity of a resonance ω_{L} and the following equation applies

$$\chi^{(1)}_{\mathrm{Lorentz}} = \frac{\omega^2_{\mathrm{L}}}{\omega^2_0 - \omega^2 + i\gamma_{\mathrm{L}}\omega} \tag{2.14}$$

with the Lorentz plasma frequency $\omega^2_{\mathrm{L}} = Ne^2/\epsilon_0 m^*_{\mathrm{e}}$ [6]. ω_0 is the resonant frequency of the bound state, γ_{L} is an associated damping constant, N is the density of the dipoles and m^*_{e} is the effective mass of the oscillating charge.

The susceptibility $\chi^{(1)}$ in semiconductors is also influenced by free charge carriers. These absorb photons and recombine non-radiatively in the process. This can be derived via Eq. (2.14), where the resonance frequency of the bound states must of course be omitted. This leads to the so-called Drude model which is expressed by

$$\chi^{(1)}_{\mathrm{Drude}} = \frac{\omega^2_{\mathrm{p}}}{-\omega^2 + i\gamma_{\mathrm{D}}\omega} \tag{2.15}$$

with the plasma frequency $\omega^2_{\mathrm{p}} = Ne^2/\epsilon_0 m_{\mathrm{e}}$ and $\omega_{\mathrm{L}} \neq \omega_{\mathrm{p}}$. Since both forms of charge carriers (bound and free) occur in silicon, both influence the complex refractive index and it is

$$n^2 = 1 + \chi^{(1)}_{\mathrm{Lorentz}} + \chi^{(1)}_{\mathrm{Drude}}, \tag{2.16}$$

so that the refractive index in semiconductors depends on both the incident wavelength and the total charge carrier concentration N [6]. In order to empirically determine the dependence of the refractive index on the free and bound charge carriers, the so-called Sellmeier relation is used, which describes the material dispersion of silicon and is of great importance for the construction of photonic structures (waveguides). For silicon it takes the form [58]

$$n(\lambda) = \varepsilon + \frac{A}{\lambda^2} + \frac{B\lambda^2_{\mathrm{g}}}{\lambda^2 - \lambda^2_{\mathrm{g}}}, \tag{2.17}$$

where $\varepsilon = 11.6858$, $A = 0.9398\,\mu\mathrm{m}^2$ and $B = 8.1046 \times 10^{-3}$ are numerically determined values and $\lambda_{\mathrm{g}} = 1.1071\,\mu\mathrm{m}$ is the wavelength of the silicon bandgap. From this, one can see that the closer the photon gets to the bandgap energy of silicon, the stronger the change in refractive index becomes [6].

$\chi(2)$ **processes**

The second-order susceptibility from Eq. (2.13) is absent in centrosymmetric crystals such as silicon. However, since these processes allow the generation of electro-optic modulators in silicon that are not subject to carrier-dependent velocity constraints and could thus open up useful applications, methods are being developed to allow these processes to take place in silicon. For example, by depositing a voltage layer on the silicon surface, the crystal symmetry can be broken [59] or the photonic silicon structure can be embedded in a $\chi^{(2)}$-active, electro-optic polymer cladding [60]. An important application of such processes is the creation of entangled photon pairs by spontaneous parametric down-conversion (SPDC) for the development of linear optical quantum computing (LOQC) with the Knill-Laflamme-Milburn (KLM) protocol [23, 11, 61] (see Sec. 3.3.2).

$\chi(3)$ **processes**

The third-order processes are the most important non-linear optical processes in silicon, since the associated relaxation processes are almost instantaneous and thus extremely fast, and a large number of useful effects are associated with them. The third-order polarization, $\chi^{(3)}E^3(t)$, leads to a variety of wave mixing and wave coupling processes, which are briefly presented below [6, 61].

- **Self-phase modulation (SPM)** originates from dipole excitations induced by three photons and leads to an intensity-dependent change of the refractive index n_2, that causes broadening of the pulse spectrum even up to a supercontinuum. The involved photons can also excite higher states by a two-photon absorption (TPA) process. The latter generates free carriers in the conduction band that can in turn cause changes of the refractive index (see $\chi^{(1)}$ processes). The main application for this process is the generation of ultrabroadband spectra ("supercontinuum"), which can be used in optical coherence tomography, frequency metrology at high accuracy or all-optical signal regeneration for efficient transmission of signals over very long distances.

- **Cross-phase modulation (XPM)** In XPM, the wavelength of a first photon affects the refractive index of the medium through the Kerr effect. These new conditions will influence the wavelength of a second photon. By this, XPM finds important applications for phase-matching and dispersion engineering of SOI waveguides.

- **Third-harmonic generation (THG)** In THG, three photons with the same frequency ω_0 interact with the non-linear material, are combined and generate a new photon, with a frequency equal to $\omega_n = 3 \times \omega_0$. This effect works also for two and four photons, but with even numbers, the medium must have no center of symmetry. Harmonic generation is theoretically also possible at photon numbers > 4, but due to the high number of interacting photons, higher harmonics have very low probabilities. Due to the centrally symmetrical crystal structure of silicon, only THG takes place in this medium. It offers application in scanning microscopy, light emission, optical performance monitoring or material and signal processing [61].

- **Four-wave mixing (FWM)** is an ultrafast process where one photon (frequency ω_j) is generated from three incident photons with frequency ω_i. This process has a wide range of applications like wavelength conversion [62–64], parametric amplification and sampling. Furthermore, spontaneous FWM generates entangled photon pairs, that can be used as photonic qubits for the creation of a scalable quantum computer solely based on linear optical tools [61] (see Sec. 3.3.2).

- **Stimulated Raman scattering (SRS)** In SRS, a photon with the Stokes-shifted frequency $\omega_S = \omega_P - \Omega_R$ is created from the annihilation of a pump photon. $\hbar\Omega_R$ corresponds to the phonon excitation energy. The electromagnetic wave interacts with a crystalline lattice wave by inelastic scattering, leading to an frequency shift and energy gain. This process has already been used to demonstrate amplification [65–68] and lasing [69–71] from silicon.

2.3.3 Dislocation loops

Dislocation loops (DL) are extended interstitial defects in a crystal. They cause a mono-atomic layer of crystal atoms to be enclosed by the rest of the lattice (Fig. 2.4). Such defects can be created, for example, by ion implantation with foreign or intrinsic ions [72, 73] and suppress thermal quenching in silicon. Thus, dislocation loops have already been used to improve the efficiency of silicon-based LEDs [74] or to demonstrate electroluminescence (EL) of the silicon band edge at room temperature [75]. The atoms located at the edge of the dislocation loops are forced apart, creating a negative hydrostatic pressure at the edges of the loop of up to -50 GPa [33]. The pressure dependence, as shown in Fig. 2.7 (a), can be calculated from the elasticity theory of dislocations [76], as well as Young's modulus and Poisson's ratio [77]. Since the bandgap energy of semiconductors is pressure-dependent, it is shifted due to the DL-induced pressure. In the case of silicon, increasing pressure leads to a decrease in the bandgap energy of ≈ -14 meV/GPa [78] between the conduction band minimum (X point) and the valence band maximum (Γ point). Due to the negative hydrostatic pressure of -50 GPa caused by the DL, the bandgap energy at the location of the loops increases by ≈ 0.7 eV. According to [79], this potential barrier prevents charge carriers from diffusing to defects in the bulk and on the surface of the crystal, where they could recombine non-radiatively, thus leaving them only the path via radiative recombination as illustrated for a forward biased pn junction in Fig. 2.7 (b).
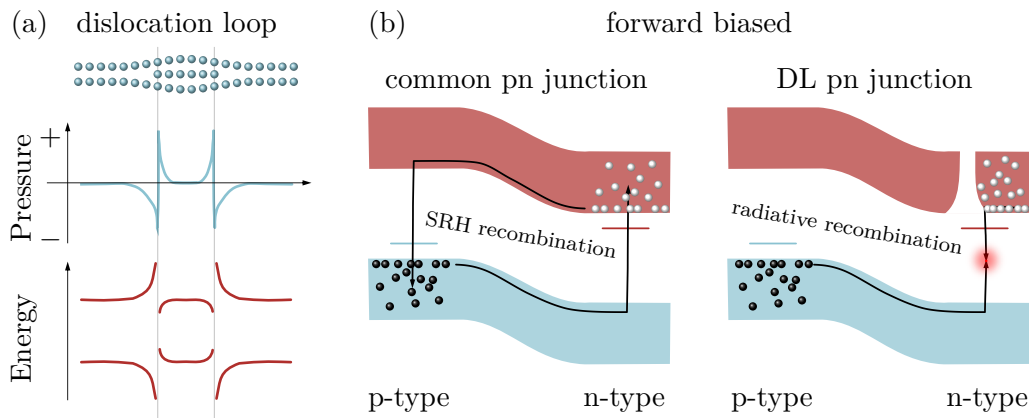
Figure 2.7 Description of dislocation loops. (a) Due to the higher concentration of atoms, areas of strongly increased or decreased pressure arise at the boundaries of the dislocation loops. **(b)** Since the band structure is pressure-dependent, it is strongly deformed in the respective areas, so that diffusion to non-radiative recombination centers is impeded and thus the probability of radiative recombination is increased. Graphics adapted and recreated with permission of *Elsevier* from [79].

2.3.4 Quantum confinement effects

Quantum confinement effects can be used to increase the rate of radiative or to suppress non-radiative transitions, so that LEDs with high efficiency and lasing can be realized with them. Quantum confinement refers to the generation of energy states due to a spatial restriction on the motion of an electron. In the simplest case of an one-dimensional potential well of width w and infinitely high energy barriers, the Schrödinger equation is defined as

$$-\frac{\hbar^2}{2m}\frac{\mathrm{d}^2\Psi(x)}{\mathrm{d}x^2} = E\Psi(x) \tag{2.18}$$

or

$$\frac{\mathrm{d}^2\Psi(x)}{\mathrm{d}x^2} + k^2\Psi = 0 \tag{2.19}$$

respectively with $k^2 = \frac{2mE}{\hbar^2}$. The solutions of this differential equation are waves of the form $\Psi(x) = \sin(k_j x)$ with $k_j = j\frac{\pi}{w}, j \in \mathbb{N}$, each having the energy

$$E_j = \frac{\hbar^2 k_j^2}{2m} = \frac{\hbar^2 j^2 \pi^2}{2mw^2}. \tag{2.20}$$

This means the smaller the width of the potential well w and the mass m of the electron, the higher discrete energy levels are produced by the spatial confinement. However, this effect only comes into play when the width of the potential well corresponds approximately to the de Broglie wavelength λ_B of the electron with the effective mass m_e^* in the silicon lattice, which at RT takes the value [80]

$$\lambda_B = \sqrt{\frac{2\pi\hbar^2}{m_e^* k_B T}} \approx 5\,\mathrm{nm} \tag{2.21}$$

However, some simplifications were made in this illustration. For example, in a real semiconductor the potential well is not infinitely high, which leads to tunneling effects, and confinement can occur in different dimensional degrees (0D, 1D, 2D, 3D). As shown in Fig. 2.8, confinement does not occur in a spatially extended three-dimensional bulk crystal because there is no spatial constraint and the energies are distributed over two broad, continuous bands. In two-dimensional quantum wells (1D confinement) and one-dimensional quantum wires (2D confinement), overlapping subbands arise, which become narrower as the confinement increases. In zero-dimensional quantum dots (3D confinement), all degrees of freedom of the electron motion are quantized and discrete, separated energy levels arise, whose densities of states can be described by δ-functions [81]. In reality, however, the absorption and emission lines of such quantum dots also show a natural, homogeneous line broadening, which can be represented by a Lorentz function. The more quantum dots there are, the broader the linewidth becomes. If, in addition, quantum dots of different sizes are distributed inhomogeneously, the absorption/emission spectrum shows several lines due to the different energy levels, which are Gaussian distributed and thus, in addition to the homogeneous broadening, produce the real absorption/emission spectrum of a quantum dot ensemble. In order to create low-dimensional structures in silicon and to use the resulting quantum confinement effects for the generation of light, there are various possibilities, which will be briefly explained below.

Porous silicon

2D confinement effects occur in porous silicon and exhibit room temperature luminescence in the visible wavelength range [83, 84]. Porosity is produced by electrochemical anodisation of mostly p-doped silicon in a $50\,\%$ mixture of hydrofluoric acid and ethanol. The porosity or size of the nanostructures depends on the current density used and the concentration of implanted charge carriers. In lightly p-doped silicon, the average structure size is $2 - 5\,\mathrm{nm}$, while in heavily p-doped silicon it is about $10\,\mathrm{nm}$. Since the exciton Bohr radius in silicon is
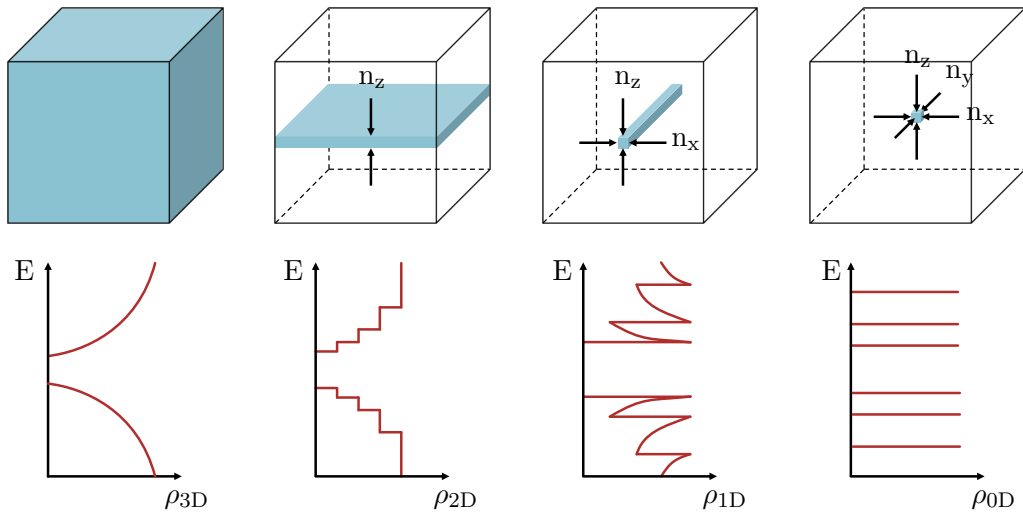
Figure 2.8 Illustration of the quantum confinement effect. A spatially trapped electron performs oscillations thats energy and density of states (DOS) ρ depends on the size of the potential well. As the confinement of the electron increases (the size of the potential well decreases, respectively), the broad energy bands first develop into overlapping sub-bands, which become narrower and ultimately lead to individual, discrete levels at the quantum dot. Graphic adapted from [82].

4.3 nm, confinement effects, especially PL efficiency, are more pronounced in lightly doped Si, while in highly doped Si the luminescence can be tuned over a larger range [85]. Although porous silicon offers some disadvantages (e.g. broad linewidths, poor long-term stability due to desorption of H_2 molecules, generation of non-radiative recombination paths due to dangling bonds at the surfaces [86]) that lead to electronic and optical losses, which reduces their suitability for photonic applications, various optical devices have been realized from it in the past. These include, among others:

- **Photonic structures** Multilayer systems like Fabry-Perot structures or distributed Bragg reflectors are used for narrowing and strengthening the PL signal and controlling the emission direction [87–90]

- **Sensors** Due to the sponge-like structure and the associated large surface area, porous Si is highly reactive and can be used, for example, as a sensor for biological molecules like DNA or lipids [91, 92]

- **LEDs** An electrically driven PL signal was already reported in 1991 and further improved by integrating a bipolar transistor or an electrochemical oxidation treatment, leading to an achieved external quantum efficiency of greater than 1% and a power efficiency of 0.37% [93–96]

Nanocrystals and quantum dots

For the production of silicon nanocrystals (NC) with spatial dimensions of a few nanometers, various possibilities exist, of which the following are the most common and most successful ones [5]:

- **Production of nanoclusters in SiO_x structures with x < 2.** Silicon is enriched by magnetron sputtering, chemical vapour deposition (CVD) or implantation of high

Si fluences into SiO_2 layers. Subsequent annealing at $> 1000\,°C$ leads to phase separation of Si and SiO_2 and the formation of Si nanoclusters by a so-called Ostwald ripening [97–100].

- **Production of superlattices** of alternating SiO_x and SiO_2 layers by plasma enhanced CVD, sputtering or reactive evaporation [101–104].

- **Production of colloidal solutions** of Si nanocrystals from porous Si, plasma-synthesized powders or directly synthesized by sol-gel or wet-chemical processes [105–107]

Depending on the process parameters such as silicon and oxygen concentration, dopants, annealing temperature and annealing time, the size of the nanocrystals can be varied and a large, tunable range of wavelengths can be generated through the confinement effect, which emit very stably and with high quantum yield. Since the influence of the surface becomes increasingly important as objects become smaller, the band structure can also be influenced by changing the arrangement of the surface atoms in a controlled manner. By combining both effects, the recombination rates of radiative and non-radiative transitions can be varied or even a transformation from indirect to direct bandgap can take place. Thus, RT photoluminescence can be generated in Si-NC with sizes of $2.5 - 5.5\,nm$, that emit photons of wavelengths between $\lambda \approx 400 - 1100\,nm$ [108, 109] and whose quantum yield can be increased by up to three orders of magnitude compared to bulk Si (from 10^{-7} to 10^{-4}) [5, 110].

Photonic crystals

Two-dimensional photonic structures such as waveguides, nanocavities or microdisks allow the creation of light in silicon that is emitted into the third dimension by total internal reflections [111, 112]. These structures are fabricated in SOI material by relatively simple and widely used tools, namely EBL and reactive ion etching (RIE). This makes the fabrication of such structures CMOS-compatible, so that they can be manufactured industrially on a large scale. In combination with non-linear photonic effects and other light-generating processes, these structures can be used to realize a wide range of optical components in silicon and cover a broad spectrum of wavelengths in the IR range and applications. Thus, electronically operated and efficient light-emitting devices could already be fabricated, which operate at room temperature and produce narrow linewidths in the technologically important range of $\lambda = 1300 - 1600\,nm$ [113–115]. Since the electromagnetic field intensity and the light-matter interaction depend mainly on the ratio of the quality factor Q and the modal volume V, nanophotonic structures with high Q factors ($\geq 4 \times 10^6$) and volumes of $< (\lambda/n)^3$ are targeted [5, 116, 117]. The goal is to be able to create structures in which single photons can be manipulated by non-linear processes, thereby realizing single-photon sources at room temperature on nanophotonic microchips and thus bridging the gap from silicon photonics to quantum optics and quantum communication.

2.3.5 Rare-Earth (Erbium) doping

Rare earth elements can be used as light-emitting centers due to their particular electron shell. Optical transitions take place in the incompletely occupied 4f shell of the triple positively charged ions [118], which are shielded by the larger, also occupied 5s, 5p and 6s

shells. As a result, no band structure is formed for the f orbitals and discrete energy levels are created between which electrons can be exchanged. The resulting luminescence depends mainly on the rare earth itself and only to a small extent on the surrounding crystal field. Erbium is of particular interest in this context, since the electronic transition $^4I_{13/2} \rightarrow^4 I_{15/2}$ of the Er^{3+} ion emits light with a wavelength of $\lambda = 1535$ nm, which is in the telecom C-band with highest transmission. Light from erbium atoms in optoelectronic devices would accordingly enable maximally efficient and low-loss optical data transmission.

Erbium ions can be introduced into silicon, for example, by ion implantation [119, 120], molecular beam epitaxy (MBE) [121, 122], or magnetron sputtering [123]. However, the use of rare earths as optically active centers in silicon is complicated by the fact that these large atoms have poor solubility in the crystal and non-radiative processes decrease the recombination rate and thus the emission efficiency [124]. Silicon is considered a poor host material for erbium ions because of an energy back-transfer from the Er^{3+} ions to the Si host. This occurs due to a resonant level created by erbium doping in the silicon bandgap, which couples to the Er^{3+} states [57]. However, due to the promising optical properties of erbium, many efforts have been made to make these elements useful for optoelectronic photonic applications.

The first erbium-based LED was introduced by Zheng et al. in 1994. However, their intensity suffered strongly from temperature quenching (decrease of luminescence by three orders of magnitude when heated from 77 K to RT), which, however, according to [118], can be significantly reduced by oxygen co-doping (PL decrease only by a factor of 30). Thus, the photo- as well as electroluminescence of the Er^{3+} could be improved at RT and based on this, an efficient LED was demonstrated in [125]. The luminescence can also be enhanced and stabilized by embedding the erbium atoms in a SiO_2 matrix that simultaneously contains silicon nanocrystals [56]. According to [126], a Si-NC captures an exciton, that recombines within the Si-NC, releasing the energy to an erbium ion nearby. This energy is sufficient to lift an electron of the erbium ion from the ground state to the first excited state, which in turn emits the 1535 nm radiation upon relaxation (Fig. 2.9). The development of Er-
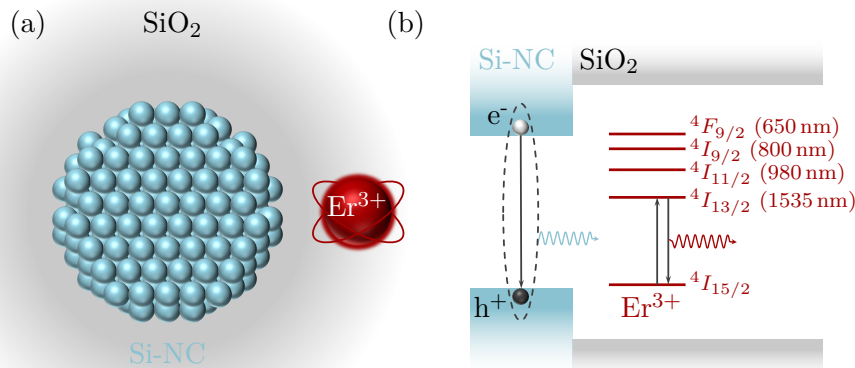
Figure 2.9 Principle of erbium PL enhancement by silicon nanocrystals. (a) A Si-NC within the SiO_2 matrix can trap optically excited excitons, that recombine and release its energy to a nearby erbium ion. **(b)** The Er^{3+} ion is thereby excited from the ground state to the first excited state. Graphic adapted with permission of *Springer Nature* from [126], values taken from [57].

doped SiO_2 microresonators on Si chips already enabled CMOS-compatible fabrication of silicon-based lasers [127–129]. It was also shown by Yin et al. in 2013 that the charge state of individual erbium ions can be changed by optical excitation and readout electronically in a silicon-based single-electron transistor [130]. Despite the promising properties and many advances in the creation of optoelectronic devices, there are some problems associated with the use of erbium [131]. The large amount of excitation and de-excitation processes makes it a complex system whose competing processes need to be better understood and controlled. In addition, rare-earth ions tend to aggregate, that is, they form larger clusters that enhance ion-ion interactions and thus reduce luminescence efficiency.

2.3.6 Light emitting defects in silicon

The first fundamental work on light-emitting effects in silicon was done by Watkins and Corbett between 1959-1965 [132–138]. Through various EPR and absorption measurements, many structural and quantum mechanical properties of numerous defects in silicon could already be investigated in more detail at that time. Some of these centers are summarized in Tab. 2.1. In this process, G centers were also discovered, that will be the main topic of the present work. In the following section, the most important of these defects will be presented and described before the main focus is placed on the properties and formation of G centers as they were known at the beginning of this work.

C center

The C center was first measured on electron-irradiated silicon in 1971 [139] and identified as the Si-G15 (K) center from EPR studies based on its energy level, annealing properties and dependence on oxygen concentration [140]. It consists of a $(C_iO_i)^+$ pair whose photoluminescence, similar to the G center, arises from a ZPL transition at an energy of ≈ 789 meV or a wavelength of ≈ 1570 nm. According to [141], the transition takes place between unthermalized excited singlet ($S = 0$) and triplet ($S = 1$) states with a lifetime of the excited state of $\tau = 2.3$ µs at 3 K. In contrast to G centers, which are destroyed at temperature higher than 200 °C, this defect is more resistant to high temperatures. According to [142, 143], the C center intensity reaches a maximum at an annealing temperature of about 250 °C, but subsequently decreases at higher temperatures and disappears completely from a temperature of ≈ 330 °C [33].

W center

The W center is a purely intrinsic defect in silicon which is formed by the implantation of silicon ions into a silicon crystal [144]. It is thought to have a trigonal structure [145] and to form a quantum center through three interstitial Si (I_3) whose ZPL energy is $E = 1018$ meV or $\lambda = 1218$ nm, respectively [146–149]. It was first observed in boron- and phosphorus-implanted float-zone (FZ) silicon in 1976 [150, 151] and has already been used to create waveguide-integrated LEDs by implanting W centers in the intrinsic part of a p-i-n diode [152, 153].

In a recent unpublished work within our project [158], we were able to detect the first isolated W centers and thus gain new insights into this purely intrinsic defect. Thus, it could be shown that W centers exhibit strong antibunching (see Sec. 3.2.1) and possess a metastable triplet state that makes them potentially ODMR active. Polarization measurements on individual W centers show a clear alignment of the dipole emission along the along

Center	Energy	Wavelength	Composition
M-line [143]	761 meV	1630 nm	C-H
P-line [143]	767 meV	1617 nm	O-pertubated C-line
C-line [143]	790 meV	1570 nm	C_i-O_i
A-line [154]	856 meV	1448 nm	C_i
H-line [143]	926 meV	1340 nm	C-O
T-line [143]	935 meV	1326 nm	C-H
G-line [50]	970 meV	1279 nm	C_i-C_s
W-line [146]	1018 meV	1218 nm	Si_i
X-line [143]	1040 meV	1192 nm	tetrainterstitial
O^j-line [155, 156]	1052 meV	1179 nm	Oxygen
1096.9 meV-line [157]	1097 meV	1130 nm	self-interstial + O
J-line [143]	1107 meV	1120 nm	hexavacancy + H
$O^{j'}$-line [155, 156]	1117 meV	1110 nm	Oxygen

Table 2.1 Overview of different defect centers in silicon. These centers are created by high-energy irradiation of crystalline silicon. The intrinsic concentration of carbon, oxygen and hydrogen in combination with silicon interstitials and an appropriate annealing treatment leads to a variety of defect centers, which can be detected by PL, IR absorption, deep-level transient spectroscopy (DLTS) or positron annihilation measurements.

$[1\bar{1}0]$ or $[110]$ axes, so that the defect aligns in the silicon crystal at two preferred directions whose probabilities are equal. Furthermore, the statistical variation of the ZPL energy for individual centers is in the range of < 1 meV, leading to the assumption that the centers have a low sensitivity to their surroundings. This is an important property for the generation of indistinguishable photons and thus for the construction of long-range quantum networks. Different saturation behaviors of the individual defects indicate that there are various configurations and charge states of the defect, which however become unstable with increasing temperatures. The excited state lifetime of individual W centers is unusually lower than in the ensemble ($\tau^{\text{ens}} = 34.5$ ns, [146]) and in the range of $\tau^{\text{sin}} = 3 - 30$ ns. The fluctuations of τ are probably related to excitation-transfer mechanisms between W centers and nearby non-radiative recombination centers. Density functional theory (DFT) calculations of the crystal and energy structure have shown that among the different possible structures of the I_3 configuration, the $I_3 - V$ agrees best with experimental data like local vibrational mode (LVM), symmetry and formation energy. The neutral W^0 state is located just below the VB edge, but is shifted by ionization into W^+ in the bandgap, where it can be occupied by a hole that subsequently attracts an electron through the Coulomb interaction. The exciton thus formed recombines to produce the ZPL with very good agreement between experimental and theoretical energy values. W centers are more heat-resistant than e.g. G centers. Thus, their concentration increases at annealing temperatures of 300 °C [159], while G centers are destroyed at this temperature. On the other hand, they show significant quenching already at temperatures of $T \gtrsim 45$ K, which is more pronounced than for G centers.

T center

The T center, which was first investigated in 1981 [160], is currently experiencing a strong increase in interest and major developments. According to ab initio cluster calculations, the structure is built from an interstitial C-H defect that binds to a substitutional C atom [161]. Due to the hydrogen atom, the defect has an unpaired electron dangling bond to the second carbon atom and a monoclinic I (C_{1h}) symmetry. The ZPL has an energy of $E = 935\,\text{meV}$ or a wavelength of 1326 nm and shows isotopic splitting between ^{12}C and ^{13}C, as well as local mode satellites ("L_j"). The T center remains stable over a temperature range of $400 - 600\,°\text{C}$. It is formed by high-energy electron irradiation followed by an annealing step at $450\,°\text{C}$. According to recent work, it has an unpaired electron in the neutral ground state and an additionally bound exciton in the excited state ("TX"). Due to the reduced symmetry of the defect, the excited state splits into the two levels TX_0 and TX_1, which have a separation of $\Delta E = 1.76\,\text{meV}$. Due to its energetic structure, the T center is ODMR-active and exhibits both energy level splitting and Rabi oscillations [162].

2.4 G centers in silicon

2.4.1 Structural properties and creation of G centers

The G center is a bistable defect in silicon, which consists of two carbon atoms connected by a silicon atom. Bistable means that two stable configurations (A- and B-form) exist. In the A-form, one carbon atom is located on a substitutional lattice site and one adjacent silicon and carbon atom are located around a second substitutional site (C_s-Si_i-C_i). In contrast, in the B-form, both carbon atoms are on substitutional lattice sites and one silicon atom is pushed to an interstitial lattice site (C_s-Si_i-C_s), with the covalent bond to the neighboring Si atom switching to the substitutional carbon. Fig. 2.10 shows the crystallographic structure of both forms. In the literature, the defect is often also commonly referred to as the $C_i C_s$ complex. Recent theoretical studies based on first-principle DFT and many-body perturbation theory (MBPT) calculations assume that two additional forms (C- and D-form) exist, which, however, have not yet been observed experimentally [163, 164].

The formation of G centers is described by the Watkins exchange mechanism [165–167]. Silicon always contains impurities with carbon atoms occupying predominantly substitutional lattice sites (C_s) in silicon. Mobile silicon interstitials (Si_i), which are formed, for example, by high-energy electron, gamma, or ion irradiation, are captured by C_s, displacing them from their lattice sites and thus forming mobile carbon interstitials (C_i). These continue to migrate through the lattice at room temperature and are eventually trapped by other defects. If carbon is the main impurity in the crystal, the C_i are predominantly trapped by C_s, and the $C_i C_s$ complex is formed. When these encounter another interstitial silicon, the previously described C_s-Si_i-C_s defect is formed.

With the help of extensive DLTS, EPR and PL measurements, the energy structure of the $C_i C_s$ complex was investigated in [37]. The corresponding configurational-coordinate energy diagram is shown in Fig. 2.11. Accordingly, the bistability comes from a simple molecular bond switching between the different forms, which requires only a small energy input of $\sim 0.02\,\text{eV}$ in all three charge states due to the chemical similarity between silicon and carbon. From this, the positions of the energy levels of the donor and acceptor states of the $C_i C_s$ complex were determined to be $E_c - 0.15\,\text{eV}$ and $E_v + 0.07\,\text{eV}$, respectively. The definition of a defect energy-level position with respect to the conduction (or valence) band
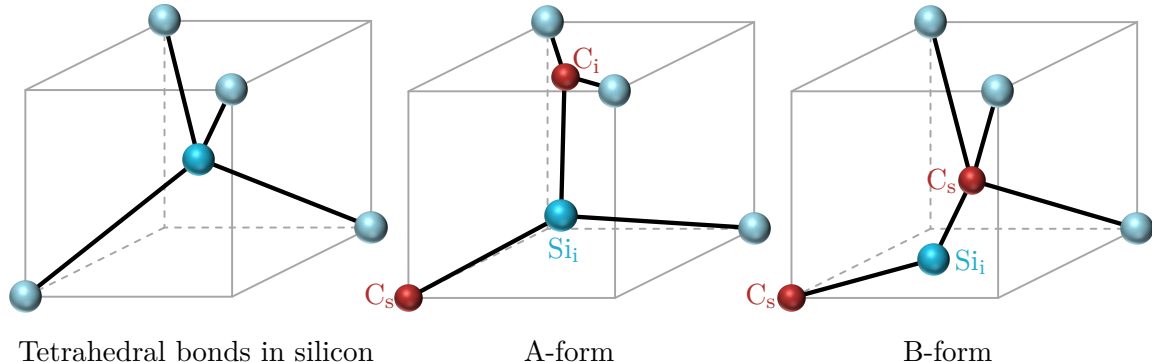
Figure 2.10   Comparison of the tetrahedral bonds of a silicon lattice with the A- and B-form of G centers. In the A-form, one carbon atom is on a substitutional lattice site and another carbon atom arranges itself around another substitutional lattice site together with a silicon atom bonded to another adjacent silicon atom. In the B-form, both carbon atoms are on substitutional lattice sites and displace the silicon atom to an interstitial lattice site. The bond to the neighboring silicon atom is transferred to the substitutional carbon [168].

edge is the total energy difference between the lowest energy state when the trap is filled and the lowest energy state when the trap is empty [37]. In the acceptor state, the energy-level position is given therefore by the energy difference between A^- and $B^0 + e^-$, whereas in the donor state it is determined by the difference between A^+ and $B^0 + h^+$. Note that the variety of defect structures and charge states of the G center and other carbon-related centers give rise to different signals in an EPR spectrum, that are often referred to in literature. The most discussed are the Si-G12 (C_i^+), Si-G11 ($C_iC_s^+$), Si-G15 ($C_iO_i^+$), Si-L6 (C_i^-), Si-G17 ($C_iC_s^-$ A-form) and Si-L7 ($C_iC_s^-$ B-form) [37].

The first concrete studies of G centers took place in the early 1960s by Watkins et al. on electron-irradiated, n-type FZ silicon [132,134,136,137]. Since the natural carbon content in silicon is large enough, high-energy irradiation with electrons, γ rays, neutrons, or protons was sufficient to form the required mobile silicon interstitials. However, recent works show that G centers can also be generated by other processes. For example in 2005, Cloutier et al. [169] produced G centers by nanostructuring an SOI sample using hydrofluoric based wet etching and RIE through a nanostructured anodic aluminum oxide (AAO) mask. In this process, the G centers are formed by the enhanced generation of the necessary silicon interstitials, which are formed when the crystal interacts with the energetic ion etchants. This principle was taken further in 2007 by Rotem et al. [168,170,171] and supplemented by enrichment of carbon via solid-phase epitaxial regrowth. This resulted in a 33-fold increase of the PL intensity in the nanostructured sample. In 2020, G centers of nanopatterned silicon were supplemented by a dielectric metasurface (periodic asymmetric holes fabricated by inductively coupled plasma (ICP) etching) by Zhu et al. [172], which achieved 40-fold enhancement and polarization state control of the PL intensity. Further, the surface of a silicon sample was coated with organic molecules hexamethyldisilizanes (HMDS) and the contained carbon was then incorporated and activated into the sample by a high-power laser with a spot diameter of $10\,\mu m$ in 2011 by Murata et al. [173]. These carbon atoms were introduced into depths of up to $600\,nm$ and a maximum carbon concentration of $4 \times 10^{19}\,cm^{-3}$ was achieved close to the surface, enabling the measurement of both strong PL and EL.
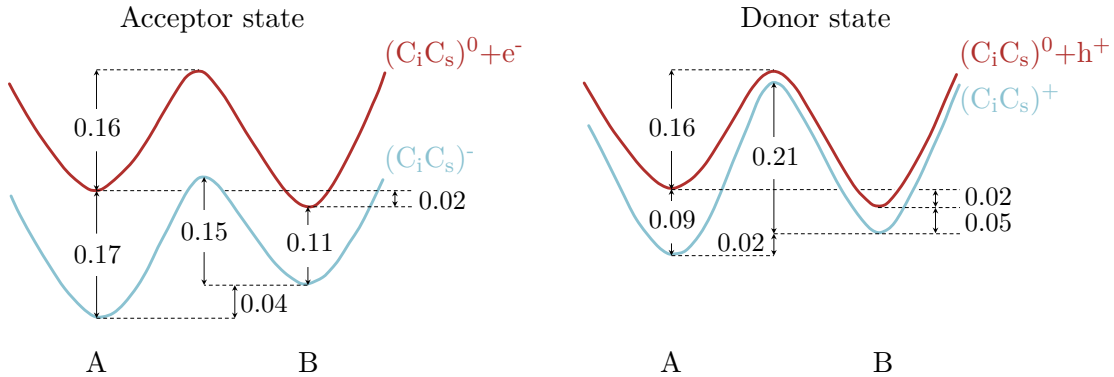
Figure 2.11   Configurational-coordinate energy diagram for the C_iC_s acceptor and donor states in A- and B-form. Due to the chemical similarity of both forms, the transformation between the A- and B-form takes place with low energy input. Numerical values are given in eV. This model was adapted with permission of *American Physical Society* from [37] and, however, does not consider lattice relaxation.

2.4.2 Optical properties and applications of G centers

G centers as defects can bind so-called Mott-Wannier excitons (isoelectronic, bound electron-hole pairs) by the following mechanism: the short-range defect potential of the C_iC_s complex first traps either an electron or a hole, which subsequently attracts a second particle of opposite charge due to its long-range Coulomb potential. Both charge carriers orbit each other according to their effective masses and eventually recombine, producing light with a characteristic spectrum [141]. The G-centers strong electronic zero-phonon transition has an energy difference of $E = 969\,$meV, that creates light with a wavelength of $\lambda = 1280\,$nm within the O-band of optical telecommunication (see Fig. 2.12), which makes G centers suitable for photonic and quantum applications. In addition to the ZPL, a broad emission band is found, which is caused by the emission of photons under simultaneous emission of phonons. Since the absorption of phonons during the process at low temperatures is much less probable than the emission, the phonon sideband (PSB) is asymmetric and formed in the direction of low energies. Furthermore, two other lines (E and E') are found in the spectrum of a G center, which are local vibrational modes of the carbon atoms in the C_s-Si_i-C_s molecule [36, 37]. The evaluation of ODMR measurements on the $0.97\,$eV line [35] and the already mentioned EPR measurements have shown that the luminescence is caused exclusively by the uncharged B^0 configuration of the defect. The associated mechanism is explained as follows: the G center is usually in a charged state of the non-radiative form A^-. Excitation with laser light results in enhanced bond switching and consequent conversion to the B^0 form, that captures the bound electron-hole pair. In [174], screened hybrid density functional theory was used to calculate the electronic structure, density of states (DOS), and formation energy of the various forms and charge states of the G center. Accordingly, in the A-form, the DOS for electrons and holes exhibit sharp peaks at the C_i- and Si_i-Atom, respectively, while in the B-form, the DOS for both charge carriers are strongly increased only at the silicon interstitial. The latter thus corresponds to a direct transition in real space with a shorter lifetime and could provide the explanation why only the B-form of the G center is optically active [151]. Lee at al. [34] performed stress-dependent ODMR measurements in 1982 on the $0.97\,$eV luminescence previously produced by neutron irradiation of an n-type silicon sample. Based on their results, they postulated
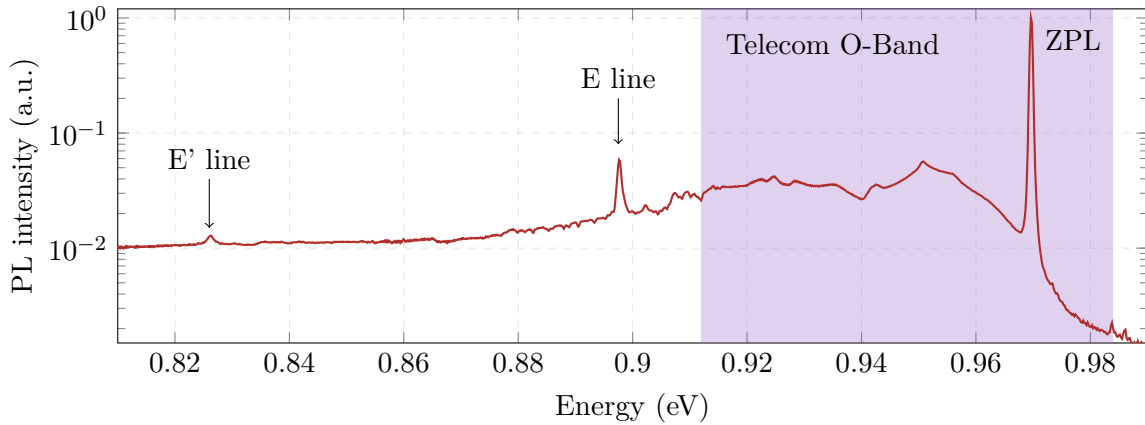
Figure 2.12 Typical normalized G center photoluminescence spectrum. The strong ZPL and broad PSB are clearly visible. E and E' line correspond to local vibrational modes between the two carbon atoms in the C_s-Si_i-C_s molecule [37]. The purple shaded area highlights the important O-band of optical telecomunication.

two possible models to explain the spin-dependence of G center recombination. According to these models, luminescence arises during the transition between a singlet ground state S_0 and an excited singlet state S_1. The spin-dependence arises from an additional triplet state, which is either above the S_1 or between the S_0 and S_1 states. In the first case, the triplet state would spin-selectively relax into the excited singlet state, increasing its population at resonance and thus leading to more radiative transitions. In the second case, charge carriers under resonance relax more non-radiatively from the triplet state to the singlet ground state, increasing the ground state population and making it available again for the luminescence cycle. Recent measurements validate the triplet state model between the two singlet states [39] (see Ch. 5).

The PL intensity of the G centers ZPL decreases with increasing temperature. This behavior can be described by the formula

$$I(T) = I_0 \left(1 + Be^{-E_A/k_b T}\right)^{-1} \tag{2.22}$$

This expression refers to a two-level model where the lower level is the ZPL transition upper state, which can thermally be depopulated into the higher level split by E_A and B is the ratio of degeneracy of these two levels [36]. Temperature-dependent experiments on this confirm that the PL intensity drops rapidly in the range of about $T = 50\,\text{K}$ and completely vanishes at temperature above $100\,\text{K}$, but the ground state and excited state each appear to be temperature-independent and there is also no change in configuration [32]. However, it has been suggested that the sharp decrease in intensity, similar to other systems, is due to thermal ionization of loosely bound electrons or holes into the excited state. At temperatures above $100\,\text{K}$, the photoluminescence disappears completely, but can be recovered by cooling again, even if the samples were stored at room temperature. However, from various experiments it is known that G centers dissolve at temperatures above $200\,°\text{C}$ [175]. In 2002 Pinacho et al. [176] showed by infrared absorption spectroscopy (IRS) that the intensities of the C_i-C_s-related absorption lines decrease at temperatures above $200\,°\text{C}$ and disappear completely upon further heating. By evaluating the IRS spectra in conjunction with Monte Carlo simulations, it was confirmed that the cause of this is mainly the emission of C_i from

the C_iC_s complex, which is trapped by other, more stable clusters and contributes to the growth of larger clusters. Another possible breakup process, namely dissociation of both carbon atoms from the interstitial silicon was less frequent in these studies. Furthermore, in 2018, Chartrand et al. [177] showed by high-resolution PL measurements on electron-irradiated high-purity ^{28}Si that the ZPL of the G center splits into four symmetrically distributed components with an intensity distribution of 1:2:2:1. This behavior is usually hidden by the natural line broadening in the crystal. Although G centers have been known since the late 1960s and have been intensively studied due to the steadily increasing interest in silicon for technological applications, only estimates of the upper limit of the lifetime of 4 µs [142] or 10 ns [36] existed until the beginning of this work.

Despite the optical difficulties in silicon, a LED based on G centers was already realized in 1987 by Canham et al. [175]. For this purpose, a n-type Czochralski (Cz)-grown silicon sample with a high carbon content (2×10^{18} cm^{-3}) was first implanted with boron (50 keV) and phosphorus (100 keV). The sample was then annealed and ohmic contacts of 1 µm thick aluminum were evaporated onto the surface. The resulting p^+-n--n^+ diode structure was irradiated with a 300 keV electron beam to generate G centers. The resulting G center electroluminescence at $T = 77$ K was 1000 times more intense than the band-to-band recombination of an unirradiated but otherwise identical diode under the same conditions. Besides the fabrication of electronically controllable light sources, deterministic amplification of light emission in the crystal is of enormous importance for the fabrication of fully integrated optoelectronic circuits and on-demand single-photon sources. Accordingly, several successful attempts have already been made to achieve stimulated emission and optical amplification in silicon by, for example, confinement effects [98, 178, 179] or Raman-laser conversion [69, 71]. In 2005, Cloutier et al. [169] showed that stimulated emission and optical gain of G center luminescence could be achieved by an etched nanopore array in crystalline silicon. However, the exact mechanism could not be clarified and thus a deterministic lasing of G centers by photonic structures is still missing.

Despite all the progress, it has long been unknown whether the small bandgap of silicon is suitable for creating sufficiently isolated defects whose spin states can be manipulated and which can serve as single-photon sources. Likewise, there is still a lack of high-Q optical micro-cavaties to control the spontaneous emission rate of the G centers by the Purcell effect and thus to achieve lasing. All these are important feautures for the development of silicon-based quantum devices and therefore, despite the long research on these quantum centers, the most important questions and tasks regarding this defect were still open at the beginning of this work.

Chapter 3

Solid-state quantum technologies

Introduction

This chapter will describe in detail the ion implantation devices used to fabricate the quantum centers of this thesis. Techniques described for this purpose include those previously presented in the publication* [26]. This will be followed by a section on quantum optical properties and the detection of single photons, before giving a short introduction on quantum computing and how photons and spins from solid-state single-photon sources can be harnessed as qubits. The aim of this chapter is to provide a simple and clear overview on the topic of quantum technologies based on solid-state qubits.

3.1 Ion implantation for defect engineering

Particle accelerators and ion implanters have existed for several decades and are used for a wide variety of applications, e.g. doping of semiconducting devices, cancer treatment in medicine or analytical techniques in material science. With the development of quantum technologies, new applications like quantum sensing or quantum computing based on defects in high-purity crystals emerged. These applications require the spatially-selective, high-resolution placement of ions into a crystal lattice by advanced ion implantation techniques. In this work, mainly two accelerators were used, which will be described in the following sections. While the Lipsion high-energy particle accelerator was mainly used to generate high concentrations of vacancies by a highly focused proton beam, the $100\,\text{keV}$ microbeam was used to spatially-selectively incorporate low concentrations of various elements into the different layers of SOI samples.

3.1.1 High-energy accelerator "Lipsion"

An electrostatic Singletron$^{\text{TM}}$ linear accelerator from High Voltage Engineering Europa B. V. with a maximum accelerating voltage of $3\,\text{MV}$ was used to produce high concentrations of G centers. According to [180], the accelerator has a stability of up to $\pm 20\,\text{V}$ over a period of several hours. The necessary vacuum is generated throughout the accelerator by

a combination of backing pumps, turbomolecular pumps and ion getter pumps, establishing a vacuum in the order of at least 10^{-7} mbar. The setup is illustrated in Fig. 3.1.

High-frequency ion source

The ions to be implanted are generated in a high-frequency (HF) ion source. For this purpose, a gas (in our case hydrogen) flows into a glass discharge vessel and is ionized in a HF electromagnetic field [181]. A negatively charged electrode accelerates the positively charged ions from the generated plasma through an extraction channel into the accelerator tube. The shape of the beam can be adjusted by an additional focusing voltage.

High-voltage generation

The high-voltage (HV) generation of the Singletron$^{\mathrm{TM}}$ accelerator is based on the principle of a diode cascade according to Cockcroft and Walton. This has the advantage that no mechanical components are necessary, so that vibrations and attrition are reduced. A generator produces electrical energy, which is transferred to a resonant circuit with a resonant frequency of $f_{\mathrm{res}} = 36$ kHz [181]. Connected to the generator is a cascade of capacitors and diodes. The capacitors are charged in parallel by the alternating voltage of the oscillating circuit via the diodes. If a consumer is connected, the capacitors discharge in the form of a series connection and output a DC voltage. The achievable output voltage then corresponds to the peak voltage of the AC voltage of the resonant circuit multiplied by the number of diodes. Theoretically, with a sufficiently high number of diodes, an arbitrarily high output voltage can be achieved, but the capacitance becomes smaller and smaller due to the series-connected capacitors, so that the further increase becomes steadily more ineffective.

Beamline

The generated ion beam must now be guided into one of the two sample chambers via a evacuated beamline system. To do this, it can first be aligned horizontally and vertically via two pairs of electrostatic deflection plates (steerers) to guide it into the electromagnets. In order to perform Rutherford backscattering (RBS), proton-induced x-ray emission (PIXE) or channelling measurements, the ion beam is deflected in the switching magnet so that it is guided into the analysis chamber. This should only be mentioned here, as it played no role in the experiments performed in this work. If the beam is to be used for ion microscopy or irradiation as in this work, it goes straight through the switching magnet and is deflected in the 90° magnet. In both cases, the deflection takes place via a magnetic field that is aligned vertically and perpendicular to the direction of movement of the ions. The magnetic field causes a Lorentz force to act on the ions (mass m, velocity v and charge q), which causes them to move along a circular path according to their energy. The radius of this circular path can be derived classically from the equilibrium of the Lorentz force F_{L} and the centripetal force F_{ZP} and is given by

$$r = \frac{\sqrt{2mE_{\mathrm{kin}}}}{qB}. \tag{3.1}$$

The deflection of ions with equal charge and kinetic energy in a constant magnetic field thus depends only on their mass, which can be used to select between different ions or molecules. Their kinetic energy in turn is determined by the electrical work that occurs when a charge q is displaced by a voltage U ($E_{\mathrm{kin}} = qU$). Since the resulting velocities are significantly smaller than the speed of light, relativistic effects do not have to be taken
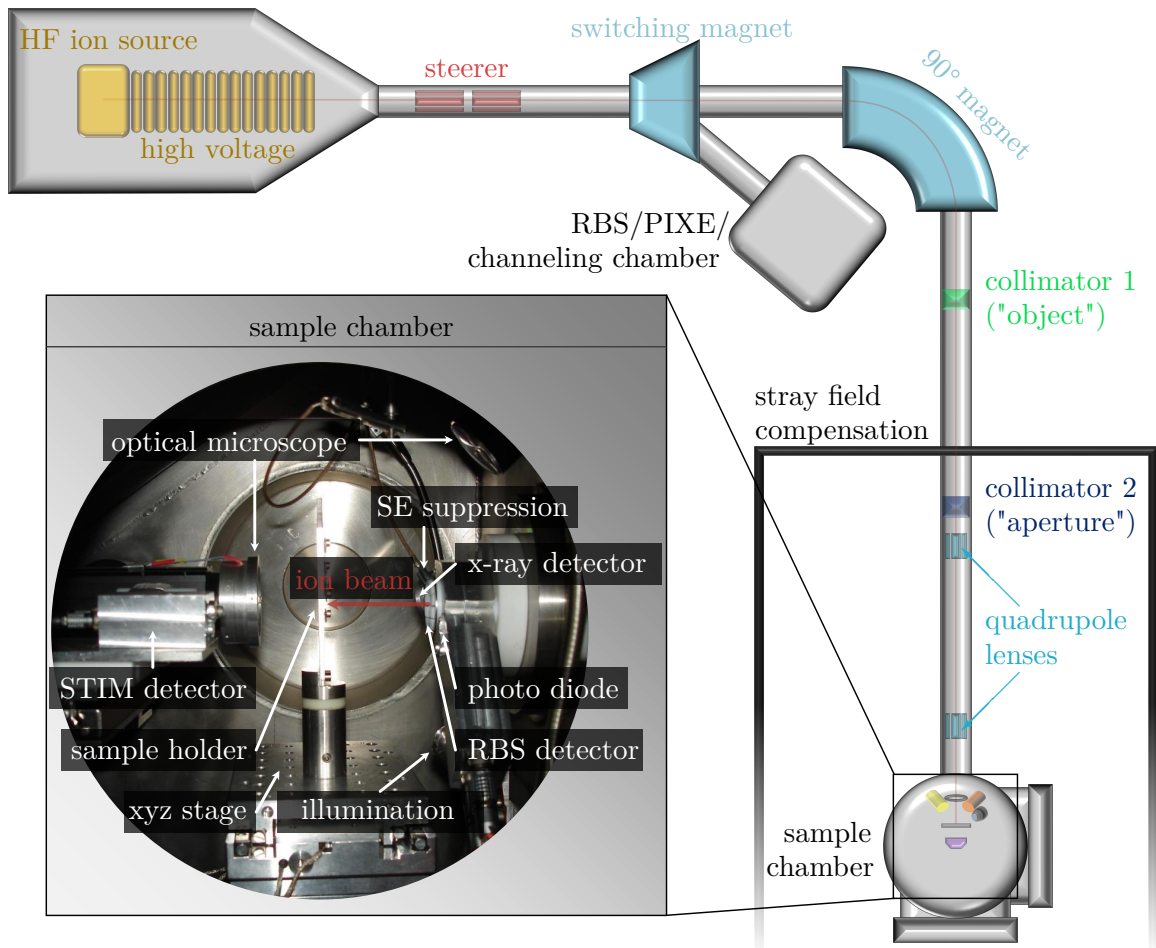
Figure 3.1   Schematic of the Singletron$^{\text{TM}}$ high-energy particle accelerator "Lipsion".
Ions from a high-frequency ion source are accelerated at up to 3 MeV, passed through a 90° electro-magnet before the ion beam is focused to a spot size of approximately 1 μm by a system of collimators and electromagnetic quadrupole lenses. This setup was used to perform the proton irradiations in Ch. 4. The sample chamber image was taken from the side viewing window [182].

into account, so that the ions have a kinetic energy of $E_{\text{kin}} = \frac{m}{2}v^2$, thats numerical value (given in units of eV) is equal to the applied voltage for singly charged ions. The element selected by the magnitude of the magnetic field passes through a vertical slit at the end of the magnet, on thats left and right side a measurement of the beam current takes place. If voltage fluctuations cause an ion beam shift, it will be detected by the current difference on both sides of the slit and automatically be corrected by adjusting the accelerating voltage.

Ion nano probe
For the high-energy irradiations with high lateral resolution, as performed in this work (see Ch. 4), the ion beam was passed through the 90° magnet to the sample chamber. Here, the ion beam has a lateral extension in the sub-micrometer range (down to 41 nm [183]) which is achieved by a system of apertures and ion optical devices.
Behind the magnet, the beam first reaches the object box. It consists of circular apertures

with diameters of $5, 10, 20, 50, 100, 150, 200, 300\,\mu m$ and additional microslits, which subsequently allow continuously variable adjustment of the lateral beam width. In the $4.90\,m$ distant aperture box, circular apertures ($5, 10, 20, 30, 50, 100, 200, 300\,\mu m$) are then used to adjust the divergence of the ion beam before it enters the focusing system. This consists of four magnetic quadrupole lenses arranged in two doublets with a distance of $2.49\,m$ to focus the ion beam. To realize symmetrical focusing, the optical axes of the doublets must coincide exactly. Since it proves difficult to perform this alignment using the adjusting screws of the quadrupole lenses alone, there is another magnetic correction quadrupole lens directly behind the second doublet, rotated by 45°. Since the focus generated in this way is also strongly dependent on external stray magnetic fields, an active stray field compensation is constructed around the beamline. This consists of three pairs of Helmholtz coils, which are positioned around the beamline, three magnetic field sensors and a control unit. The coils are arranged in such a way that the second quadrupole doublet, which is most decisive for the focal properties of the ion beam, is located exactly in the center of the compensation. The magnetic sensors are located directly in front of this second quadrupole doublet and measure the magnetic field strength with a sensitivity of $2\,mV\,nT^{-1}$ [183]. They then transmit these signals to the control unit, which subsequently adjusts the power of the Helmholtz coils so that magnetic stray fields are compensated and the magnetic field at the location of the sensors remains constant.

In order to scan the ion beam over the sample, a scanning unit is located between the focusing unit and the sample chamber. This unit contains two pairs of deflection coils through which the ion beam can be deflected magnetically in horizontal and vertical directions. The maximum deflection of the beam depends on the physical properties of the ion type and can be adjusted by switching the number of turns of the coils as well as choosing the number and density of pixels in the control program. The former can be set manually for each pair of deflection coils by repositioning the connectors ($N_{x,y} = 1, 2, 4, 8, ..., 256$), allowing scan field sizes of up to $\approx 2 \times 2\,mm^2$.

After the scan unit, the ion beam enters the sample chamber. In addition to the sample holder, it also contains a x-ray, RBS, scanning transmission ion microscopy (STIM) and secondary electron (SE) (Channeltron) detector, as well as a SE suppression, which will not be discussed further here, as they do not play an essential role in this work. Further information on the technical data of these detectors can be found, for example, in [181]. The sample holder can cover distances of up to 100 mm in xy-direction and additionally be moved along the z-direction as well as be rotated around the vertical axis, so that the samples can be tilted with respect to the beam direction to minimize channeling effects. The beam current that arrives at the sample is measured using a Faraday cup located directly behind the sample. The diameter of the beam was either estimated optically via the beam spot made visible on a quartz glass sample or determined by a PIXE measurement of a transmission electron microscopy (TEM) copper mesh and the subsequent evaluation of the edge sharpness of the grating structure.

3.1.2 100 kV Microbeam

To produce low-concentration G centers, the $100\,kV$ Microbeam of the AQS department of the University of Leipzig was used. It consists of three definable sections (ion source, beamline, sample chamber) that are illustrated in Fig. 3.2 and which will be described separately in the following.
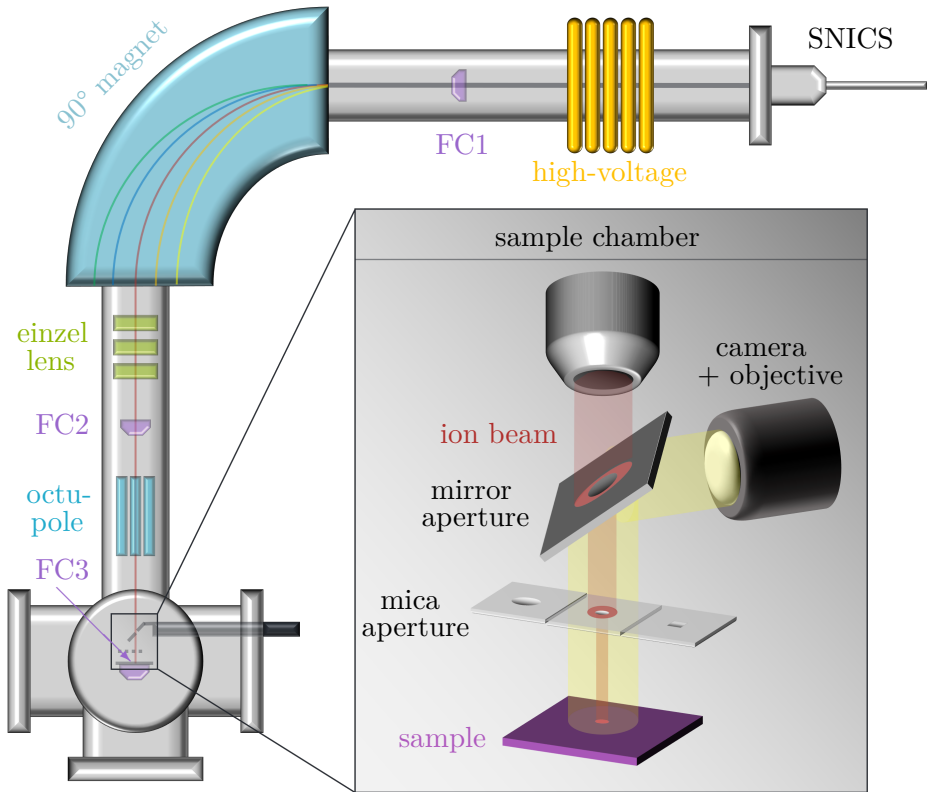
Figure 3.2   Basic concept of the 100 kV implanter. Ions are generated in a SNICS ion source (see Fig. 3.3), extracted and accelerated before entering the 90° magnet, working as mass separator. After focusing and deflecting the ion beam by an electrostatic einzellens and octupole, respectively, it enters the sample chamber and is cut down to a few µm in diameter by a combination of mirror and mica apertures. The final beam current is measured with the FC3, which can be approached directly on the sample holder.

Ion source

Single negatively charged ions are generated in a source of negative iony by cesium sputtering (SNICS), which is a solid-state ion source thats principle is illustrated in Fig. 3.3. More specifically, ions are generated from powders that contain the desired element and that is pressed into the cavity of a copper cylinder ("cathode"). In this way, most of the elements from the PSE can be extracted from solid compounds, enabling the implantation of a wide variety of different ions. Since the magnitude of the ion beam current I_{ion} depends on the ionizing ability of the elements within the powder, some elements that are difficult to ionize must be implanted as ionized molecular compounds. The copper cathode is screwed onto the so-called cathode rod, which is subsequently pushed into the ion source chamber. Cesium (Cs) atoms, that were previously vaporized in a heatable reservoir ($T \approx 140\,°\text{C}$), are introduced into the source chamber, where a part of the gaseous cesium now condense at the tip of the cooled copper cathode while the remaining gas travels to the hot surface of the Cs ionizer (controlled via the ionizer current $I_{\text{Cs}} = 22 - 25\,\text{A}$), where the atoms emit an electron and become single positively charged. The Cs^+ ions are now accelerated to the copper cathode by an applied negative voltage of $-10\,\text{kV} \leq U_{\text{cat}} \leq 0\,\text{kV}$ and are additionally focused on the powder of the cathode by the electric field of a focus voltage
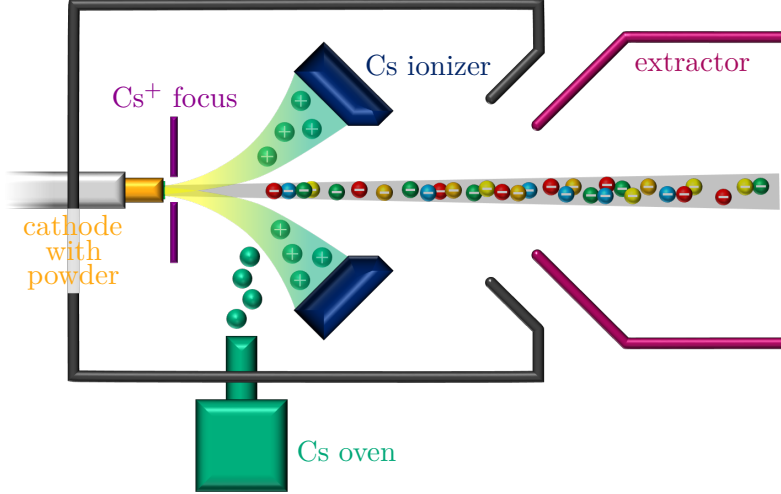
Figure 3.3 Operating principle of a SNICS (source of negative ions by cesium sputtering). Vaporized cesium atoms are ionized by the hot surface of the Cs ionizer, focused and accelerated onto the negatively charged cathode, where they sputter the powder within. The sputtered atoms become negatively charged on their path through a thin layer of condensed cesium on the cathode and are extracted by an extractor voltage [184].

$0\,\mathrm{kV} \leq U_{\mathrm{foc}} \leq 15\,\mathrm{kV}$. The accelerated Cs^+ ions sputter the powder in the cathode cavity and thus generate neutral atoms, which can receive electrons when passing through the cooled neutral cesium layer on the cathode tip and thus become negatively charged. The resulting negative ions from the powder are then accelerated out of the source chamber by a positive extraction voltage of $0\,\mathrm{kV} \leq U_{\mathrm{ext}} \leq 15\,\mathrm{kV}$ before entering the beamline.

Beamline

The ion beam coming from the source is further accelerated to the desired energy by applying a high-voltage of $0\,\mathrm{kV} \leq U_{\mathrm{HV}} \leq 100\,\mathrm{kV}$, leading to the final energy U_{tot} that is determined by

$$U_{\mathrm{tot}} = U_{\mathrm{cat}} + U_{\mathrm{ext}} + U_{\mathrm{HV}}. \tag{3.2}$$

Now, having the final energy, the first ion beam current measurement takes place using a movable Faraday cup (FC1), that can be shifted into the beam line and measures the incoming charges from the ions. Afterwards, the multi-elemental ion beam passes through a 90° electromagnet, which, as described in Sec. 3.1.1, deflects the different ions of the beam to different orbital radii according to their mass (see Fig. 3.2). As a result, only ions of a certain energy (mass) pass through the slits at the end of the magnet. Afterwards, the beam can be focused by an electrostatic einzel lens with a voltage of $0\,\mathrm{kV} \leq U_{\mathrm{lens}} \leq 35\,\mathrm{kV}$. With the following second Faraday cup (FC2), the measurement of the ion beam current as a function of the magnetic field is possible by sweeping the electric current through the electromagnet. By converting the magnet current I_{mag} to the corresponding ion mass, a mass spectrum of the powder can be recorded, thats peaks occur at selected magnet currents according to

$$I_{\mathrm{mag}} = B_{\mathrm{mag}} \cdot \frac{I_{\mathrm{max}}}{B_{\mathrm{max}}} = \sqrt{\frac{2U_{\mathrm{tot}} \cdot m_{\mathrm{ion}}}{r^2 Q_{\mathrm{ion}}}} \cdot \frac{I_{\mathrm{max}}}{B_{\mathrm{max}}} \tag{3.3}$$
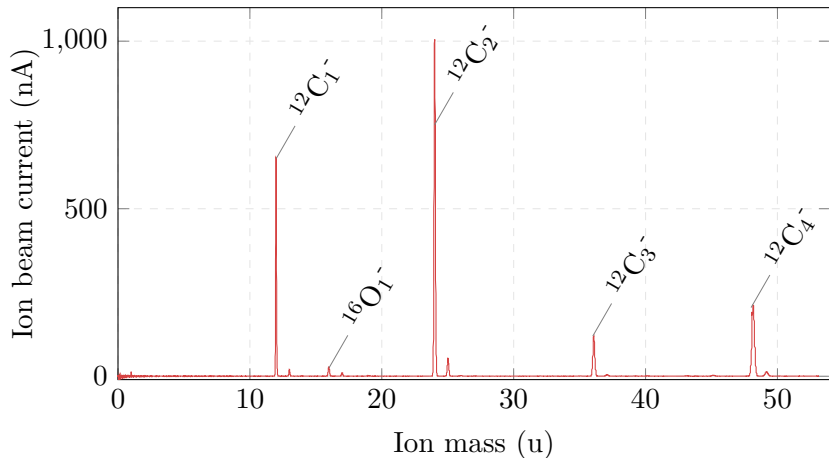
Figure 3.4   Typical mass spectrum measured from a SNICS cathode filled with pure ^{12}C powder. The spectrum is recorded in dependence of the magnet current, which can be converted to the ion mass by Eq. (3.4). In this way, the occuring peaks corrsepond to the mass of different elements and molecules, which can easily be identified and selected.

Here, $I_{max} = 153\,\text{A}$, $B_{max} = 1.05\,\text{T}$, and $r = 0.5\,\text{m}$ are values that are predefined by the magnet. The different ions of mass $m_{ion}\,[\text{kg}] = A_u \cdot u$ in the ion beam generally have the electric charge $Q_{ion} = q \cdot e$. Since the SNICS produces only singly charged ions ($q = 1$), Eq. (3.3) can be simplified for a fixed total voltage U_{tot} to be

$$I_{mag} = \sqrt{c \cdot m_{ion}}. \tag{3.4}$$

Mass spectra like shown in Fig. 3.4 can then be calibrated by using the I_{mag}^2/m_{ion} correlation between the magnet current and the mass of Eq. (3.4). After choosing the desired ions from the mass spectrum, the focused ion beam can be deflected horizontally and vertically by an electromagnetic octupole consisting of two crossed quadrupoles to guide it through the next aperture into the following sample chamber.

Sample chamber
The sample chamber as shown in Fig. 3.2 consists of three functional units. The incident ion beam has a diameter of $\approx 1\,\text{cm}$ and first passes through the drilled hole of a mirror in the sample chamber which is inclined to the beam axis by 45°, allowing the optical observation of the sample and simultaneous implantation. The bore has a diameter of $\approx 1.4\,\text{mm}$ and serves as ion beam aperture. The mirror is mounted together with a microscope objective on a rail that allows the mirror and objective to be moved. The image that enters the objective via the mirror is recorded in time resolution by a camera behind it and displayed on the computer. Behind the mirror hole, the ion beam passes a perforated transparent silicate film ("mica mask"), that has a thickness of a few micrometer. The mask was previously pierced by a focused ion beam, whereby various structures and sizes in the micrometer range can be realized. Several different masks are placed on a holder which is connected to a xyz stage that allows positioning with micrometer precision. The mask serves as a further aperture for the ion beam, which has a lateral extension of a few micrometers after passing through it and before reaching the sample. The sample is placed on a sample carrier, which in turn is mounted on an xyz stage with micrometer precision. This design allows the mirror hole, mica mask and sample to be aligned and thus the spatially-selective ion implantation

with high-resolution.

The sample holder also has a hole behind which a third Faraday cup FC3 is located, that can be used to measure the incoming ion beam current relevant for implantation. The implantation time for the desired fluence depends on the implantation area (size of the hole in the mica foil) as well as on the ion beam current and can be calculated by

$$t = \frac{\Phi A_{\mathrm{mica}} e}{I_{\mathrm{ion}}^{\mathrm{FC3}}} \tag{3.5}$$

where the fluence Φ is usually given in ions/cm^2 and the mask area A_{mica} in cm^2, respectively. Furthermore, a silicon chip, which is coated with the photoresist polymethylmetacrylate (PMMA), is put close to the sample. The chip is used to localize the position of the ion beam before the actual implantation by irradiating the PMMA with ions, which causes a discoloration of the photoresist. This discoloration can be observed via the microscope and marked accordingly on the screen.

3.2 Quantum optics

At the end of the 17th century, there were two competing opinions on the composition of light. While Huygens explained the properties of light in terms of wave optics, Newton explained the same properties in terms of a stream of fast particles. Today we know that light as an electromagnetic quantum object can have both wave and particle character, whose properties depend on the measurement itself. By the development of new measuring methods, however, properties of the light could be discovered, which cannot be explained with the classical picture of a wave and make the consideration of the photon statistics necessary.

3.2.1 Properties of single photons

Due to the discrete nature of photons, they obey Poisson statistics. Photons in a perfectly coherent light beam of constant intensity have accordingly the Poisson distribution

$$P(n) = \frac{\bar{n}^n}{n!} e^{-\bar{n}} \tag{3.6}$$

where the mean value $\bar{n}$ denotes the amount of photons within a beam segment [185]. The coherence is a measure for the stability of the light beam. It can be determined by the coherence time $\tau_{\mathrm{c}} \approx 1/\Delta\omega$, that describes the time interval in which the phase of the wave train does not change and that can be expressed by the spectral width $\Delta\omega$ of the light. Due to statistical fluctuations in short timescales, deviations from the perfectly coherent beam occur, which can be expressed by the standard deviation

$$\Delta n = \sqrt{\bar{n}} \tag{3.7}$$

of the photon number n. Thus, light can be divided into three classes:

- sub-Poissonian statistics: $\Delta n < \sqrt{\bar{n}}$

- Poissonian statistics: $\Delta n = \sqrt{\bar{n}}$

- super-Poissonian statistics: $\Delta n > \sqrt{\bar{n}}$

Super-Poissonian light is also called chaotic, incoherent or thermal light, whose intensity varies with time and which we encounter most often in nature. Poissonian light, in contrast, is perfectly coherent and thus has a constant intensity and few photon number fluctuations. Sub-Poissonian light, on the other hand, is described as non-classical light because there is no classical explanation for it and can only be explained by the quantum nature of light [185]. In Tab. 3.1 these different cases are summarized and illustrated. It can be seen that chaotic light arrives in bunches of photons, while sub-Poissonian light is referred to as antibunched light, since it consists of a stream of individual photons, which all have the same temporal distance τ to each other. Coherent light, on the other hand, consists of a stream of individual photons whose distances from each other are irregular, which is why this form of light is called random. Experimentally, chaotic and coherent light can be measured classically by intensity fluctuations of the light beam. The light beam is separated by a beam splitter, directed to two detectors and examined whether the intensity fluctuations of both beams are correlated. Such a measurement quantifies the intensity fluctuations in the second-order correlation function

$$g^{(2)}(\tau) = \frac{\langle I(t) \cdot I(t+\tau) \rangle}{\langle I(t) \rangle \cdot \langle I(t+\tau) \rangle} \qquad (3.8)$$

thats curves for the different photon distributions are shown in Fig. 3.5. Since intensity fluctuations are in the order of τ_{c}, they are always completely uncorrelated for long timescales $(g^{(2)}(\tau \gg \tau_{\mathrm{c}}) = 1)$. Only when short timescales are measured, the differences in the various statistics become apparent. While perfectly coherent light yields $g^{(2)}(\tau) = 1$ for all timescales due to the time-independent intensity, the fluctuations in chaotic light lead to an increase of $g^{(2)}(\tau)$. This increase depends on the type of light source and can be determined by the broadening $\Delta\omega$ of the spectral line. If light is generated from the excited state of atoms or defects, oscillations and motions of particles lead to a Doppler broadening of the spectral line, which can be approximated by a Gaussian curve. Likewise, fluctuations in the lifetime of the atoms excited state lead to a Lorentz-shaped line broadening, since the lifetime is correlated with the energy and thus the wavelength via the Heisenberg uncertainty relation $\Delta E \Delta t \gtrsim \hbar/2$ [185]. Accordingly, external influences that reduce the lifetime (e.g. interactions with other particles) lead to an undesired line broadening.

The cases discussed so far can still be measured and explained purely classically by intensity considerations. However, if one proceeds now to the measurement of single quantum objects, Eq. (3.8) must be modified to the detection of single photons

$$g^{(2)}(\tau) = \frac{\langle n_1(t) \cdot n_2(t+\tau) \rangle}{\langle n_1(t) \rangle \cdot \langle n_2(t+\tau) \rangle} \qquad (3.9)$$

where $n_{\mathrm{i}}(t)$ denotes the number of photon counts at detector i at time t.

Distribution	Classical	Statistical	$g^{(2)}(0)$	Visualization						
bunched	chaotic	super-poisson	>1	***	**	***				
random	coherent	poisson	$=1$	* *	**	*	**	*		
antibunched	missing	sub-poisson	<1	*	*	*	*	*	*	*

Table 3.1 Classification of the different types of photon statistics.
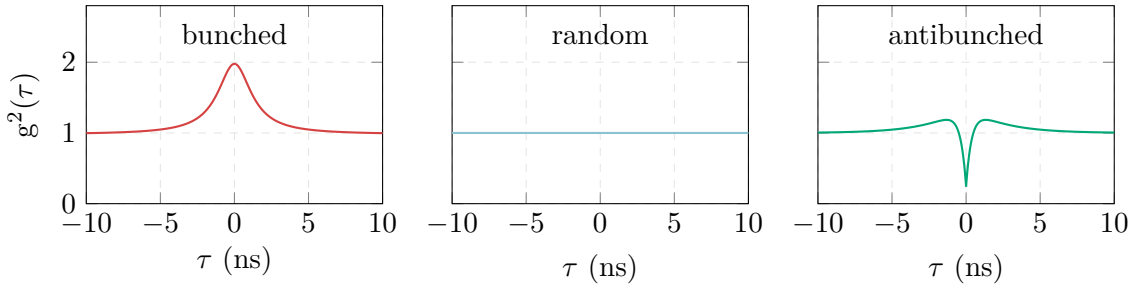
Figure 3.5 **Second-order autocorrelation function g²(τ) for three different photon distributions.** Bunched light can be explained by classical chaotic light, where photons are clumped together, thus increasing the probability for measuring multiple photons on short timescales. The random photon distribution instead corresponds to classical coherent light, with random time intervals between photons and therefore a constant probability of detecting photons. Antibunched light is a pure quantum optical phenomena with $g^{(2)}(\tau)$ being < 1 for short timescales. In a pure quantum mechanical 2-level system, $g^{(2)}(\tau)$ increases to a maximum of unity, whereas in combination wih a metastable state it can be even higher than unity [186].

Single photons are indistinguishable and can be created deterministically ("on-demand") by single-emitter systems like isolated particles, quantum dots and color centers or from non-deterministically sources that are based on probabilistic non-linear optical effects like e.g. parametric downconversion or four-wave mixing [187] (see Sec. 2.3.2). Eq. (3.9) describes the probability of detecting a photon at detector 2 after time τ, when a photon was measured at detector 1 at time $t = 0$ (as a reference). Since the excited state of a single, isolated defect has a certain lifetime, no photons can be generated until the excited state relaxes. Accordingly, there are short-timed and regular periods between each of the individually generated photons, leading to time intervals where no counts are registered. Therefore, under perfect conditions, $g^{(2)}(0) = 0$ since no photons can be registered simultaneously and $g^{(2)}(\tau)$ increases with increasing time intervals τ. In the case of a pure 2-level system, $g^{(2)}(\tau)$ takes at most the value 1 for long timescales. However, if a metastable state is involved in the relaxation, in which the system briefly resides, the temporal distribution of the photons varies and thus partially lead to values $g^{(2)}(\tau) > 1$ [186].

3.2.2 Photoluminescence and single-photon measurements

For the measurement of $g^{(2)}(\tau)$ and thus the detection of antibunching, a Hanbury Brown-Twiss (HBT) interferometer is used in combination with two avalanche photodiodes (APD), with which single photons can be registered. For the PL studies in this work, such an experiment was combined with a confocal laser scanning microscope (CLSM) to detect photon counts as well as to record PL spectra. Such a setup is shown schematically in Fig. 3.6. Since the respective devices of the experimental setups in Ch. 4 and Ch. 5 differ from each other, the general operation of the PL spectrometer is first described before the respective differences are elaborated.

Generally, a continuous wave (CW) laser beam is directed through a system of optical lenses (L), mirrors (m) and beam splitter (BS) to a steering mirror (SM), which can deflect the beam and direct it onto an objective. By deflection of the SM, the laser beam is scanned over the sample over an area of $100 \times 100\,\mu\text{m}^2$ and the number of PL photon counts from the excited quantum centers is recorded by an APD. The scan reveals areas on the sample with higher or lower PL intensity or even single-photon sources, which can be selected

for further investigations. By simply shifting a movable mirror (MM), the optical path is changed and the PL of the sample is directed to the monochromator with an attached charge-coupled device sensor (CCD) camera, where a spectrum of the PL is recorded. From the characteristics of the spectrum, the investigated quantum center can be identified. By shifting the MM back again, the PL can be directed to a 50 : 50 BS that distributes the photon beam equally to two APDs. These are connected to a timer, which receives a start signal from APD 1 and a stop signal from APD 2. By measuring the time between the start and stop signals, a histogram can be recorded which corresponds to the course of $g^{(2)}(\tau)$.

For time-resolved measurements, a pulsed laser signal is required, that can be produced by an acousto-optic modulator (AOM). The AOM consists of a transparent crystal in which ultrasonic waves are generated by a piezo oscillator, creating an optical grating in the crystal. The incident laser beam is diffracted at the grating so that higher diffraction orders can be specifically selected by a diaphragm. Due to the controllable frequency at which the AOM is operated, a pulsed laser beam can be generated.

For the ensemble measurements in Ch. 4, the deflected laser beam is always centered on the objective (100x Mitutoyo Plan Apo NIR HR Infinity Corrected Objective, magnification
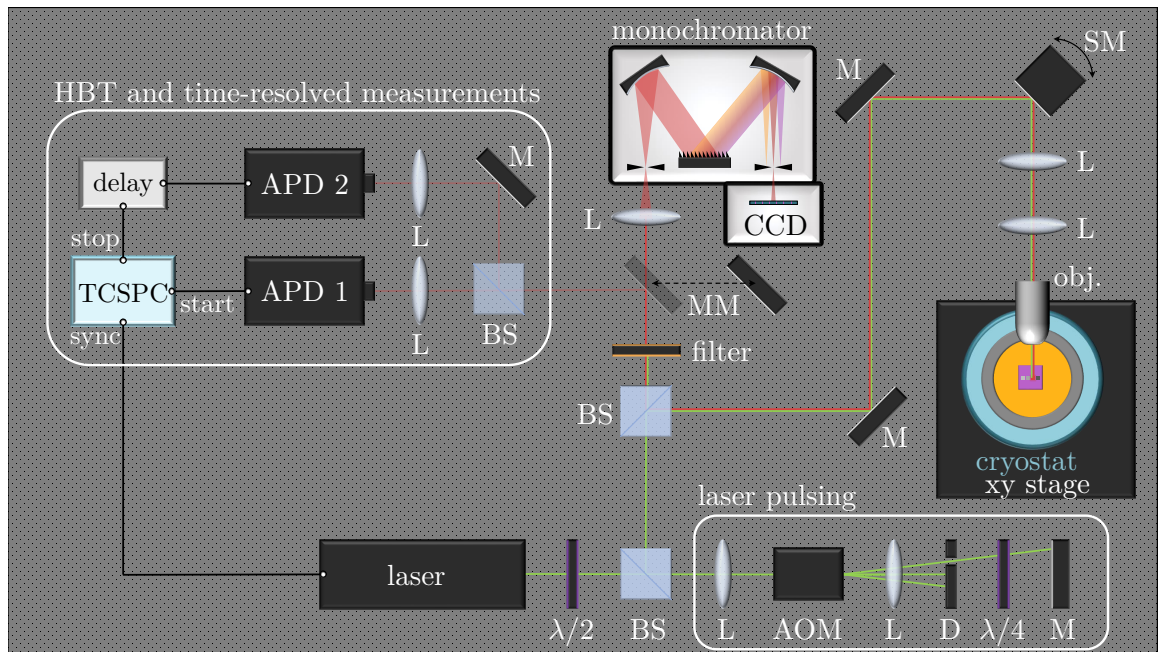
Figure 3.6 Experimental setup for PL measurements used in this thesis. The excitation CW laser beam can be manipulated and pulsed by the optional AOM line, that consists of lenses (L), AOM, diaphragm (D), $\lambda/4$ waveplate and mirror (M). The prepared laser beam is directed through a beam splitter (BS) to a steering mirror (SM), before it is focused by an objective onto the sample within the cryostat. The reflected laser light and the resulting PL from the sample are collected from the same objective and guided to a filter that allows only the PL to cross. A movable mirror allows to decide whether the PL is directed to a spectrometer or a HBT setup. The spectrometer consists of a monochromator with CCD camera for recording the spectrum of the light. If the PL is guided to the HBT setup, it crosses a 50:50 BS, that divides the photon stream onto two APDs for photon counting, time-resolved and autocorrelation measurements. The correlation between the APD signals is measured by the TCSPC card. Further information on the optical paramter of the setup can be found in the text or in [151].

$G = 100\times$, effective focal length $f_{\text{obj}} = 2\,\text{mm}$, numerical aperture NA = 0.7), which is optimized for the IR wavelength range of $\lambda = 480 - 1800\,\text{nm}$. A telecentric system ("$4f$-mount") was used to conjugate the plane of the SM with the plane of the objective. This system consists of two lenses (focal length f, distance $2f$), where the first lens has a distance f to the SM and the second has the same distance to the objective. The objective focuses the laser beam through an optical window onto the sample, that is located within a liquid helium (He) cryostat (MicroStatHighResII from Oxford Instruments). The cryostat allows cooling of the sample down to $T = 5 \pm 0.1\,\text{K}$. It is mounted on a xy stage through which it can be moved via two micrometer screws to travel longer distances on the sample.

In the single-photon measurements from Ch. 5, the telecentric system consisted of two parabolic mirrors, which significantly reduced chromatic aberrations and thus improved the excitation efficiency. The laser light was subsequently directed to an objective (Olympus LCPLN100XIR), which has a higher numerical aperture of NA = 0.85 and can thus collect more photons. Furthermore, a new liquid He cryostat (OptiDry 200 from MyCryofirm) was used, which allowed the integration of the objective inside the cryostat and thus the reduction of the distance between sample and objective, as well as reducing aberrations and resulting optical losses that would occur when the collected light passes through the cryostat window.

The excited PL from the sample, along with the reflected laser light, passes through the objective and back to the beam splitter, which reflects the light onto a filter that is opaque to the laser light. Then the movable mirror is used to decide whether the light is directed to the spectrometer or to the HBT interferometer. The spectrometer consists of a Czerny-Turner monochromator in which the PL first passes through a slit whose aperture width determines the intensity and resolution. The PL is then reflected via a concave mirror onto one of three possible reflection diffraction gratings optimized for the IR range (150 lines/mm (blazed at $1.2\,\mu\text{m}$), 300 lines/mm (blazed at $2\,\mu\text{m}$) and 600 lines/mm (blazed at $1.6\,\mu\text{m}$)). The light diffracted at the grating is focused via a second concave mirror onto a liquid N_2 cooled sensor array consisting of 1024 InGaAs diodes with a quantum efficiency of 80 %. With a typical input slit aperture width of $100\,\mu\text{m}$, a spectrum with a resolution of $150\,\mu\text{eV}$ can thus be recorded [151]. On the other hand, when the PL is directed by the movable mirror towards the HBT setup, the photon flux is distributed equally via a BS and fiber optic cables to two N_2 cooled InGaAs APDs with a quantum efficiency of $10 - 25\,\%$. These are each connected to a time-correlated single-photon counting (TCSPC) card. APD 1 sends a signal to the start input of the TCSPC, while the signal from APD 2 first passes through a delay line, which causes a time shift of 250 ns between the two detection channels. The delayed signal then enters the stop input of the TCSPC card, which subsequently measures the time between the start and stop signals.

For the evaluation of the photon statistics, optical losses and interferences, which reduce the efficiency of the photon-counting experiments, must be further considered. Such losses are caused by [185]:

- inefficient collection optics, which collect only a fraction of the emitted light,

- losses due to absorption, scattering or reflections at the surface of optical components such as mirrors, lenses or optical windows

- inefficient detectors with imperfect quantum efficiency and dark count noise due to thermally generated charge carriers.

Detector dark counts and unavoidable residual background photons thereby interfere with the measurement of single photons and lead to deviations from the expected value of $g^{(2)}(0) = 0$ for a single-photon source. Taking these interferences into account, values of $g^{(2)}(0) < 0.5$ are already considered as evidence of emission from single quantum centers [188]. If one wishes to perform a time-resolved PL measurement instead of the auto-correlation measurement, the signal from a pulsed laser beam is fed to the sync input of the TCSPC card and the time is measured until a stop signal (without delay) arrives from the APD 2. More information about the optical components used can be found in [151].

3.2.3 Applications of single-photon sources - quantum key distribution

Single-photon sources are crucial for the development of future quantum networks that interconnect quantum computers and ensure secure, quantum-based information exchange ("quantum cyptography"). They can be used to realize efficient, all-optical quantum repeaters that receive, store, and transmit quantum mechanical signals, enabling long-distance quantum communication [189]. In 2001 [23], it was shown that scalable quantum computing is also possible with single photons and simple, linear optical circuits [190] (see Sec. 3.3.2). However, the most important application for single photons is probably the development of secure communication protocols using quantum key distribution (QKD). In classical data transmission, encryptions are exchanged via bits consisting of laser pulses of defined power (high power: bit = 1, low power: bit = 0). Since these are purely optical processes, they can be easily manipulated. For example, a 50:50 beam splitter could be used to split the laser pulse from an optical fiber and bring it back to the original intensity using an optical amplifier with a gain of 2 [185]. Such a procedure is shown in Fig. 3.7. Accordingly, the information can be intercepted without leaving any traces. In quantum cryptography, on the other hand, encryption takes place via qubits, which are most often realized by single photons, since they represent flying qubits that can be guided over long distances. In 2015, the largest distance for QKD with single photons was achieved with a maximum transfer of 120 km using a quantum-dot SPS that emitted photons in the telecom band at 1.5 μm [191]. In the same work, secure key rates of about 28 bits s^{-1} were also demonstrated over a distance of 100 km. However, these key rates were still 1-2 orders of magnitude smaller than those achievable by attenuated-laser QKD. Accordingly, SPS with improved brightness and extraction efficiency need to be developed in order to use them competitive for QKD [189].

The advantage of qubits over classical bits lies in quantum physical properties such as the no-cloning theorem. This prohibits the existence of a system that can perfectly copy any
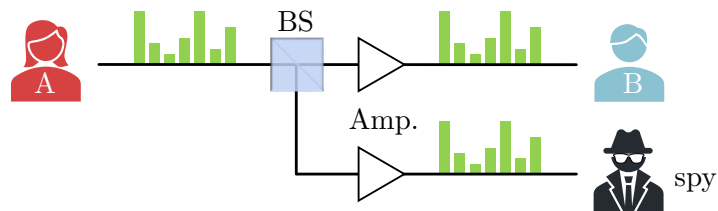
Figure 3.7 Classical encryption. Light pulses are transmitted which can be intercepted by means of a 50:50 BS. In order to remain unnoticed, the light signal just needs to be amplified again to the initial intensity by an optical amplifier (amp) with a gain of 2. Adapted from [185].

	A's basis	sent bits	B's basis	received bits	same basis?	sifted bits	error analysis	private key
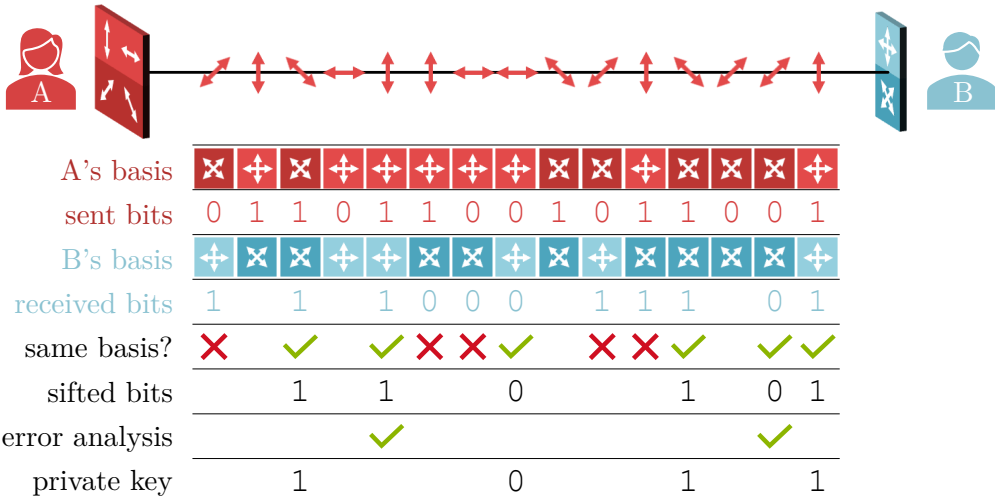
Figure 3.8 Quantum key distribution with the BB84 protocol. By executing certain schemes (e.g. the BB84 protocol as shown here, adapted with permission of *Elsevier* from [192]), eavesdropping attempts can be detected by statistical considerations and unwanted information exchange can be avoided.

qubit without changing the state of the copied qubit [193]. From this, it follows that an eavesdropping attempt leads to errors in the decoding of an encryption, which are measurable and thus expose a communication as not secure. Accordingly, the quantum key can be discarded and a new one generated before sensitive data has been exchanged. Quantum key distribution can be realized by certain schemes with both, pure quantum mechanical or entangled states. The first QKD scheme was the so-called BB84 protocol by Bennett and Brassard [192], which is well suited for a basic understanding of the concept of quantum cryptography and that will be briefly summarized in the following.

In QKD using photons, the qubits are determined by the linear polarization of the light in a two-dimensional Hilbert space. Two polarizations orthogonal to each other form a basis. For the BB84 protocol usually two bases are used, namely rectilinear (polarization $0° = |0\rangle$ and $90° = |1\rangle$) and diagonal (polarization $45° = |0\rangle$ and $135° = |1\rangle$). Fig. 3.8 illustrates the following quantum key exchange: Person A sends single photons, determining the polarization, i.e. whether the direction of oscillation is 0°, 45°, 90° or 135°. Without knowing the chosen base, this corresponds to a string of binary data $|0\rangle$ and $|1\rangle$. Person B must decide which polarization direction (rectilinear or diagonal) to measure for each incoming photon, which corresponds to a random choice of basis. Statistically, he chooses (without knowing it and just like a possible eavesdropper) in 50 % of the cases the same basis as person A. At the same time, photons can also be lost or not registered by the imperfect detectors. Accordingly, QKD applications require very efficient quantum detectors, optical fibers and error correction techniques to minimize the errors.

Subsequently, person A and B communicate over a public channel and exchange information about which photons were successfully received and which basis was used without revealing the result (the binary value). The photons for which the basis does not match are sorted out and not considered in the evaluation. From the remaining photons, person B selects individual ones that will be used by person A to perform an error analysis. However, these qubits can subsequently no longer be used for the key. If the line was eavesdropped, a

spy would also select the correct base in 50 % of the cases and forward individual photons with the correct polarization to person B. However, for the remaining 50 %, where the spy chose the wrong basis, person B receives equally random results with a probability of 50 %. Accordingly, B registers errors even when the basis of person A and B match, increasing the error rate. The error probability is then calculated as the product of the probability that a spy chose the wrong base (50 %) multiplied by the probability that person B gets the wrong result (50 %) despite having the correct base, yielding $P_{\mathrm{err}} = 25\,\%$ [185]. Accordingly, higher error rates indicate an eavesdropper, so the quantum key can be discarded and a new one generated before sensitive data has been exchanged.

3.3 Quantum computing

3.3.1 Basic principle

The major goal of current quantum research is the construction of a scalable quantum computer. For this, the DiVincenzo criteria already mentioned in Ch. 1 have to be fulfilled. The basis for this is provided by quantum mechanical systems that can assume at least two reliably distinguishable (measurable) eigenstates, e.g. $|0\rangle$ and $|1\rangle$. These qubits (for two-state systems) can be realized in several ways, including [194]:

- polarization of single photons,

- nuclear spins of ions or atoms in ion traps or crystal lattices,

- electron spins bound in quantum dots or defects,

- charge, flux and phase of Cooper pairs in SQUIDs.

The eigenstate of such a qubit is described by its wave function $\psi(\vec{x}, t)$ or $\psi(\vec{p}, t)$ and corresponds to a normalized state vector $|\psi\rangle$ in a two-dimensional Hilbert space. Due to the quantum mechanical superposition principle, the eigenstate of such a system can also be represented as a linear combination of two orthogonal states:

$$|\psi\rangle = \alpha|0\rangle + \beta|1\rangle \tag{3.10}$$

where α and β are complex numbers, which fulfill the normalization condition $|\alpha|^2 + |\beta|^2 = 1$ [195]. Until its measurement, such a system is in a superposition of an infinite number of states which, due to the normalization, are located on a spherical surface, the so-called Bloch sphere, which is shown in Fig. 3.9 (b). This is the main difference to classical bits. While a classical bit can only take the values 0 and 1 (Fig. 3.9 (a)), qubits can appear in a mixed state of different pure states. Only by measuring the quantum system, its actual pure state, which depends on the probability amplitudes α and β, will be defined. The states $|+\rangle = \frac{1}{\sqrt{2}}(|0\rangle + |1\rangle)$ and $|-\rangle = \frac{1}{\sqrt{2}}(|0\rangle - |1\rangle)$ are important superposition states in this context, where the two pure base states $|0\rangle$ and $|1\rangle$ are equally probable and accordingly lie on the equator of the Bloch sphere.

Since a single bit or qubit does not yet allow large computational operations, several of them must be connected together. For classical bits, this is done e.g. in a circuit of transistors. If there are n bits in this circuit, it can adopt 2^n states (represent 2^n numbers binary, respectively). If n qubits, on the other hand, are arranged in a so-called quantum registers, they attain a common, superimposed mixed state of the 2^n possible pure states,

(a) 0 1 Bits

(b) $|0\rangle$ $|-\rangle$ $\frac{1}{\sqrt{2}}(|0\rangle + i|1\rangle)$ $|+\rangle$ $|1\rangle$ single Qubit state (2 eigenvectors)

(c) $|00000\rangle$ $|00010\rangle$ $|01001\rangle$ $|01110\rangle$ $|11110\rangle$ $|11111\rangle$ 5 Qubit state ($2^5 = 32$ eigenvectors)

Classical states   **Quantum states**
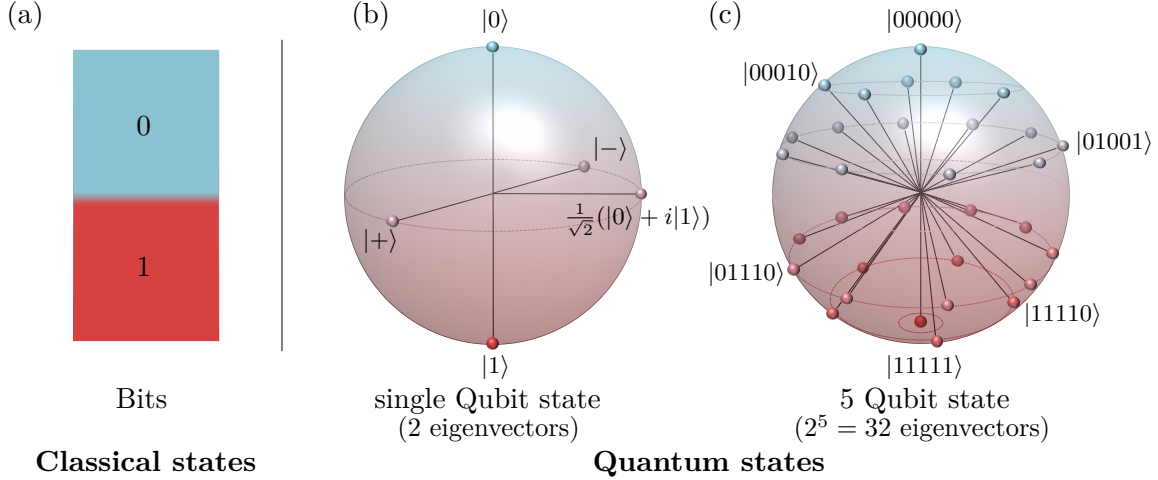
Figure 3.9   Comparison of the states of classical bits and qubits. (a) While classical bits have only two defined states 0 and 1, a single qubit **(b)** is in an undefined superposition state of its two eigenvectors $|0\rangle$ and $|1\rangle$. The final state is determined only by a measurement on the system, which causes the collapse of the wave function, and also allows only the two possibilities $|0\rangle$ and $|1\rangle$. **(c)** The mixed state of a system of several qubits then corresponds to the superposition of 2^n eigenstates. Adapted from [196].

which are now vectors in a 2^n-dimensional Hilbert space (Fig. 3.9 (c)). In the case of two pure qubits in the states $|\psi_\alpha\rangle = \alpha_0|0\rangle + \alpha_1|1\rangle$ and $|\psi_\beta\rangle = \beta_0|0\rangle + \beta_1|1\rangle$, the entire quantum register R takes the eigenstate [195]

$$|\psi_{\mathrm{R}}\rangle = |\psi_\alpha\rangle|\psi_\beta\rangle \tag{3.11a}$$

$$= (\alpha_0|0\rangle + \alpha_1|1\rangle) \cdot (\beta_0|0\rangle + \beta_1|1\rangle) \tag{3.11b}$$

$$= \alpha_0\beta_0|0\rangle|0\rangle + \alpha_0\beta_1|0\rangle|1\rangle + \alpha_1\beta_0|1\rangle|0\rangle + \alpha_1\beta_1|1\rangle|1\rangle \tag{3.11c}$$

where the coefficients and state vectors are combined for the sake of clarity to the form

$$|\psi_{\mathrm{R}}\rangle = \gamma_{00}|00\rangle + \gamma_{01}|01\rangle + \gamma_{10}|10\rangle + \gamma_{11}|11\rangle \tag{3.12}$$

or further simplified:

$$|\psi_{\mathrm{R}}\rangle = \gamma_0|0\rangle + \gamma_1|1\rangle + \gamma_2|2\rangle + \gamma_3|3\rangle. \tag{3.13}$$

Accordingly, $|\gamma_0|^2 + |\gamma_1|^2 + |\gamma_2|^2 + |\gamma_3|^2 = 1$ must be true again. The superposition state of such a 2-qubit system can be represented as the product of the individual qubit eigenstates and is thus separable. The 2^n-dimensional state vectors have for $n = 2$ the form:

$$|00\rangle = |0\rangle = \begin{pmatrix} 1 \\ 0 \\ 0 \\ 0 \end{pmatrix}, \quad |01\rangle = |1\rangle = \begin{pmatrix} 0 \\ 1 \\ 0 \\ 0 \end{pmatrix}, \quad |10\rangle = |2\rangle = \begin{pmatrix} 0 \\ 0 \\ 1 \\ 0 \end{pmatrix}, \quad |11\rangle = |3\rangle = \begin{pmatrix} 0 \\ 0 \\ 0 \\ 1 \end{pmatrix}.$$

Thus, a quantum register of n qubits can be written in general terms as

$$|\psi_R\rangle = \sum_{i=0}^{2^n-1} \gamma_i|i\rangle \tag{3.14}$$

with the requirement

$$\sum_{i=0}^{2^n-1} |\gamma_i|^2 = 1. \tag{3.15}$$

In order to be able to perform calculations with such a quantum register, certain operations (so-called quantum gates) have to be applied to the qubits. Mathematically, these operations are matrices which are brought to the required dimensionality by means of a tensor product and then applied to the states of the qubits. This matrices can be classified according to the set of qubits on which they act. Among the best known quantum gates are CNOT ("controlled not"), Hadamard, Swap, the Pauli matrices, and the Toffoli gate [197]. The matrix representations and effects of the respective gates on the qubits are summarized in Tab. 3.2.

To build an efficient quantum computer, the qubits must be entangled with each other. To do this, a sequence of quantum gates must be executed that produce a superposition state that is not separable (i.e. cannot be represented as a product of basis vectors). For example, if one has a 2-qubit system in the $|00\rangle$ state and applies the 2^2-dimensional Hadamard gate $H \otimes I_2$ to the first qubit $|0\rangle$ only, the system takes the separable superposition state [195]

$$H \otimes I_2 |00\rangle = \frac{1}{\sqrt{2}}(|0\rangle + |1\rangle)|0\rangle) = \frac{1}{\sqrt{2}}(|00\rangle + |10\rangle). \tag{3.16}$$

If one would measure this 2-qubit system, the first qubit would take either the $|0\rangle$ or $|1\rangle$ state with a probability of $50\,\%$ in each case, while the second qubit would be in the $|0\rangle$ state. However, if one subsequently executes the CNOT gate, the second qubit is flipped if the first one is in the $|1\rangle$ state. Accordingly, a superposition state $\Phi^+ = \frac{1}{\sqrt{2}}(|00\rangle + |11\rangle)$ arises, which cannot be factorized into the individual pure states. If one now measures this non-separable system, the result of the measurement at the first qubit determines the state of the second qubit. If one measures the state $|0\rangle$ (or $|1\rangle$) at the first qubit, then the second qubit takes the state $|0\rangle$ (or $|1\rangle$) [198]. This inseparable superposition state is called entanglement. Since the two states $|00\rangle$ and $|11\rangle$ have the same probability, they are considered maximally entangled. In total, for a 2-qubit system, there exist four such maximally entangled states, which are so-called Bell states or also Einstein-Podolsky-Rosen pairs. These are:

$$\Phi^{\pm} = \frac{1}{\sqrt{2}}(|00\rangle \pm |11\rangle) \tag{3.17a}$$

$$\Psi^{\pm} = \frac{1}{\sqrt{2}}(|01\rangle \pm |10\rangle) \tag{3.17b}$$

These highly entangled states of multiple qubits belong to the group of cluster states. Such cluster states were already demonstrated for photonic qubits [199] and trapped atoms [200] and are more difficult to eliminate than other entangled states such as Greenberger–Horne–Zeilinger (GHZ) states or W states [201, 202]. For systems with n qubits, larger gates must be used to convert them into an entangled state. If all n qubits are entangled with each other, the execution of a single quantum gate can manipulate all 2^n states simultaneously. Because of this quantum parallelism, quantum computers are superior to classical computers for certain tasks [203]. For example, a classical gate operation on a bit sequence results in exactly one change to that bit sequence (linear growth). For entangled qubits, on the other hand, a quantum gate operation leads to 2^n manipulations of the state (exponential growth). Suitable quantum gates can thus be used to perform 2^n calculations

Name	Operation	Effect
Identity	$\begin{pmatrix} 1 & 0 \\ 0 & 1 \end{pmatrix}$	no effect (used e.g. for changing dimensions)
Hadamard	$\frac{1}{\sqrt{2}} \begin{pmatrix} 1 & 1 \\ 1 & -1 \end{pmatrix}$	single qubit rotation of π around X-Z-axis, creating the superposition states $\lvert+\rangle$ and $\lvert-\rangle$
Pauli X, Y, Z	$\begin{pmatrix} 0 & 1 \\ 1 & 0 \end{pmatrix}, \begin{pmatrix} 0 & -i \\ i & 0 \end{pmatrix}, \begin{pmatrix} 1 & 0 \\ 0 & -1 \end{pmatrix}$	single qubits rotation of π around X, Y, Z axis (Bit- or phaseflips)
SWAP	$\begin{pmatrix} 1 & 0 & 0 & 0 \\ 0 & 0 & 1 & 0 \\ 0 & 1 & 0 & 0 \\ 0 & 0 & 0 & 1 \end{pmatrix}$	swapping of two qubit states
CNOT	$\begin{pmatrix} 1 & 0 & 0 & 0 \\ 0 & 1 & 0 & 0 \\ 0 & 0 & 0 & 1 \\ 0 & 0 & 1 & 0 \end{pmatrix}$	flips the second (target) qubit by π, if the first (control) qubit is $\lvert1\rangle$, creation of fully entangled Bell states
Toffoli	$\begin{pmatrix} 1 & 0 & 0 & 0 & 0 & 0 & 0 & 0 \\ 0 & 1 & 0 & 0 & 0 & 0 & 0 & 0 \\ 0 & 0 & 1 & 0 & 0 & 0 & 0 & 0 \\ 0 & 0 & 0 & 1 & 0 & 0 & 0 & 0 \\ 0 & 0 & 0 & 0 & 1 & 0 & 0 & 0 \\ 0 & 0 & 0 & 0 & 0 & 1 & 0 & 0 \\ 0 & 0 & 0 & 0 & 0 & 0 & 0 & 1 \\ 0 & 0 & 0 & 0 & 0 & 0 & 1 & 0 \end{pmatrix}$	universal and reversible gate for applying AND, OR and NOT commands on a 3-qubit system

Table 3.2 Examples for quantum logic gates. Summarized from [195, 197].

in parallel, which results in a probability distribution.

Since the qubits are affected by external influences and individual qubits in a quantum register can be faulty, errors occur in the computation by the quantum gates. Accordingly, additional operations must be performed to minimize these external disturbances ("quantum error correction"). The decoherence time, i.e. the period during which the state of the qubit system is maintained, also plays a decisive role here, since it determines how many operations can be performed on the system. Moreover, since the result of a quantum calculation is a probability distribution, calculations must be performed several times to become statistically significant. Only by the optimal combination of entanglement of numerous qubits, a long decoherence time, and suitable quantum gates for computation and quantum error correction, the full potential of a quantum computer can be achieved. Further information on quantum error correction, decoherence, and quantum algorithms or quantum gates can be found, for example, in [185, 195, 204].

3.3.2 Photonic qubits

The quantum mechanical properties of single photons can be harnessed for the development of purely photonic quantum computers in different ways. The advantage of photons for these applications is that they are potentially free of decoherence and that they can be transmitted over long distances as flying qubits. However, photons do not naturally interact with each other, so two-qubit quantum gates are difficult to realize [11]. Nevertheless, a variety of methods have been developed to exploit the properties of photons for quantum computing. One way to generate entangled single-photon pairs are non-linear optical processes such as spontaneous parametric down-conversion and spontaneous four-wave mixing (see Sec. 2.3.2). The problem here is that the generation is probabilistic and not on-demand [205]. In 2001, Knill et al. showed that universal quantum computation with active linear optics can also be realized with non-deterministic single-photon sources (KLM protocol) [23], but scalability suffers from the low efficiency of such SPS. However, it is possible to use photon-photon interaction induced by cross-Kerr non-linearity to generate two-qubit quantum gates, but these processes are extremely weak ($\chi^{(3)} \approx 10^{-22} \, \mathrm{m^2 \, V^{-2}}$) and suffer from photon losses and strong noise, making such optical gate operations error-prone and correspondingly impractical [11].

Photons from reliable on-demand single-photon sources in solids allow the realization of e.g. non-universal QC schemes like the so-called boson sampling, which is a promising candidate for photonic QC. Such an experimental design is depicted in Fig. 3.10 and allows calculations with single photons even without their entanglement. Instead, sampling of the probability distribution of indistinguishable photons (bosons), which are scattered in a linear interferometer, is used to perform quantum computational tasks (see figure caption or [206] for details).

Other concepts usually rely on the deterministic generation of single photons that encode the information of a stationary qubit, e.g. a quantum center in optical cavities [205]. Such single photons depend on the properties of their solid-state quantum source and can be entangled by LOQC techniques, enabling fault-tolerant, near-deterministic quantum computer architecture [11]. This has the advantage that the stationary qubits can be well separated and thus do not interact directly with each other. Instead, their interaction takes place specifically through entangling operations mediated by single-photon interference effects [207]. According to [208], three schemes exist for entangling single atoms in distant cavities by atom-photon interaction. The first scheme is a direct interaction between two
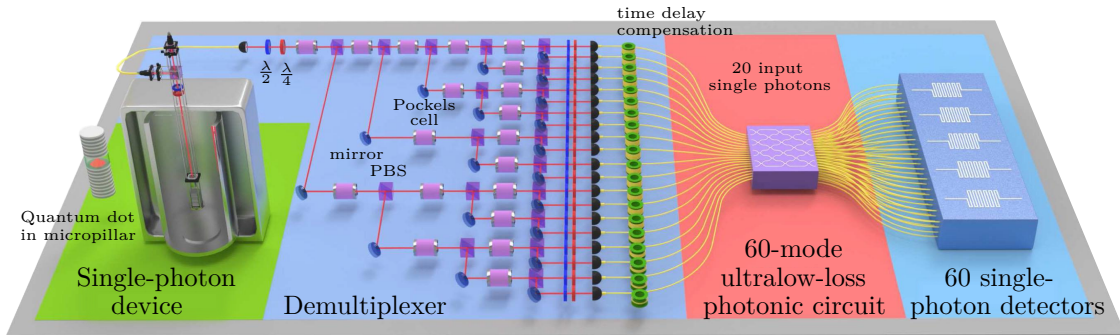
Figure 3.10 Example for boson sampling of 20 photons in an optical network, as demonstrated in [206]. Pulsed single-photon streams ($g^2(0) = 0.025$), generated in a cooled InGaAs/GaAs quantum dot, were deterministically coupled to a micropillar cavity and actively translated into 20 spatial modes. This is implemented by a demultiplexer consisting of a set of 19 Pockels cells, polarizing beam splitters (PBS) and mirrors. The photons are coupled into optical fibers of different lengths to compensate time delays and to ensure indistinguishability. The 20 demultiplexed modes are fed into a fully connected 60-port linear optical network, that allows the implementation of 60×60 unitary transformations. The photonic circuits output ports are connected to 60 superconducting nanowire single-photon detectors to measure the probability distribution of the single photons. Graphic taken with permission of *American Physical Society* from [206].

atoms, where a photon is generated in atom 1 and sent to atom 2 [209, 210]. The second scheme relies on the generation of entangled photons in a common source, which are simultaneously sent to different atoms in cavities, whereby the entanglement is transferred to the atoms via their cavity modes [211, 212]. In the third scheme, different single-photon sources generate photons, whose properties depend on the state of the respective source and entanglement between the atomic stationary qubits takes place via entangling measurements on the photons. This scheme will be discussed exemplarily in more detail in the following.

A process like the one just mentioned is described, for example, in [11, 205, 207, 213] using a system of two stationary qubits (e.g. NV centers) that are entangled with each other via newly generated photons ("ancillas"). A state measurement on the photons leads to a multiqubit entangling operation, where the state of the stationary qubits remains unaffected and the information remains stored (the measurement result is said to be mutually unbiased). The pure state of two stationary qubits (A in state $|0\rangle$ and B in state $|1\rangle$) in cavities is

$$|\psi_{\text{in}}\rangle_{\text{AB}} = (\alpha|0\rangle + \beta|1\rangle)(\alpha'|0\rangle + \beta'|1\rangle) = \alpha\alpha'|00\rangle + \alpha\beta'|01\rangle + \beta\alpha'|10\rangle + \beta\beta'|11\rangle \quad (3.18)$$

Both stationary qubits generate single photons (P and Q) whose states depend on the respective single-photon source. In general, one can write that the $|i\rangle_{\text{A}}$ state of the first SPS is entangled with a photon in the $|x_i\rangle$ state and the second SPS in the $|i\rangle_{\text{B}}$ state is entangled with a photon in the $|y_i\rangle$ state, leading to

$$|i\rangle_{\text{A}} \rightarrow |i, x_i\rangle_{\text{A}}, \quad |i\rangle_{\text{B}} \rightarrow |i, y_i\rangle_{\text{B}} \quad (3.19)$$

where $|x_i\rangle$ and $|y_i\rangle$ correspond for example to vertical $|v\rangle$ and horizontal $|h\rangle$ polarization. An appropriate measurement on the two photons P and Q leads to an entanglement of the

stationary qubits A and B and thus to the quantum state [208]

$$|\psi_{\text{enc}}\rangle = (\alpha|0\rangle_A|h\rangle_P + \beta|1\rangle_A|v\rangle_P)(\alpha'|0\rangle_B|h\rangle_Q + \beta'|1\rangle_B|v\rangle_Q) \tag{3.20a}$$
$$= \alpha\alpha'|00\rangle|hh\rangle + \alpha\beta'|01\rangle|hv\rangle + \beta\alpha'|10\rangle|vh\rangle + \beta\beta'|11\rangle|vv\rangle \tag{3.20b}$$

To entangle atoms A and B, the states of the photons must be projected onto one of the four Bell states ($|hh\rangle \pm |vv\rangle)/\sqrt{2}$ or $|hv\rangle \pm |vh\rangle)/\sqrt{2}$). However, it has been shown [214, 215] that completely deterministic Bell measurements using only linear optical elements are not possible and at most two out of four states can be distinguished, resulting in a success rate of only 50 %. However, by choosing the basis such that two basis states are maximally entangled and the other two basis states are product states (partial Bell state measurement), two results can be achieved. Either a Bell state is measured, thus accomplishing the qubit gate operation, or a product state is measured without modification of the stationary qubit state, so the initial state can be restored and the protocol repeated (repeat-unitl-success, "RUS quantum computing") [205]. Thus, on average, after two repetitions of the photon pair generation and the measurement process, a successfully performed quantum phase gate operation can be achieved. A Bell state measurement in this scheme works as follows: Two atoms in cavities each generate single photons, so that the combined atom-cavity photon system takes the state described in Eq. (3.20). When the photons are sent through a Hadamard beam splitter, the polarizations transform to the superposition states ($|h\rangle \rightarrow |h\rangle + |v\rangle)/\sqrt{2}$ and ($|v\rangle \rightarrow |h\rangle - |v\rangle)/\sqrt{2}$, causing the entire system to adopt the state [208]

$$|\psi'_{\text{enc}}\rangle = \frac{1}{2}\alpha\alpha'|00\rangle(|hh\rangle + |hv\rangle + |vh\rangle + |vv\rangle) + \frac{1}{2}\alpha\beta'|01\rangle(|hh\rangle - |hv\rangle + |vh\rangle - |vv\rangle) \tag{3.21a}$$

$$+ \frac{1}{2}\beta\alpha'|10\rangle(|hh\rangle + |hv\rangle - |vh\rangle - |vv\rangle) + \frac{1}{2}\beta\beta'|11\rangle(|hh\rangle - |hv\rangle - |vh\rangle + |vv\rangle). \tag{3.21b}$$

The photons then reach a polarizing beam splitter (PBS), which transmits photons in the $|h\rangle$ state and reflects those in the $|v\rangle$ state. Photons in the $|hh\rangle$ and $|vv\rangle$ superposition states take correspondingly different paths in the beam splitter and are registered individually at single-photon detectors (antibunching), while photons in the $|hv\rangle$ or $|vh\rangle$ superposition states leave the PBS together (bunching). After the PBS the system is in the state

$$|\psi''_{\text{enc}}\rangle = \frac{1}{2}(\alpha\alpha'|00\rangle + \beta\beta'|11\rangle)(|hh\rangle + |vv\rangle) + \frac{1}{2}(\alpha\beta'|01\rangle + \beta\alpha'|10\rangle)(|hh\rangle - |vv\rangle) \tag{3.22a}$$

$$+ \frac{1}{2}(\alpha|0\rangle + \beta|1\rangle)(\alpha'|0\rangle - \beta'|1\rangle)|hv\rangle + \frac{1}{2}(\alpha|0\rangle - \beta|1\rangle)(\alpha'|0\rangle + \beta'|1\rangle)|vh\rangle. \tag{3.22b}$$

A partial or incomplete Bell measurement can now take place by using a rotated basis (that is, without concrete measurement of the $|h\rangle$ and $|v\rangle$ states). If the states ($|h\rangle \pm |v\rangle)/\sqrt{2}$ are detected at both outputs of the PBS, it is possible to distinguish between the two Bell states Φ_1, Φ_2 (maximum entanglement) and the two product states Φ_3, Φ_4:

$$|\Phi_{1/2}\rangle = \frac{1}{\sqrt{2}}(|hh\rangle \pm |vv\rangle), \quad |\Phi_3\rangle = |hv\rangle, \quad |\Phi_4\rangle = |vh\rangle \tag{3.23}$$

Thus, when $|\Phi_1\rangle$ or $|\Phi_2\rangle$ are measured, the stationary qubits are maximally entangled, while when $|\Phi_3\rangle$ and $|\Phi_4\rangle$ are measured, the atoms can be re-initiated to their ground state and the measurement can be repeated. Since each result has a probability of 25 % and maximum entanglement occurs with 50 %, on average two measurements are needed to successfully perform a quantum gate operation [208].

No matter which technique one will use for pure photonic QC, all rely on the reliability of on-demand SPS and the quantum efficiency of the detectors used. Accordingly, reliable single-photon sources implemented in solids can also help to support this development.

3.3.3 Solid-state qubits

Among the different methods to create qubits, they can also be realized by defects in crystals. The advantage over other methods such as SQUIDs or ion traps lies in the better scalability (CMOS compatible fabrication and control, storage of entire qubit registers without major additional technical effort) and the possibility of utilization at room temperature. Important quantum physical parameters such as a long spin decoherence (T_2) and dephasing (T_2^*) time, high fidelity and fast initialization of the qubit depend on both the crystallographic environment and the nature of the defect [194, 216]. Optically active defects with spin-selective relaxation paths can provide qubits in two different ways. On the one hand, they can emit single photons whose polarization itself is used as a qubit. On the other hand, the quantum mechanical states of the defects can be used as qubits, forming a spin-photon interface that allows the conversion of stationary in flying qubits. The nuclear spin of the defect can thereby be used as quantum memory due to its long coherence time, while electronic states are used for coumputation, thats information is coupled to photons, enabling the transfer of qubits over long distances [217, 218].

The first theoretical model of a solid-state quantum computer was proposed by Loss and DiVincenzo in 1997 (Loss-DiVincenzo spin qubit quantum computer) [219]. Here, the qubits should be realized by the intrinsic spin of electrons (magnetic spin quantum number $m_{\mathrm{s}} = \pm 1/2$) localized in quantum dots. The state of the qubits is generated by controlled electrical gating of the tunneling barrier between neighboring quantum dots and the spin state of the qubits is subsequently converted into an electrical signal by spin-to-charge conversion. Since the energy of the electrons depends on their spin states, the tunneling barrier can be adjusted to distinguish between the two possible states. Charge sensors near the quantum dots finally measure the occupancy of the dots and convert them into electrical signals [220].

Kane quantum computer   Only one year later, a scalable quantum computer based on defects in silicon was proposed by Kane in 1998 [221]. Here, the qubits are realized by the nuclear spin (nuclear magnetic quantum number $m_{\mathrm{I}} = \pm 1/2$) of ^{31}P atoms spaced 20 nm apart in an isotopically pure ^{28}Si substrate (nuclear spin of ^{28}Si $I = 0$) and aligned by a strong constant magnetic field $\vec{B}$. An insulating layer of SiO_2 is grown over the silicon, on which in turn metallic gate structures are deposited (A gates above phosphorus atoms, J gates between two phosphorus atoms, see Fig. 3.11). Applying a voltage to the A gates shifts the electron wavefunction (shown here in green) away from the ^{31}P atom and toward the SiO_2 barrier. This, in turn, reduces the hyperfine interaction between the electron and nucleus and thus the Larmor frequency of the ^{31}P nuclei. An alternating magnetic field $\vec{B}_{\mathrm{AC}}$, which is perpendicular to the permanent magnetic field, now flips the nuclear spins with resonant Larmor frequency, so that individual nuclei can be specifically manipulated
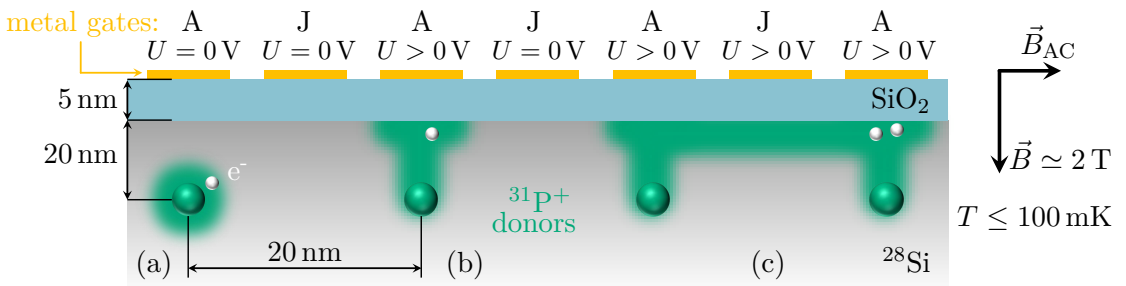
Figure 3.11 Principle of the Kane quantum computer. Three different scenarios are shown. **(a)** If no voltage is applied to the A gate, the electron wave function remains at the ^{31}P atom. **(b)** When a voltage is applied, the electron is pulled toward the insulating layer, changing the hyperfine interaction and thus the Larmor frequency of the nuclear spin. **(c)** Only by applying a voltage to the J gate can neighboring ^{31}P$^+$ spins couple with each other via the exchange interaction and thus higher dimensional quantum gates can be realized. More information can be found in the main text. Graphic adapted and recreated with permission of *Springer Nature* from [221].

by NMR pulse sequences (quantum gates) and initialized to the corresponding $|0\rangle$ and $|1\rangle$ states. However, in order to apply higher-dimensional quantum gates, the individual qubits must be coupled. This is accomplished by applying a voltage to the J gates, which varies the electrostatic potential barrier between two adjacent ^{31}P donors and thus enhances or reduces the exchange coupling J. As a result, neighboring donor electrons (whose spins are coupled to their nuclear spins via the hyperfine interaction) are pulled into a common region, thus significantly enhancing the electron-mediated nuclear spin interaction. If electrons are in the $|01 - 10\rangle$ superposition state, they can subsequently bind to a single ^{31}P atom for energetic reasons, converting the nuclear spin states to states of different electron polarization (D$^+$ and D$^-$) [221]. These states have different binding energies and thus a differentially applied voltage to an A gate can lead to different charge motions, which are determined by capacitance measurements between the gates. The difficulties of this concept lie in the precise alignment of ^{31}P atoms in silicon, the interactions with deep defects of dangling bonds at the Si/SiO$_2$ interface, and in uncontrolled tunneling effects of electrons into the conduction band [222, 223]. In addition, low temperatures are necessary for this concept so that the electrons occupy only the lowest energy spin levels. The electrons are completely spin-polarized and allow controlled couplings between the nuclei only at temperatures of $T \leq 100$ mK and magnetic fields of $B \geq 2$ T. However, due to the numerous advantages (silicon as the base material, CMOS compatible fabrication, long coherence time of $T_2 = 35.6$ s of the ^{31}P nuclear spin [224] and manipulation by known NMR methods), the concept has been steadily developed [225–228] and is one of the most promising candidates for a solid-state quantum computer, although a spin-photon interface is missing in this scheme.

NV center Around the same time, in 1997, the nitrogen defect center in diamond was shown to exhibit photostable photoluminescence measurable at room temperature [29]. Since the PL is related to a paramagnetic electron ground state, the NV center offers the possibility of optically manipulating and detecting its electron spin state and thus allows the construction of a quantum computer that, unlike other and more established methods, operates at RT. Furthermore, such a QC could be fabricated in a compact and CMOS
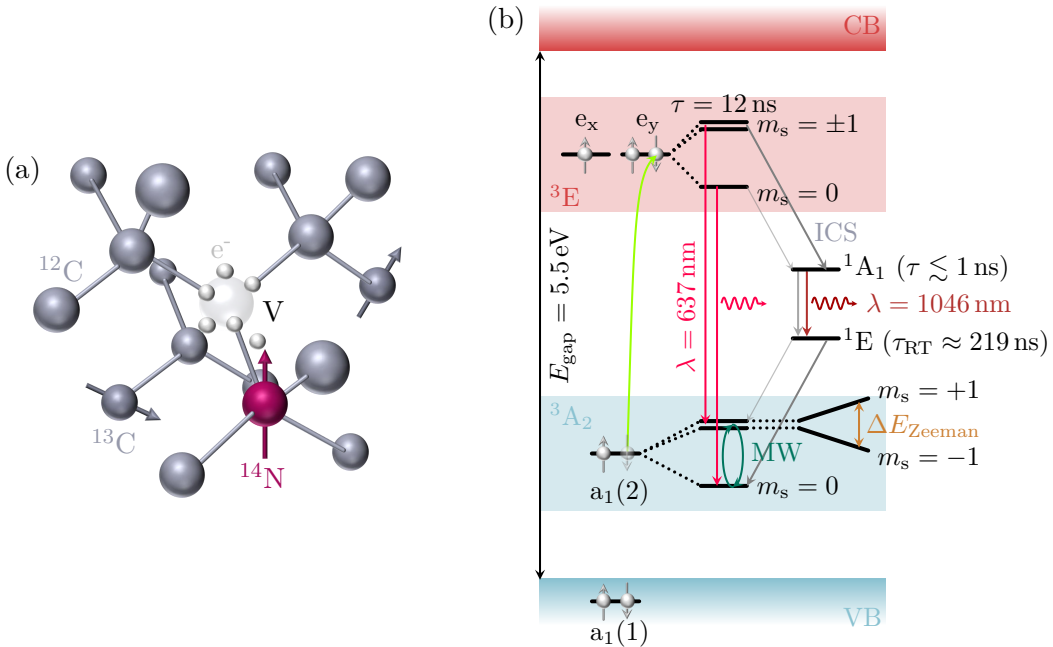
Figure 3.12   NV⁻ center qubits in diamond. (a) Defect structure depicting the spatial proximity of the ^{14}N and vacancy in the carbon lattice as well as the formation of the six unpaired electrons. **(b)** Electronic structure of the NV⁻ center. Relaxation takes place either by direct spin-conserving radiative transition between the $m_{\mathrm{s}} = \pm 1$ states of two triplet states, or via intersystem crossing. The ground state population between $m_{\mathrm{s}} = 0$ and $m_{\mathrm{s}} = \pm 1$ can further be manipulated by a microwave field, thus controlling the PL intensity. See main text for details.

compatible manner using ion implantation, and provides manipulation of electronic states as well as both, quantum memory through the nuclear spin and flying qubits in the form of photons.

The defect structure of the NV center is shown in Fig. 3.12 (a) and consists of a substitutional nitrogen atom (^{14}N) located next to a vacancy. The ^{14}N atom has five valence electrons, three of which are covalently bonded in the diamond lattice. The neighboring vacancy is further leading to three unbound electrons, so that the optically active defect has a total of five free electrons. The vacancy can bind another electron from the vicinity to itself, resulting in the negative charge state NV⁻ with $C_{3\mathrm{v}}$ symmetry, which is mainly used for quantum applications and has the electronic structure shown in Fig. 3.12 (b). The six electrons of the NV⁻ occupy four molecular orbitals, three of which ($a_1(2)$, e_{x}, e_{y}) are located within the diamond bandgap [229, 230]. Irradiation with green laser light can excite spin-conserving transitions of an electron from the $a_1(2)$ state to the e_{x} or e_{y} state. In the multielectron representation, both the ground state ^{3}A$_2$ and the excited state ^{3}E (where A and E labeling the symmetry) are spin triplet states. Relaxation takes place again spin-conserving either from the excited ^{3}E $m_{\mathrm{s}} = 0$ to the ^{3}A$_2$ ground state with $m_{\mathrm{s}} = 0$, or from the excited ^{3}E $m_{\mathrm{s}} = \pm 1$ to the ^{3}A$_2$ ground state with $m_{\mathrm{s}} = \pm 1$. Furthermore, the excited state can also relax via intersystem crossing (ISC) over two metastable singlet states ^{1}A$_1$ and ^{1}E, where both non-radiative and radiative transitions occur with luminescence in the IR region ($\lambda = 1046$ nm) [231]. This point is of great importance for the initialization of the NV center qubit: relaxation via the metastable non-radiative path is much more likely
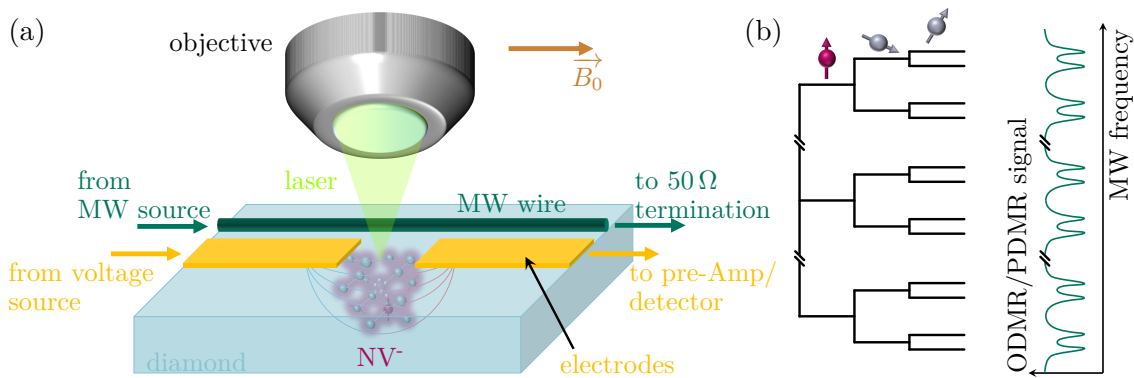
Figure 3.13 Manipulation and readout of NV⁻ center qubits. (a) NV centers are located between two electrodes and close to a wire, that mediates the microwave field and thus manipulates the occupation of the triplet ground state. After defect excitation with laser light, the manipulation can be measured either by its changes in PL intensity or photocurrent **(b)** NV electron-mediated hyperfine coupling of three nuclear spins generates 12 spin transitions, which can be addressed individually by different magnetic field alignments [232], adapted with permission of *Springer Nature* from [233]. See text for details.

for excited electrons in the $m_\text{s} = \pm 1$ state than in the $m_\text{s} = 0$ state, which are more likely to relax spin-conserving and radiative to the $m_\text{s} = 0$ ground state. If an excited electron with $m_\text{s} = \pm 1$ relaxes via the non-radiative path, it dwells longer in the metastable state ($\tau \approx 219\,\text{ns}$ [234]) than in the excited state ($\tau \approx 12\,\text{ns}$ [235]), so that after several excitation cycles the state of the NV center will always be in the ground state with $m_\text{s} = 0$, regardless of the state at the beginning.

Another important property is the splitting of the electron spin sublevels $m_\text{s} = 0$ and $m_\text{s} = \pm 1$ in the $^3\text{A}_2$ ground state by spin-spin interaction [230]. The resulting energy difference between the ground state sublevels without an external magnetic field, the zero-field splitting (ZFS), is $\Delta f_\text{ZFS} = 2.87\,\text{GHz}$. An external magnetic field additionally lifts the degeneracy of the $m_\text{s} = \pm 1$ states ($\Delta f_\text{Zeeman} = 2\gamma_\text{NV}B_0$), so that transitions between the states $m_\text{s} = 0$ and $m_\text{s} = +1$ or $m_\text{s} = -1$ can be excited by an applied microwave (MW) field. This allows the electronic states to be measured both optically and electronically. The basic principle for this is shown in Fig. 3.13 (a). When electrons are excited to the $m_\text{s} = \pm 1$ $^3\text{A}_2$ ground state by MW radiation, they are spin-selectively raised to the $m_\text{s} = \pm 1$ ^3E state by photon excitation. In this excited state, the electrons have two options: Either they are lifted into the conduction band by a second irradiated photon (two-photon ionization), where they are withdrawn by a voltage applied to the electrodes, leaving behind a neutral NV^0 center, or they decay back to the $^3\text{A}_2$ ground state, choosing the radiative transition with a probability of about 2/3 and 1/3 taking the non-radiative path via ISC [230]. In the latter case, the electrons do not contribute to luminescence, which leads to a decrease in PL intensity in in the case of resonance of the MW frequency and the energy splitting between $m_\text{s} = 0$ and $m_\text{s} \pm 1$ (ODMR signal). At the same time, the electrons relaxing via the ISC stay longer in the metastable state, so that they are also not available for the two-phonon ionization process, which in resonance also reduces the amount of electrons lifted into the conduction band (PDMR signal) [40]. Through an additional superimposed magnetic field or nuclear spin interactions with other atoms such as ^{13}C ($I = 1/2$), the

lifting of the $m_\mathrm{s} = \pm 1$ degeneracy is shown by a splitting of the resonance lines in the MW spectrum (Fig. 3.13 (b)). The sensitivity of these line splittings to ambient parameters such as temperature, pressure, and electromagnetic fields make NV centers also enormously efficient quantum sensors.

The great potential of these defects has led to a plethora of far-reaching developments. For example, ion implantation has allowed ensembles of just a few individual NV centers to be artificially fabricated [25] and further developments in ODMR and PDMR techniques have allowed both optical and electronic measurements of just a few single centers [41,42]. Defect engineering has also led to an increased NV creation yield of 70 % for NV centers fabricated by ion implantation and doping of the diamond [236]. New decoherence-protected quantum logic gates achieved the record for the longest solid-state qubit coherence time $T_2 = 75\,\mathrm{s}$ using the ^{14}N spins of NV centers in 2019 [237].

Following the promising developments of NV centers for quantum computing, many other optically active centers in various crystal systems such as silicon, silicon carbide, hexagonal boron nitride, etc. are currently under investigation. ODMR active color centers in silicon such as the G center could play a crucial role, as they combine the advantages of silicon as solid-state host material and defect qubits with spin-photon interfaces. But to evaluate the suitability for quantum technologies, however, the quantum physical properties of such centers must be examined and processes for the fabrication and manipulation must be developed. This will be the topic of the following chapters, where new properties of G centers are discovered and their suitability for quantum applications will be investigated.

Optical properties of an ensemble of G centers in silicon

Subject matter

In the following chapter, the results of our joint publication* [50] will be described in detail with kind permission from *American Physical Society*. Within this work, basic properties of an ensemble of G centers should be confirmed and supplemented by new measurements. For this purpose, five areas with different defect densities were created with the combination of carbon implantation, annealing and high-energy hydrogen irradiation as described in Sec. 3.1.1, and subsequently investigated by extensive temperature-dependent and time-resolved spectroscopic measurements at the L2C. The results were used to make statements about the ensemble recombination dynamics of this quantum center.

Contribution: different carbon and hydrogen implantations during the development process, discussions and presentations in project meetings, proof-reading of the publication

4.1 Experiment description and basic properties

4.1.1 Sample fabrication

The examined SOI sample consisted of a 220 nm thick Si layer, which was separated from the Si substrate by a 1 µm thick SiO_2 layer (see Fig. 4.1 (a)). The SOI structure was produced using the Soitec Smart Cut technology [238]. Since the whole sample area needed to be implanted with carbon ions, the ^{12}C implantation took place at the Institute of Physics at the University of Oslo with a fluence of $\Phi = 2 \times 10^{14}\,\mathrm{cm^{-2}}$ and an energy of $E = 36\,\mathrm{keV}$. At this energy, the ^{12}C ions stopped in the center of the Si layer in a depth of 100 nm with a statistical distribution range of 10 nm. After implantation, the sample was annealed at the IM2NP in Marseille in a commercial rapid thermal processing (RTP) device at 1000 °C for 20 s in N_2 atmosphere to incorporate the implanted carbon atoms into the silicon lattice and thus creating the substitutional C_s. Subsequently, five squares of 25 µm × 25 µm
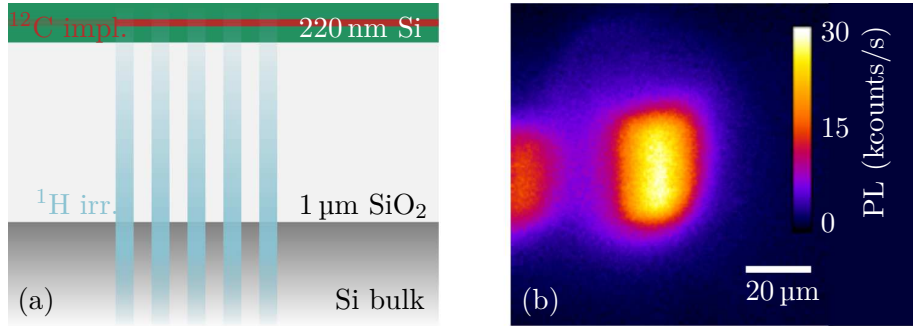
Figure 4.1   Description of the examined sample. (a) Sketched cross section of the ^{12}C implanted and ^{1}H irradiated SOI layer stack. **(b)** PL raster scan of a $25\,\mu m \times 25\,\mu m$ proton irradiated spot with a ^{1}H fluence of $9 \times 10^{14}\,cm^{-2}$ (previously implanted with $2 \times 10^{14}\,cm^{-2}$ ^{12}C^{-} ions at an energy of $36\,keV$) and measured with a CW excitation energy of $2.33\,eV$ at $T = 10\,K$.

size, as shown in Fig. 4.1 (b), were irradiated with ^{1}H ions each with a different fluence (1×10^{13}, 3×10^{13}, 1×10^{14}, 3×10^{14}, $9 \times 10^{14}\,cm^{-2}$) and an energy of $2.25\,MeV$ at the Lipsion accelerator in Leipzig. The high-energy irradiation produces mobile interstitial C_i, which can be subsequently trapped by the C_s, thus creating the C_i-C_s defect called G center. The five different areas show different PL intensities, indicating different defect densities.

4.1.2 Optical spectroscopy

The optical evaluation of the generated centers was performed at the L2C in Montpellier with a confocal laser scanning microscope with near-IR optics similar to the one described in Sec. 3.2.2. Since G center luminescence vanishes at temperatures higher than $100\,K$, the sample was cooled in a closed-cycle cryostat that allows temperature-dependent measurements down to $5\,K$. The optical excitation of the G centers was done either by a CW HeNe laser ($632\,nm$ or $1.96\,eV$), a CW laser diode ($532\,nm$ or $2.33\,eV$) or by a pulsed laser diode ($532\,nm$) with a repetition rate of $20\,MHz$. The laser light was focused on the sample through a microscope objective with a numerical aperture of NA = 0.75, which simultaneously allowed the collection of the photoluminescence of the G centers. The excitation and collection took place through a quartz glass window of the cryostat, which has a particularly high transmission in the near-IR range, in order to pass the luminescence of the quantum centers as loss-free as possible.

Continuous-wave detection: The PL signal was diffracted in a $f = 300\,mm$ Czerny-Turner monochromator ($600\,grooves/mm$ grating blazed at $1600\,nm$) and recorded with an InGaAs photodiode array (quantum efficiency $\eta_{QE} = 80\,\%$ at $\lambda = 1300\,nm$) over integration times of $60\,s$.

Time-resolved measurements: The PL signal was detected by an InGaAs photodiode with a cut-off detection at $\lambda = 1700\,nm$, after spectral selection with a long-pass filter at $\lambda = 1250\,nm$. For investigation of different parts of the emission spectrum, namely ZPL and PSB, two $20\,nm$ bandpass filters, centered at either $1280\,nm$ or $1300\,nm$, have been additionally used. The PL lifetime of the defect was recorded by time-correlated single-photon counting measurements with a temporal resolution of $400\,ps$.
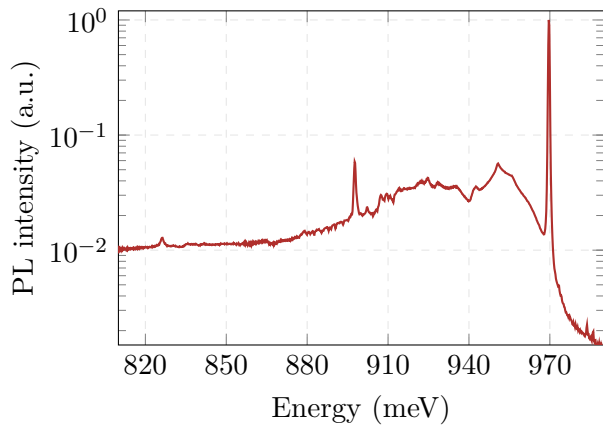
Figure 4.2   Typical normalized G center spectrum measured from the center of the spot shown in Fig. 4.1 (b). The sharp and intense ZPL at 969 meV, caused by the direct radiative recombination without phonon emission, the LVM E and E' as well as the broad phonon-assisted sideband, expanding to lower energies, are clearly visible.

PL excitation measurements: For investigation of the PL response under varying excitation energy, a CW TiSa laser and a pseudo-CW source (supercontinuum Fianium SC400-4) filtered by a holographic tunable bandpass filter with a bandwidth of 2 nm was used. The average power density of the laser was monitored while tuning the excitation energy but remained in the order of $4 - 10\,\text{kW}\,\text{cm}^{-2}$ all throughout the excitation window. The data are normalized to a constant power density of $10\,\text{kW}\,\text{cm}^{-2}$.

4.1.3 PL response of different defect densities

To characterize the sample, the five different defect densities were first examined by confocal PL spectroscopy. Therefore, the individual proton-irradiated areas were selected in the center and a spectrum was recorded (Fig. 4.2). The total intensity of the PL was determined by integrating the PL signal over the whole spectral width. As shown in Fig. 4.3, the intensity increases with increasing proton fluence, since more defects are generated. The decrease of intensity measured in [38] at proton fluences higher than $1 \times 10^{14}\,\text{cm}^{-2}$ was not ascertained in our experiment, despite similar carbon and proton fluences and energies. This could be caused by inaccuracies in the beam current measurement or by the different sample materials (pure SOI versus n-type bulk Si wafer) that could lead to different recombination paths. We observe a slightly superlinear increase with a power law of exponent 1.25 ± 0.05 of the G center emission with increasing proton fluence in the investigated range of the log-log diagram. A deviation from the purely linear progression can be explained by the complex structure of the defect, consisting of two carbon atoms, and was also observed for low defect densities in [38].

4.1.4 Photoluminescence excitation measurement

In order to obtain new insights about absorption and carrier relaxation, which is important e.g. for the evaluation of the spectral dependence of the effective pump efficiency for a given irradiated power, the first photoluminescence excitation (PLE) measurements on this system ever were performed. The progression of the PLE spectrum measured at $T = 10\,\text{K}$ is
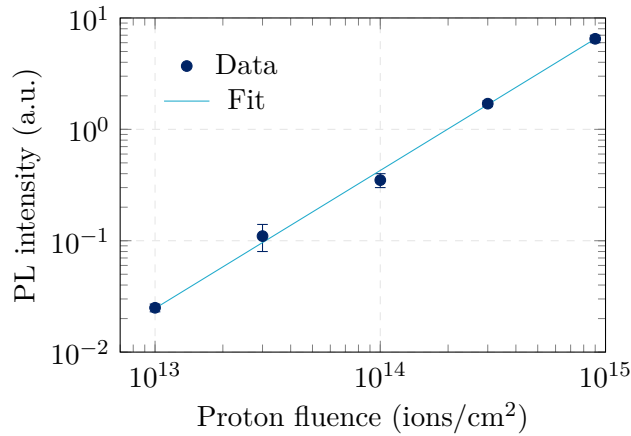
Figure 4.3 Correlation between proton fluence and G center emission in a log-log scale. Within the examined regime we observe a superlinear increase of the PL intensity with increasing ^{1}H fluence.

shown in Fig. 4.4. For this purpose, the ZPL intensity at a constant incident power density of $10\,\mathrm{kW\,cm^{-2}}$ was plotted against the excitation energy. In the range between $1.2\,\mathrm{eV}$ and $3.0\,\mathrm{eV}$ an increase in intensity of the ZPL by two orders of magnitude is observed. Since the indirect bandgap of silicon at low temperatures is at $E_{\mathrm{indir.}} = 1.1\,\mathrm{eV}$, the measured signal corresponds to a non-resonant, above bandgap excitation for all accessible energies. This means that the generated charge carriers first fall to the extrema of conduction band and valence band by non-radiative relaxation before they are captured in the G centers, where subsequently the excitonic recombination takes place. The resulting spectrum essentially corresponds to the silicon absorption of thin films at excitation energies above the bandgap [239]. Compared to the steadily increasing evolution of the absorption coefficient of pure silicon in the studied region [240], within our PLE spectrum also minima are observed, which are most likely caused by local small deviations of the crystal and electronic strucutre, introduced by the G center.

4.1.5 Saturation behavior

In the following section the saturation behavior of an ensemble of G centers at $10\,\mathrm{K}$ for increasing laser powers P at constant CW excitation energy of $1.96\,\mathrm{eV}$ is presented and discussed. Special care was taken to ensure that no significant heating of the sample occurs at higher laser powers, since it is known that the PL intensity decreases with increasing temperatures (see Sec. 4.2) and could therefore falsify the result. By controlling the position and width of the ZPL, which are also sensitive to temperature changes, it can be ensured that the temperature remained constant over the entire measurement. As can be seen in Fig. 4.5, for low laser powers ($P < 20\,\mathrm{kW\,cm^{-2}}$) we observe a quasi-linear increase in emission with increasing P, whereas for powers $P \gtrsim 20\,\mathrm{kW\,cm^{-2}}$ a saturation with sublinear increase is detected. Since an influence of temperature can be excluded, this measurement is an indication of an intrinsic saturation behavior, which will be explained in more detail below.
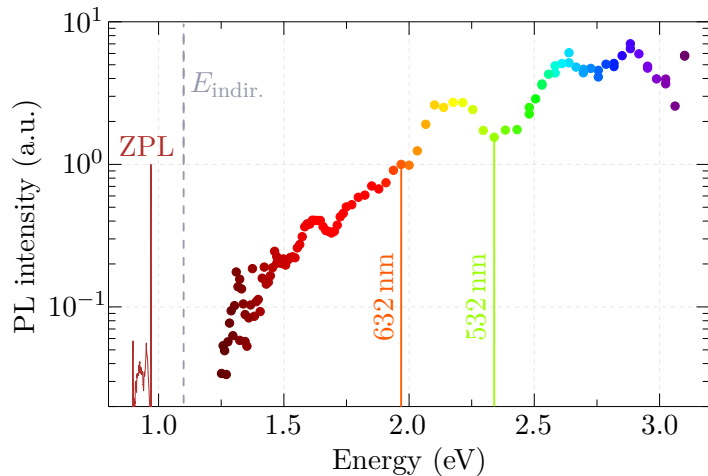
Figure 4.4 PL excitation spectrum of an ensemble of G centers. PL intensity of the ZPL was measured at T = 10 K and fixed incident laser power of P = 10 kW cm^{-2} for varying laser excitation energies, resulting in reproduction of an absorption spectrum of a silicon thin film. Also shown are the position of the ZPL and the indirect bandgap E$_{\text{indir.}}$ of silicon.

Saturation model for an ensemble of two-level systems

For a first approximation of the saturation power P_{sat} of an ensemble of G centers we make the following assumptions:

- G centers are excited by a laser spot with Gaussian distribution

- all G centers are identical and distributed in a two-dimensional plane (reasonable for a 200 nm thick Si layer)

- emission intensity corresponds to a standard saturation curve with saturation power density P_{sat}

Since certain information, like e.g. emission of different defect orientations, are still missing for a precise description of the saturation power, this model provides only a first approximation to the actual value of P_{sat}. However, in contrast to other nanostructures such as epitaxial quantum dots or nanocrystals, in which fluctuations of e.g. lifetime or dephasing time prevent the observation of saturation behavior in ensemble measurements, the procedure used here for point defects, where identical saturation performance can be assumed for all defects, allows a sufficiently accurate interpretation of the saturation behavior.

Due to the Gaussian shape of the laser beam, the defects in the center of the spot are excited with a higher power density than those at the edge of the laser spot. Consequently, the progress of the saturation curve corresponds to a superposition of saturated defects in the center and still unsaturated G centers at the spot periphery. Therefore, the saturation curve of an ensemble of G centers cannot be described with a standard saturation model of a single quantum mechanical two-level system ($I(P) = I_0(1 + P_{\text{sat}}/P)^{-1}$). Under the given assumptions, the power-dependent PL signal intensity can be written as

$$I_{\text{PL}} \propto \int_0^\infty 2\pi r \, \mathrm{d}r \left(P_0 \, e^{-r^2/w^2} \right) \left(1 + \frac{P_0 \, e^{-r^2/w^2}}{P_{\text{sat}}} \right)^{-1} \tag{4.1}$$
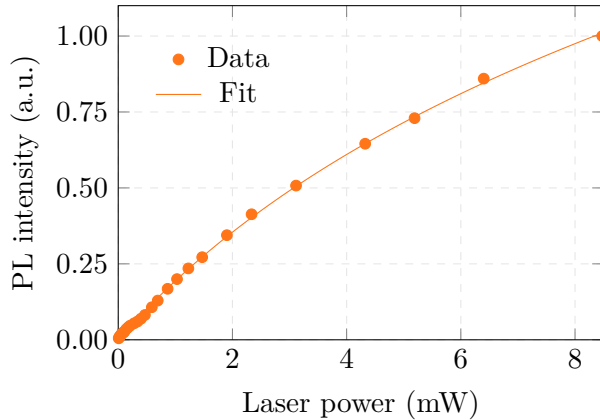
Figure 4.5 PL intensity of an ensemble of G centers for increasing incident laser power. The measurement was performed at $T = 10\,\mathrm{K}$ and with an excitation wavelength of $532\,\mathrm{nm}$. Experimental data (circles) are fitted (line) by Eq. (4.2) with $P_{\mathrm{sat}} = 5.8\,\mathrm{mW}$, corresponding to a laser power density of $P_{\mathrm{sat}} = 35\,\mathrm{kW\,cm}^{-2}$ [151]. The fit function describes the saturation of an ensemble of identical two-level systems excited by a Gaussian excitation spot [50].

where P is the average (measured) incident laser power over the entire spot and P_0 is the power density in the center of the Gaussian laser spot of waist w. With the relation $P = P_0/\ln(2)$ and after integration, one obtains

$$I_{\mathrm{PL}} = I_0 \ln\left(1 + \frac{P}{P_{\mathrm{sat}}/\ln(2)}\right) \tag{4.2}$$

for the correlation between measured intensity I_{PL} and saturation power P_{sat}, where I_0 corresponds to the emission intensity for an incident power of $P_{\mathrm{sat}}(e-1)/\ln(2)$. The experimental data (circles) in Fig. 4.5 are perfectly reproduced with a fit parameter for the saturation power of $P_{\mathrm{sat}} = 5.8\,\mathrm{mW}$, which corresponds to a laser power density of $P_{\mathrm{sat}} = 35 \pm 7\,\mathrm{kW\,cm}^{-2}$. This value can now be used to estimate the carrier capture volume of G centers: Based on a Poisson distribution of the occupation probability of a two-level system [241, 242], there is on average one exciton in each G center when saturation is reached. With a lifetime of $\tau = 6\,\mathrm{ns}$ (see Sec. 4.3) and an absorption length of $\sim 5 \times 10^{-4}\,\mathrm{cm}$ for a laser excitation of $1.96\,\mathrm{eV}$, one obtains a steady-state carrier density of $\sim 2 \times 10^{17}\,\mathrm{cm}^{-3}$, whose inverse corresponds to the capture volume. Assuming a spherical geometry of the defect, a capture radius of $20 \pm 2\,\mathrm{nm}$ is obtained. This value is similar to that of extrinsic centers in III-V alloys [243] and is significantly larger compared to the actual defect extent (about two orders of magnitude compared to the extent of the electronic wave function of G centers, which will be derived in Sec. 4.3.3). It also plays a decisive role for the line broadening of the ZPL (see Sec. 4.2.2), since the trapped charge carriers can influence the optical signal by spectral diffusion [242, 244].

4.2 Temperature-dependent photoluminescence spectroscopy

In the following the results of our temperature-dependent measurements are presented. The influence of temperature on the position and width of the ZPL, as well as on the intensity and lifetime of the photoluminescence is investigated. Based on these results, considerations about the temperature-dependent radiative and non-radiative rates are made.
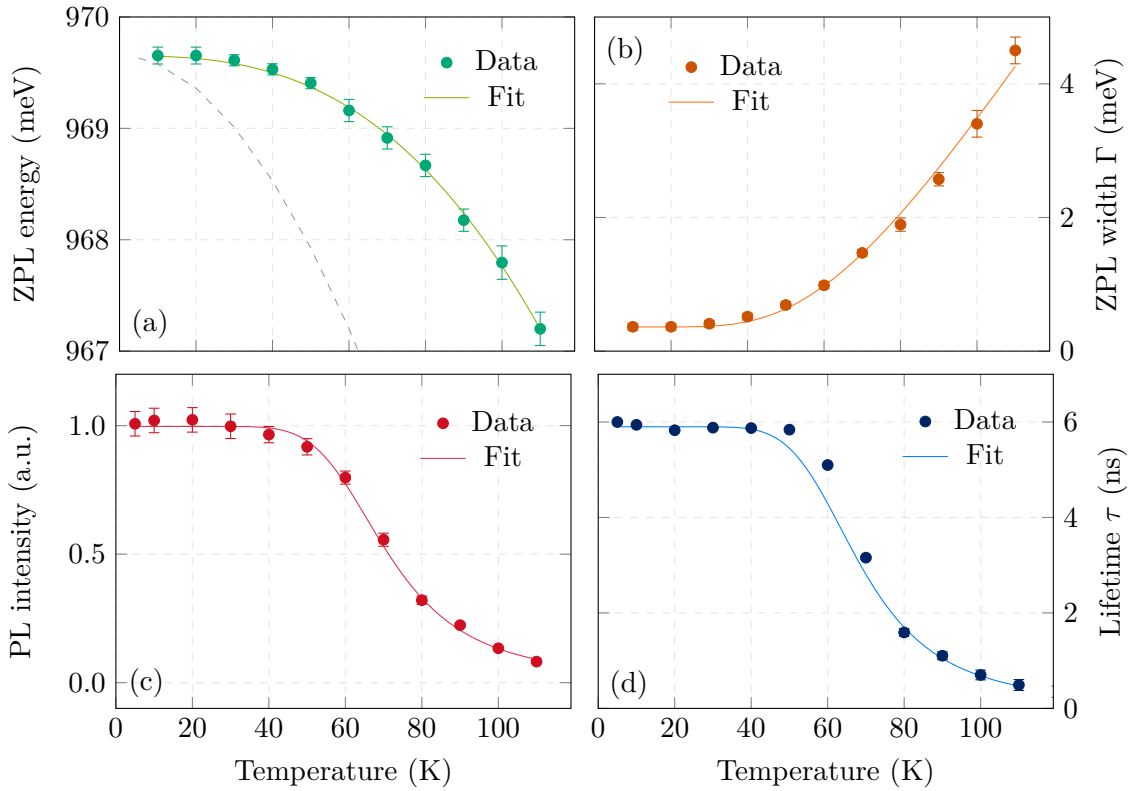
Figure 4.6 Temperature-dependent properties of an ensemble of G centers. (a) Measurement of the ZPL energy shift with increasing temperature. Data have been fitted with Eq. (4.3). The grey dashed line shows in comparison the temperature-dependent progress of the bulk Si bandgap determined by Varshni's law. **(b)** Temperature-induced broadening of the ZPL. Data have been fitted with Eq. (4.4), showing an upper limit of the ZPL width of 0.3 meV. **(c)** PL signal intensity from PSB and ZPL. The intensity decay with increasing temperature can be observed, which is fitted by the Arrhenius law from Eq. (4.5) **(d)** Temperature-dependent PL lifetime, fitted by the inverse of Eq. (4.7) and exhibiting a nearly constant lifetime of 5.9 ns at temperatures below 50 K.

4.2.1 Thermal redshift

The temperature dependence of the ZPL energy is shown in Fig. 4.6 (a) together with the bandgap shift of pure bulk Si (grey dotted line, according to [245]). The different courses indicate changes in electron-phonon interaction in the G center compared to the silicon lattice. The shift of the bulk Si bandgap is caused by lattice expansion at increasing temperatures and by zero-point fluctuations at very low temperatures and can be described by Varshni's law [246]. The different course of the G center ZPL, on the other hand, indicates a changed zero-point fluctuation within the G centers and can be reproduced with a polynomial expression corresponding to

$$E_{\text{ZPL}} = E_0 - AT^p \tag{4.3}$$

with the parameters $E_0 = 969.6 \pm 0.1$ meV, $A = 1.9 \pm 0.2 \times 10^{-6}$ meV K^{-3} and $p = 3 \pm 0.1$ meV, where the latter value fits well into the series of measured exponents $2 \lesssim p \lesssim 3.3$ for other semiconductors [246].

4.2.2 ZPL broadening

As can be seen in Fig. 4.6 (b), the ZPL width in the range $0 - 20\,\mathrm{K}$ remains approximately constant at $0.3\,\mathrm{meV}$ (spectral resolution of our setup $0.15\,\mathrm{meV}$) and then increases exponentially with rising temperatures in the investigated range. This measured progress is well fitted by the function [247]

$$\Gamma = \Gamma_0 + a e^{-\Omega/k_\mathrm{B}T} \tag{4.4}$$

with the parameters $\Gamma_0 = 0.3 \pm 0.05\,\mathrm{meV}$, $a = 34 \pm 5\,\mathrm{meV}$ and $\Omega = 21 \pm 2\,\mathrm{meV}$. However, the zero-temperature width $\Gamma_0 = 0.3\,\mathrm{meV}$ determined here represents only an upper limit of the homogeneous/single-center linewidth, since the inhomogeneous line broadening and spectral diffusion, caused by the ensemble measurement and captured charge carriers (Sec. 4.1.5), affect the linewidth [248]. The exponential term in Eq. (4.4) describes the phonon-induced line broadening. It should be noted that the mean phonon energy $\Omega = 21\,\mathrm{meV}$ is in good agreement with the maximum of the phonon DOS (shown in Fig. 4.12) at $\Delta E \approx 20\,\mathrm{meV}$. According to our model, this corresponds to a particularly large influence of the TA(X) phonon mode on the ZPL line broadening. The exponential increase of the ZPL width is correlated to the Bose-Einstein occupation factor $n(T)$ of phonons at low temperatures ($\Omega \ll k_\mathrm{B}T$), since the probability of phonon absorption is proportional to $n(T)$. Overall, Eq. (4.4) is similar to that usually used for bulks, quantum wells and quantum wires [247]. However, phonon dephasing at zero-dimensional point defects cannot be described with the same model. Further investigations, especially of the homogeneous line broadening at single G centers, are necessary to understand the exact mechanism of line broadening and especially the influence of spectral diffusion.

4.2.3 Temperature-dependent PL intensity

To determine the temperature-dependence of PL intensity, spectra were recorded at different temperatures and integrated within a range of $0.82 - 1.00\,\mathrm{eV}$. As already expected from former experiments [32], the emission intensity decreases between $10 - 110\,\mathrm{K}$ by more than one order of magnitude. The resulting course in Fig. 4.6 (c) can be reproduced with an Arrhenius equation

$$I(T) = I_0 \left(1 + B\, e^{-E_\mathrm{A}^{(1)}/k_\mathrm{B}T}\right)^{-1} \tag{4.5}$$

and the parameter $B = 700 \pm 200$ as well as an activation energy $E_\mathrm{A}^{(1)} = 41 \pm 5\,\mathrm{meV}$. This energy agrees well with values found in literature [33], but differs strongly from the confinement energy of other nanostructures (e.g. epitaxial quantum dots).

If one determines the fraction of the intensity that is only radiated into the ZPL, one obtains the Debye-Waller factor $\Theta(T)$. As can be seen in Fig. 4.7, the proportion of the ZPL in the total intensity decreases from $18\,\%$ at $10\,\mathrm{K}$ to $\sim 3\,\%$ at $110\,\mathrm{K}$. According to [51], assuming that the entire phonon bath can be approximated by a single phonon energy Λ, the temperature dependence of the Debye-Waller factor can be described with

$$\Theta(T) = \exp\left[-\xi^2 \coth\left(\frac{\Lambda}{2k_\mathrm{B}T}\right)\right] \tag{4.6}$$

where ξ describes the coupling strength of a linear electron-phonon interaction. By fitting the data in Fig. 4.7, one gets $\xi = 1.3 \pm 0.05$ and $\Lambda = 11 \pm 2\,\mathrm{meV}$. Thus, the phonon energy Λ determined here is smaller than the mean phonon energy of $\Omega = 21\,\mathrm{meV}$, determined
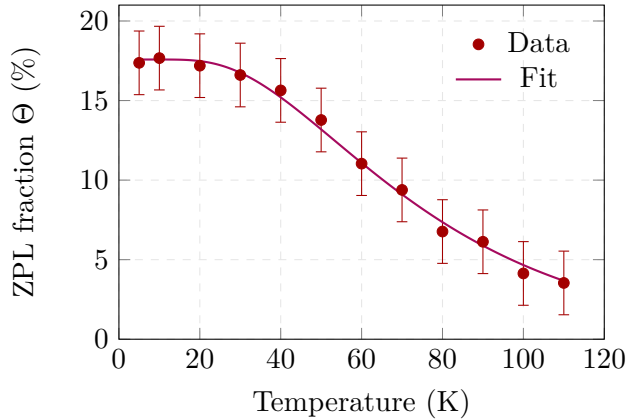
Figure 4.7   Fraction of the ZPL intensity to the total intensity (Debye-Waller factor).
From fitting the data with Eq. (4.6), we assume different origins of the thermal ZPL broadening and
ZPL fraction decrease.

in Sec. 4.2.2, which suggests different origins for the temperature behavior of ZPL line
broadening and ZPL fraction loss. As described in Sec. 4.1.5, line broadening seems most
likely to be influenced by the TA(X) mode with increasing temperature, while the decrease
of ZPL fraction is more likely due to defect-induced vibrational resonance [249], which is
also suspected to be responsible for the energy dip in the spectrum of the G centers between
$0.95 - 0.97$ eV. At $T \approx 0$ K the coupling strength ξ alone determines the ZPL fraction, since
$\Theta(T \to 0) = \exp(-\xi^2)$. It usually increases either with electronic confinement or electron-
phonon interaction, which makes a direct comparison between point defects to quantum
dots or between different materials difficult. Nevertheless, it can be stated that although
G centers possess shallow levels in the Si bandgap, they have a relatively high coupling
strength compared to the deep levels of NV centers in diamond ($\xi = 1.87$) [249] or in
hexagonal boron nitride ($\xi = 1.1$) [250].

4.2.4 Temperature-dependent lifetime and decay rate

The following section deals with the temperature-dependent lifetime of an ensemble of
G centers and thus also represents the transition to Sec. 4.3, in which phonon-supported
recombination dynamics is investigated.
In Fig. 4.8 (a) the spectra of an ensemble of G centers measured at different temperatures
are shown. The already described increase in intensity at low temperatures as well as
the ZPL shift and broadening are visible. In Fig. 4.8 (b) the decay traces corresponding
to the respective temperature are shown in a semi-log diagram. At temperatures below
$T \approx 50$ K, the decay traces almost overlap and thus a nearly identical lifetime of $\tau \approx$
5.9 ns is determined. The recombination time becomes clearly shorter with further rising
temperatures and drops by about one order of magnitude to $\tau \approx 0.5$ ns at $T \approx 110$ K.
The origin of this behavior is expected to originate from the temperature-dependence of
the recombination rate of the radiative or non-radiative transitions. From [251–253] we
know that the temperature-dependent radiative recombination time is an intrinsic property
of semiconductors with translational invariance in at least one direction (bulks, quantum
wells, quantum wires, carbon nanotubes). However, in zero-dimensional nanostructures
such as epitaxial quantum dots or colloidal nanocrystals, the radiative lifetime does not
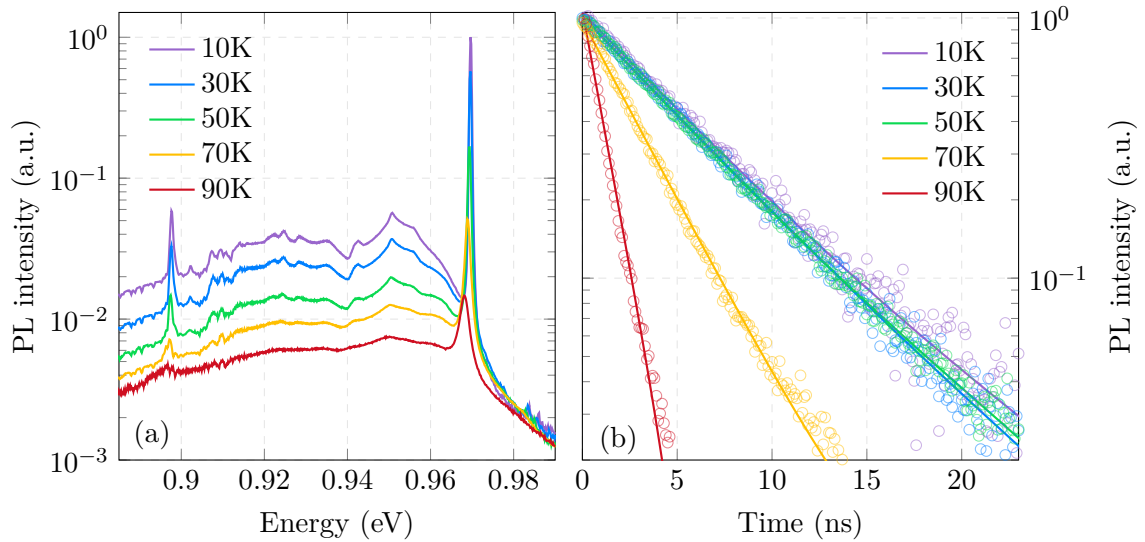
Figure 4.8 Temperature-dependent PL measurements of a G center ensemble. (a) Emission spectra with PL intensity dependency and discernible ZPL shift and broadening with increasing temperature. **(b)** Time-resolved measurements of the PL signal intensity. A faster recombination rate of the PL at temperatures higher than $T = 50\,\mathrm{K}$ can be observed.

change with temperature, since thermalization effects along the exitonic dispersion are suppressed. This behavior is also valid for point defects and will be investigated in the following. In Fig. 4.6 (d) the temperature-dependent decay time of G centers is plotted. In order to evaluate these data regarding the decay rates, the inverse of the decay time is shown in Fig. 4.9 (a). These data can be fitted by the formula [50]

$$\frac{1}{\tau} = \frac{1}{\tau_0} + C\,\mathrm{e}^{-E_\mathrm{A}{}^{(2)}/k_\mathrm{B}T} \tag{4.7}$$

with the parameters $\tau_0 = 5.9 \pm 0.1\,\mathrm{ns}$, $C = 120 \pm 20\,\mathrm{ns}^{-1}$ and $E_\mathrm{A}^{(2)} = 39 \pm 5\,\mathrm{meV}$. The activation energy $E_\mathrm{A}^{(2)}$ determined in this way agrees well with the value of $E_\mathrm{A}^{(1)} = 41\,\mathrm{meV}$ found in Sec. 4.2.3 with Eq. (4.5). We now use this fact to make statements about the temperature-dependence of radiative and non-radiative lifetime.

Let γ_r and γ_nr be the radiative and non-radiative decay rate (inverse of the decay time), respectively. The time-integrated PL intensity is proportional to $\gamma_\mathrm{r}/(\gamma_\mathrm{r} + \gamma_\mathrm{nr})$, while the inverse PL decay time τ^{-1} is equal to $\gamma_\mathrm{r} + \gamma_\mathrm{nr}$. Assuming that at low temperatures $\gamma_\mathrm{r} \gg \gamma_\mathrm{nr}$ applies, the PL signal intensity can be expressed as a function of the decay rates and thus the inverse decay time. From this, the temperature-dependence of the radiative decay rate can be derivated:

$$I(T) = I_0\,\frac{\gamma_\mathrm{r}}{\gamma_\mathrm{r} + \gamma_\mathrm{nr}} = I_0\,\tau\,\gamma_\mathrm{r} \quad \Longrightarrow \quad \gamma_\mathrm{r}(T) = \frac{I(T)}{I_0} \cdot \tau^{-1}(T). \tag{4.8}$$

This situation is illustrated in Fig. 4.9 (b). A nearly temperature-independent decay rate of the radiative transitions can be observed, as expected for zero-dimensional systems. From this, we can assume that the lifetime of radiative transitions in G centers remains constant with changing temperature and that the measured, faster recombination at higher
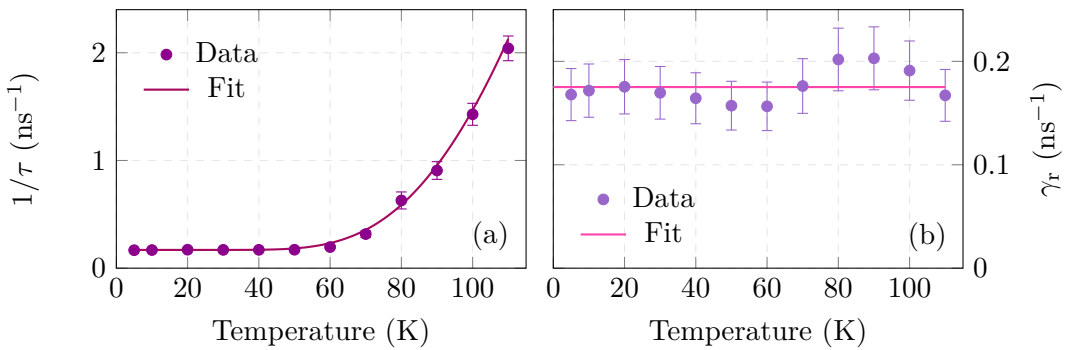
Figure 4.9 Recombination rates. (a) Plot of the inverse of the lifetime τ measured in Fig. 4.6 (d), depicting the total recombination rate γ. **(b)** The product of the temperature-dependent PL signal intensity in Fig. 4.6 (c) times the measured inverse lifetime τ^{-1} results in an almost temperature-independent radiative recombination rate.

temperatures only occurs due to the influence of non-radiative recombination paths, which also results in a decrease of PL intensity. This assumption is further supported by the nearly identical activation energies $E_A^{(1)}$ and $E_A^{(2)}$, since a temperature dependence of the radiative decay rate would lead to a shift in the activation energy $E_A^{(2)}$ in Eq. (4.7).

4.3 Recombination dynamics

In the following section, the recombination dynamics of G centers will be investigated. For this purpose, spectral-selective, time-resolved PL measurements with a temporal resolution of 400 ps will be evaluated to draw conclusions about the influence of the phonon interaction on the decay time of the luminescence. Afterwards, the influence of different proton fluences on the lifetime is investigated before a theoretical model is discussed to describe the influence of different phonon modes.

4.3.1 Spectrally selective recombination dynamics

In general, an electronic two-level system in a phonon bath can recombine either directly via radiative paths (corresponds to ZPL) or indirectly by additional momentum from phonons (responsible for PSB). Both mechanisms contribute simultaneously to the recombination dynamics of the excited two-level state. Since the lifetime of the state depends on the electronic dipole itself and on the strength of the electron-phonon interaction, time-resolved measurements should accordingly output the same lifetime for ZPL and PSB. These facts have hardly been checked and documented [254, 255], but will be discussed in the following. In Fig. 4.10 (a) an ordinary G center spectrum, measured at 10 K, is shown. The spectral ranges of ZPL and PSB, which were examined separately by two band-pass filters of spectral width 20 nm, are highlighted. Their intensities, as well as those of the overall spectrum (1250 − 1700 nm), were measured time-resolved in Fig. 4.10 (b) respectively. In this semi-logarithmic diagram, an identical, purely exponential decay with a characteristic time constant of $\tau = 5.9$ ns is shown for each individual spectral range. This value lies between those of InAs quantum dots (1.3 ns, [256, 257]) and NV centers in diamond (12 ns, [29]) and opens up the possibility of producing a bright, G center based single-photon source in silicon. The identical decay time of the two spectral ranges thus suggests the common
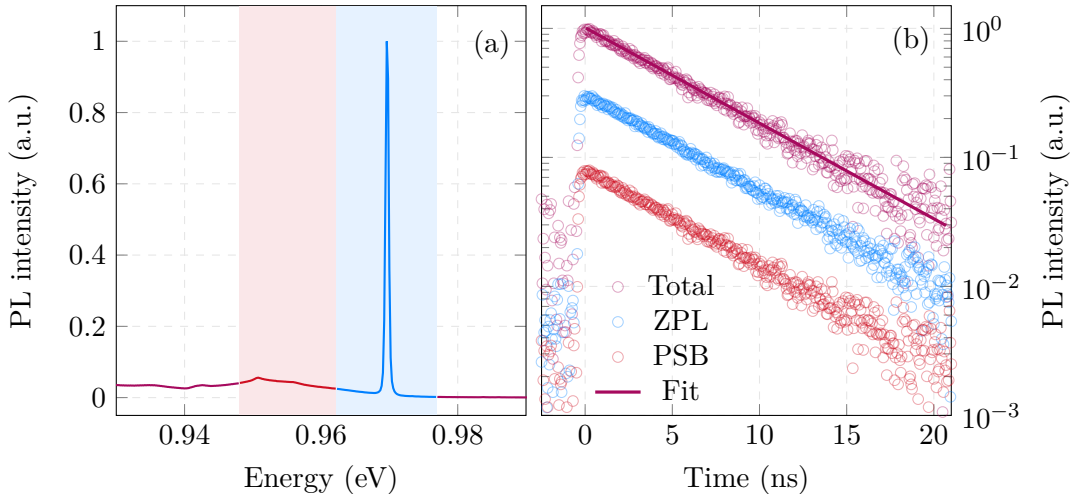
Figure 4.10 Spectrally-selective and time-resolved PL luminescence. (a) G center PL spectrum measured at $10\,\mathrm{K}$. The shaded areas define the spectral width of the utilized bandpass filters for measurement of the PL response of either ZPL or PSB. **(b)** Decay time of the full spectrum (purple), ZPL (blue) and PSB (red) measured at an average laser power of $1\,\mathrm{kW\,cm^{-2}}$. All investigated bandwidths show the same exponential decay with $\tau = 5.9\,\mathrm{ns}$.

atomic origin of ZPL and PSB, i.e. photons of different energies.

4.3.2 Lifetime and defect density

Since an increased defect density influences the phonon propagation in the vicinity of the defects, the spots of different proton fluences were examined for the G center lifetime. The stronger luminescence at higher proton fluences as shown in Fig. 4.3 indicates an increased G center density, which possibly generates additional non-radiative relaxation channels [50]. To verify this, time-resolved PL measurements were performed at $40 - 50$ different areas per proton spot and histograms of the measured lifetime were recorded. Fig. 4.11 (a) shows such a histogram recorded at the $3 \times 10^{14}\,\mathrm{cm^{-2}}$ spot. Due to the low laser power of the pulsed laser diode (average $P = 1\,\mathrm{kW\,cm^{-2}}$) only the three spots with the highest proton fluence could be measured correctly. The results are shown in Fig. 4.11 (b). The shown values correspond to the respective mean value of the recorded statistical distribution for each spot and the error bars correspond to the standard deviation. Although the average lifetime of $6.1\,\mathrm{ns}$ at $1 \times 10^{14}\,\mathrm{cm^{-2}}$ seems to decrease to $5.9\,\mathrm{ns}$ at $9 \times 10^{14}\,\mathrm{cm^{-2}}$, the values are still in the statistical error range of $\pm 0.2\,\mathrm{ns}$. Therefore, we cannot give a final answer about the dependence of the lifetime on the proton fluence/defect concentration for the range of fluences measured here.

4.3.3 Phonon-assisted recombination model

In the last section of this chapter, the phonon side band is now to be examined in detail by modern theoretical approaches with non-perturbative calculations [250, 258]. For this purpose we consider again the G center spectrum displayed in Fig. 4.12. As already known, the narrow ZPL at $0.97\,\mathrm{eV}$ and the PSB expanding to lower energies is detected. According to [250, 258] phonon emission causes a redshift after phonon-assisted recombination, while phonon absorption causes a blue shift with respect to the ZPL. Since at low temperatures
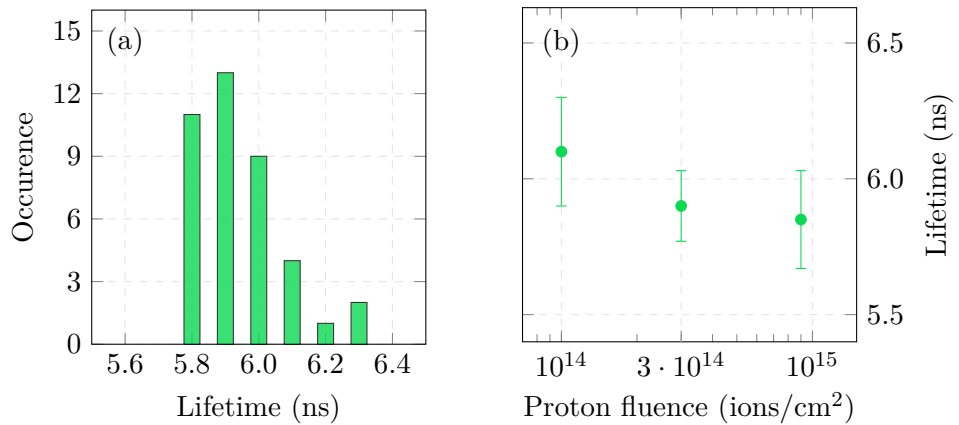
Figure 4.11 G center lifetime measured for different proton fluences. (a) Histogram of the lifetime measured at the $3 \times 10^{14}\,\mathrm{cm}^{-2}$ spot. **(b)** The mean value of the PL lifetime seem to decrease with increasing proton fluence, but since the values are within the error range, no final conclusion on the defect concentration dependency of the lifetime of G centers could be drawn. Lower fluences have not been available due to lack of pulsed laser power.

the probability of phonon absorption is negligibly small compared to phonon emission, the known asymmetry of the spectrum occurs. The PSB further consists of two broad peaks (approximately $0.91 - 0.94\,\mathrm{eV}$ and $0.94 - 0.96\,\mathrm{eV}$) and two local vibrational modes of the ZPL at approximately $0.90\,\mathrm{eV}$ (E line) and $0.83\,\mathrm{eV}$ (E' line) [36]. According to [250, 258] such a wide phonon sideband is created by the superposition of two processes: On the one hand, there is a broad base in the spectrum, which results from recombination under interaction with acoustic phonons (blue dotted line in Fig. 4.12). On the other hand, the detuning between phonon replica and ZPL increases with increasing phonon energy, so that the broad peaks at about $0.93\,\mathrm{eV}$ and $0.95\,\mathrm{eV}$ are directly correlated with the corresponding phonon modes of the phonon DOS, that is shown in the inset of Fig. 4.12. A quantitative analysis by theoretical calculation of the acoustic phonon sideband then allows an estimation of the spatial extent of the electronic wave function in the defect. This will be shown in the following.

Theroretical modeling

Using a theoretical approach derived from the Huang-Rhys model, which is used to calculate the coherent non-linear response in semiconductor quantum dots and carbon nanotubes [258, 259], we have modelled the PSB from the coupling between acoustic phonons and a defect in a silicon lattice. Near the zone center, i.e. for small wave vectors, interaction with a deformation potential is allowed only for LA phonons, while piezoelectric coupling is allowed for both LA and TA phonons [258]. Since silicon is centrosymmetric and therefore non-piezoelectric, only the interaction with the deformation potential affects the LA phonons [260]. Therefore, the emission spectrum can be represented by a Fourier transformation of the time-dependent linear susceptibility $\chi(t)$ from [258]:

$$\chi(t) = \exp\left(\sum_{\mathbf{k}} |\gamma_{\mathbf{k}}|^2 \left(\mathrm{e}^{-i\omega(\mathbf{k})t} - n(\mathbf{k})|\mathrm{e}^{-i\omega(\mathbf{k})t} - 1|^2 - 1\right)\right) \tag{4.9}$$

where $\omega(\mathbf{k})$ is the energy of an LA phonon with wave vector $\mathbf{k}$ and $n(\mathbf{k})$ is the corre-
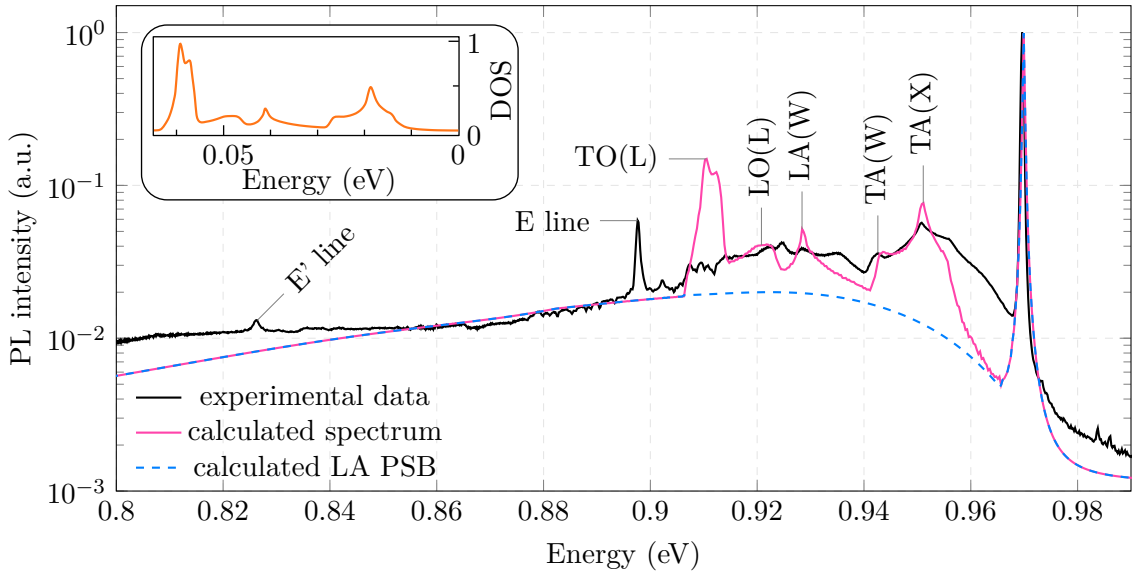
Figure 4.12 Modelling the emission spectrum via non-perturbative calculations. The black line is the measured G center spectrum recorded at 10 K and an excitation energy of 1.96 eV. The blue dashed line corresponds to the Fourier transformation of Eq. (4.14) for the LA phonon sideband with a spatial extension of the electronic wave function of the point defect $\sigma = 1.6$ Å. The pink graph shows the combination of the derived function plus the phonon DOS of bulk Si (shown in the inset, taken from [261]), thus enabling the attribution of different phonon modes to characteristic points in the emission spectrum.

sponding Bose-Einstein phonon occupation factor. $\gamma_{\mathbf{k}}$ is further a dimensionless coupling strength of the form

$$\gamma_{\mathbf{k}} = \frac{g_{\mathbf{k}}^e - g_{\mathbf{k}}^h}{\omega(\mathbf{k})} \tag{4.10}$$

where $g_{\mathbf{k}}^\alpha$ generally describes the coupling strength for electrons ($\alpha = e$) or holes ($\alpha = h$) and depends on the electron-phonon interaction $G_{\mathbf{k}}^\alpha$ and the electronic wave function $F_{\mathbf{k}}^\alpha$ in reciprocal space:

$$g_{\mathbf{k}}^\alpha = G_{\mathbf{k}}^\alpha F_{\mathbf{k}}^\alpha \tag{4.11}$$

According to [258], the electron-phonon interaction, which is only dependent on the deformation potential, reads

$$G_{\mathbf{k}}^\alpha = \frac{kD^\alpha}{\sqrt{2\rho\hbar\,\omega(\mathbf{k})V}} \tag{4.12}$$

with the deformation potential D^α, the silicon density ρ and the normalized volume V. On the other hand, $F_{\mathbf{k}}^\alpha$ corresponds to the Fourier transformation of the squared absolute value of the electronic wave function $\Psi^\alpha(\mathbf{r})$ of a point defect, that is:

$$F_{\mathbf{k}}^\alpha = \int \mathrm{d}^3\mathbf{r}\,|\Psi^\alpha(\mathbf{r})|^2\,e^{i\mathbf{k}\mathbf{r}} \tag{4.13}$$

Assuming a Gaussian distribution with an identical extension σ for electrons and holes, the wave function takes the form $F_{\mathbf{k}}^\alpha = \exp(-k^2\sigma^2/4)$. Since the model considers only

linear terms of the electron-phonon interaction, the phonon-induced line broadening is not considered and must therefore be introduced phenomenologically by a convolution of the emission spectrum of Eq.(4.9) with a Lorentz function of width Γ_{ZPL} (FWHM). In the temporal domain this corresponds to a simple multiplication of $\chi(t)$ by an exponential function with the time constant $2\hbar/\Gamma_{\text{ZPL}}$:

$$\widetilde{\chi(t)} = \chi(t)\, e^{-\Gamma_{\text{ZPL}}t/2\hbar} \tag{4.14}$$

For the fitting of our spectrum we take the values of the deformation potentials ($D^e = 10\,\text{eV}$ and $D^e = 5\,\text{eV}$) from [262]. Only the extension σ of the electronic wave function in the G center and the ZPL width Γ_{ZPL}, whose reference value was assumed as $\Gamma_{\text{ZPL}} = 0.3\,\text{meV}$ according to Sec. 4.2.2, serve as fit parameters. The resulting graph corresponds to the interaction with LA phonons only and is represented by the blue dotted line in Fig. 4.12. Obviously, this does not yet reflect the actual spectrum well, so further contributions must be considered. We take an unusual approach and add to the calculated LA PSB a fraction proportional to the phonon DOS in silicon [261], which is shown in the inset of Fig. 4.12. It should be noted that this approach introduces two simplifications:

- constant electron-phonon matrix elements, which does not take into account the exact form of the electron-phonon coupling and interaction selection rules

- phonon-assisted recombination is dominated by emission processes involving only one phonon

The second point is a legitimate assumption at low temperatures as in our experiments [250]. By means of this simple approach, a significant optimization of the fit (pink line in Fig. 4.12) can be achieved. The best match between experimental and fitted G center spectrum is achieved for a wave function extension parameter of $\sigma = 1.6 \pm 0.1\,\text{Å}$. This value is lower than the distance between two nearest neighbors in silicon ($2.3\,\text{Å}$), but similar to the C-Si bond length in G centers [263, 264, 174, 265], which supports our original method for estimating the extension of the electronic wave function in G centers. However, based on EPR measurements of the ^{29}Si hyperfine interaction, it was assumed in [37] that the spin wave function is spread over approximately 24 silicon neighboring sites, which corresponds to an extension of about $7\,\text{Å}$ and is thus above our value.

With our model and the combination with phonon DOS, we can now assign the individual characteristics of the spectrum to specific phonon modes. Accordingly, the two peaks at $0.94\,\text{eV}$ and $0.95\,\text{eV}$ seem to correspond to the extrema of the DOS caused by TA phonons at the X and W point of the Brillouin zone. The wide band from about $0.90\,\text{eV}$ to $0.93\,\text{eV}$, however, is less consistent with the measurements. The LA and LO phonons at the W and L points can still be vaguely suggested, but the sharp maximum of the DOS of the TO mode at the L point is completely missing, which we attribute to a suppression of the corresponding phonon replica by the selection rules. The decreasing intensity in the range from $0.95\,\text{eV}$ to $0.97\,\text{eV}$ is also not sufficiently reproduced. We explain this dip with defect-induced vibrational resonance, which does not originate from the bulk phonons in silicon, but from atomic vibrations of the G center itself. Such a behavior has already been observed in the vibronic spectrum in NV centers and has been justified accordingly [249]. As already mentioned, the E and E' lines are caused by localized phonon modes of the G centers, which is why they cannot be reproduced by our model either. Further theoretical models beyond pure phonon Bloch modes in a perfect silicon matrix are necessary for a

deep understanding of the phonon-assisted recombination in this defect. Nevertheless, our model provides a quick and easy way to estimate the spatial extent of the electronic wave function in the G center.

Scientific gain

In the previous section, the results from the joint publication "Optical properties of an ensemble of G-centers in silicon" [50] were presented and discussed. The goal was to verify and complete the results of previous works. The new findings about G center ensembles are:

- sublinear correlation of the PL intensity with incident laser power with a saturation power of $35\,\mathrm{kW\,cm^{-2}}$

- first measurement of the defect lifetime $\tau \approx 6\,\mathrm{ns}$ at low temperature, without significant influence of the irradiated proton fluence

- proof of the same microscopic origin of ZPL and PSB

- extensive temperature-dependent measurements, revealing the zero-temperature values of the ZPL energy and width, as well as calculations of the activation energy and radiative decay rates

- new model for the interpretation of the acoustic phonon sideband of the emission spectrum by non-perturbative calculations, providing a value of the spatial extension of the electronic wave function in the G center of $\sigma = 1.6\,\mathrm{\AA}$

Due to the steadily increasing interest in photonics and quantum systems, G centers are of particular interest to economy and industry because of their simple, CMOS compatible manufacturing capabilities. Therefore, the results presented here will be the first step towards a silicon-based future-oriented technology. However, for some questions and for most modern applications the generation of single centers is indispensable. Despite the long and intensive research on G centers, however, none have yet been produced or proven. This situation will be remedied in the next chapter.

G centers as single-photon sources in silicon

Subject matter

This chapter presents, with kind permission from *Springer Nature*, the results of our second publication "Single artificial atoms in silicon emitting at telecom wavelengths"* [39], in which we were able to detect for the first time ever artificially generated single-photon sources hosted in a silicon matrix, that were created only by ion implantation of carbon into a SOI wafer with participation of the Department of Physics in Oslo. The detection of these centers were made possible by an optimized PL spectroscopy setup with very high resolution at the L2C. PL investigations indicate excellent properties of the single-photon source, such as high brightness, long-term photostability and a high quantum efficiency, which are important for the utilization of the single photons.

Contribution: different carbon and hydrogen implantations during the development process, assistance with confocal PL measurements during a one-month stay in Montpellier, discussions and presentations in project meetings, proof-reading of the publication

5.1 Experimental description

5.1.1 Sample fabrication

Since the aim of this work was the creation and detection of individual G centers, a particularly low defect density was required. Therefore, a SOI wafer with a Si top layer of 200 nm and a 1 μm thick SiO_2 interlayer was cut to a $5 \times 5\,\mathrm{mm}^2$ chip and implanted with ^{12}C at the Department of Physics of the University of Oslo with a fluence of $\Phi = 5 \times 10^{13}\,\mathrm{cm}^{-2}$ and an energy of $E = 36\,\mathrm{keV}$ to distribute the carbon atoms in the center of the Si top layer. According to stopping and range of ions in matter (SRIM) simulations, the implanted ^{12}C ions stop in a depth of about 110 nm with a straggling of about 41 nm. The implanted chip was then flash annealed in a commercial RTP device for 20 s at $T = 1000\,°\mathrm{C}$ under N_2 atmosphere. No proton post-irradiation was used for this sample to keep the defect concentration as low as possible.
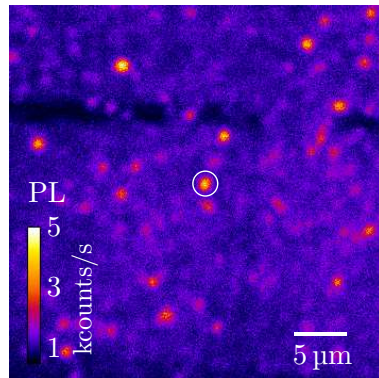
Figure 5.1 PL raster scan of the investigated sample. The scan was recorded at $10\,\mathrm{K}$ with a $532\,\mathrm{nm}$ laser excitation at a power of $P = 10\,\mathrm{\mu W}$. The encircled spot shows properties of a single-photon source with a PL spectrum close to the typical G center spectrum, thus concluding the creation of single, isolated G centers in silicon.

5.1.2 Optical spectroscopy

To measure individual G centers, a part of the self-built CLSM was installed in a He-closed-cycle cryostat from MyCryoFirm. The optical excitation of the centers was performed by a $532\,\mathrm{nm}$ CW laser beam, whose power was measured shortly before entering the window of the cryostat vacuum chamber. After entering the chamber, the laser beam was directed through a microscope objective (Olympus, LCPLN100XIR) within the cryostat and with a numerical aperture NA $= 0.85$. The objective focuses the laser spot on the sample and achieves a focal spot size of approximately FWHM $\approx 500\,\mathrm{nm}$ due to the confocal setup. The corresponding PL response was recorded by the same objective and directed by single-mode fiber-optics either to the spectrometer or to two near-IR single-photon detectors from IDQuantique (ID230) with a quantum efficiency $\eta_{\mathrm{det}} = 10\,\%$ and dark counts $< 50\,\mathrm{counts/s}$. The laser light was filtered from the PL signal by means of a dichroic mirror from Thorlabs (DMLP1000) and by coupling the PL into a single-mode optical fiber. Experimental control and data acquisition was performed with the Python-based Qudi software [266]. Fig. 5.1 shows a raster scan of the PL intensity of the investigated sample recorded at $T = 10\,\mathrm{K}$ and a laser power of $P = 10\,\mathrm{\mu W}$. The encircled spot shows exemplary a spectrum nearly identical to the G center spectrum as well as properties of a single-photon sources, which will be discussed in the following.

5.2 Evidence of a single-photon source

5.2.1 Autocorrelation study

A clear proof for the presence of a single-photon source is the evaluation of the photon statistics (see Sec. 3.2). Only photons coming from a SPS can be measured individually and with equal time intervals. For this, an HBT setup with two single-photon detectors is required, as explained in Sec. 3.2.2, that allows measurement of the temporal distribution of photon counts, which corresponds to the second-order autocorrelation function $g^{(2)}(\tau)$. Fig. 5.2 shows the result of such a measurement performed at $T = 10\,\mathrm{K}$. The measured value of $g^{(2)}(0) \approx 0.3$ is well below the limit of $g^{(2)}(0) \approx 0.5$ which is a clear evidence for anti-
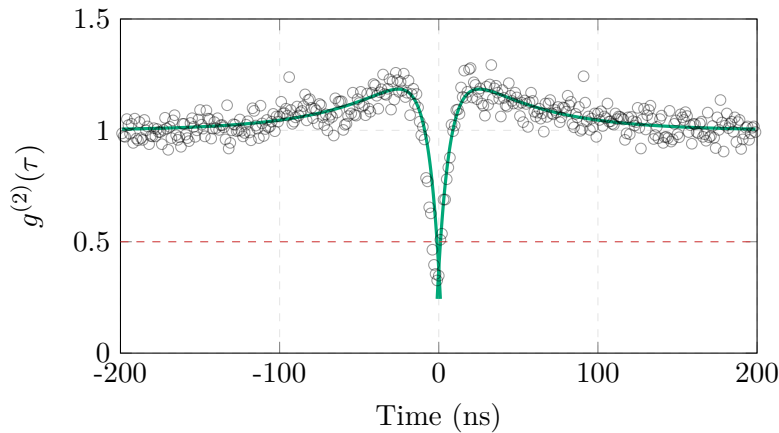
Figure 5.2 Second-order autocorrelation function g$^{(2)}$(τ). The measurement was performed at $T = 10\,\mathrm{K}$ with a laser excitation power of $P = 10\,\mu\mathrm{W}$. Black circles indicate the measured data and the solid green line corresponds to the fit function derived in Eq. (5.6) for a three-level model. Antibunching is observed at zero delay with a value of $g^{(2)}(0) \approx 0.3$, revealing the first observation of a single optically-active point defect hosted in a pure crystalline silicon lattice.

bunching and thus indicating the presence of a single-photon source [267, 268]. Fig. 5.3 (a) shows graphs of $g^{(2)}(\tau)$, recorded at different excitation powers. The deviation from an ideal single-photon source with $g^{(2)}(0) = 0$ is due to residual background photons and detector dark counts, leading to a signal-to-noise ratio (SNR) of ≈ 4. To determine the pure value of the second-order autocorrelation function of the single-photon source, the influence of background radiation and detector dark counts must be subtracted from the measured signal. According to [186] the corrected $g^{(2)}(\tau)$ can be described by the formula

$$g_{\mathrm{cor}}^{(2)}(\tau) = \frac{g^{(2)}(\tau) - (1 - \rho^2)}{\rho^2} \tag{5.1}$$

where ρ is related to the SNR via

$$\rho = \frac{1}{1 + 1/\mathrm{SNR}}. \tag{5.2}$$

The SNR of ≈ 4 was determined from the PL spectra. Taking the correction into account, the autocorrelation function $g_{\mathrm{cor}}^{(2)}(0)$ takes the value zero at zero delay, as can be observed in Fig. 5.3 (b) for a different powers.

5.2.2 Photodynamics

For the simulation of the photodynamics of the individual G centers we assume a 3-level system. The existence of a third triplet state, which is located between the ground and excited state, was already suspected by former ODMR measurements [34]. After optical excitation from the ground state $|1\rangle$ to the excited state $|2\rangle$, the defect can relax to the original state in two different ways: either via the direct, radiative transition, i.e. by emitting a $0.97\,\mathrm{eV}$ photon, or by taking a non-radiative path via the metastable state $|3\rangle$. The second-order autocorrelation function of this 3-level system (3LS) can be expressed by the occupation ratio of the excited state $p_2(\tau)$ to the equilibrium state $p_2(\infty)$:

$$g_{\mathrm{3LS}}^{(2)}(\tau) = \frac{p_2(\tau)}{p_2(\infty)}. \tag{5.3}$$
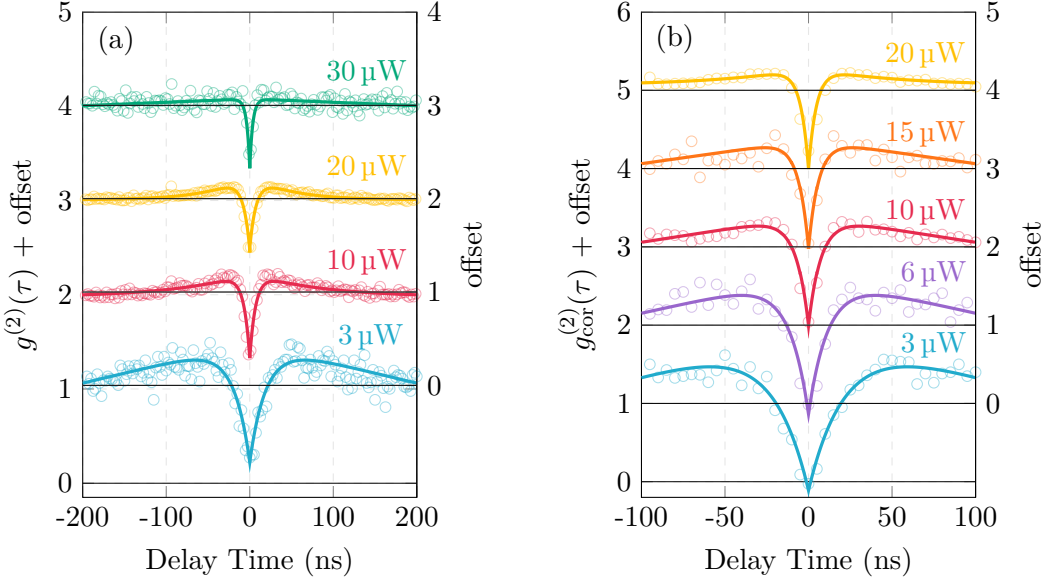
Figure 5.3 **Second-order autocorrelation functions $g^{(2)}(\tau)$ at different laser powers. (a)** Purely measured $g^{(2)}$, fitted with Eq. (5.6). **(b)** Measured data are corrected from background PL and detector dark counts by Eq. (5.1) and fitted with Eq. (5.5), leading to a value of $g^{(2)}_{\text{cor}}(0) = 0$.

The time evolution of the occupation $p_i(t)_{\{i \in [1,2,3]\}}$ is obtained by solving the rate equation

$$d\vec{p}/dt = \mathbf{A}\vec{p}, \tag{5.4}$$

where $\vec{p}(t) = \{p_i(t)\}_{i \in [1,2,3]}$ and $\mathbf{A} = \begin{pmatrix} -k_{12} & k_{21} & k_{31} \\ k_{12} & -k_{21}-k_{23} & k_{32} \\ 0 & k_{23} & -k_{31}-k_{32} \end{pmatrix}$ being the matrix of the effective recombination rates k_{ij}, defined in Fig. 5.4. Assuming an ideal single-photon source, the first boundary condition is $g^{(2)}_{\text{3LS}}(0) = 0$. The second boundary condition results from the consideration that all correlations must vanish after a correspondingly long duration, i.e. $g^{(2)}_{\text{3LS}}(\infty) = 1$. From these conditions and the fact that the matrix $\mathbf{A}$ has two eigenvalues that are different from zero, the formula for the autocorrelation function results in:

$$g^{(2)}_{\text{3LS}}(\tau) = 1 - (1-a)e^{-\Lambda_0 \tau} + ae^{-\Lambda_1 \tau} \tag{5.5}$$

with the three free parameters a, Λ_0 and Λ_1, which are non-trivial functions of the effective rates k_{ij} [269]. To a first approximation, the first exponential term describes the antibunching effect at short timescales, while the second exponential term dominates the bunching at long timescales. The factor a corresponds to the bunching amplitude and Λ_0 and Λ_1 to the respective antibunching and bunching distributions. To determine these, the autocorrelation data measured at different laser powers in Fig. 5.3 (a) were corrected from background noise and detector dark counts using Eq. (5.1) and fitted with Eq. (5.5), leading to the graphs shown in Fig. 5.3 (b). Furthermore, the uncorrected autocorrelation measurements, shown in Fig 5.3 (a), were fitted with the formula

$$g^{(2)}(\tau) = 1 - \rho^2 + \rho^2 \cdot g^{(2)}_{\text{3LS}}(\tau). \tag{5.6}$$

Fig. 5.5 shows the course of the fit parameters Λ_0, Λ_1 and a as a function of the laser power. While the antibunching related rate Λ_0 increases with increasing laser power, the rate Λ_1
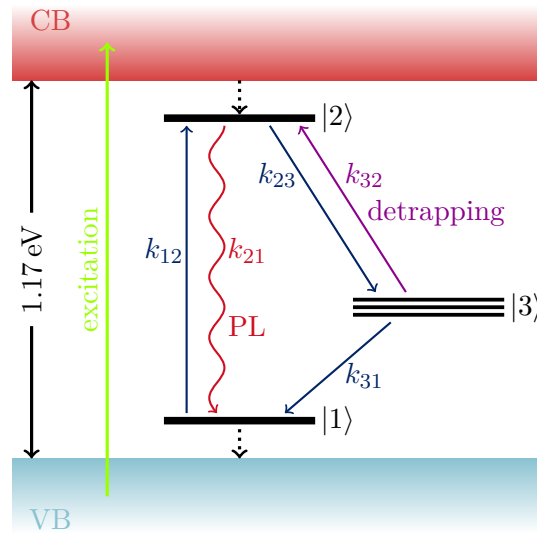
Figure 5.4 3-level recombination model of a G center. Autocorrelation measurements indicate a metastable state $|3\rangle$ located between the ground $|1\rangle$ and excited state $|2\rangle$. Relaxation takes place via radiative (k_{21}) or non-radiative (k_{23}, k_{31}) paths. The high brightness of single G centers and their decreasing bunching amplitude with increasing excitation power can be explained by a detrapping of charge carriers from the metastable triplet to the excited singlet state.

associated with bunching remains rather constant over the investigated power range. With increasing Λ_0, the width of the $g^{(2)}(\tau)$ antibunching dip decreases. According to [270], when the pump rate at high laser powers exceeds the emission rate, the average time between two successive photon detections in the experiment decreases. Accordingly, the value Λ_0 at laser powers approaching zero corresponds to the inverse of the lifetime τ_e of the excited state. By a linear fit of Λ_0 in Fig. 5.5 (a), one thus obtains a lifetime of the excited state of $\tau_e = 37 \pm 9\,\text{ns}$ at the intersection with the ordinate axis. This value agrees well with the lifetime determined directly by time-resolved PL measurments, that will be presented in
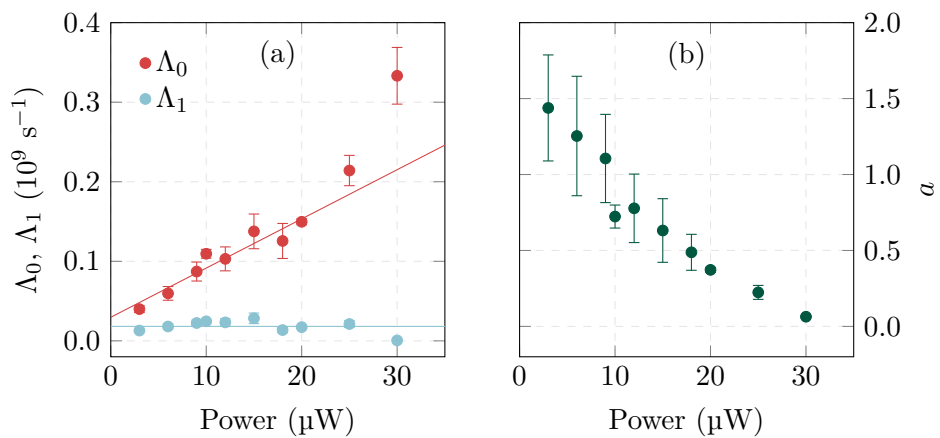
Figure 5.5 Fit parameter derived from $g_{\text{cor}}^{(2)}(\tau)$ shown in Fig. 5.3 (b) with Eq. (5.5). (a) The positive slope of the linear fit of Λ_0 with increasing laser powers corresponds to a narrowing of the antibunching dip, whereas the bunching rate, represented by Λ_1, is not affected by changing the excitation power. **(b)** The bunching amplitude a decreases with higher laser power.

Sec. 5.3.3. While usually in 3-level systems with $k_{32} = 0$ the bunching amplitude a increases with increasing laser power [270], a decreasing amplitude is observed in Fig. 5.5 (b), which tends to zero at higher powers. This behavior can be described by a non-zero effective transition rate k_{32}, which increases with increasing laser power and describes the population transfer of electrons from the metastable state $|3\rangle$ to the excited state $|2\rangle$. Furthermore, a bunching effect ($g^{(2)}(\tau) > 1$) is observed at low laser powers, which is an indication that non-radiative processes via the metastable triplet state are also involved in the relaxation. This behavior disappears with increasing laser powers, so that the course of $g^{(2)}(\tau)$ at a power of $30\,\mu W$ corresponds again to the behavior of a pure 2-level system. This can be explained by a photo-induced detrapping transition between the metastable and excited state (see Fig. 5.4) that most likely contributes to the high brightness of the individual G centers.

5.2.3 PL polarization

To investigate the emission dipole orientation and polarization of the photoluminescence of G centers, a polarization filter was placed in front of the single-photon detector and the PL intensity of an isolated G center was measured as a function of the polarizer angle. The result is depicted in Fig. 5.6 (a) as a typical polarization diagram and exhibits properties of a single emitting dipole. The normalized photoluminescence decreases to almost zero at angles of 90° and 270° and takes the maximum at $\alpha = 10°$. If one considers the part of the luminescence that emerges perpendicularly from the silicon surface with (001)-orientation (i.e. the projection), the position of the dipole is correspondingly inclined by $\alpha = 10°$ to the [110] crystal axis. Identical measurements were performed on 29 other single G centers. All exhibited linearly polarized photoluminescence, and the orientations of the polarization axes can be divided into four groups, each tilted by approximately $\Delta\alpha = 45°$ as shown
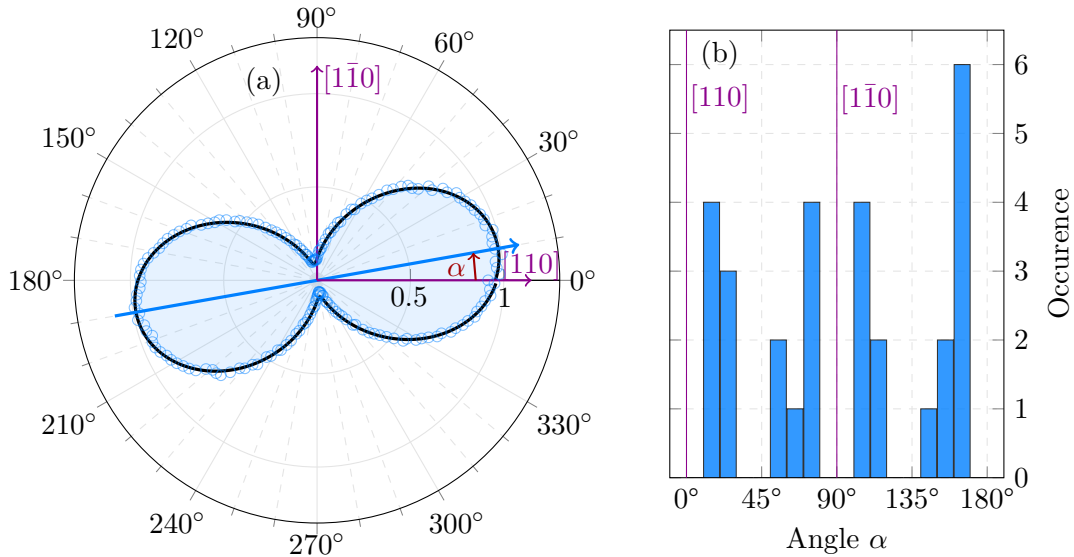
Figure 5.6 Polarization properties of G centers in silicon measured at T = 10 K. (a) Polarization diagram of the PL intensity of a single G center. The direction of the emission dipole is tilted by $\alpha \simeq 10°$ from the [110] crystal axis of the (001)-oriented SOI sample. **(b)** Histogram of the emission dipole angle α for 29 different single G centers. The dipoles and therefore G centers are oriented in four preferred directions in the silicon crystal, each tilted by $\approx 45°$.

in Fig. 5.6 (b). These polarization axes coincide with the four possible orientations of G centers in the silicon lattice [34] and exclude alignment along the [110] and [1$\bar{1}$0] axes.

5.3 Properties of single photons from G centers

5.3.1 ZPL shift

Fig. 5.7 (a) shows the PL spectrum measured at the circled spot in Fig. 5.1. A sharp ZPL is clearly visible at an energy of $E_{\mathrm{ZPL}} = 0.975\,\mathrm{eV}$ or a wavelength of $\lambda = 1270\,\mathrm{nm}$ as well as a PSB spreading towards lower energies. Although the PSB has a slightly different structure to that measured in Ch. 4, it is reasonable to assume that the PL signal stems from the C_s-Si_i-C_s defect. The fraction of the ZPL intensity in the total intensity (DWF) was measured to be $\approx 15\,\%$ and is thus somewhat lower than in the ensemble measurement from Sec. 4.2.3. The comparison of 29 different PL spectra of individual G centers shows variations of the ZPL energy, thats statistical distribution is depicted in Fig. 5.7 (b). A Gaussian fit of the corresponding histogram yields an expectation value of the ZPL energy (wavelength) of $\langle E_{\mathrm{ZPL}} \rangle = 976.3 \pm 0.9\,\mathrm{meV}$ ($\langle \lambda_{\mathrm{ZPL}} \rangle = 1270.9 \pm 1.1\,\mathrm{nm}$) and a standard deviation of $\sigma_E = 6.8 \pm 1\,\mathrm{meV}$ ($\sigma_\lambda = 9 \pm 1\,\mathrm{nm}$). The variation of the ZPL can be explained by local mechanical stress fields in the crystal. The G centers experience different displacements according to their orientation relative to the compression axis, which in turn leads to different shifts of the energy levels and thus to a shift of the ZPL [271], which is usually hidden in the line broadening of the ensemble measurement.
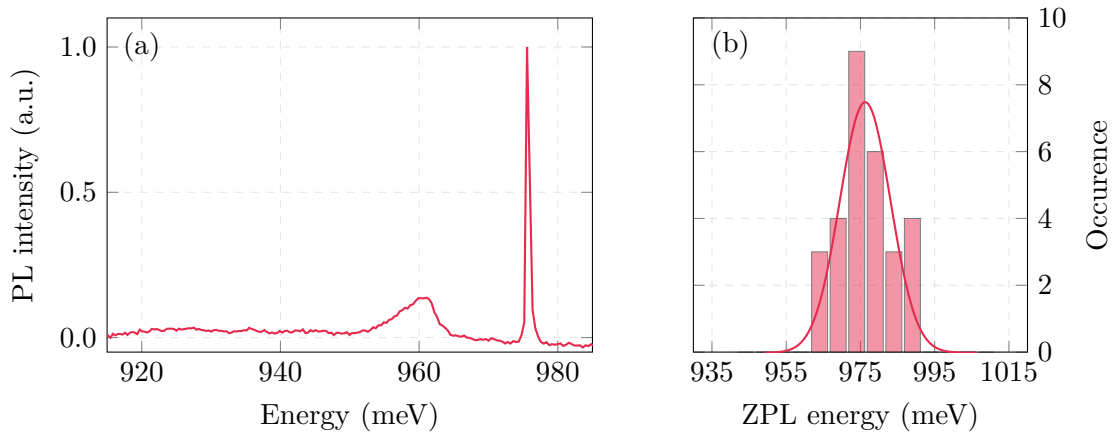
Figure 5.7 Spectral properties of a single G center. **(a)** PL spectrum of an isolated G center, showing the typical ZPL and PSB. The PSB is predominantly flat and exhibits, in contrast to the ensemble spectrum, only one broad signal at about $960\,\mathrm{meV}$, which, according to Sec. 4.3.3, can most likely be attributed to the TA(X) phonon mode. **(b)** Examination of the PL spectra for 29 different single G centers shows a Gaussian distribution of the ZPL energy, whose statistical expectation value is $\langle E_{\mathrm{ZPL}} \rangle = 976.3 \pm 0.9\,\mathrm{meV}$.

5.3.2 Saturation and stability

Individual G centers exhibit high brightness and long-term photostablity. Fig. 5.8 (a) shows the PL intensity as a function of the incident laser power, measured at $T = 10\,\mathrm{K}$ and an excitation wavelength of $\lambda_{\mathrm{ex}} = 532\,\mathrm{nm}$. Up to a laser power of about $20\,\mathrm{\mu W}$ the intensity
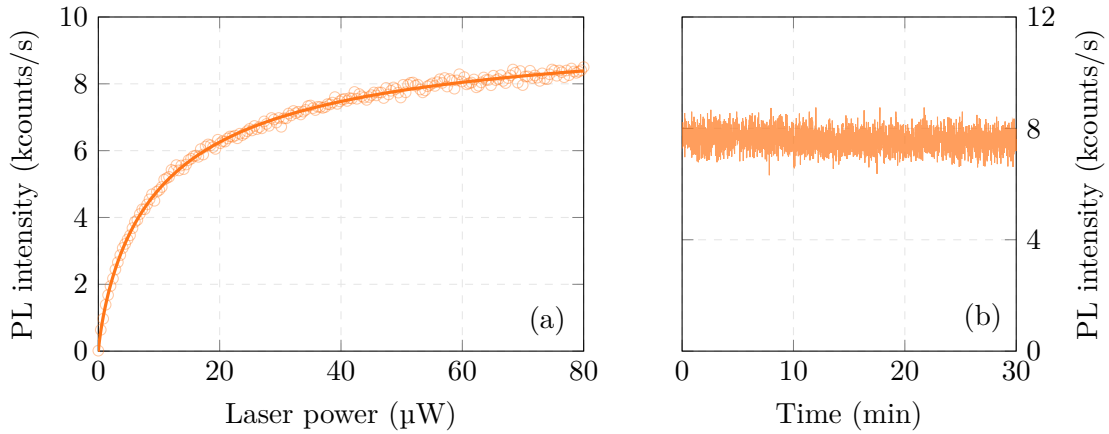
Figure 5.8 Laser power dependence of the PL intensity. **(a)** PL saturation curve of a single G center. The measured data were fitted with the 2-level saturation function in Eq. (5.7), leading to a saturation power of $P_{\text{sat}} = 9\,\mu\text{W}$ which is significantly less than the ensemble value. The reason for this might be that the ensemble saturation power does not take into account the different orientations of the G centers. **(b)** Time-trace of the PL intensity under saturation of the optical transition, shown with a bin time of 57 ms per point. The luminescence is very stable in the observed period of 30 min.

increases rapidly, then starts to flatten slowly and reaches the saturation intensity of about 8000 counts/s from about $60\,\mu\text{W}$. The data points were fitted with a typical saturation curve (solid line) for a quantum mechanical 2-level system:

$$I(P) = I_{\text{sat}} \left(1 + \frac{P_{\text{sat}}}{P} \right)^{-1} \tag{5.7}$$

and yield a saturation power of $P_{\text{sat}} = 9\,\mu\text{W}$, which is significantly lower than that of the ensemble measurement in Sec. 4.1.5. The discrepancy can be explained by the saturation model used in the ensemble measurement, as it does not take into account the different orientations of the centers [151]. The achieved intensity of ≈ 8000 counts/s is a surprisingly high value considering the high refractive index of silicon ($n \approx 3.5$), which leads to photon losses due to large total reflections at the interface between silicon and vacuum. Furthermore, the single-photon detectors used have a low quantum efficiency ($\eta_{\text{det}} = 10\,\%$), so that not all photons are detected and a decreased number of photon counts is measured. Thus, the measured brightness can be significantly increased by using more efficient detectors and silicon-based photonic structures [272, 273]. As shown in Fig. 5.8 (b) for a period of 30 min, the PL of the G centers remains permanently stable at 8000 counts/s under constant excitation in the saturation range. The absence of blinking and bleaching effects and the measured stability even under multiple cooling cycles are important features for the future utilization of G centers in photonic and quantum technology applications.

5.3.3 Lifetime of an isolated G center

To obtain information on the lifetime of individual G centers, time-resolved measurements of the PL decay process were carried out. For this purpose, the isolated G centers were irradiated at $T = 10\,\text{K}$ with pulsed laser light of wavelength $\lambda = 532\,\text{nm}$ and pulse length of 50 ps and the decrease of PL intensity was recorded. Fig. 5.9 (a) shows the decay of the
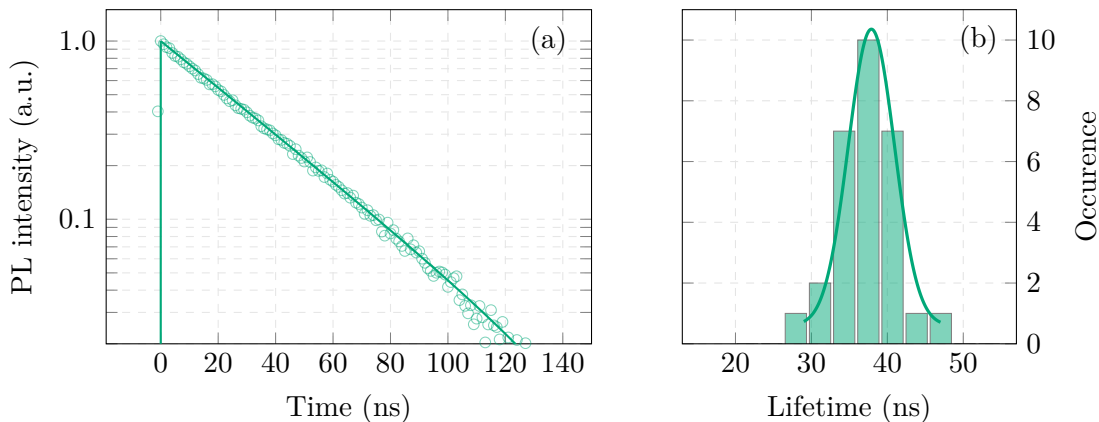
Figure 5.9 Lifetime properties of single G centers measured at T = 10 K. (a) Time-resolved PL decay of a single G center, revealing a lifetime of $\tau_{\mathrm{e}}^{\mathrm{single}} = 32.8 \pm 0.6\,\mathrm{ns}$. The excitation was executed by 50 ps laser pulses at a wavelength of 532 nm. **(b)** Histogram of the PL decay time for 29 single G centers, giving a Gaussian distribution with a mean value of $\langle \tau_{\mathrm{e}} \rangle = 35.8 \pm 0.2\,\mathrm{ns}$.

normalized PL intensity in a semilogarithmic diagram, that can be well reproduced with a mono-exponential function (solid line) containing the lifetime of the excited state τ_{e}. In this way, the lifetime was measured at 29 different, isolated G centers, which show slight fluctuations in the lifetime. It should be noted that these fluctuations do not correlate with the shift of the ZPL energy nor with the orientation of the dipole axis. The corresponding distribution of the measured decay times is shown in Fig. 5.9 (b) and can be well reproduced with a Gaussian normal distribution with the mean lifetime of $\langle \tau_{\mathrm{e}} \rangle = 35.8 \pm 0.2\,\mathrm{ns}$ and a standard deviation of $\sigma_{\tau} = 3.5 \pm 0.2\,\mathrm{ns}$. The lifetime measured at individual G centers is thus larger than the lifetime $\tau_{\mathrm{e}}^{\mathrm{ens}} = 6\,\mathrm{ns}$ of the ensemble measurement, determined in Sec. 4.3. This behavior can be explained by the fact that the recombination dynamics changes at higher concentrations of G centers due to different charge states and defect conformations [274]. Such an effect is already known for NV centers in diamond, where the excited state lifetime decreases from 12 ns for a single center in high-purity diamond lattice to about 4 ns for an ensemble in a heavily nitrogen-doped sample [275].

5.3.4 Estimation of the quantum efficiency

The quantum efficiency of a single-photon source plays a decisive role for the practical use in quantum technology applications. For example, a high efficiency is necessary to realize linear-optical quantum computation schemes [23] and a low efficiency would limit practical applications in quantum key distribution [276, 277]. The quantum efficiency η_{QE} of a SPS indicates the probability with which the excited system emits a photon. To determine this probability, individual G centers were irradiated with pulsed laser light ($\lambda = 532\,\mathrm{nm}$) and the number of emitted photons was detected with time-resolved measurements. The excitation laser pulse length was 50 ps, which was followed by a delay time of 270 ns. This sequence was repeated 2.8 billion times and results in the distribution shown in Fig. 5.10. To calculate the probability of detecting one photon per optical excitation, the photon counts in the timeframe of $0 - 150\,\mathrm{ns}$ were integrated, subtracted from the background noise (grey) and divided by the number of runs. The resulting probability is $P_{\mathrm{photon}} \simeq 4.1 \times 10^{-4}$. This probability can be expressed mathematically via the quantum efficiency η_{QE} of the
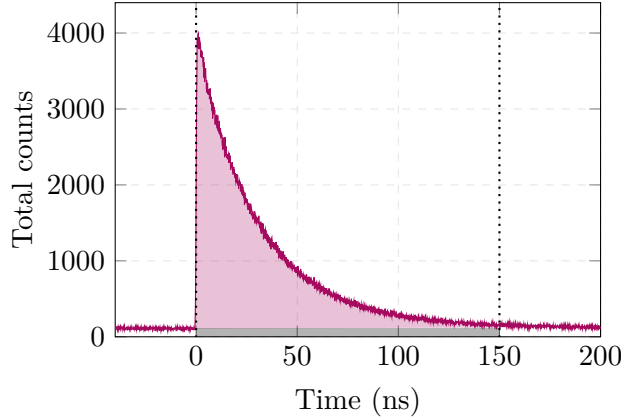
Figure 5.10 Histogram of the PL counts from a single G center after pulsed laser excitation. Time-resolved PL counts were recorded after $50\,\mathrm{ps}$ laser pulses at $532\,\mathrm{nm}$ with a periodicity of $270\,\mathrm{ns}$. This sequence was repeated 2.8 billion. The counts were integrated from 0 to $150\,\mathrm{ns}$, subtracted from noise and divided by the number of sweeps to determine the probability to detect a photon per optical excitation of $P_{\mathrm{Photon}} \approx 4.1 \times 10^{-4}$.

single-photon source by the following formula:

$$P_{\mathrm{photon}} = \eta_{\mathrm{QE}} \cdot \eta_{\mathrm{coll}} \cdot T_{\mathrm{setup}} \cdot \eta_{\mathrm{det}}. \tag{5.8}$$

Here, η_{coll} describes the photon collection efficiency, which depends on the setup and the sample geometry, T_{setup} the optical transmission of the setup and $\eta_{\mathrm{det}} = 10\,\%$ the detector efficiency according to the manufacturer's specifications. Since only estimations can be given for the individual parameters, only the minimum quantum efficiency of the emitter can be calculated. For this purpose, the maximum collection efficiency $\eta_{\mathrm{coll}}^{max}$ is derived in the following, which is determined from the preferred dipole configuration. The resulting lower limit of the quantum efficiency will thus be calculated by

$$\eta_{\mathrm{QE}} \geq \frac{P_{\mathrm{photon}}}{\eta_{\mathrm{coll}}^{max} \cdot T_{\mathrm{setup}} \cdot \eta_{\mathrm{det}}} \tag{5.9}$$

The optical transmission of the setup T_{setup} results from the product of the respective transmission values of all optical components between the microscope objective and the detectors that limit the transmission of photons. These are:

- 1x microscope objective ($T_{\mathrm{MO}} \simeq 0.70$)

- 1x cryostat window ($T_{\mathrm{CW}} \simeq 0.87$)

- 8x mirror reflection ($T_{\mathrm{MR}} \simeq 0.98$)

- 1x all fiber coupling ($T_{\mathrm{FCp}} \simeq 0.85$)

- 1x all fiber connections ($T_{\mathrm{FCn}} \simeq 0.90$)

Based on these values, the total transmission of the entire setup is thus approximately $T_{\mathrm{setup}} \simeq 40\,\%$.

For the estimation of the maximum PL collection efficiency, numerical calculations of the
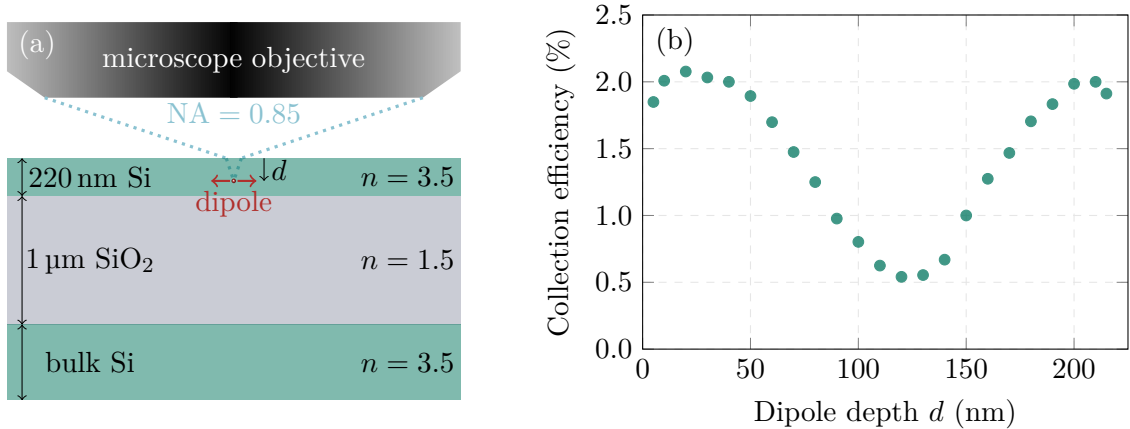
Figure 5.11 Simulation of the photon collection efficiency. (a) The model consists of a SOI layer structure with a 220 nm Si layer, that contains the emitter in the variable depth d. The dipole axis is lying parallel to the surface, therefore maximizing the photon collection efficiency. (b) Calculated collection efficiency η_{coll} as a function ot the depth of the emitter.

emission properties were performed with the commercially available software RSOFT (Synopsis, version 19.09) and the finite-difference time-domain method (FDTD). In the used model, the emitter is located in a 220 nm-thick SOI layer with a high refractive index ($n = 3.5$). Since the lifetime and photon collection efficiency of the emitter depends on the position and orientation of the optical dipole, we assume the best case in our model to estimate a lower limit of the quantum efficiency. Accordingly, we assume an optical dipole located at the variable depth d with its axis parallel to the silicon-air interface, as described in Fig. 5.11 (a).

The photon collection efficiency $\eta_{\mathrm{coll}}(d)$, which depends on the depth of the dipole, can be calculated by forming the ratio of the power emitted vertically into the microscope objective $P_{\mathrm{NA}}(d)$ to the total emitted power $P_{\mathrm{tot}}(d)$. This ratio is shown for different emitter depths in Fig. 5.11 (b). The collection efficiency is minimum with 0.5 % when the dipole is in the center of the 220 nm layer and reaches a maximum of about 2 % near the boundary layers. If we use this maximum value in Eq. (5.9), we obtain as lower limit for the quantum efficiency of individual G centers $\eta_{\mathrm{QE}} \gtrsim 50\,\%$. This lower limit is already above the intrinsic quantum efficiency of SiV centers ($\leq 30\,\%$ [278]) and can be compared to η_{QE} of e.g. SnV centers in diamond (80 % [279]). A further improvement of the quantum efficiency could be achieved via coupled plasmonic nano-resonators [280] giving the possibility to achieve even higher efficiencies comparable to that of NV centers (up to 99 % [281]).

Scientific gain

In this chapter, the first ever measured artificially generated single-photon sources hosted in pure silicon are characterized. The optical properties suggest that isolated G centers were detected and analyzed. These exhibit promising SPS properties, including

- a sharp ZPL whose wavelength ($\lambda \approx 1270$ nm) is in the range of optical telecommunication bandwidth and thus allows low-loss information transmission

- high brightness (≈ 8000 counts/s) despite photon losses due to total internal reflections ($n_{\mathrm{Si}} \simeq 3.5$) and weak detection efficiency ($\eta_{\mathrm{det}} = 10\,\%$) of the single-photon detectors

- optical stability over long periods without blinking and bleaching effects

- an excited state lifetime of $\langle \tau_{\mathrm{e}} \rangle = 35.8 \pm 0.2\,\mathrm{ns}$

- existence of a metastable triplet state allowing the possibility of electronic control of the state.

The measured properties indicate that single G centers are well suited for photonic and quantum applications. Thus, this work makes a great contribution to the further development of new silicon-based quantum technologies. However, in order to harness the promising quantum optical properties, the next step is to develop methods to manipulate and measure the quantum state. This will be the topic of the following chapter.

Optical and photoelectric readout of G centers in silicon

Subject matter

In this chapter, the construction of an experimental setup for ODMR and PDMR measurements on G centers and first unpublished results will be presented. These techniques would enable the optical as well as electronical control and readout of G center quantum states and thus combine photonic and quantum applications with CMOS compatible silicon on-chip integration and low loss quantum information processing. The experimental setup will be described in detail and the advancement of different measurement steps will be presented, before the experimental results are evaluated and discussed.

6.1 Setup

An important step for the development of quantum technologies from solid-state defects like the G center is the manipulation of their quantum states by an external MW field and the subsequent detection of the modified state. This low-temperature detection can take place either with a PL spectrometer by measuring the variation of the PL intensity (ODMR) or by an electronical measurement of the photocurrent (PDMR). The construction of such a low-temperature ODMR/PDMR experiment comprises several steps, which will be explained in more detail below. First, the sample under investigation will be analyzed in detail, before the electronic and optical components for the ODMR and PDMR measurement are described.

6.1.1 Sample preparation

The investigated $5 \times 5 \, \text{mm}^2$ SOI sample was prepared in the Quantum Photonics, Electronics and Engineering Laboratory in Grenoble and consists of a 60 nm thick top layer of ultra-pure ^{28}Si grown on a 4 nm thick layer of natural silicon. The high isotopic purity (99.992 % ^{28}Si) was generated by the procedure described in [282]. The top Si layers are isolated from the bulk Si by a 145 nm thick layer of SiO$_2$ (see Fig. 6.1 (a)). To generate G centers in the thin ^{28}Si layer, ^{12}C ions were first implanted with an energy of $E = 8 \, \text{keV}$ and a fluence of $\Phi = 1 \times 10^{14} \, \text{cm}^{-2}$. According to SRIM simulations, carbon ions with this energy stop at a depth of 30 nm and are accordingly located in the center of the ^{28}Si layer, whereby channeling effects are not taken into account by the simulation. After the implantation, the crystal lattice was annealed for 20 s at $T = 1000 \, °\text{C}$ in N$_2$ atmosphere to incorporate the carbon into the lattice, before metal contacts for the electrical wiring were generated
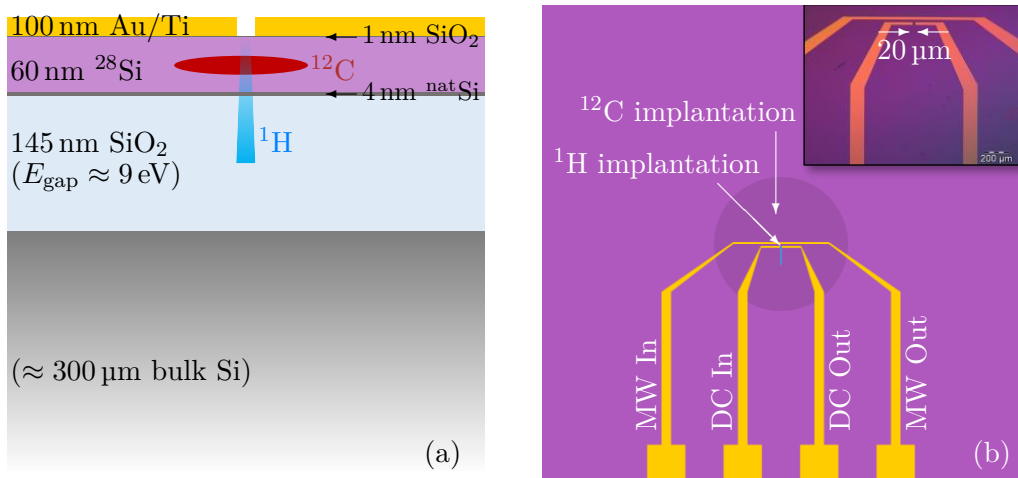
Figure 6.1 Description of the sample design. **(a)** Layer structure of the finished sample. An increased carbon concentration is located in the center of the ^{28}Si layer and hydrogen ions stop in the 145 nm SiO$_2$ layer, thus creating G centers only in the top layer. **(b)** Sample scheme with structures and implantations. The 5×5 mm^2 ultrapure ^{28}Si SOI sample is first implanted with a circular ^{12}C spot (1×10^{14} cm^{-2} at 8 keV) in the center of the sample. After an annealing step (20 s at $T = 1000\,°$C in N$_2$ atmosphere), the sample was patterned with EBL before it was coated with a thin Ti/Au layer. Subsequently, remaining resist with metal on top was removed in a remover/acetone solution, revealing the depicted structure. G centers were produced between the electrodes by proton implantation with $\Phi = 1 \times 10^{14}$ cm^{-2} and at $E = 6$ keV.

on the top surface of the sample. For this purpose, the sample was first cleaned with an acetone-ethanol mixture in an ultrasonic bath, coated with a PMMA positive resist (AR-P 671.05) from ALLRESIST GmbH, which was subsequently patterned with an electron beam from a dual-beam system. The resist in the irradiated areas was removed by bathing in a developer solution (10 s in AR-600-55) and further development was stopped by a stopper solution (60 s in AR-600-60). The patterned sample was uniformly coated with a metal layer of 20 nm titanium and 80 nm gold by physical vapor deposition (PVD). Subsequently, the remaining unirradiated resist was removed together with the metal layer on top of the resist in an ultrasonic bath of remover solution and acetone ("lift-off"). The resulting structure is shown in Fig. 6.1 (b). It consists of four bond pads, of which the two outer ones allow the connection of a microwave (MW In and MW Out) and the two inner ones allow the connection of a DC voltage source (DC In and DC Out). The MW wire has a distance of 20 µm to the two electrodes and the electrodes are also separated by a gap of 20 µm. A high concentration of G centers was then generated between the electrodes by a proton implantation at $E = 6$ keV and $\Phi = 1 \times 10^{14}$ cm^{-2} using a 20×200 µm^2 mica mask. At this energy, the protons stop in the center of the 145 nm thick SiO$_2$ layer, thus creating interstitials in the ^{28}Si layer but not in the bulk Si. Further, by stopping in the SiO$_2$, no hydrogen related defects should be generated in the ^{28}Si layer.

6.1.2 Circuit board and cryostat

Low temperatures are necessary to measure ODMR on G centers. Therefore, the sample had to be wired and placed in a cryostat, which required the development of a printed circuit board (PCB) as well as a modification of the Oxford Instruments Janis ST-500
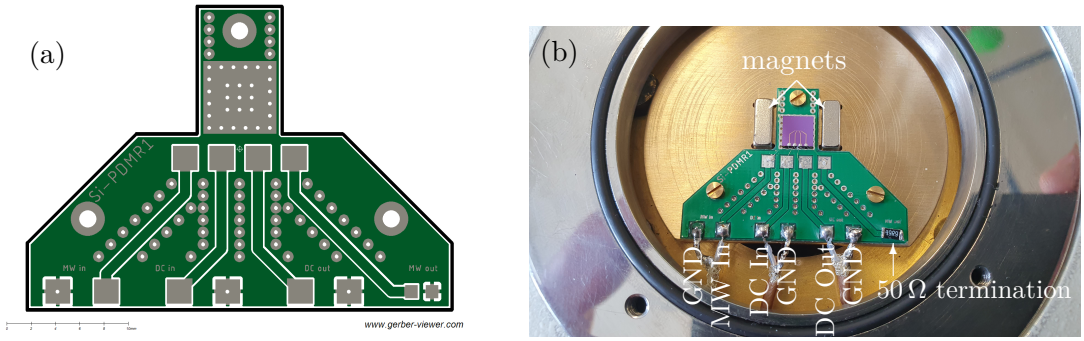
Figure 6.2 Circuit board to apply a microwave and DC voltage to the sample. (a) The PCB was designed with the EAGLE Autodesk software and saved as Gerber file to be processed by the Fischer Leiterplatten GmbH. **(b)** The design allows the placement of a $5 \times 5\,\mathrm{mm}^2$ sample between two permanent magnets. It offers the shielded connection of four coaxial cables to the sample. In the setup used in this work, the fourth bond pad was connected to an $50\,\Omega$ resistor to terminate the MW and reduce the emergence of reflections.

cryostat, thats dimension needed to be considered while designing the new components. The PCB, which is shown in Fig. 6.2 (a), was designed with the EAGLE Autodesk program and the resulting Gerber file was sent to a manufacturer of PCB (Fischer Leiterplatinen GmbH). The dimensions of the PCB were chosen in a way that the sample was centrally located on the heatsink of the cryostat, to ensure the best possible heat conduction, and its four bond pads could be connected to the PCB bond pads by thin, non-insulated gold wires. The four PCB bond pads are wired to the edge of the board and end in further bond pads where coaxial cables can be connected by soldering the copper core to the in- and output pads and the woven copper shield of the cable is soldered to the ground (GND) pads. Furthermore, the wire for guiding the MW output ends at a bond pad where a $50\,\Omega$ resistor can be soldered to terminate the MW signal. The high number of perforations ("vias") in the PCB is intended to improve the thermal contact between the top and bottom of the board. To gain space for the cables and to place the sample in a magnetic field generated by two neodymium permanent magnets, a new heatsink was designed for the cryostat, which is shown in Fig. 6.2 (b). The usual circular shape was cut and the straight edge of the resulting circular segment was congruent with the edge of the PCB where the coaxial cables are soldered. Furthermore, two millings of the size $8 \times 3 \times 2\,\mathrm{mm}^3$, located respectively on the left and right of the sample, where prepared to insert two permanent magnets with a size of $8 \times 3 \times 4\,\mathrm{mm}^3$, to generate an almost constant magnetic field at the height of the sample. Neodymium magnets of this size offer a good compromise between space-saving and sufficient field strength, considering the spatial limitation in z-direction, caused by the cryostat window. Three threaded perforations allow the board to be screwed tightly to the heatsink to improve the thermal conduction. Three $20\,\mathrm{cm}$ long RG316 coaxial cables, that ends were stripped to expose the core and shielding of the cables and which have an impedance of $50\,\Omega$ were used for the wiring inside the cryostat. One end of the cable was connected and crimped to an SMA plug, while the other end was soldered directly to the PCB bond pads. For the connection from the inside of the cryostat to the outside, a commercially available flange (IFDCG042013) from Kurt J. Lesker Company with four vacuum-tight SMA feedthroughs was attached, which is shown in Fig. 6.3. The prepared cables were connected to the existing SMA feedthroughs and guided through a
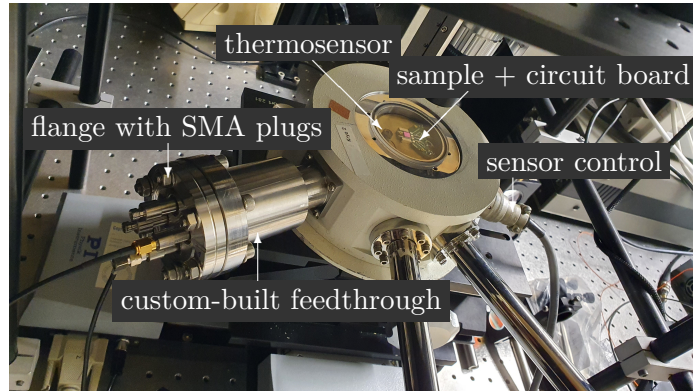
Figure 6.3 Sample and circuit board in the closed and modified He cryostat. One side of the coaxial cables is soldered onto the bond pads of the circuit board, whereas the other side is connected to the female SMA plugs of the flange. The cables run across the custom-built feedthrough.

cable passage, which was specially adapted to the dimensions of the flanges of feedthrough and cryostat. This cable passage was screwed to the cryostat from the outside, so that a complete wiring from the sample to the control devices was possible.

6.1.3 Measuring and control devices

To measure ODMR and PDMR, a microwave field must be applied to the sample. For this purpose, the optional tracking generator function of a $3\,\text{GHz}$ spectrum analyzer (GSP-830) from the company GW Instek was initially used. This outputs frequencies between $9\,\text{kHz} - 3\,\text{GHz}$ at powers of $-50\,\text{dBm} - 0\,\text{dBm}$ (corresponding to $1 \times 10^{-5}\,\text{mW} - 1\,\text{mW}$). Since the maximum output power alone was too low, an additional MW amplifier (ZHL-16W-43+) from Mini-Circuits was interconnected between the spectrum analyzer and the MW input of the flange. Unfortunately, this amplifier had a bandwidth of $1800\,\text{MHz} - 4000\,\text{MHz}$ and was therefore not certified for the necessary frequency range. But due to the lack of alternatives and the need for signal amplification, this amplifier had to be used despite not fitting specifications. The amplification in the certified range was about $45\,\text{dB}$, so that in combination with the bandwidth of the spectrum analyzer, powers of about $0.3\,\text{mW}$ to $31\,\text{W}$ could theoretically be achieved. The generated MW was sent via the conducting path shown in Fig. 6.1 (a) and terminated at a $50\,\Omega$ resistor on the circuit board. Later, the setup was optimized by a signal generator (SMIQ 03B) from Rohde & Schwarz, that covers a frequency range of $300\,\text{kHz} - 3.3\,\text{GHz}$ and delivers a maximum output power of $15\,\text{dBm}$ ($\approx 32\,\text{mW}$). This enabled the measurement without an additional amplifier, which improved the SNR. In addition, the SMIQ 03B allowed the computer-aided control, so that automated measurements were possible by developing a suitable program.

For the PDMR measurement, a voltage source was connected to the two electrodes ("DC In", "DC Out"). At the beginning of the experiment, the voltage source was a $9\,\text{V}$ block battery whose negative polarity was connected to DC In whereas the positive polarity was connected to GND, resulting in an effective negative voltage. Later, the block battery was replaced by a high-voltage source (Keithley 237 High Voltage Source Measure Unit) that enables measurements at different and more stable voltages. The current flowing between the electrodes was measured with a lock-in amplifier (MFLI from Zurich Instruments), which

was connected to the DC Out plug via an SMA cable, and displayed using the company's LabOne program. The reference signal, which is necessary for the lock-in measurement, was generated by an optical chopper. The slotted chopper wheel was brought into the optical path to interrupt the laser beam with a frequency of 1.93 kHz. The charge carriers, that are generated by the laser pulses, occur with the same frequency. The reference output signal of the chopper control unit is passed on to the lock-in amplifier, where it is locked to the same frequency and multiplied by the measured, modulated photocurrent of the electrodes. At the beginning of the experiment, the time evolution of the photocurrent measured by the lock-in amplifier was recorded over 20 s at different MW frequencies and then averaged using a Matlab script. Later, by combining the SMIQ 03B and MFLI, the MW frequency could be varied automatically and the corresponding photocurrent was measured directly. This had the advantages, that the probability of heating effects due to the MW is reduced and the PDMR measurement is accelerated. The optimized setup with the final devices of SMIQ 03B, MFLI and the Horiba-InGaAs CCD detectors, that was used at later measurements, is shown in Fig. 6.4 and allowed fully automated PDMR and ODMR measurements, resulting in a significant improvement in resolution and an acceleration of the measurement process.
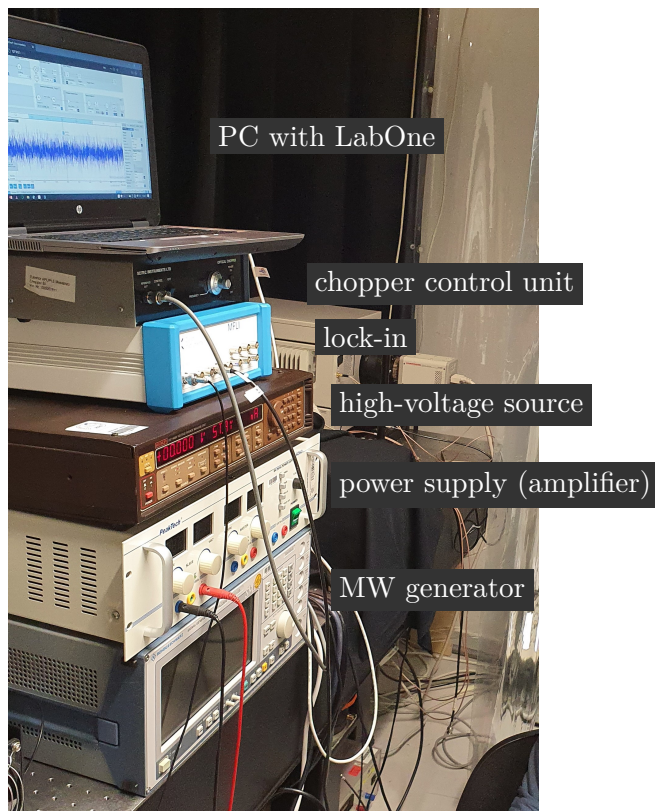
Figure 6.4 Control devices of the ODMR/PDMR setup. The LabOne program on the computer was used to control the optical chopper and lock-in amplifier. The voltage was manually set to a value at the voltage source while the MW parameters (e.g. power, step size, delay time) of the SMIQ 03B MW generator were set via a Python script, that enables the communication between lock-in, MW generator and the CCD.

6.1.4 PL spectroscopy

In order to measure the PL intensity and to determine the ODMR signal, a setup for time-integrated photoluminescence measurement as described in [283] was prepared in the Semiconductor Physics Group of the Universität Leipzig with support from M. Sc. Evgeny Krüger. Fig. 6.5 depicts this setup together with the components already mentioned in this chapter, thus showing the complete ODMR/PDMR setup. All optical components are located on a vibration-damped table. For the excitation of the G centers, two different CW lasers, either a diode-pumped solid-state laser Verdi V18 from Coherent (532 nm) or a HeNe laser 45-5p from Spindler & Hoyer (632 nm), were used. According to [284], the penetration depths of these lasers are approximately 1.3 μm at 532 nm and 3.1 μm at 632 nm. The laser beam was directed via dielectric or broadband metal mirrors to a neutral density (ND) filter, which can attenuate the power of the laser beam by up to nine orders of magnitude. By the use of a beam splitter, 50 % of the beam was directed to a Si photodiode,
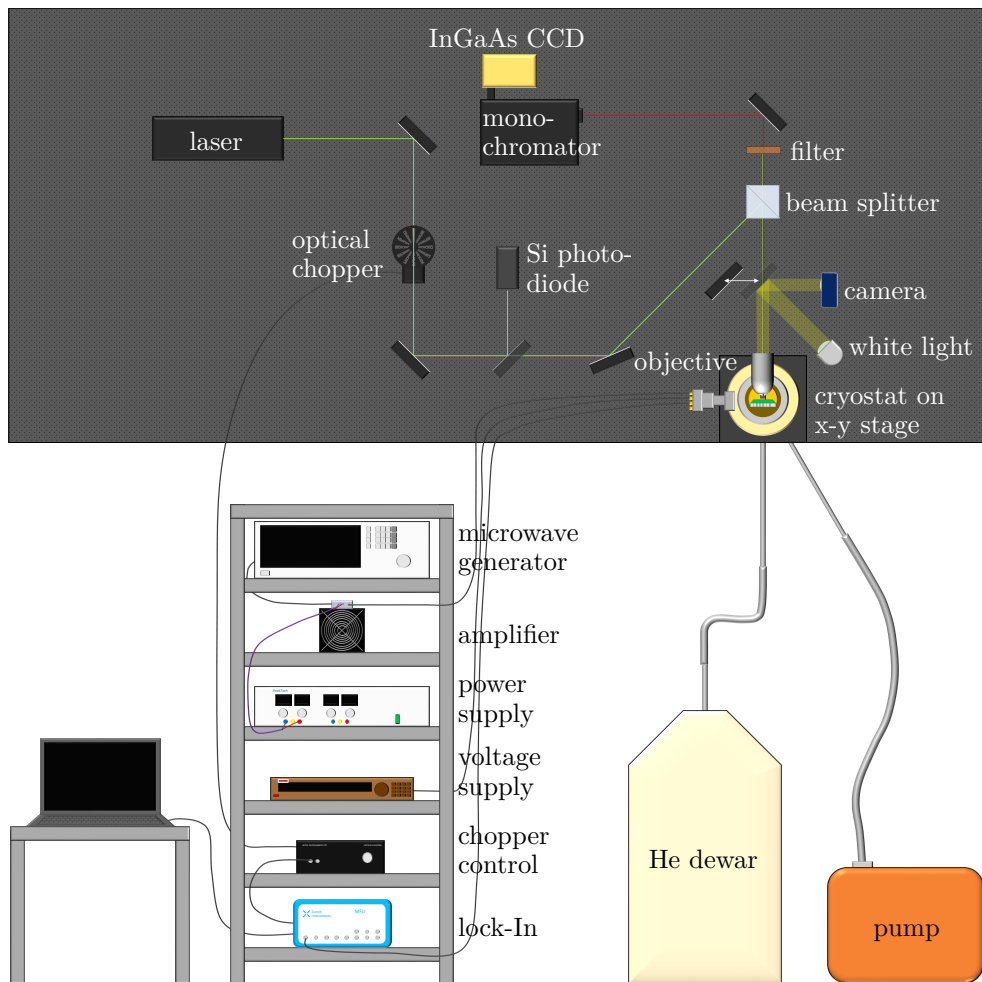
Figure 6.5 Complete setup for automated, temperature-dependent ODMR and PDMR measurements. A laser beam is focused between two electrodes on a sample with implanted quantum centers. An applied microwave field changes the occupation of the energy levels of the centers, resulting in changes of PL and photocurrent that is measured by IR spectroscopy and lock-in amplification. See main text for details.

through which the effective power of the beam could be determined during the measurement. The remaining 50 % of the laser beam were guided via a beam splitter to a 100× NIR objective (APO HR Mitutoyo), which focuses the beam on the sample inside the cryostat and collects the generated photoluminescence of the G centers. The objective mounting can be precisely controlled by a piezo element and thus the focus can be sensitively adjusted. An x-y positioning stage from Princeton Instruments allows lateral movement of the sample. Furthermore, white light from a lamp is directed onto the sample through a mirror that can be tilted into the beam path behind the objective, so that an optical image of the sample can be recorded with a digital camera, thus enabling observation and alignment of the laser spot and sample. If the camera mirror is not in the beam path, the PL signal from the sample and the laser light is passed through the beam splitter to an edge filter, which filters out the excitation wavelength. Thus, only the PL signal arrives at the Horiba HR320 monochromator (150′/mm grating, blaze wavelength 1200 nm), where the spectrally separated light is detected and processed by a N_2 cooled InGaAs CCD array (Horiba Yobin Yvon IGA-1024x1-25-1700-1LS).

6.2 Manual ODMR and PDMR at cryogenic temperature

The results of the manual ODMR and PDMR measurements are presented below. For the ODMR measurements, PL spectra were recorded at a temperature of $T = 40\,\text{K}$ and at different MW frequencies. As shown in Fig. 6.6 (a), the measurements exhibit the typical shape of G center spectra. To determine the dependence of the PL intensity on the MW frequency, a Matlab script was used to integrate the ZPL of each PL spectrum and the respective PL intensity was plotted over the MW frequency. In addition, to determine the optimal excitation power, a saturation curve for a 532 nm laser was recorded, which is shown in Fig. 6.6 (b). Unless otherwise mentioned, each measurement was performed with an excitation power of $\approx 60\,\text{mW}$, which corresponds to a power density of $\approx 76.4\,\text{kW}\,\text{cm}^{-2}$ for a laser spot diameter of $\approx 10\,\mu\text{m}$ and is thus above the ensemble saturation power according to Sec. 4.1.5. At the beginning of the experiment, it was not yet possible to use
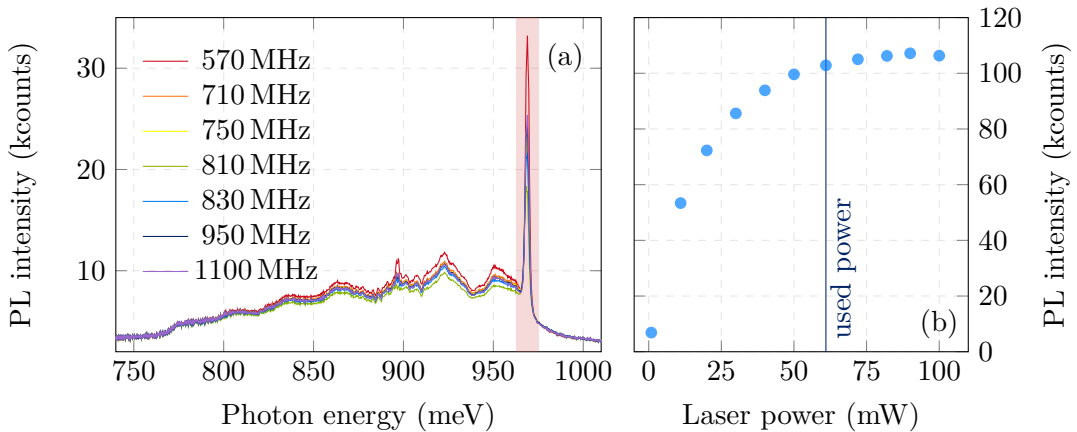
Figure 6.6 Preliminary considerations. **(a)** G center spectra for different MW frequencies. To investigate the frequency dependence, the ZPL intensity was determined by integrating each spectrum within the red shaded area. **(b)** Laser power dependence of the PL intensity. P_{Laser} was chosen to be briefly below the saturation determined here.
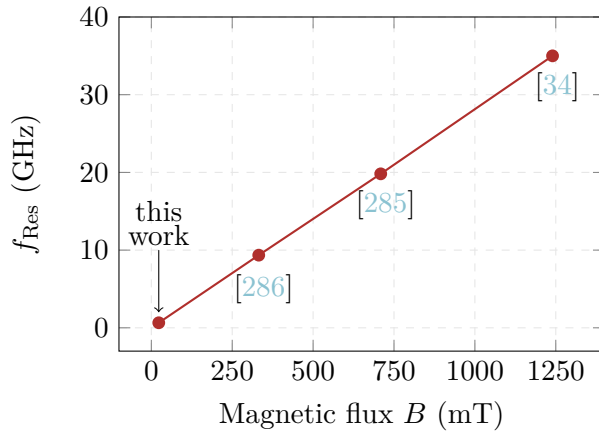
Figure 6.7 Estimation of the resonance frequency. From previous works, the resonance frequency at $B = 20\,\text{mT}$ was estimated to be approximately $730\,\text{MHz}$.

the optimized setup with automation, as the necessary equipment was not yet available. As a consequence, the tracking generator function of the GW Instek GSP-830 was used for these measurements in conjunction with the ZHL-16W-43+ MW amplifier, which is not certified for this frequency range, to achieve MW powers of $> 1\,\text{mW}$. However, the advantage of this approach was that ODMR and PDMR could be measured simultaneously, making the results more comparable. Only a few papers exist about PDMR on G centers. However, the setups and magnetic field strengths used there differ from those used in this work. Nevertheless, an estimation of the position of the resonance frequency was carried out on the basis of these. As shown in Fig. 6.7, a linear fit through the known resonances from [34, 285, 286] at different magnetic flux densities allows the estimation of the resonance frequency to be in the range between $600 - 1000\,\text{MHz}$. Accordingly, in a first series of measurements, the range from $400\,\text{MHz}$ to $1000\,\text{MHz}$ was manually scanned in
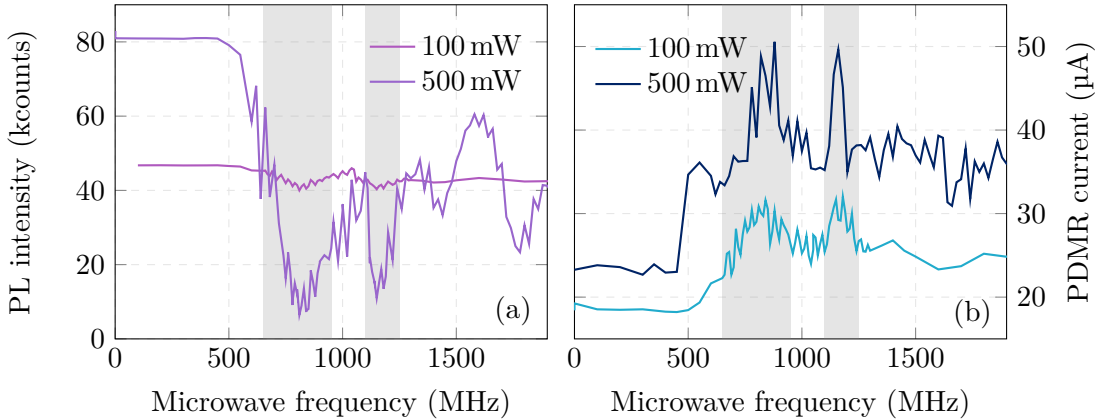
Figure 6.8 Manual measurement of (a) ODMR and (b) PDMR at T $= 40\,\text{K}$ and different MW powers. Excitation was executed with $532\,\text{nm}$. The microwave was generated by the GW Instek GSP-830 spectrum analyzer in combination with the ZHL-16W-43+ amplifier. The MW frequency was swept manually from 0 to $2000\,\text{MHz}$ with varying step size. At high MW power, a strong decrease of PL intensity and an increase of the photocurrent is detected at certain MW frequencies (grey shaded areas).
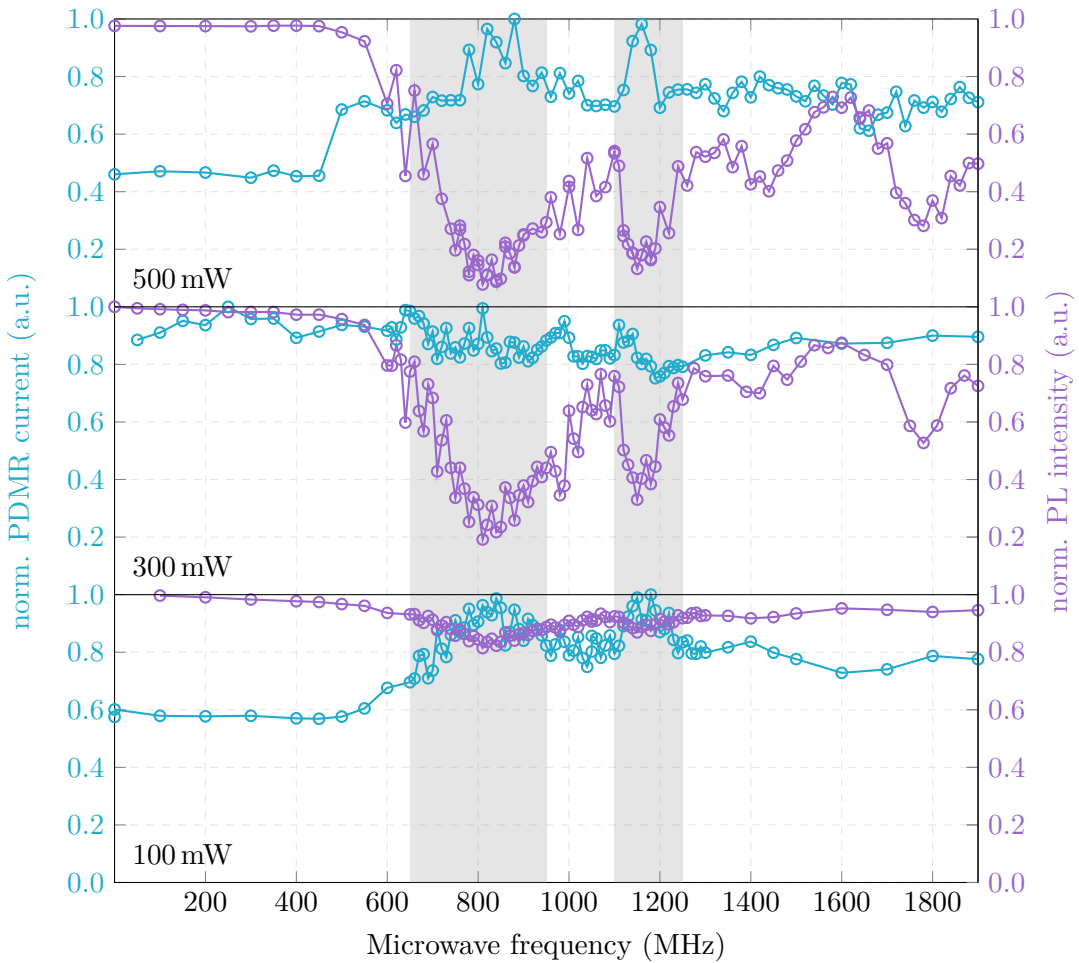
Figure 6.9   Comparison of the normalized ODMR and PDMR signals at different MW powers. Dips in the PL intensity are correlated to peaks in the photcurrent. At high microwave powers, the PL intensity nearly vanishes, indicating an unusual strong manipulation of the G centers probably caused by the inappropriate MW amplifier.

20 MHz steps and changes in both PL intensity and photocurrent were observed at certain broad MW frequency ranges. The photocurrent was detected between the electrodes with an applied DC voltage generated from the 9 V battery. Fig. 6.8 compares the ODMR and PDMR spectra recorded at the lowest and highest MW powers. The PL intensity at $P_{MW} = 500$ mW was determined to be ≈ 80 kcounts/s at the maximum and drops to a minimum of ≈ 6 kcounts/s at $f_{MW} = 810$ MHz. The PDMR signal at the same MW power shows a maximum of ≈ 50 µA at 880 MHz and a minimum of ≈ 22 µA. For a better comparison of PL intensity and photocurrent, the normalized values at all three measured MW powers are additionally presented in Fig. 6.9. For all spectra, no change in PL intensity and PDMR current was observed in the range of 0 MHz − 500 MHz. Between 600 MHz − 900 MHz and 1100 MHz − 1250 MHz, changes in PDMR current and PL intensity could be detected, but with opposite signs between the two methods. While the ODMR signal decreases in these areas, the measured PDMR current increases in parallel. The amplitude of the ODMR dip increases steadily with increasing MW power, whereas the PDMR peak also increases from 100 mW to 500 mW, but shows a lower value at the 300 mW

measurement. The ODMR spectrum also shows another dip at 1800 MHz at higher powers, which was not observed in the PDMR measurement.

In comparison with other ODMR and PDMR experiments, the unusual high contrast of the ODMR signal, which drops to almost zero at $P_{MW} = 500$ mW and at MW frequencies of 800 MHz and 1150 MHz frequencies and the huge width of the signals, suggests that the non-certified amplifier could potentially couple spurious signals, that affect the ODMR and PDMR measurement. Therefore, the experimental setup needed to be optimized for the next measurements to reduce interfering effects.

6.3 Automated PDMR measurements

As described in Sec. 6.1, due to the utilization of a new MW source, the automatization of the setup was possible, which allowed to measure spectra with higher resolution (smaller step sizes and thus more data points within the same frequency range) and to reduce heating of the sample by random changes of the MW frequency. Furthermore, the new MW source enabled the measurement without an additional amplifier. In comparison to the manual measurements, the Keithley 237 high-voltage source was used instead of a 9 V battery. This made it possible to investigate the influence of different voltages on the PDMR signal. Unfortunately, the communication between the Python program and the SMIQ03B MW source was arbitrary interrupted and the respective measurement was thus terminated after an undefined number of passes leading to different numbers of iterations for the PDMR spectra. Since only PDMR was measured in the following experiments, it was examined if a G center PDMR signal would be observable even at room temperature.

6.3.1 Spectrum analysis

Fig. 6.10 shows an example of a PDMR spectrum, recorded with a DC voltage of $U = -800$ mV on the sample described in Sec. 6.1.1. It was measured within the cryostat, but without cooling and cryostat window. Since no ODMR signal was to be measured, it was possible to reduce the laser power in order to prevent heat generation as much as possible. The position between the electrodes, i.e. where the G centers are located, was irradiated with laser light with an energy of 1.96 eV (632 nm) and a power of 40 µW. The radio frequency (RF) wave generated in the MW generator was not additionally amplified and had a power of 31.6 mW (15 dBm). The MW frequencies were automatically randomly switched between $10 - 2000$ MHz with a step number of 2000, leading to a spectrum resolution of 0.995 MHz. The spectrum shows, in contrast to the broad signals observed in the manual measurements at much higher voltage and MW as well as laser power, several strongly pronounced, narrow features in the range of $0 - 1100$ MHz. Between $30 - 450$ MHz several single peaks can be observed. From $450 - 600$ MHz strong and sharp oscillations appear. In the following range up to 800 MHz no signals are perceivable, before within $800 - 1100$ MHz three asymmetric signals can be detected, which are very similar in shape and intensity, each accompanied by a smaller, shifted peak. The measured linewidths (Lorentz fit with orthogonal distance regression) are in the range of about $5 - 28$ MHz. An overview of the different signals with resonance frequency and linewidth (if a fitting was possible) is given in Tab. 6.1. At 1100 MHz, a jump in the baseline from 243.8 nA to 249.3 nA was detected. Between 1100 MHz and 2000 MHz the photocurrent remains almost constant at this level and shows no further signals.
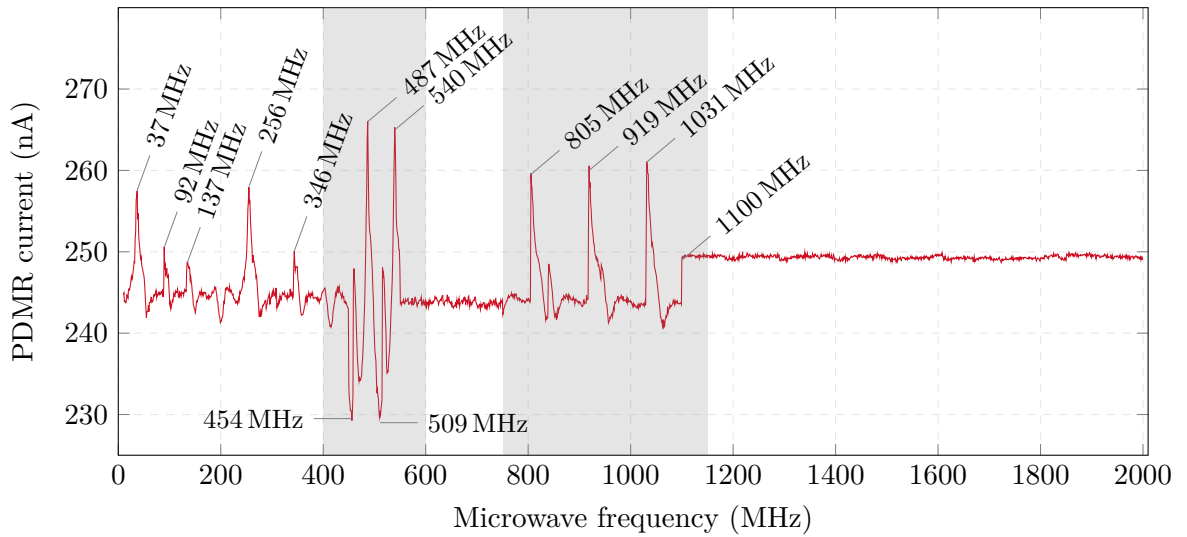
Figure 6.10 Typical spectrum of an automated PDMR measurement at room temperature. This measurement was performed with an applied voltage of $-800\,\text{mV}$ between the electrodes, a CW laser excitation of $40\,\mu\text{W}$ at $632\,\text{nm}$ and an applied magnetic field of $B \approx 23\,\text{mT}$. The microwave had a power of $31.6\,\text{mW}$ (without amplifier) and was switched randomly.

f_res	E_res	FWHM	Contrast
36.95 MHz	0.15 µeV	10.82 MHz	5.20 %
92.18 MHz	0.38 µeV	13.89 MHz	1.68 %
136.96 MHz	0.57 µeV	11.16 MHz	1.83 %
255.70 MHz	1.06 µeV	12.96 MHz	4.70 %
345.96 MHz	1.43 µeV	16.40 MHz	1.88 %
453.71 MHz	1.88 µeV	15.01 MHz	−5.69 %
486.80 MHz	2.01 µeV	5.30 MHz	8.04 %
508.59 MHz	2.10 µeV	27.89 MHz	−5.15 %
540.23 MHz	2.23 µeV	6.96 MHz	7.88 %
805.36 MHz	3.33 µeV		5.96 %
918.90 MHz	3.80 µeV		6.27 %
1031.46 MHz	4.27 µeV		6.50 %

Table 6.1 Properties of the peaks observed in the PDMR spectrum in Fig. 6.10. The peaks between $30-550\,\text{MHz}$ could be fitted with a Lorentzian function. The corresponding resonance frequencies/energies as well as the linewidth are listed. The contrast was determined by normalizing the spectrum, subtracting the baseline and measuring the baseline-peak distance.

6.3.2 Etiology

Since the automatically measured spectrum in Fig. 6.10 is clearly different from the manual measurement and the comparison to the ODMR signal, which is directly related to the G centers, is missing, it has to be checked whether the measured PDMR is actually correlated to the G centers. For this purpose, a measurement was first performed without laser
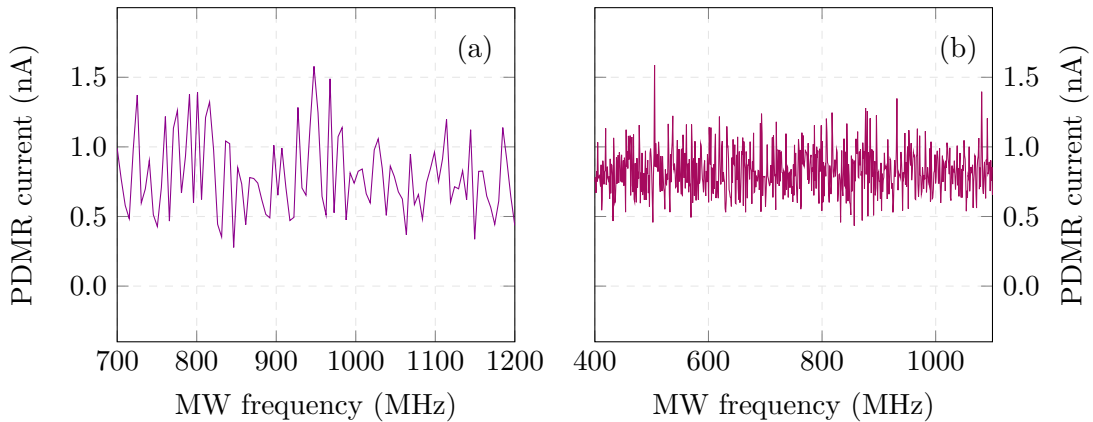
Figure 6.11 PDMR current without laser excitation at different locations. (a) Between electrodes and (b) between electrode and microwave wire.

light but with an applied voltage ($-800\,\mathrm{mV}$) to verify whether the PDMR signal is induced only by the microwave. In Fig. 6.11 such a measurement is shown at two different sample positions, namely between the electrodes (high G center concentration) and between an electrode and the MW wire (low G center concentration from the carbon implantation). As could be expected, no distinct signals can be seen apart from a dark current of about $1\,\mathrm{nA}$. However, the situation is different as soon as the sample is irradiated with laser light. Fig. 6.12 shows PDMR spectra measured with an applied voltage of $-800\,\mathrm{mV}$ and $40\,\mathrm{\mu W}$ laser excitation at three different points on the sample, namely (a) between the electrodes (many G centers), (b) between electrode and MW wire (few G centers) and (c) between two bond pads at the edge of the sample (no G centers). It can be seen that the same features appear in the spectrum even when no G centers are present. Although the spectra differ in the amount of total current, it must be assumed, that the measured signals are not related to the G centers and thus have a different cause. In order to be able to make a well-founded assessment, individual properties and dependencies of the spectra are compared and discussed below.
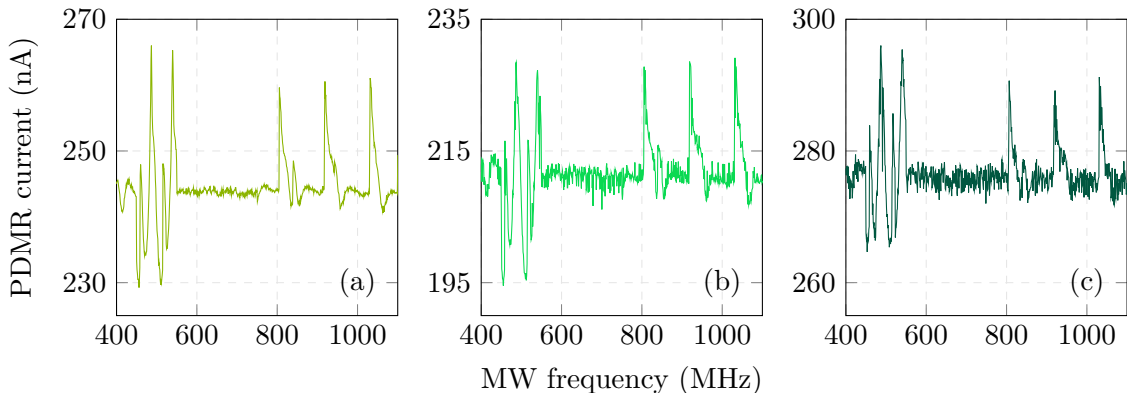
Figure 6.12 PDMR current with laser excitation at different locations. **(a)** Between electrodes, **(b)** between electrode and microwave wire and **(c)** between two bond pads.

6.3.3 Voltage dependence

Fig. 6.14 shows PDMR spectra for different voltages measured under the same conditions as in Fig. 6.10. The observed differences in the SNR are due to both the applied voltage and the different number of iterations. The number of iterations differs because of random interruptions in the recording, which probably emerged from problems in the communication between the SMIQ03B MW generator and the Python program. The previously described features in the spectrum can be found at all voltages investigated, but the intensity of the peaks decreases when the voltage goes towards zero. If one changes the polarity, the sign of the respective peaks also changes. In addition to the height of the peaks, the averaged total current also changes with the applied voltage. As can be seen in Fig. 6.13, the increase of the average photocurrent between voltages of $0\,\mathrm{mV}$ and $-200\,\mathrm{mV}$ is flat at first and then takes a linear progress with increasing voltages, which is characteristic of a non-ohmic resistor and hence can be expected for a semiconductor material such as silicon.

The current measured at a voltage of $0\,\mathrm{mV}$ surprisingly also shows the features already mentioned. Moreover, the three peaks between $800 - 1050\,\mathrm{MHz}$ are even more pronounced than in the $-200\,\mathrm{mV}$ measurement, so that it is suspected that the MW itself generates a current flow to the electrodes and overlaps with the original current. The fact that even with opposite polarity the total current remains positive and only the peaks change their signs suggests that the peaks have another origin than the average current with its I-V characteristic. The missing zero crossing of the characteristic curve might therefore be also related to additional effects, such as spin-dependent recombination (SDR) centers, as will be discussed later. Due to the long duration of the measurements, which ran partially overnight, a smaller range of the spectrum was examined for the experiments presented in the following. Since the G center related resonances were expected to be in the range around $800\,\mathrm{MHz}$, the respective peaks close to this frequency were examined in more detail.
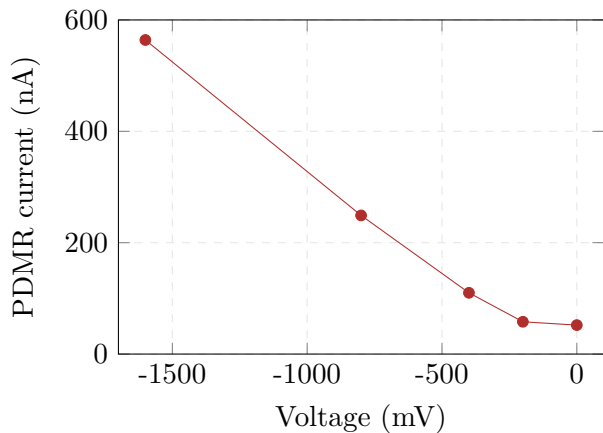
Figure 6.13 Averaged PDMR current as a function of the applied voltage. The slope of the I-V characteristic increases with increasing absolute voltage, showing a non-ohmic behavior as it would be expected for a semiconducting material like silicon. The missing zero-crossing indicates an additional contribution from the applied microwave or other defect centers.
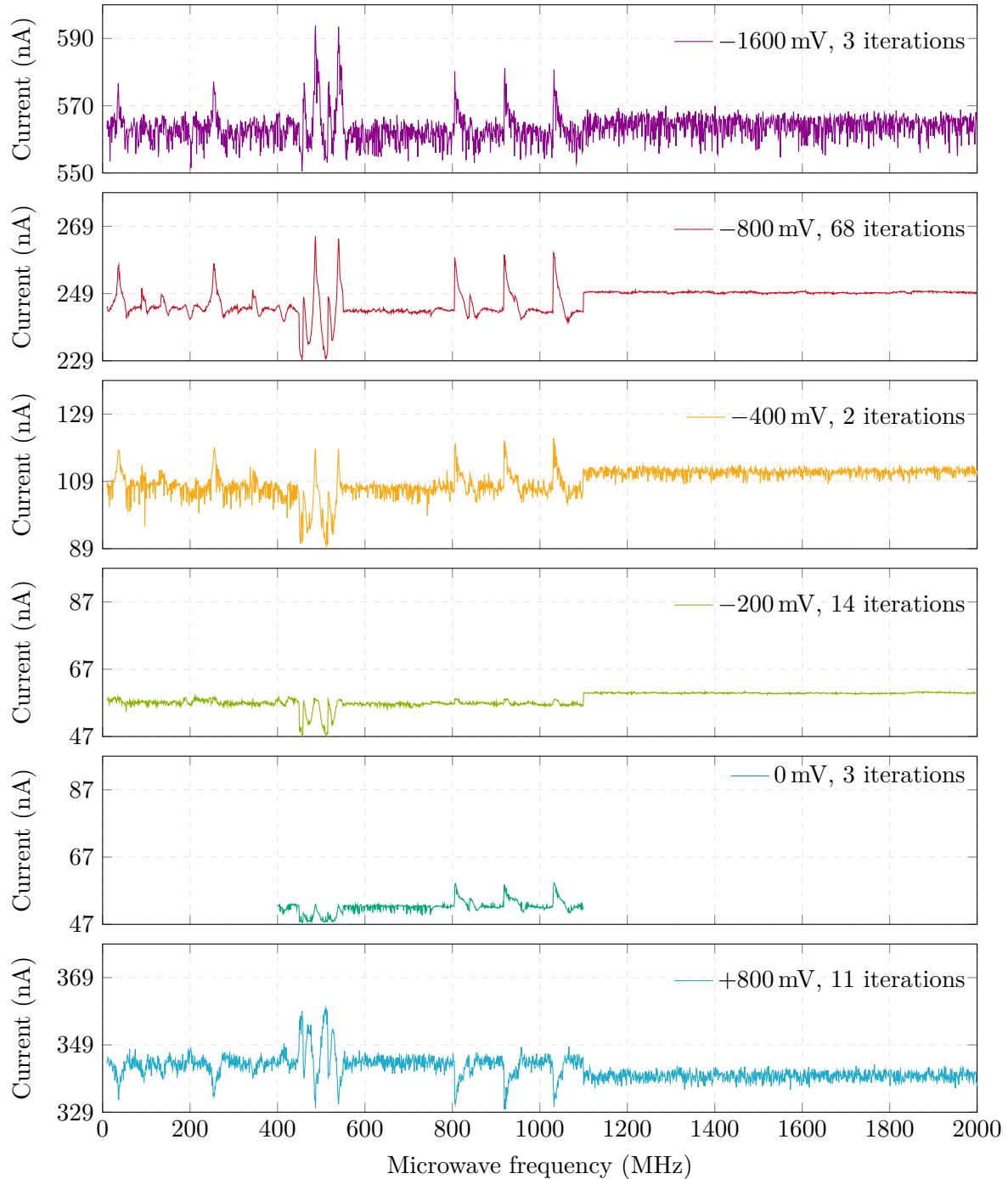
Figure 6.14 Voltage-dependent PDMR spectra. Measurements were performed at RT with a laser excitation at 632 nm (except of 0 mV, that was measured at 532 nm) and an excitation power of 40 μW. The applied MW power was 31.6 mW (without amplifier) and the MW frequency was randomly switched with a 0.995 MHz resolution in the range of 10 − 2000 MHz. The sample was placed between two magnets with a magnetic flux of ≈ 20 mT. The different numbers of iterations comes from arbitrary software crashes, most probable related to communication problems between MW generator and software.

6.3.4 Temperature dependence

Fig. 6.15 compares the PDMR spectra at room temperature and at $T = 40\,\mathrm{K}$ in the range of $800 - 1100\,\mathrm{MHz}$. The measurements were made under a laser excitation of $532\,\mathrm{nm}$ ($P_{\mathrm{Laser}} = 40\,\mathrm{\mu W}$), with an applied voltage of $U = -800\,\mathrm{mV}$ and a MW power of $P_{\mathrm{MW}} = 15\,\mathrm{dBm}$. It can be clearly seen that the previously observed jumps in the photocurrent appear at exactly the same frequencies for both temperatures. The magnitude of the total photocurrent decreases significantly with decreasing temperature, while however the current contrast (measured from minimum to maximum) in resonance at $40\,\mathrm{K}$ is about $1.5\times$ as large as at RT. A striking feature is the asymmetric line broadening towards higher energies at increased temperature. Each narrow peak at $40\,\mathrm{K}$ is followed by a dip whose width corresponds to the line broadening observed at RT. Between two peaks oscillations occur, that seem to be broader at RT and shifted with respect to the $40\,\mathrm{K}$ measurement. The observed line broadening might therefore be related to an overlap of the resonance signal with the shifted oscillation, whose origin is currently not yet known .

However, according to [287], there is also a correlation between the homogeneous line broadening of optical transitions and spin-resonant (ODMR) transitions, since the spin-orbit interaction of singlet and triplet states produce the homogeneous broadening. The broadening in both cases is said to depend on how strongly excited singlet states, ground states and spin-orbitally uncoupled spin levels dephase in the phonon bath. In Sec. 6.2 it was observed that a direct correlation between ODMR and PDMR exists, so explanations that apply to the line broadening in ODMR spectra should also apply to PDMR measurements. Assuming that the observed ODMR and PDMR effects are indeed directly related to light-emitting defects and are not just electronic disturbances, the line broadening can be described with ordinary explanations for line broadening in solids and semiconductor materials.

According to [40] and derivated for measurements on NV centers, two mechanisms contribute to the line broadening in ODMR measurements: on the one hand, the intrinsic broadening, which is determined by the spin properties of the sample (longitudinal and transversal spin relaxation times, Rabi frequency), on the other hand, an inhomogeneous broadening, which arises from variations of the local environment of the different NV
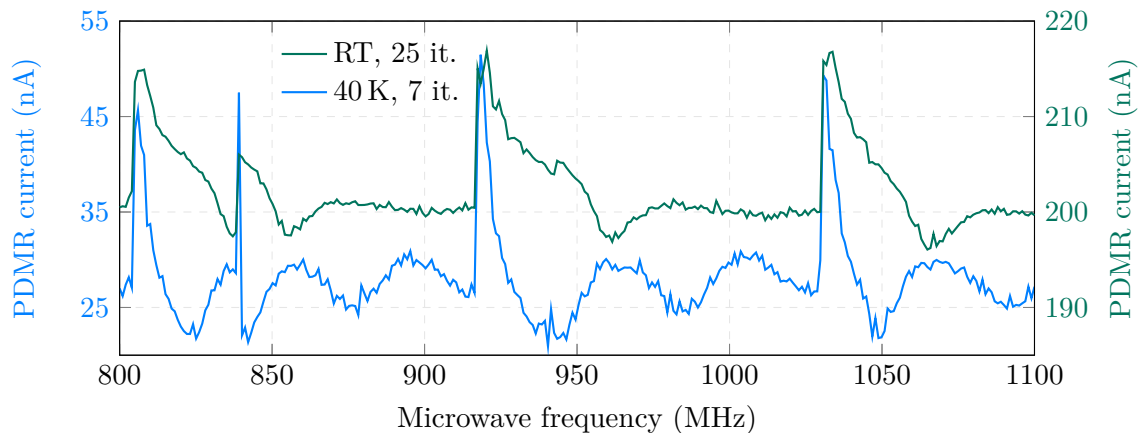
Figure 6.15   Comparison of the PDMR spectrum between 800 - 1100 MHz at T = 40 K vs. RT. Laser excitation took place at $532\,\mathrm{nm}$ with $P_{\mathrm{Laser}} = 40\,\mathrm{\mu W}$. The MW power was $P_{\mathrm{MW}} = 15\,\mathrm{dBm}$ and the applied voltage $U = -800\,\mathrm{mV}$. The resonance peaks appear at the exact same position for both temperatures, but the linewidth is broadened to higher energies at RT.

centers within the ensemble, that lead to mechanical stresses or magnetic dipole interactions due to spin impurities [288]. Considering the temperature dependence of the ODMR linewidth, a decrease of the homogeneous linewidth with increasing temperature in the range of $300 - 550\,\mathrm{K}$ is observed in [289] for NV centers, which is explained with a five-level model. According to this, the homogeneous linewidth consists of the $^3\mathrm{E}$ orbital decay rate, which increases at high temperatures, and a motional narrowing, whose fraction depends on the electron-phonon coupling and increases at higher temperatures, since the population transfer rates increase. Since it is uncertain, if the measured effects in Fig. 6.15 are caused by quantum mechanical transitions and they furthermore contradict the mentioned work, it must be assumed that the observed effects have other causes. In general, an asymmetric line broadening indicates a thermal Doppler shift, which shifts either to higher energies (blue shift) or to lower energies (red shift) depending on the observer. According to [250], phonon emission leads to a red shifted emission after phonon-assisted recombination, while phonon absorption produces a blue shift (relative to the ZPL). Since the probability of phonon absorption increases with increasing temperature, a broadening of the phonon assisted recombination towards higher energies might be conceivable. This effect already appears in the evolution of the phonon sideband and could equally cause an asymmetric line broadening of the ZPL. Such an explanation would also apply to other recombination centers, so that the measured effect would also occur if the measured resonances are not due to G centers but to other resonant defects in silicon.

6.3.5 Laser dependence

To investigate the influence of the laser power on the photocurrent and resonances, PDMR spectra were recorded only at cryogenic temperatures ($T = 40\,\mathrm{K}$) to avoid potential heating at higher powers and thus the destruction of the G centers or sample structures. Excitation was performed with $\lambda = 532\,\mathrm{nm}$ and a MW power of $P_{\mathrm{MW}} = 15\,\mathrm{dBm}$. The permanent magnets were removed during this measurement, so no magnetic field is present. Fig. 6.16 (a) shows the PDMR spectra in the range of $800 - 1100\,\mathrm{MHz}$ for laser powers of $0\,\mathrm{\mu W}$ (laser blocked), $40\,\mathrm{\mu W}$, $6\,\mathrm{mW}$ and $60\,\mathrm{mW}$. In Fig. 6.16 (b) a close-up of a single resonance is also shown. As can be seen in both graphs, high laser power results in a higher total current. Interestingly, the average current is higher with the laser blocked than with an excitation of $40\,\mathrm{\mu W}$. The reason for this could be that similar to the $0\,\mathrm{mV}$ measurement in Sec. 6.3.3 several effects overlap. Thus, the measured current at $P_{\mathrm{laser}} = 0\,\mathrm{\mu W}$ might correspond to the actual dark current, while the current at $40\,\mathrm{\mu W}$ is compensated e.g. by a bias current, which is amplified by additional defect centers, which have a smaller influence in the absence of laser light. However, it can be seen that the signals described above occur at all laser powers and at the same frequencies. A look at the close-up image also shows that at low temperatures, a signal is produced at the corresponding frequencies even without a laser, but it has a different (negative) sign, despite the same applied voltage of $-800\,\mathrm{mV}$. If the laser power is increased to $40\,\mathrm{\mu W}$, the average current decreases, but the intensity of the several peaks increases and the sign becomes positive. By further increasing power to $6\,\mathrm{mW}$ and $60\,\mathrm{mW}$, both the total currents and the intensity of the peaks continue to increase.

Another effect lies in the structure of the resonances. While without laser the sign is negative and becomes positive at low laser powers, a further increase leads to the formation of additional absorptions within the peak. However, the difference between the $6\,\mathrm{mW}$ and the $60\,\mathrm{mW}$ measurement is probably due to the lower step size ($2\,\mathrm{MHz}$ instead of $1\,\mathrm{MHz}$).
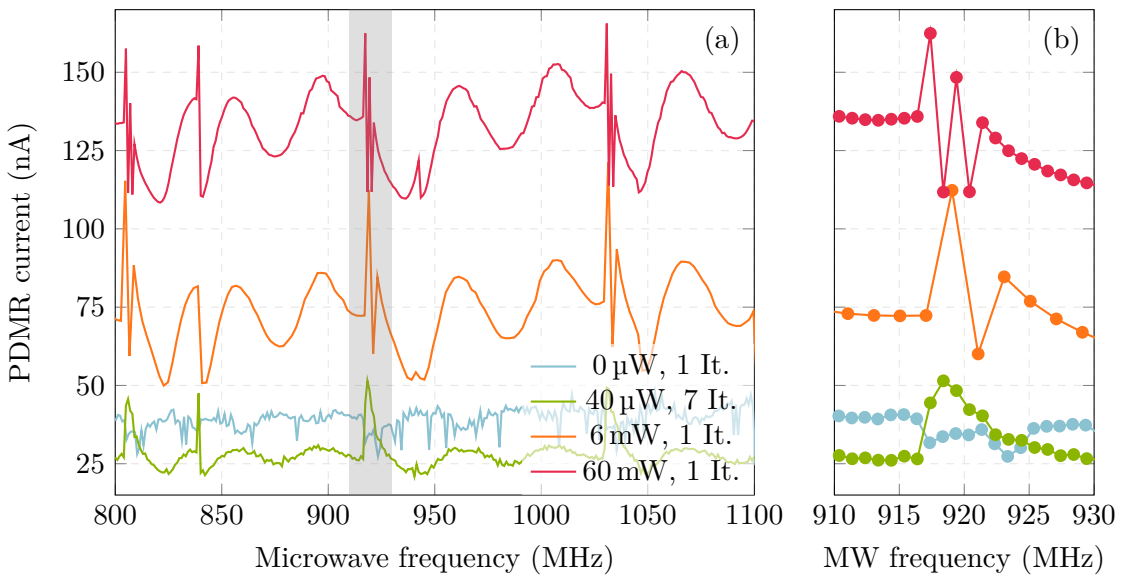
Figure 6.16 PDMR spectrum for different laser excitation powers at T = 40 K. The laser power dependence was only investigated at lower temperatures to avoid a possible heating of the sample and the G centers. Measurements were performed at $T = 40\,\mathrm{K}$ with an excitation wavelength of $\lambda = 532\,\mathrm{nm}$, an applied voltage of $U = -800\,\mathrm{mV}$ and without magnetic field. **(a)** Recorded spectrum from $800 - 1100\,\mathrm{MHz}$. **(b)** Close-up of an exemplary peak at $\approx 920\,\mathrm{MHz}$. Note the different step size of $2\,\mathrm{MHz}$ instead of $1\,\mathrm{MHz}$ for the $6\,\mathrm{mW}$ spectrum.

An explanation of this structure could be the light-narrowing effect, which was observed in [290] during ODMR measurements at NV centers and explained by MW-induced simultaneous spin-flips of the NV and P1 centers. According to this, the linewidth of the ODMR signal of an ensemble of NV centers could be reduced by a factor of 2 when the laser light power is increased from $20\,\mu\mathrm{W}$ to $500\,\mathrm{mW}$. The resulting increased resolution of the spectrum thus allowed the measurement of special features, e.g. hyperfine structures, which were not resolved at low light power. In our case, this means that the $40\,\mu\mathrm{W}$ peak is a superposition of the individual peaks measured at $60\,\mathrm{mW}$. In addition, there may be other hidden features that become visible at even higher powers and a corresponding step size. Furthermore, the influence of the excitation energy on the PDMR signal was investigated. Unfortunately, only two lasers with the sub-bandgap energies $1.96\,\mathrm{eV}$ ($632\,\mathrm{nm}$) and $2.33\,\mathrm{eV}$ ($532\,\mathrm{nm}$) were available at the time of the experiments. As can be seen in Fig. 6.17, the normalized spectra recorded at RT with magnetic field and $40\,\mu\mathrm{W}$ excitation power are almost congruent. The measured absolute current for the $632\,\mathrm{nm}$ measurement was on average about $3\,\mathrm{nA}$ higher than the value of the $532\,\mathrm{nm}$ measurement. This behavior is unexpected, since at the same laser power a higher excitation energy should produce more charge carriers due to the increased radiant flux. On the other hand, the $632\,\mathrm{nm}$ laser light has a higher penetration depth and could therefore reach more recombination centers where charge carriers can be released.

In general, a defect in the excited state either relaxes directly to the ground state by emitting a photon, via non-radiative and spin-dependent intersystem crossing, or is re-excited to the conduction band, whereby the charge state of the defect is changed from n to $n+1$. The latter point is crucial for the PDMR signal. In order to return the defect to its equilibrium charge distribution, according to [291] there are three decisive effects, which thereby
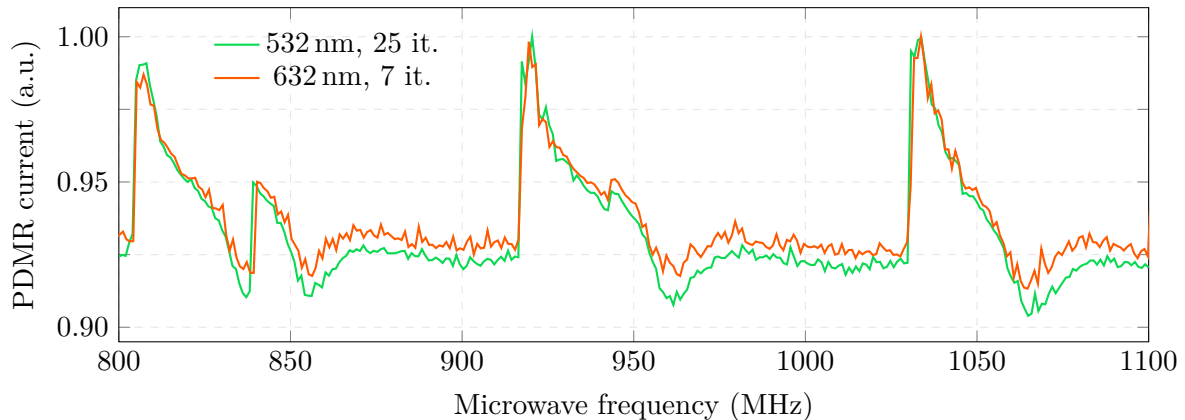
Figure 6.17 Comparison of different excitation energies. Spectra were recorded at RT and with $-800\,\text{mV}$ applied voltage, $15\,\text{dBm}$ MW power, a magnetic field of $(20\,\text{mT})$ as well as a laser power of $P_{\text{laser}} = 40\,\mu\text{W}$ for both wavelengths.

influence the PDMR signal:

- the defect recaptures an electron from the conduction band

- an electron is captured from the valence band by photo-induced hole generation

- a charge transfer from other traps or defects recharges the defect

While the total current does not change for the first point and thus does not contribute to the PDMR signal, the last two points mentioned have an influence. The corresponding mechanisms depend strongly on factors such as band-bending, defect density, excitation wavelength and temperature, so that a correlation between the laser wavelength and the measured PDMR current does not have to be linear [291]. In Sec. 4.1.4 the dependence of the PL intensity on the excitation energy was plotted. As can be seen there, the PL intensity for $532\,\text{nm}$ is larger than for $632\,\text{nm}$ excitation, which, depending on the polarity, can lead to a drop in current. Generally speaking, this would mean that at higher laser energy, radiative recombination becomes more likely which leads to less free charge carriers for the photocurrent. Even if the cause of the PDMR signals is not due to G centers, a similar relationship of competing radiative or non-radiative recombination processes could explain the slightly decreased PDMR current at higher energy.

6.3.6 Magnetic field dependence

An unambiguous sign of a relation between the measured resonances and a MW-induced change of the quantum state would be a frequency shift of the resonances in the presence of a magnetic field. Accordingly, the sample holder was designed to allow the mounting of two permanent magnets whose magnetic field was parallel to the samples (001) plane and measured with a Hall sensor to be $B \approx 20\,\text{mT}$. Fig. 6.18 shows PDMR spectra in the range $800 - 1100\,\text{MHz}$, which were recorded in the presence and absence of the permanent magnets, respectively. Fig. 6.18 (a) shows such a measurement at RT and (b) at $40\,\text{K}$. Since at low temperatures the resonances are very narrow, a section of the spectrum (b) is shown enlarged in (c).

At RT as well as at $40\,\text{K}$ no frequency shifts of the resonances are observed. At cryogenic
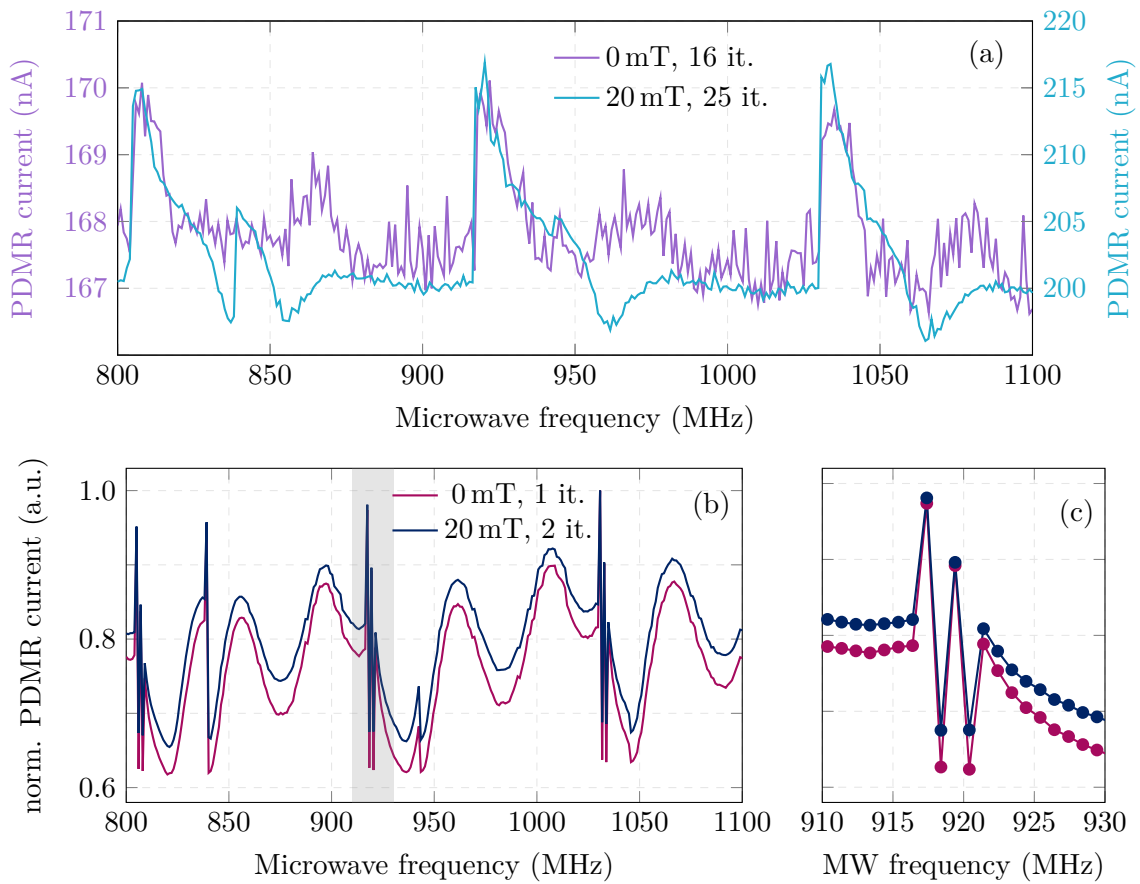
Figure 6.18   Comparison of PDMR spectra in the presence and absence of a magnetic field B ≈ 20 mT. The measurement were performed under excitation with 532 nm and an applied voltage of −800 mV. Spectra at **(a)** RT ($P_{Laser} = 40\,\mu W$) and **(b)** at 40 K ($P_{Laser} = 60\,mW$) are compared. **(c)** shows a close-up of the spectrum at 40 K. No explicit magnetic field-related frequency shifts of the investigated peaks were observed. Only the features of the RT measurement, which were interpreted as osccilations, but thats origin is unknown, partly seem to be shifted.

temperatures, the normalized spectra with and without magnetic field are almost parallel in the whole investigated range and differ only by a current increased by 25 nA with magnetic field applied. The section in (c) shows that no shift is discernible even within the resonance. The RT measurement shows a slightly different behavior. In general, it can first be said that at RT, both the average current and the amplitude are significantly higher with magnetic field than in absence of the magnetic field. This leads to a poorer SNR in the measurement without magnetic field, although the number of iterations was relatively high at 16. The reason for this difference is currently not clear. However, if one compares both graphs directly with each other, some interesting features can be recognized. For example, the resonances appear at the same frequencies, but the peaks of the 20 mT measurement have a shoulder to higher frequencies, while the 0 mT peaks tend to slope straight down. Similarly, the oscillations between the peaks show differences. Thus, in the 20 mT measurement, one again recognizes the accompanying peaks, which appear together with the main peaks and seem to move into these with increasing frequencies. The accompanying peaks are always followed by a minimum before the current oscillates back and levels off to the

baseline value. On the other hand, in the $0\,\mathrm{mT}$ measurement, accompanying peaks are also observable, which have a greater distance to the main peak compared to the $20\,\mathrm{mT}$ measurement, but still move towards the main peak with increasing frequencies. Further measurements must show whether these shifted peaks are actually resonances that are influenced by the magnetic field. It is also conceivable that they are due to the oscillations, which are somewhat more prominent due to the poorer SNR. But even in this case there would be a small difference between the frequency of the $0\,\mathrm{mT}$ and the $20\,\mathrm{mT}$ measurement, thats origin needs to be investigated by further measurements.

6.4 Automated PDMR and ODMR at cryogenic temperature

While the automated PDMR setup was extensively tested and a number of measurements were carried out, a setup for the automated measurement of ODMR spectra was implemented. Once completed, high-resolution ODMR and PDMR spectra could be recorded automatically and simultaneously. However, the MW power was still limited to $P_{\mathrm{MW}} = 15\,\mathrm{dBm}$, as there was still no amplifier available that was approved for the intended frequency ranges. Accordingly, the ODMR signal are expected to differ significantly from the measurements in Sec. 6.2. Fig. 6.19 shows the automated and normalized (a) ODMR and (b) PDMR spectra recorded without magnetic field ($B = 0\,\mathrm{mT}$) at $T = 40\,\mathrm{K}$ with a laser excitation of $P_{\mathrm{laser}} = 60\,\mathrm{mW}$ at $\lambda = 532\,\mathrm{nm}$, an applied voltage of $U = -800\,\mathrm{mV}$ and a MW power of $P_{\mathrm{MW}} = 15\,\mathrm{dBm}$. The PDMR spectrum shows again the oscillatory characteristic, which has been observed several times before. The ODMR spectrum also shows oscillations that are mirror symmetrical to the PDMR signal. This means that within the broad oscillations an increasing PDMR current is accompanied by a decreasing ODMR luminescence, as was previously observed in Sec. 6.2 for negative voltages. In the ODMR spectrum, fluctuations in the PL intensity can also be seen at the already known frequencies, but these are much less pronounced than in the manual measurements. This is probably due to the lower MW power and the significantly lower applied voltage, which was over $11\times$ higher in the manual measurements with $-9\,\mathrm{V}$. In order to better evaluate the changes of PDMR and ODMR at the resonance frequencies, the first derivative was formed from each of the two spectra. The Fig. 6.19 (c)-(e) each show an enlarged section of the derivated spectrum at different frequencies. A correlation between the ODMR signal and the PDMR signal is clearly visible. Interestingly, the ODMR and PDMR peaks have the same sign, which contradicts the other course of the curve and thus allows the assumption that the resonances have a different origin than the broad oscillations.

In the measurements from Sec. 6.3.2 it was shown that the peaks in the PDMR spectrum also occur when areas of the sample are irradiated where no G centers should be present. If the ODMR signal, which is based exclusively on the luminescence of the G centers, is affected at the same frequencies as the PDMR signal, mechanisms must take effect that indirectly influence the ODMR signal. These will be discussed in the following section.
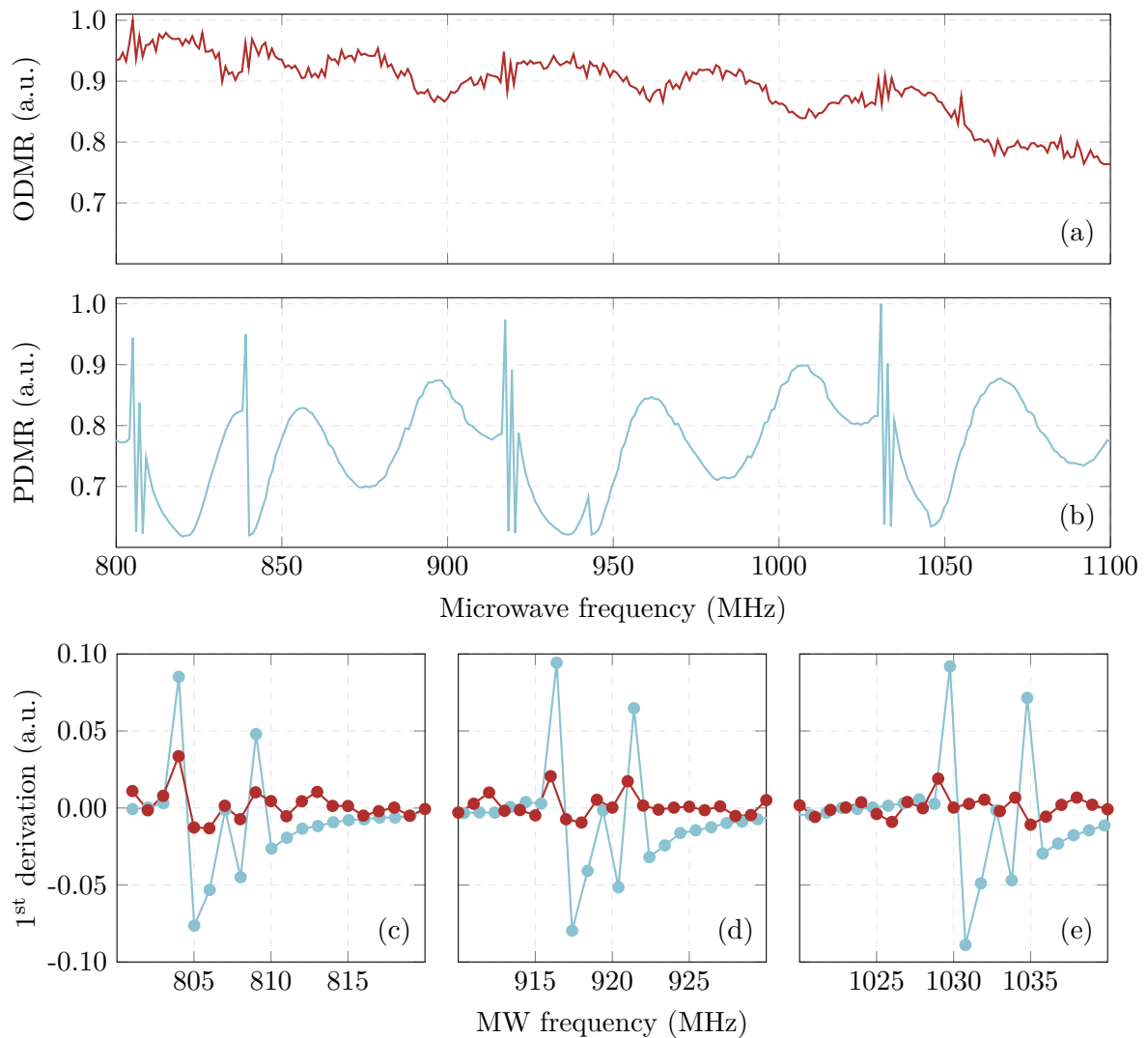
Figure 6.19 Automated ODMR and PDMR measurements. (a) ODMR and **(b)** PDMR were recorded simultaneously at $T = 40\,\mathrm{K}$ with a laser excitation of $\lambda = 532\,\mathrm{nm}$, with $P_{\mathrm{laser}} = 60\,\mathrm{mW}$, an applied voltage of $U = -800\,\mathrm{mV}$, a MW power of $P_{\mathrm{MW}} = 15\,\mathrm{dBm}$ and without magnetic field. The G center ODMR spectrum shows resonances at the same frequencies as observed for PDMR. **(c)-(e)** Detailed depiction on the first derivation of the spectra at resonant frequencies shows changes in photocurrent and PL intensity with the same sign, in contrast to the frequencies out of resonance, that show an opposite behavior.

6.5 Discussion

The PL intensity of the G centers is, apart from the optical settings, significantly influenced by three factors. These are

- **defect density** - luminescence depends on the carbon and vacancy concentration and therefore on the $^{12}\mathrm{C}$ and H fluences during implantation

- **temperature** - with increasing temperature, the PL intensity decreases

- **number of free charge carriers** - with less free charge carriers, fewer radiative recombinations take place

Since the PDMR signals occur even without the G centers being directly irradiated, the first point, i.e. a direct influence on the states of the G centers, should play a minor role and the observed variation of the photocurrent and the 0.97 eV luminescence should be caused indirectly. Temperature could have a greater influence in the experiments shown here. Since the cryostat only reaches a temperature of 40 K (at the location of the sensor) and the PL intensity of G centers is very sensitive to temperature in the range of $40 - 80$ K, as shown in Sec. 4.2.3, small frequency-dependent temperature variations induced by the microwave could lead to significant changes in PL.

6.5.1 Microwave dielectric heating in silicon

According to [292], depending on the dielectric and magnetic properties of a body, the energy of microwaves are converted into heat energy. The heating thus generated depends on the one hand on the macroscopic geometry of the body and on the other hand on the interaction of the electromagnetic fields of a MW with the microscopic building blocks of the body. This interaction can be described by Maxwell's equations, in which the parameters permittivity and permeability of the material mainly determine the conversion of the wave energy into heat. In non-magnetic materials, the permeability can be neglected, so that in the case of silicon, only the complex permittivity

$$\varepsilon = \varepsilon' - i\varepsilon'' = \varepsilon_0(\varepsilon_{\rm r}' - i\varepsilon_{\rm eff}'') \tag{6.1}$$

defines the heat generation, where ε_0 is the permittivity in vacuum, $\varepsilon_{\rm r}'$ is the relative dielectric constant and $\varepsilon_{\rm eff}''$ is the effective relative dielectric loss factor. The real part of ε is the dielectric constant and indicates how much electrical energy can be stored in a heated material. The imaginary part of ε is called the dielectric loss factor and determines the ability of the material to convert the MW energy into heat. Various mechanisms exist for this heat conversion, so that according to [293] the effective loss factor can be written as

$$\varepsilon_{\rm eff}'' = \varepsilon_{\rm d}''(\omega) + \varepsilon_{\rm e}''(\omega) + \varepsilon_{\rm a}'' + \varepsilon_{\rm s}'' + \frac{\sigma_{\rm e}}{\varepsilon_0\omega} \tag{6.2}$$

where d, e, a and s stand for dipolar, electronic, atomic and space charge. While the first four terms in Eq. (6.2) are associated with the different dielectric loss mechanisms, the last term describes the fraction that depends on the material conductivity σ.

The absorbed heat also depends on the penetration depth of the MW into the body, which is defined as the distance from the surface after which the power has dropped to $1/e$ from the surface value. While the MW penetration depth for metals is very small ("skin depth"), it takes the following form for non-metallic materials according to [294]:

$$D_{\rm P} = \omega^{-1} \cdot \left[\frac{1}{2}\mu_0\mu'\varepsilon_0\varepsilon' \left\{ \sqrt{1 + \left(\frac{\varepsilon''}{\varepsilon'}\right)^2} - 1 \right\} \right]^{-1/2} \tag{6.3}$$

For thin, non-magnetic layers, the absorbed power can be derived with the help of the Poynting vector and according to [293] results in

$$P = \omega\varepsilon_0\varepsilon_{\rm eff}'' E_{\rm rms}^2 \tag{6.4}$$
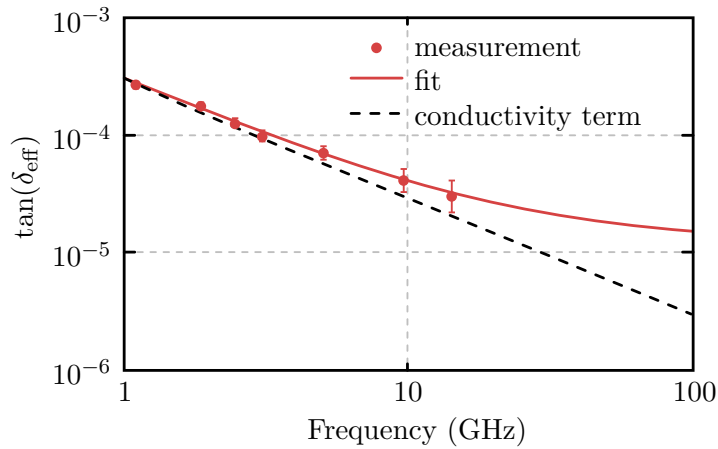
Figure 6.20 Frequency-dependent dielectric loss tangent for high-purity silicon with semi-insulating properties. The dashed line shows the proportion of the conduction losses to the total measured loss tangent. Adapted with permission of *AIP Publishing* from [295].

where E_{rms} is the root-mean-square value of the waves electric field intensity. The ratio of dielectric loss and dielectric constant has become established as another key figure, which is called electrical loss tangent $\tan(\delta_{eff}) = \varepsilon''_{eff}/\varepsilon'_r$ and indicates the efficiency with which materials convert microwaves into heat. The mechanism responsible for heat generation is generally based on the agitation of the orientation, position and motion of dipoles, free electrons, domain walls and electron spins by the electric and magnetic field components of the MW. Non-magnetic materials are only affected by the electric field component of the MW, so that mainly two loss mechanisms are responsible for the heating. Thus, dipolar losses dominate the heating in dielectric insulators and conduction losses dominate the heating in conductive and semiconductive materials such as silicon. Here, the free electrons are excited to move along the electric field component. Due to the conductive properties, the field is strongly damped and induces a high current. This in turn generates a magnetic field which, according to Lenz's rule, opposes its effect. The induced magnetic field leads to a Lorentz force on the moving electrons, so that the conduction electrons move in the opposite direction. The kinetic energy thus generated is constrained by inertial, elastic, frictional and molecular interaction forces, resulting in volumetric and uniform heating due to the motion and collisions. This mechanism is particularly important at lower frequencies, as the time for electron motion along the field decreases with increasing frequency.

Fig. 6.20 shows the total dielectric loss tangent for high-purity silicon with semi-insulating properties in the frequency range of $1 - 100\,\mathrm{GHz}$, adapted from [295]. It can be seen that with decreasing frequencies, the proportion of ε''_{eff} increases and thus the heat generation should also increase, leading to a generally lower luminescence at small MW frequencies, which was not observed in the measurements of this thesis. The theoretical course of $\tan(\delta_{eff})$ and thus of the heat generation is steady over a wide range and does not show any clear resonances. Accordingly, the observed sharp peaks in the PDMR spectra should not be caused by frequency-dependent temperature variations. Heating due to the current flow in the MW wire can also be excluded, since this is mainly determined by the ohmic resistance of the wire, which is independent of frequency. Admittedly, the previously mentioned, frequency-dependent skin effect leads to a reduction in the effective conductor cross-section and thus to an increase in the effective resistance, but this effect also runs steadily with

frequency and thus cannot explain any occuring resonances.

If both, the frequency-dependent heat evolution and a direct manipulation of the G center quantum states are not responsible for the changes of the PL intensity, different mechanisms must take effect. Thus, additional frequency-dependent and preferential recombination paths, induced by other defects in the sample, could reduce the number of free charge carriers, which in turn reduces the probability of radiative recombination in the G centers and therefore the PL intensity at certain frequencies.

6.5.2 Spin-dependent recombination centers in Si and Si/SiO$_2$ interfaces

SDR models

In 1972, Lepine [296] showed by measurements of photoconductivity on silicon that spin-dependent recombination (SDR) of charge carriers takes place and that this behavior is due to surface defects. He explained this phenomenon with a simple thermal polarization model based on Shockley-Read-Hall recombination, assuming that any free excess electron in the system can recombine at any time [297]. According to this model, the photoconductivity σ_{ph} is indirectly proportional to the recombination rate R of the equilibrium spin polarizations of conduction electrons (p_{e}) and recombination centers (P_{rec}). For $\Delta R \ll R$, the change in the recombination rate can be approximated by a Taylor expansion and yields

$$\frac{\Delta \sigma_{\mathrm{ph}}}{\sigma_{\mathrm{ph}}} = -\frac{\Delta R}{R} = p_{\mathrm{e}} \cdot P_{\mathrm{rec}} = -\frac{g^2 \mu_{\mathrm{B}}^2 B_0^2}{16 k_{\mathrm{B}}^2 T^2} \tag{6.5}$$

Accordingly, the recombination rate in an applied magnetic field of $B_0 = 300\,\mathrm{mT}$ at room temperature should be at most of the order 10^{-6} [297, 298]. However, experiments under these conditions have shown changes in the photoconductivity current in the order of $\Delta I_{\mathrm{ph}}/I_{\mathrm{ph}} \approx 10^{-4}$ [299, 300]. Eq. (6.5) is also independent of exchange or dipole coupling between electrons and holes and would depend quadratically on the ratio of magnetic field and temperature. After various attempts to figure out the experimental discrepancies, an explanation based on intermediate pairs of charge carriers was presented in 1978 with the Kaplan-Solomon-Mott (KSM) model [298], which could explain the SDR process and its properties such as the strength of the signal and the magnetic or temperature dependence. In this model, spin conservation is mainly responsible for the spin dependence of recombination, which is imposed by the weak spin-orbit coupling between neighboring spin pairs. In the case of charge carriers in shallow states, as they exist in silicon, the Coulomb interaction leads to a large overlap of bound pairs (excitons). According to [298], a thermal energy can separate the charge carriers from each other by a distance of up to $e^2/\kappa k_{\mathrm{B}}T$ without them becoming free. At this distance, the exchange interaction is small enough to change the angle between the electron and hole spin vectors by an RF field, thereby increasing the probability of recombination when the charge carriers return to the ground state of the pair. This general model can be well applied to different recombinations and materials, but still ignores phenomena such as strong interaction or triplet recombination, which were previously considered negligible. Consequently, further models were developed, which mostly used the KSM model as a basis and supplemented it with phenomena such as triplet recombination, spin-spin interactions (spin-exchange and spin-dipole coupling) and spin relaxation [301–305]. Accordingly, the time-independent spin Hamiltonian for a

coupled spin pair in a constant magnetic field B_0 is [306]:

$$H_0 = \underbrace{\mu_\text{B}\mathbf{S}_\text{A}\mathbf{g}_\text{A}\mathbf{B}_0 + \mu_\text{B}\mathbf{S}_\text{B}\mathbf{g}_\text{B}\mathbf{B}_0}_{\substack{\text{Zeeman}\\\text{interaction}}} + \underbrace{\mathbf{J}\hbar(\mathbf{S}^2 - 1)}_{\substack{\text{exchange}\\\text{interaction}}} - \underbrace{\mathbf{S}_\text{A}\mathbf{D}_\text{dip}\mathbf{S}_\text{B}}_{\substack{\text{dipolar}\\\text{interaction}}} + \underbrace{\sum_{i=A,B}\sum_{j}\mathbf{I}_\text{i}\mathbf{A}_\text{ij}\mathbf{S}_\text{i}}_{\substack{\text{hyperfine}\\\text{interaction}}} \tag{6.6}$$

The first two terms describe the Zeeman interaction of the electron spins $\mathbf{S}_\text{A}$ and $\mathbf{S}_\text{B}$ with the magnetic field B_0 via the anisotropic g-tensors $\mathbf{g}_\text{A}$ and $\mathbf{g}_\text{B}$. The third and fourth terms describe the exchange and dipole interactions of the electron spins with each other. These interactions are determined by electron-electron exchange $\mathbf{J}$ with $\mathbf{S} = \mathbf{S}_\text{A} + \mathbf{S}_\text{B}$ and the dipolar coupling constant $\mathbf{D}_\text{dip}$. The fifth term describes the hyperfine interaction of the i-th electron spin $\mathbf{S}_\text{i}$ with the j-th nuclear spin $\mathbf{I}_\text{j}$ via the anisotropic hyperfine tensor $\mathbf{A}_\text{ij}$. Current models that take into account the parameters just mentioned are based on the work of Boehme et el. [297, 307–309] which deals with the time-resolved measurement of spin-dependent recombination (TSR model). According to this model, two spin-dependent processes take place in silicon under the influence of a MW field, which lead to a change in the photocurrent: spin-dependent recombination (SDR) and spin-dependent hopping (SDH).
In general, the conductivity σ at electrically detected magnetic resonance (EDMR) measurements in silicon depends on the concentration n of electrons (e) and holes (h) and their mobilities μ:

$$\sigma = e(n_\text{e}\mu_\text{e} + n_\text{h}\mu_\text{h}) \tag{6.7}$$

In the SDR model, which is depicted in Fig. 6.21 (a), a photoexcited excess electron from the conduction or valence band is captured by a tail state (TS) near the respective band edges. Interfacial defects create singly occupied dangling bond states (DB), which are located energetically lower in the bandgap. According to the Pauli principle, a transition from TS to DB can only occur if the involved spins are antiparallel. A MW that is in resonance with one of the spins involved leads to a spin-flip and thus increases the transition probability of the spin pair, assuming that the spin is conserved during the transition. According to the Hartree-Fock model, the correlation energy ΔU increases in the doubly occupied state and allows the trapping of a hole from the valence band, which leads to a change in the photocurrent:

$$\Delta\sigma_\text{SDR} = e(\Delta n_\text{e}\mu_\text{e} + \Delta n_\text{h}\mu_\text{h}) \tag{6.8}$$

At low temperatures, a spin-dependent hopping transport between localized, paramagnetic states occurs, that is described in Fig. 6.21 (b). In this process, a single charge carrier hops to a singly occupied state. This hopping rate depends on the localization length and separation, as well as the energy difference between the localized states [310]. Furthermore, the conservation energy ΔU must be smaller than the width of the energy distribution function of the localized states, as it is the case for TS of interface defects. Since transitions between adjacent singly occupied states also depend on the spin orientation, a MW-induced spin-flip can increase the transition probability and thus the hopping rate, leading to an enhanced mobility and thus to a change in conductivity:

$$\Delta\sigma_\text{SDH} = e(n_\text{e}\Delta\mu_\text{e} + n_\text{h}\Delta\mu_\text{h}) \tag{6.9}$$

Despite the progress in modelling experimental results, the TSR model could not explain how individual lines in the EDMR spectrum arise or where the high signal intensities and current enhancement/quenching come from. For this purpose, a new model was developed
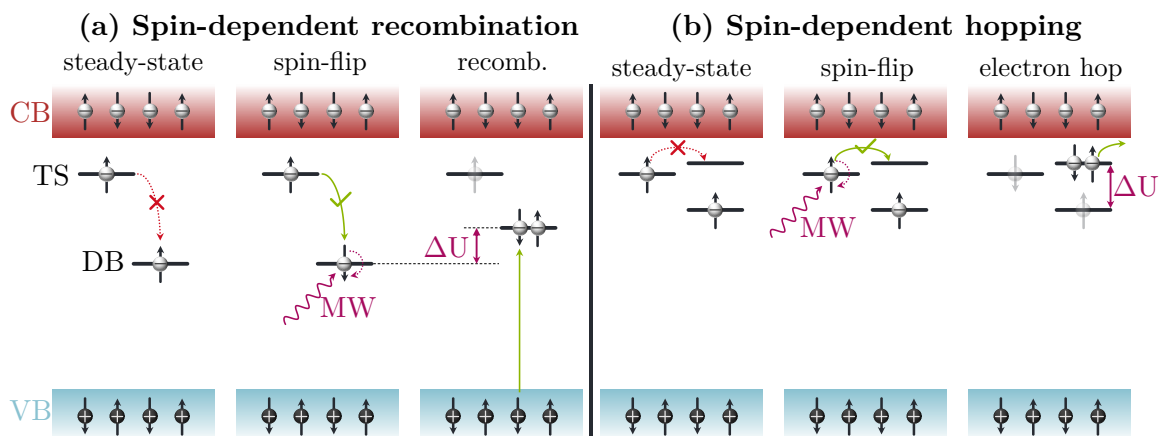
Figure 6.21 KSM model for spin-dependent processes according to [306, 311].
Microwave-induced spin-flips of electron spins in tail states (TS) or dangling bond states (DB) close to the band edges lead to an increased probability for allowed transitions that previously have been forbidden. **(a)** This either creates new recombination possibilities (SDR) or **(b)** increases the mobility of charge carriers (SDH), thus increasing the conductivity of the silicon. More information can be found in the main text and in [307, 309, 312]. Graphic adapted with permission of *Royal Society of Chemistry* from [306].

by Behrends [307], which supports the work of Boehme et al. and Vranch et al. [313, 314] and assumes a three-spin system in which an electron from the CB and a hole from the VB are trapped near a singly occupied defect state and form an exciton (defect-trapped excitons (DTE)), which subsequently interacts with another defect electron (bound exciton model (BEM)). An influence of excitonic effects on the recombination dynamics was already suspected in various low-temperature experiments [315, 316]. Such defects can be e.g. dangling bonds, P_b states occuring at Si/SiO$_2$ interfaces or G centers and should accordingly occur in large amounts in the sample studied here.

In Fig. 6.22 the three possible spin configurations are shown. If the exciton electron and hole are in a singlet state, i.e. with antiparallel spin (population N_S), they recombine almost instantaneously and independently of the defect electron. If, on the other hand, they are in a triplet state, i.e. with parallel spin, recombination is unlikely and depends on the spin of the defect electron. Then the cases are distinguished in which the spins of exciton-electron and defect electron are parallel (population N_{TP}, low recombination probability) or antiparallel (N_{TA}, high recombination probability) to each other. Furthermore, depending on the sample structure and the measurement parameters, intersystem crossings, i.e. transitions between singlet and triplet excitons, can occur. Since the populations N_{TP} and N_{TA} depend on the lifetime of the states, the state with the longest lifetime, i.e. trapped triplet excitons with parallel electron spin to the defect electron, dominate the equilibrium state. If the applied MW coincides the resonance frequency of the defect electron, its spin state changes so that the popultation N_{TA} and thus the recombination rate of the DTE increases. Since excitons are electrically neutral, their recombination does not directly lead to a change in the number of free charge carriers and thus to a change of the conductivity. During exciton recombination, however, energy is released, which is transferred to the defect electron via an Auger process, whereby it can be excited into the conduction band. This Auger recombination process has already been experimentally proven several times and, according to [317], is very efficient for bound excitons in silicon, therefore playing an important role
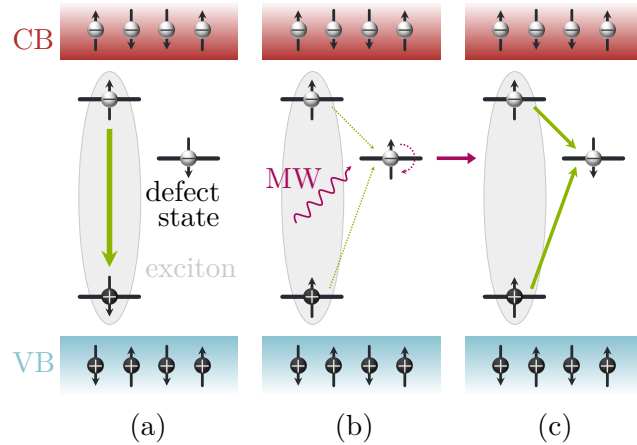
Figure 6.22 **Three possible configurations of the Bound Exciton Model according to [307]. (a)** Singlet exciton state with high recombination probability. **(b)** Triplet exciton state with an electron spin parallel to the defect electron spin state. A MW field flips the defect electron spin, resulting in a **(c)** higher antiparallel triplet population compared to the initial state and thus increasing the recombination rate.

in the measurements discussed here. Further information on spin-dependent recombination and hopping models can be found in [307, 309, 312].

SDR centers

The models just described explain the change in conductivity of a sample due to an applied electromagnetic wave and the dependence of the conductivity on the spin state of defect electrons. As on can see from Eq. (6.6) the observed resonances are related to the Zeeman effect and additional deviations from other interactions. The Zeeman effect explains the energy shift of a particle with angular momentum vector $\vec{j}$ and magnetic moment μ_j, which precedes in a magnetic field, by the formula

$$E_{\mathrm{mj}} = -\vec{\mu}_{\mathrm{j}}\vec{B} = -\mu_{\mathrm{j}}g_{\mathrm{j}}\mu_{\mathrm{B}}B \tag{6.10}$$

For a magnetic field oriented along the z-direction, the energy splitting of a previously degenerated state, that contains two electrons with spins $m_{\mathrm{s}} = \pm 1/2$, is given by [307]

$$\Delta E = g\mu_{\mathrm{B}}B_0 = \hbar\omega_{\mathrm{L}} \tag{6.11}$$

where g is the gyromagnetic factor ("g-factor") of the electron and ω_{L} is the Larmor frequency, which describes the spin precession around the magnetic field axis. The Larmor frequency is therefore direct proportional to the magnetic field and can be expressed via

$$\frac{\omega_{\mathrm{L}}}{2\pi B_0} = \frac{g_{\mathrm{e}}\mu_{\mathrm{B}}}{2\pi\hbar} = \frac{g_{\mathrm{e}}e}{4\pi m_{\mathrm{e}}} = \frac{\gamma}{2\pi} \approx 28\,\frac{\mathrm{MHz}}{\mathrm{mT}} \tag{6.12}$$

where $g_{\mathrm{e}} \approx 2.0023$ denotes the g-factor of the free electron and m_{e} and e denote its mass and charge, respectively [318]. While usually in EPR spectra the frequency is fixed and the magnetic field strength is varied, in the experiments of the present work a fixed magnetic field was used and the frequency was varied randomly. The observed resonances occur when the MW is absorbed, i.e. when $\omega = \omega_{\mathrm{L}}$ holds. Since the measured resonances correspond to

energy shifts according to Eq. (6.11), each resonance represents a deviation from the model of the free electron that is represented by the g-factor, which thus serves as a fingerprint of the investigated system and its defects. In silicon, and especially at interfaces such as between Si and SiO_2, a large number of such defects arise, which can lead to abrupt increases in the conductivity under resonance. These defects are also dependent on various properties such as magnetic field or crystal structure and thus generate a variety of different resonances themselves. To get an overview of the influences and defects, results from other works are presented below to support my discussion. The corresponding sources are referred to separately in each case. These measurements are based on the detection of changes in conductivity by SDR-EPR or EDMR, for which professional EPR spectrometers were used in both cases, unless otherwise mentioned.

Si-SL1 centers are spin-triplet states formed by photoexcitation of oxygen-vacancy centers ("A centers") with orthorhombic symmetry in silicon (Fig. 6.23 (a)). These defects occur in high concentrations at surfaces and interfaces, due to the natural content of oxygen in silicon and the required vacancies in these environments, and accordingly form clear signals in SDR-EPR measurements. In Fig. 6.23 (b) typical spectra, taken from [319], are shown for two different magnetic field orientations obtained at a fixed MW frequency of $\omega = 9.05$ GHz with power $P_{MW} = 200$ mW (≈ 23 dBm). In the upper spectrum, with the magnetic field aligned parallel to the $\langle 110 \rangle$ axis, four strong resonances can be seen, which are caused by the different EPR transitions and in dependence on the orientation of the O-V defect relative to the magnetic field [320, 321]. Each resonance is accompanied by

(a)　　　　　　　　　　　　　　　(b)
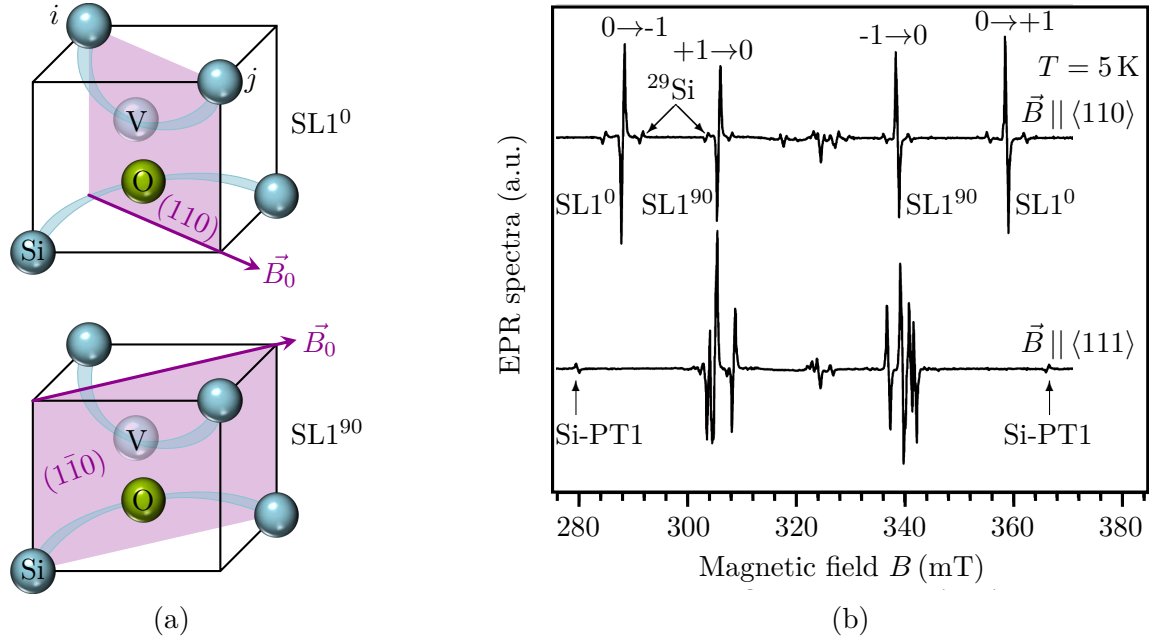
Figure 6.23　Si-SL1 center at different orientations. (a) The Si-SL1 signal originates from an excited triplet state of the A center (O-V center) in silicon (adapted from [322]). **(b)** EPR spectra taken from [319]. MW frequency was fixed at $\omega = 9.05$ GHz with a MW power of $P_{MW} = 200$ mW (≈ 23 dBm). Depending on the orientation of the magnetic field relative to the defect, different transitions and their HFS satellites are clearly visible [320, 323]. Graphics adapted with kind permission of *American Physical Society*.
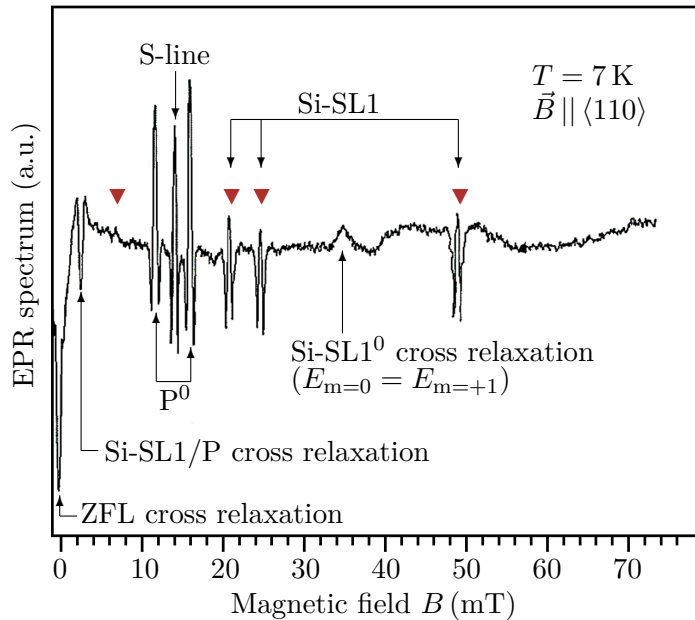
Figure 6.24 Si-SL1 spectrum at low magnetic fields, taken with permission of *Elsevier* from [324]. This EDMR measurement was performed without usage of an EPR spectrometer. Ohmic contacts were fabricated on a FZ-Si wafer that contained a phosphorous doping. A microwave frequency of $\omega = 400\,\text{MHz}$ was applied by a coil wrapped around the sample. Several Si-SL1 lines from the oxygen-vacancy center appear together with surface recombination centers (S-line), phosphorous related centers (P^0) and cross relaxation lines. Red triangles indicate the corresponding calculated Si-SL1 line positions [325].

smaller satellites caused by a strong hyperfine interaction of the $S = 1$ triplet spin with the nuclear spin $I = 1/2$ of the ^{29}Si nuclei at position i and j. The weak lines in the region of $320 - 330\,\text{mT}$ are also related to the A center and other oxygen-associated centers [323]. The different signs of the transitions 0→-1 and +1→0 versus -1→0 and 0→+1 are due to a non-equilibrium distribution of populations and opposite electron spin polarizations [319]. The lower spectrum shows the same measurement but under a magnetic field alignment parallel to the $\langle 111 \rangle$ axis. As a result, the EPR lines cluster at magnetic fields of about $305\,\text{mT}$ and $340\,\text{mT}$ and new lines (Si-PT1) become visible. Fig. 6.24 shows a spectrum of Si-SL1 from [324] recorded at a MW frequency of $\omega = 400\,\text{MHz}$ and low magnetic fields using an EDMR setup without an EPR spectrometer. A FZ-Si wafer, which was doped with phosphorus, was irradiated with γ-rays and provided with ohmic contacts. The variable magnetic field was parallel to the $\langle 110 \rangle$ axis and the MW was irradiated through a coil which was wrapped around the sample. Photoexcited carriers were generated by a 100 W halogen lamp and the sample was cooled below $20\,\text{K}$. Thus, this setup is similar to the one used in this work. However, the S-line shown in Fig. 6.24 arises from surface recombination centers and the lines marked with P^0 arise from spin-dependent electron transfer between neutral phosphor donor atoms and the surface paramagnetic centers [324, 325]. Even at low magnetic fields, the Si-SL1 lines are present and shifted by the changed magnetic field orientation. Considering the magnetic field-dependent measurement in Sec. 6.3.6, one reason for the missing resonance shift could be that the magnetic field alignment was chosen unfortunate, several resonance lines coincide and thus a possible shift is more difficult to detect. The red arrows mark the calculated line positions for a magnetic field $\vec{B} \,||\, \langle 110 \rangle$

with the spin Hamiltonian parameters determined in [323]. The zero-field line (ZFL) at $B = 0\,\text{mT}$ originates from cross relaxation among degenerate levels of single paramagnetic centers with three or more magnetic sublevels. As this applies for phosphorous and Si-SL1 centers, both contribute to the ZFL signal. Cross relaxation between those centers is also the explanation for the line at $\approx 2.5\,\text{mT}$. The weak cross relaxation line at $B \approx 35\,\text{mT}$, that originates from a level anticrossing of the magnetic sublevels with spin projections $m_S = +1$ and $m_S = 0$, does not depend on the resonance frequency and is even observable without application of a resonance field [324]. Such behavior could also be the cause for the missing shift of the resonance frequency in Sec. 6.3.6 with applied magnetic field. However, the comparison of the graphs from the literature with the measurements made in this work, does not allow any clear conclusions about the origin of the signals, since both, the sample structure and experimental setup were different and thus there are too many free parameters that can influence the measurement. Accordingly, it cannot be conclusively clarified which SDR centers generate which lines in the spectrum, so that no conclusions can be drawn about the magnetic sublevel and thus an actual connection to possible level anticrossing.

P_b centers are formed at oxidized surfaces or interfaces between Si and SiO_2. The variations in the crystal structure at the interface leads to silicon dangling bonds as shown in Fig. 6.25, which form different SDR centers depending on the defect orientation within the lattice and thus lead to individual resonances in SDR-EPR or EDMR spectra. According to [326,327], mainly P_b centers are formed at (111) interfaces whereas at (100) interfaces P_{b0} and P_{b1} centers arise in high concentrations. With good agreement between experimental data and theoretical models, it is now widely accepted that these varieties originate from chemically identical interfacial $\cdot Si \equiv Si_3$ defects without an oxygen atom in the Si back bonds [328–331]. Recently, two more DB defects have been discovered at the interface between Si and naturally grown SiO_2, namely P_m (spin $S = 1/2$) and KU1 (spin $S = 1$) [332,326], which are thought to arise from interactions of two adjacent DB forming bonding and antibonding molecular orbitals. Both defects thus possess C_{2v} symmetry with the KU1 line being an excited triplet state of the neutral P_m center. In Fig. 6.26, SDR-EPR spectra of P_b related SDR centers measured at low temperatures and a fixed excitation frequency of $\omega = 9\,\text{GHz}$ are shown. Fig. 6.26 (a) and (b) show the dependence of the P_b lines on the sample composition measured at a magnetic field excitations along the $\vec{B} \,||\, \langle 111 \rangle$ direction and in the range of $321 - 326\,\text{mT}$. According to these results, reducing the ^{29}Si content
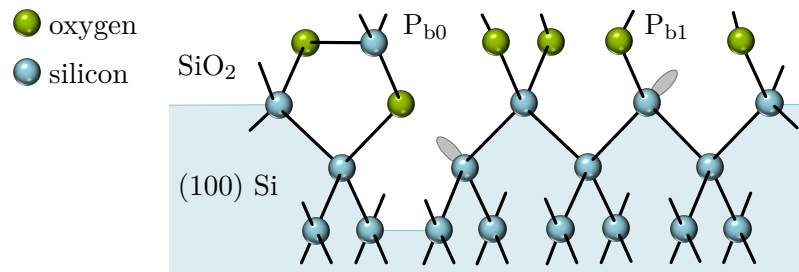
Figure 6.25 (100) Si/SiO$_2$ interface defects P_{b0} and P_{b1} according to [327]. EPR investigations suggest a correlation between P_b centers and midgap interface state density, indicating the interface position. Graphic adapted with permission of *AIP Publishing* from [329].
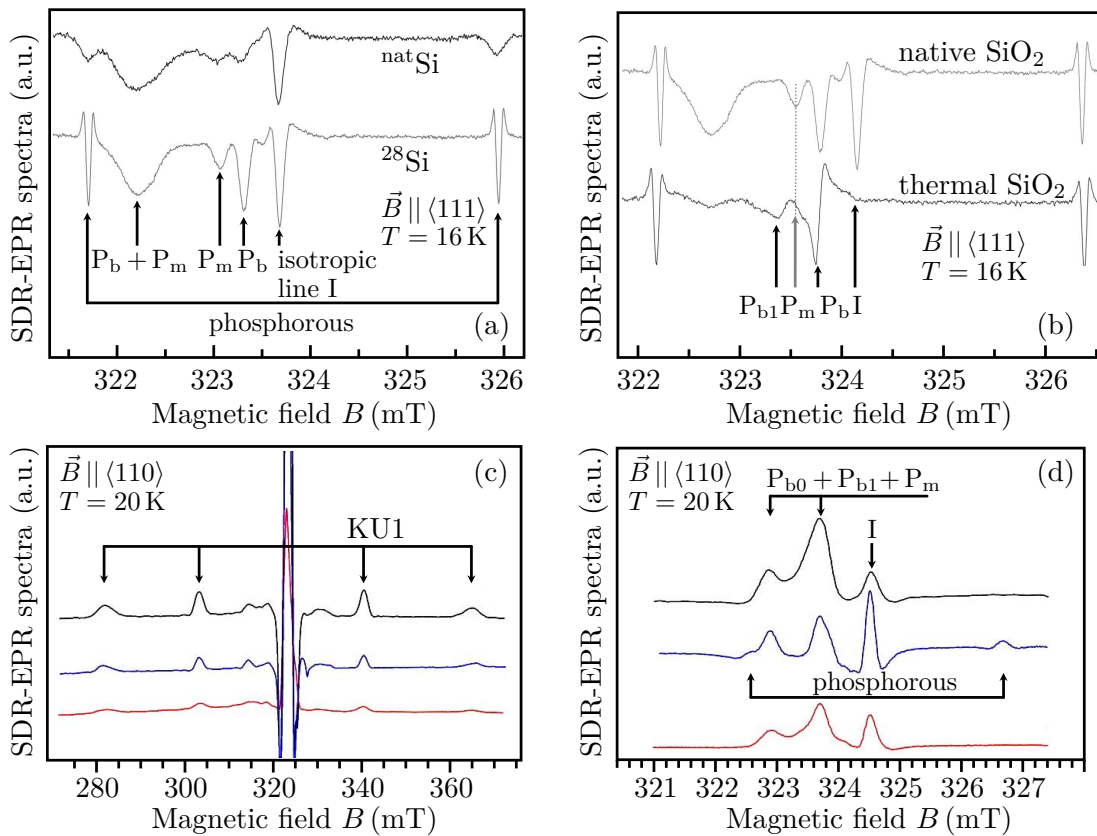
Figure 6.26 SDR-EPR spectra of Si/SiO₂ interface defects. (a) and **(b)** were adapted with permission of *AIP Publishing* from [332], **(c)** and **(d)** from [326]. All spectra were measured with an X-band (9 GHz) ESR spectrometer (JEOL JES-RE3X). Different silicon samples were placed inside a cylindrical TE011-mode cavity that was implemented in a helium-gas-flow cryostat (Oxford Instruments ESR-900). Photo carriers were excited by illumination with a 100 W halogen lamp. MW-induced changes of the photoconductivity were observed under magnetic resonance conditions when the spin-dependent recombination rate was enhanced. Sample properties like different silicon and oxide compositions, interfaces or purity lead to a large variety of resonant states. Negative signs in (a) and (b) are caused by the indirect measurement of the signal (dropping of the Q-factor of the cavity under resonant conditions). See main text and cited works for more details.

in the sample from its natural abundance of 4.67 % to 0.017 % by enrichment with ²⁸Si, leads to an enhancement of the P_b and P_m as well as phosphorus dopant lines. Similarly, compared to thermally grown oxide layers, a naturally grown surface oxide layer increases the concentration of P_b related centers and the isotropic line I that is created by a shallow thermal donor (STD) with cubic symmetry. Fig. 6.26 (c) shows similar measurements under a changed magnetic field orientation of $\vec{B} \,||\, \langle 110 \rangle$ and a broader spectral range. The intense signals around 324 mT are additionally shown enlarged in (d). The three curves show the influence of sample purity and doping on the formation of the KU1 and P_b centers (black: n-type (001) FZ-Si with 5000 Ω cm, blue: n-type (001) Cz-Si with 10 Ω cm, red: p-type (001) Cz-Si with 10 Ω cm).

It can be seen that high purity leads to more pronounced DB centers, while the STD line and the phosphorus-dopand line appear more strongly at low purity. The different signs of the peaks in (a) and (b) versus (c) and (d) can be explained by the different measuring

methods. While in Fig. 6.26 (a) and (b) the Q-factor of the TE_{011}-mode cavity decreases in the resonance case, because the electric field component of the MW is absorbed by the photoexcited carriers, in (c) and (d) the photoconductivity was measured directly, which increases in the resonance case. Since in the present work SOI samples were used, which contain layers with natural Si and high-purity ^{28}Si, as well as naturally grown surface oxide and thermally grown oxide in the insulator layer, this versatile combination could also be reflected in the spectrum and contribute to corresponding signals. Furthermore, the implantation of G centers leads to the formation of additional shallow states, which interact with the tail states and dangling bonds at the interfaces and surfaces of the sample and can thus generate a large variety of new resonances.

Carbon-related Si-PT and Si-WL centers   Due to the natural carbon content in silicon crystals, various carbon-related defects develop after high-energy irradiation, which due to unbound electrons develop dangling bonds and thus molecular orbitals, which are also EPR sensitive and can be detected in SDR experiments. In [333–335], several SDR-EPR lines were presented with Si-PT1, Si-PT4, Si-WL2, Si-WL4 and Si-KU4, which originate from different combinations and orientations of carbon atoms with silicon atoms and vacancies (Fig. 6.27). The Si-PT1 EPR signal is said to arise from the excited $S = 1$ spin state of the $(C_s\text{-}Si_i\text{-}C_s)^0$ center, which is the G center. By isochronal thermal annealing at temperatures of $200 - 300\,°C$, the intensity of Si-PT1 decreases and a new line (Si-PT4, not shown) emerges, which could be attributed to a complex of two carbon atoms with a divacancy based on symmetry studies [333]. The Si-WL2 and Si-WL4 centers arise from defects consisting of two additional C_i atoms localized to tetrahedral interstitial positions along the $\langle 111 \rangle$ axis and close to the $C_s\text{-}Si_i\text{-}C_s$, as inferred from the magnetic field angular dependence of the spectra and the values of fine structure splitting [334]. Furthermore, another SDR-EPR spectrum was discovered with Si-KU4, which exhibits orthorhombic symmetry (C_{2v}) and for whose origin a model of two equivalent C_s atoms was assumed, between which a vacancy is located $(C_s\text{-}V\text{-}C_s)$ [335].   Accordingly, carbon implantation
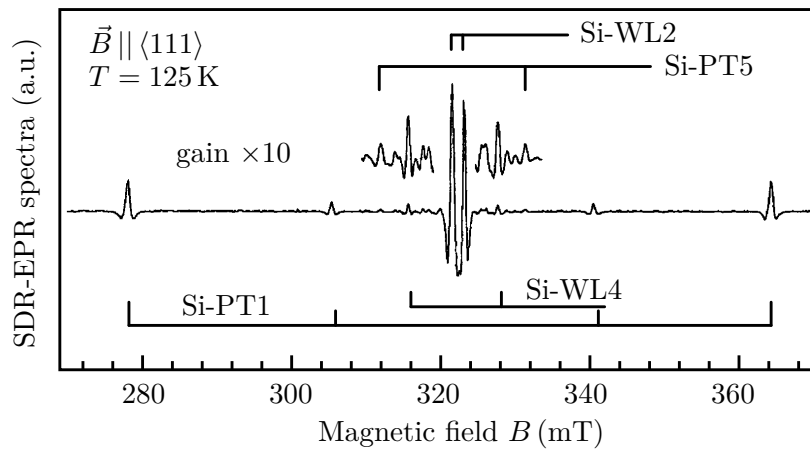
Figure 6.27   Carbon-related SDR centers in silicon. These spectra are produced after high-energy irradiation of silicon. From symmetry considerations and fine structure parameters of the SDR-EPR measurements, it can be concluded that these signals arise from di-carbon defects such as the G center and other carbon-related defects. Plot taken with permission of *Springer Nature* from [333].

and the resulting higher ^{12}C concentration can create a variety of carbon-based defects that generate additional resonances in the investigated spectral region and thus indirectly influence the measurement of G centers or superimpose the signal of G centers through additional recombination paths.

6.6 Conclusion

After discussing the various possible influences from other SDR centers on the MW resonances, a clearer picture emerges for the spectrum that arises. As it was shown in Sec. 6.5.1, the resonances cannot be explained by thermal influences, but must arise from spin-dependent excitations of crystal defects. The large number of possible defects, the dependence on parameters such as magnetic field orientation, magnetic field strength, crystal orientation and temperature, as well as the limitation of the one-dimensional, only roughly measurable magnetic field, make an exact assignment of the spectral lines difficult. The layer structure of the investigated sample complicates the goal of measuring spin-dependent recombination of G centers by PDMR and ODMR. For this type of experiment, the choice of SOI chips is disadvantageous, since dangling bonds form at all interfaces (bulk Si - thermal SiO$_2$ - natural Si - ^{28}Si - natural SiO$_2$), which can form different resonances in the spectrum due to the different crystalline structures. Furthermore, it can be assumed that due to the carbon implantation and hydrogen irradiation, a large number of different defects (e.g. A, C, G centers) are located in the sample, which additionally complicate the assignment of the individual spectral features. The spectrum shown in Fig. 6.24, which was recorded at $\omega = 400\,\mathrm{MHz}$ and magnetic flux densities of $0 - 70\,\mathrm{mT}$ and therefore under similar conditions as in this work, shows similar resonances as the measurements from Sec. 6.3, suggesting that the Si-SL1 spectra measured there, caused by A centers, are also responsible for some of the peaks measured in the present work. The P^0 lines, on the other hand, which are caused by phosphorus defects and accompany the S line (surface defects), should not play a role in this work, since the samples used here, in contrast to those from [324], were not phosphorus-doped and the natural phosphorus content in silicon is sufficiently low.

As described in Sec. 6.5.2, the signals in the spectra arise from a microwave-dependent increase in free charge carriers (electrons) due to spin-dependent recombination processes. The electrons taking these recombination paths are thus missing for the radiative recombination of the G centers, which explains the correlation between positive or negative changes in the PDMR current, depending on the polarity of the electrodes, and a decreasing ODMR signal. The more pronounced correlation of the ODMR and PDMR signals in the manual measurements from Sec. 6.2 is due to the over two orders of magnitude higher PDMR current, which can be explained by the higher MW power (with amplifier) and applied voltage ($U = -9\,\mathrm{V}$). This should also be the reason for the broader linewidth of the signals during the manual measurements, which extend over several hundred MHz. The increased process parameters can potentially excite more defects, whose signals overlap and thus broaden the spectrum. The temperature-dependent line broadening, which is shown in Fig. 6.15, can also be explained assuming defect states coming from dangling bonds. The increase in temperature leads to an expansion of the crystal, which increases the distances between the atomic cores. At the same time, the number and the energy of the phonons is increased (Bose-Einstein distribution), since the influence of optical phonons is enhanced compared to low temperatures, where only the acoustic phonons have to be considered. This leads to fluctuations in the distribution of the defect states and thus to a line broadening of the mea-

sured currents. The measured, asymmetric line shape of the peaks is explained in [336] for Si-SL1 centers by dynamic nuclear polarization (DNP), which occurs under MW saturation of the EPR lines of hyperfine interactions. The cause is thought to be the saturation of forbidden flip-flop and flip-flip transitions between electrons and more distant lattice nuclear spins ("solid-effect"), which affects the hyperfine coupling. The resonance frequencies of the signals investigated in the present work seem to be independent of temperature, since the maxima of the resonance frequency at $T = 40\,\text{K}$ and at room temperature are completely identical. If the signals arise from defects in the bandgap of silicon, they should theoretically follow Varshni's law, the course of which has already been discussed in Sec. 4.2.1. Further investigations are therefore necessary to verify the actual reasons of this.

The congruent course of the normalized spectra at excitation with different energies (i.e. $532\,\text{nm}$ and $632\,\text{nm}$) in Fig. 6.17 thus also fits into the picture, since the tail states of the dangling bonds are close to the conduction band edge of the already narrow bandgap and thus only little energy is needed to lift the spin-dependent charge carriers into the conduction band.

The investigation of the magnetic field dependence of the spectra shows no differences in the position and width of the peaks for the measurement with ($B = 20\,\text{mT}$) or without ($B = 0\,\text{mT}$) applied permanent magnetic field. This is in contradiction with the well-known magnetic field-dependent frequency shift from Eq. (6.12) and the presented data from Fig. 6.23 and Fig. 6.24, which show the same Si-SL1 resonances at different magnetic fields, i.e. shifted frequencies. However, as can be seen in Fig. 6.23, the resonance frequency of the individual lines is strongly dependent on the angle between the crystal axis and the magnetic field. Since the setup used here only allows the magnetic field to be oriented parallel to the (001) crystal direction due to spatial constraints, other magnetic field directions could not be investigated. Consequently, the choice of magnetic field orientations could have led to the fact that, similar to the lower graph of Fig. 6.23, magnetic field-dependent resonance lines coincide and thus the measurable splitting is significantly lower. The spatial restrictions in the cryostat are also responsible for the fact that no larger permanent magnets could be used, so that the magnetic field strength turned out to be relatively low with $B = 20\,\text{mT}$, which further downgrades the measurement of the magnetic field dependence. Thus, no further conclusions about the origin of the resonances can be drawn from the magnetic field dependence.

In summary for this chapter, it can be said that the experimental setup presented here seems suitable for the optical and electrical manipulation and readout of quantum states in general. For the measurement of specific defects, however, some optimizations have to be carried out. For measurements at low temperatures, an enlarged cryostat, as used in Ch. 5 should be chosen that allows the installation of a variable electromagnet. Further ODMR/PDMR measurements should start with untreated, high-purity bulk Si to detect possible interfering signals coming from pure silicon or electronical effects. Subsequently, it would be advisable to examine a sample containing a high concentration of G centers, by which newly appearing signals can be evaluated. SOI material should be completely avoided until then, since the different interfaces create additional resonances, that overlap the G center signals in the spectrum. Only after the signals of the G centers have been determined at defined frequencies and certain magnetic fields, new samples made of SOI material should be prepared to increase the optical yield. Furthermore, the equipment can be optimized. A MW amplifier suitable for these frequency ranges would allow a more variable and stronger excitation and a high-precision stage would prevent the sample from drifting and thus allow longer measurements with less error. A tunable IR laser would also

allow sub-bandgap excitation and thus a more targeted excitation of the G centers. Such a modification of the existing setup should enable the specific manipulation and selection of defect centers in general and of G centers in particular and could therefore indicate an important step for the development of silicon-based quantum technologies.

Scientific gain

In this final chapter, the setup of a system for the simultaneous measurement of ODMR and PDMR signals in the IR range and at low temperatures was described. The setup was tested on a SOI sample with a high-purity, 60 nm thick ^{28}Si layer. It was shown that ODMR and PDMR resonances occur on this sample at the same frequencies. An investigation of these resonances made it clear that they were not due to the implanted G centers. The exact origin of the resonances could not be proven, but the measurements indicate that the resonances are due to other defects, some of which form at the interfaces between Si and SiO$_2$. However, the functionality of the setup was demonstrated and ideas for optimizing future measurements on G centers were discussed.

The tasks of this work were to optimize the fabrication of G centers in silicon, to verify the already known optoelectronic properties of these light-emitting defects and to add new insights by modern measurement methods. Following the progress in the field of solid-state quantum technology, especially by NV centers in diamond, the suitability of G centers for applications in silicon-based photonic microchips on which information is processed by light-matter interaction and subsequently transmitted over long distances via photonic structures should be established. In this work, it has been shown that low-energy and spatially-selective ion implantation enables the fabrication of isolated G centers, which can be used as single-photon sources and are thus suitable as light-matter interfaces for quantum information processing. This makes ion implantation a quantum enabling technology (QET) for the development of new quantum technologies based on different crystal systems, covering a wide range of applications.

The preparation of ensembles and individual G centers allowed the investigation and evaluation of diverse properties of these defects that were previously unknown. In contrast to the results of [38], the plot of PL intensity to implanted proton fluence shown in Fig. 4.3 does not show a maximum in the range from $1 \times 10^{13}\,\mathrm{cm}^{-2}$ to $1 \times 10^{15}\,\mathrm{cm}^{-2}$, but increases steadily. However, the reason for this is most likely due to the different sample structures, since in the present work SOI material with 220 nm silicon on 1 μm silicon dioxide was processed, while in [38] n-type silicon wafers were used. The doped silicon as well as the SOI structure might have an influence on the formation of G center ensembles and thus on the concentration and the PL saturation behavior. The PLE spectrum Fig. 4.4 showed that excitation of G centers with $\lambda = 532\,\mathrm{nm}$ or $\lambda = 632\,\mathrm{nm}$ changed the PL intensity only slightly. Saturation curves were recorded for ensemble as well as individual G centers, which produced significantly different saturation laser powers. However, this was caused by the different saturation models used. The ensemble model ignored the different orientations of the G centers, which were identified subsequently on individual centers. (Fig. 5.6). The temperature-dependent study of the spectral properties of the G center ensemble provided new insights into the suitability of these defects for quantum applications, especially in comparison with other systems. Thus, the excited state lifetime of G centers was measured for the first time. The ascertained value was stable at $\tau_{\mathrm{ens}} = 5.9 \pm 0.2\,\mathrm{ns}$ in the ensembles studied here at temperatures below 50 K. The lifetime increases to $\tau_{\mathrm{sin}} = 35.8 \pm 0.2\,\mathrm{ns}$ at $T = 10\,\mathrm{K}$ in the case of single, isolated G centers. The difference here is caused by changing interactions and dynamics due to different charge states and defect orientations in the ensemble, i.e. at increased G center concentration. The longer excited-state lifetime of both individual and ensembles of G centers compared to that of NV centers ($\tau_{\mathrm{sin}} = 12\,\mathrm{ns}$ and $\tau_{\mathrm{ens}} = 4\,\mathrm{ns}$ [235, 275] at room temperature is disadvantageous for the utilization in quantum applications. However, as shown in Sec. 4.2.4 the radiative recombination rate of G centers

seems to be independent of the operating temperature, as expected for zero-dimensional systems [50]. Therefore, effects such as the decreasing PL lifetime and intensity at increasing temperatures can be attributed solely to the influence of non-radiative recombination. The effect of the proton fluence and thus the G center density on the ensemble lifetime could not be accurately verified because the power of the pulsed laser was not sufficient for this and the statistical error was too large. In addition to the numerous measurements on the ensemble, a theoretical model describing the formation of the G center PL spectrum was developed in Sec. 4.3.3, which assigns the peaks of the phonon sideband to the different phonon modes in order to thereby better understand the influence of phonon-assisted recombination.

In Ch. 5 the first ever measured results on single, isolated G centers were presented. During the review process of this paper [39] we became aware of another work announcing the measurement of single G centers that was published by Hollenbach et al. [337]. The measurements performed there confirm our findings of the long-term stability of the PL intensity, the statistical distribution of the ZPL energy and roughly the value of the Debye-Waller factor. Furthermore, the 3-level system for G centers, previously confirmed by us and consisting of ground, excited, and metastable triplet state, was also used to explain the behavior of their autocorrelation measurement. Their $g_2(\tau)$ measurements coincides with the results of our autocorrelation study, which, however, were furthermore supported by additional measurements at different laser powers. Complementary to our work, a model for a scalable quantum photonic architecture was proposed by them. On the other hand, our publication additionally included statistics on the polarization or alignments of G centers in the silicon crystal, extensive statistical measurements on the lifetime of individual G centers, and a model for estimating quantum efficiency. Thus, both works on single, isolated G centers complement and confirm each other and, due to their closeness in time and content, reflect the currentness and thus also the great potential of the research of these quantum centers.

In Ch. 6 the construction of an experimental setup for electronic and optical manipulation as well as readout of quantum states, especially of G centers, was described in detail and first measurements were demonstrated. This setup was designed similarly to the ODMR and PDMR spectrometers, which have already been used for NV centers in diamond or SiV centers in silicon carbide [40, 291, 42, 338, 339]. The process parameters for measuring G centers or carbon-based defects in silicon were chosen based on different ODMR and EPR measurements from the past [37, 34, 286, 340–344]. As it turned out later, the electronic components are very similar to those used in SDR-EPR and EDMR experiments and thus also allow the measurement of spin-dependent recombination EPR of shallow states in silicon, which is described e.g. in [306, 308, 309]. The newly developed experimental setup made it possible to irradiate a SOI chip, that was previously implanted with a high concentration of G centers, with laser light and microwaves at low temperatures and under the effect of a static magnetic field. This enabled the optical and electronical detection of spin resonances from the sample and thus the recording of the spectra shown in Sec. 6.2 - 6.4. These measurements indicated a manipulation of the G center quantum system due to the controlled variation of their ZPL intensity. However, exclusive PDMR measurements showed that the detected resonances even occur when no G centers were directly excited per laser. Consequently, different mechanisms were discussed that are independent of G centers, but could still influence their luminescence. Considering the sample structure and experimental setup, as well as the line shape and frequency of the measured resonances, the most likely explanation is that the detected signals arise from a large number of SDR

centers forming at the various interfaces and defects in the SOI sample. Accordingly, the experimental setup is basically suitable for the detection and manipulation of quantum centers. However, in order to optimize the setup for G centers, further extensive studies need to be realized (see Sec. 6.6), through which the numerous other influences can be better understood. By this, the controlled selection of G centers in the spectrum will be possible and thus enabling further investigations on the spin properties of these quantum centers.

Since the 1960s, defects in silicon have been studied both electronically and optically. However, while at that time they were considered disruptive because they could interfere with nascent microelectronics, their potential for novel technologies gradually became apparent. Accordingly, a decade-long development took place during which many different radiative defects were structurally identified. With the first proposal for a spin qubit quantum computer by Loss and DiVincenzo in 1997 [219] and the silicon-based quantum computer proposed by Kane in 1998 [221], the study and development of defect centers in semiconductor materials received a strong new impetus, leading to a technological revolution. These defects, most notably the NV center in diamond, offer completely novel possibilities in terms of sensing, computing and communication, which can significantly reform and improve our lives through the laws of quantum mechanics. The increasing number of new publications, projects and funding on this topic shows how great the potential and how important this development will be for our future. Radiative defects in silicon could play a crucial role in this process, as they offer a scalable and inexpensive manufacturing due to the compatibility with existing production chains. Moreover, some of these defects possess properties that make them ideal for photonic and quantum applications [345]. Current investigations within the project aim at the optimization of photonic structures for the generation of lasing directly in silicon [44], thus allowing on-chip excitation and measurement of the quantum centers. Also, new ways for deterministic generation of G centers by laser annealing are currently under development. Moreover, their use as single-photon sources in the IR region, as demonstrated in this work, allows low-loss transport of quantum information over fiber optic cables. Thus, G centers provide the prerequisites for the construction of a quantum technological network and may therefore be a crucial factor for the upcoming second great quantum revolution.

Bibliography

[1] G. E. Moore. **Cramming more components onto integrated circuits**, reprinted from electronics, volume 38, number 8, april 19, 1965, pp.114 ff. *IEEE Solid-State Circuits Society Newsletter*, 11(3):33–35, sep 2006. https://doi.org/10.1109/n-ssc.2006.4785860.

[2] M. Haurylau, S. M. Weiss, and P. M. Fauchet. **Dynamically tunable 1D and 2D photonic bandgap structures for optical interconnect applications**. In Philippe M. Fauchet and Paul V. Braun, editors, *Tuning the Optical Response of Photonic Bandgap Structures*. SPIE, oct 2004. https://doi.org/10.1117/12.561114.

[3] Wikipedia article "Moore's law" from 19.08.2021. https://en.wikipedia.org/wiki/Moore%27s_law.

[4] Wikipedia article "List of semiconductor scale examples" from 19.08.2021. https://en.wikipedia.org/wiki/List_of_semiconductor_scale_examples.

[5] F. Priolo, T. Gregorkiewicz, M. Galli, and T. F. Krauss. **Silicon nanostructures for photonics and photovoltaics**. *Nature Nanotechnology*, 9(1):19–32, jan 2014. https://doi.org/10.1038/nnano.2013.271.

[6] J. Leuthold, C. Koos, and W. Freude. **Nonlinear silicon photonics**. *Nature Photonics*, 4(8):535–544, jul 2010. https://doi.org/10.1038/nphoton.2010.185.

[7] B. Jalali, S. Fathpour, and K. Tsia. **Green Silicon Photonics**. *Optics and Photonics News*, 20(6):18, jun 2009. https://doi.org/10.1364/OPN.20.6.000018.

[8] Homepage "FiberLabs Inc." from 19.08.2021. https://www.fiberlabs.com/glossary/about-optical-communication-band/.

[9] H. Kagermann, F. Süssenguth, J. Körner, and A. Liepold. **The Innovation Potential of Second-generation Quantum Technologies**. Acatech IMPULS, 2020. https://www.acatech.de/publikation/innovationspotenziale-der-quantentechnologien/.

[10] F. Arute, K. Arya, R. Babbush, D. Bacon, J. C. Bardin, R. Barends, R. Biswas, S. Boixo, F. G. S. L. Brandao, D. A. Buell, B. Burkett, Y. Chen, Z. Chen, B. Chiaro, R. Collins, W. Courtney, A. Dunsworth, E. Farhi, B. Foxen, A. Fowler, C. Gidney, M. Giustina, R. Graff, K. Guerin, S. Habegger, M. P. Harrigan, M. J. Hartmann, A. Ho, M. Hoffmann, T. Huang, T. S. Humble, S. V. Isakov, E. Jeffrey, Z. Jiang, D. Kafri, K. Kechedzhi, J. Kelly, P. V. Klimov, S. Knysh, A. Korotkov,

F. Kostritsa, D. Landhuis, M. Lindmark, E. Lucero, D. Lyakh, S. Mandrà, J. R. McClean, M. McEwen, A. Megrant, X. Mi, K. Michielsen, M. Mohseni, J. Mutus, O. Naaman, M. Neeley, C. Neill, M. Yuezhen Niu, E. Ostby, A. Petukhov, J. C. Platt, C. Quintana, E. G. Rieffel, P. Roushan, N. C. Rubin, D. Sank, K. J. Satzinger, V. Smelyanskiy, K. J. Sung, M. D. Trevithick, A. Vainsencher, B. Villalonga, T. White, Z. J. Yao, P. Yeh, A. Zalcman, H. Neven, and J. M. Martinis. **Quantum supremacy using a programmable superconducting processor**. *Nature*, 574(7779):505–510, oct 2019. https://doi.org/10.1038/s41586-019-1666-5.

[11] P. Kok, W. J. Munro, K. Nemoto, T. C. Ralph, J. P. Dowling, and G. J. Milburn. **Linear optical quantum computing with photonic qubits**. *Reviews of Modern Physics*, 79(1):135–174, jan 2007. https://doi.org/10.1103/RevModPhys.79.135.

[12] D. Castelvecchi. **Welcome anyons! Physicists find best evidence yet for long-sought 2D structures**. *Nature*, 583(7815):176–177, jul 2020. https://doi.org/10.1038/d41586-020-01988-0.

[13] M. Veldhorst, J. C. C. Hwang, C. H. Yang, A. W. Leenstra, B. de Ronde, J. P. Dehollain, J. T. Muhonen, F. E. Hudson, K. M. Itoh, A. Morello, and A. S. Dzurak. **An addressable quantum dot qubit with fault-tolerant control-fidelity**. *Nature Nanotechnology*, 9(12):981–985, oct 2014. https://doi.org/10.1038/nnano.2014.216.

[14] C. Song, K. Xu, W. Liu, C. p. Yang, S.-B. Zheng, H. Deng, Q. Xie, K. Huang, Q. Guo, L. Zhang, P. Zhang, D. Xu, D. Zheng, X. Zhu, H. Wang, Y.-A. Chen, C.-Y. Lu, S. Han, and J.-W. Pan. **10-Qubit Entanglement and Parallel Logic Operations with a Superconducting Circuit**. *Physical Review Letters*, 119(18), nov 2017. https://doi.org/10.1103/PhysRevLett.119.180511.

[15] German Wikipedia article "Qubit" from 20.10.2021. https://de.wikipedia.org/wiki/Qubit#cite_note-5.

[16] X.-L. Wang, L.-K. Chen, W. Li, H.-L. Huang, C. Liu, C. Chen, Y.-H. Luo, Z.-E. Su, D. Wu, Z.-D. Li, H. Lu, Y. Hu, X. Jiang, C.-Z. Peng, L. Li, N.-L. Liu, Y.-A. Chen, C.-Y. Lu, and J.-W. Pan. **Experimental Ten-Photon Entanglement**. *Physical Review Letters*, 117(21), nov 2016. https://doi.org/10.1103/PhysRevLett.117.210502.

[17] N. Friis, O. Marty, C. Maier, C. Hempel, M. Holzäpfel, P. Jurcevic, M. B. Plenio, M. Huber, C. Roos, R. Blatt, and B. Lanyon. **Observation of Entangled States of a Fully Controlled 20-Qubit System**. *Physical Review X*, 8(2), apr 2018. https://doi.org/10.1103/PhysRevX.8.021012.

[18] Wikipedia article "Trapped ion quantum computer" from 20.10.2021. https://en.wikipedia.org/wiki/Trapped_ion_quantum_computer.

[19] D. Matthews. **How to get started in quantum computing**. *Nature*, 591(7848):166–167, mar 2021. https://doi.org/10.1038/d41586-021-00533-x.

[20] D. P. DiVincenzo. **The Physical Implementation of Quantum Computation**. *Fortschritte der Physik*, 48(9-11):771–783, sep 2000. https://doi.org/10.1002/1521-3978(200009)48:9/11<771::AID-PROP771>3.0.CO;2-E.

[21] J. Clarke and F. K. Wilhelm. **Superconducting quantum bits**. *Nature*, 453(7198):1031–1042, jun 2008. https://doi.org/10.1038/nature07128.

[22] J. I. Cirac and P. Zoller. **Quantum Computations with Cold Trapped Ions**. *Physical Review Letters*, 74(20):4091–4094, may 1995. https://doi.org/10.1103/PhysRevLett.74.4091.

[23] E. Knill, R. Laflamme, and G. J. Milburn. **A scheme for efficient quantum computation with linear optics**. *Nature*, 409(6816):46–52, jan 2001. https://doi.org/10.1038/35051009.

[24] I. Pogorelov, T. Feldker, Ch. D. Marciniak, L. Postler, G. Jacob, O. Krieglsteiner, V. Podlesnic, M. Meth, V. Negnevitsky, M. Stadler, B. Höfer, C. Wächter, K. Lakhmanskiy, R. Blatt, P. Schindler, and T. Monz. **Compact Ion-Trap Quantum Computing Demonstrator**. *PRX Quantum*, 2(2), jun 2021. https://doi.org/10.1103/PRXQuantum.2.020343.

[25] S. Pezzagna, D. Wildanger, P. Mazarov, A. D. Wieck, Y. Sarov, I. Rangelow, B. Naydenov, F. Jelezko, S. W. Hell, and J. Meijer. **Nanoscale Engineering and Optical Addressing of Single Spins in Diamond**. *Small*, 6(19):2117–2121, sep 2010. https://doi.org/10.1002/smll.201000902.

[26] T.Herzig, P. Racke, N. Raatz, D. Spemann, W. Redjem, J. W. Gerlach, J. Meijer, G. Cassabois, M. Abbarchi, and S. Pezzagna. **Creation of Quantum Centers in Silicon using Spatial Selective Ion Implantation of high Lateral Resolution**. In *2018 22nd International Conference on Ion Implantation Technology (IIT)*. IEEE, sep 2018. https://doi.org/10.1109/iit.2018.8807909.

[27] M. Lesik, N. Raatz, A. Tallaire, P. Spinicelli, R. John, J. Achard, A. Gicquel, V. Jacques, J.-F. Roch, J. Meijer, and S. Pezzagna. **Production of bulk NV centre arrays by shallow implantation and diamond CVD overgrowth**. *physica status solidi (a)*, 213(10):2594–2600, jul 2016. https://doi.org/10.1002/pssa.201600219.

[28] J. Meijer, B. Burchard, M. Domhan, C. Wittmann, T. Gaebel, I. Popa, F. Jelezko, and J. Wrachtrup. **Generation of single color centers by focused nitrogen implantation**. *Applied Physics Letters*, 87(26):261909, dec 2005. https://doi.org/10.1063/1.2103389.

[29] A. Gruber. **Scanning Confocal Optical Microscopy and Magnetic Resonance on Single Defect Centers**. *Science*, 276(5321):2012–2014, jun 1997. https://doi.org/10.1126/science.276.5321.2012.

[30] F. Fuchs, B. Stender, M. Trupke, D. Simin, J. Pflaum, V. Dyakonov, and G. V. Astakhov. **Engineering near-infrared single-photon emitters with optically active spins in ultrapure silicon carbide**. *Nature Communications*, 6(1), jul 2015. https://doi.org/10.1038/ncomms8578.

[31] Y.-C. Chen, P. S. Salter, M. Niethammer, M. Widmann, F. Kaiser, R. Nagy, N. Morioka, C. Babin, J. Erlekampf, P. Berwian, M. J. Booth, and J. Wrachtrup. **Laser Writing of Scalable Single Color Centers in Silicon Carbide**. *Nano Letters*, 19(4):2377–2383, mar 2019. https://doi.org/10.1021/acs.nanolett.8b05070.

[32] G. Davies, H. Brian, E. C. Lightowlers, K. Barraclough, and M. F. Thomaz. **The temperature dependence of the 969 meV 'G' optical transition in silicon**. *Semiconductor Science and Technology*, 4(3):200–206, mar 1989. https://doi.org/10.1088/0268-1242/4/3/010.

[33] D. D. Berhanuddin. *Generation and characterisation of the carbon G-centre in silicon*. Ph. d. thesis, University of Surrey, 2015.

[34] K. M. Lee, K. P. O'Donnell, J. Weber, B. C. Cavenett, and G. D. Watkins. **Optical Detection of Magnetic Resonance for a Deep-Level Defect in Silicon**. *Physical Review Letters*, 48(1):37–40, jan 1982. https://doi.org/10.1103/physrevlett.48.37.

[35] K. P. O'Donnell, K. M. Lee, and G. D. Watkins. **Origin of the 0.97 eV luminescence in irradiated silicon**. *Physica B+C*, 116(1-3):258–263, feb 1983. https://doi.org/10.1016/0378-4363(83)90256-5.

[36] K. Thonke, H. Klemisch, J. Weber, and R. Sauer. **New model of the irradiation-induced 0.97-eV G line in silicon: A C_s-Si* complex**. *Physical Review B*, 24(10):5874–5886, nov 1981. https://doi.org/10.1103/physrevb.24.5874.

[37] L. W. Song, X. D. Zhan, B. W. Benson, and G. D. Watkins. **Bistable interstitial-carbon—substitutional-carbon pair in silicon**. *Physical Review B*, 42(9):5765–5783, sep 1990. https://doi.org/10.1103/physrevb.42.5765.

[38] D. D. Berhanuddin, M. A. Lourenço, R. M. Gwilliam, and K. P. Homewood. **Co-Implantation of Carbon and Protons: An Integrated Silicon Device Technology Compatible Method to Generate the Lasing G-Center**. *Advanced Functional Materials*, 22(13):2709–2712, apr 2012. https://doi.org/10.1002/adfm.201103034.

[39] W. Redjem, A. Durand, T. Herzig, A. Benali, S. Pezzagna, J. Meijer, A. Yu. Kuznetsov, H. S. Nguyen, S. Cueff, J.-M. Gérard, I. Robert-Philip, B. Gil, D. Caliste, P. Pochet, M. Abbarchi, V. Jacques, A. Dréau, and G. Cassabois. **Single artificial atoms in silicon emitting at telecom wavelengths**. *Nature Electronics*, 3(12):738–743, nov 2020. https://doi.org/10.1038/s41928-020-00499-0.

[40] E. Bourgeois, A. Jarmola, P. Siyushev, M. Gulka, J. Hruby, F. Jelezko, D. Budker, and M. Nesladek. **Photoelectric detection of electron spin resonance of nitrogen-vacancy centres in diamond**. *Nature Communications*, 6(1), oct 2015. https://doi.org/10.1038/ncomms9577.

[41] E. Bourgeois, E. Londero, K. Buczak, J. Hruby, M. Gulka, Y. Balasubramaniam, G. Wachter, J. Stursa, K. Dobes, F. Aumayr, M. Trupke, A. Gali, and M. Nesladek. **Enhanced photoelectric detection of NV magnetic resonances in diamond under dual-beam excitation**. *Physical Review B*, 95(4), jan 2017. https://doi.org/10.1103/physrevb.95.041402.

[42] M. Gulka, E. Bourgeois, J. Hruby, P. Siyushev, G. Wachter, F. Aumayr, P. R. Hemmer, A. Gali, F. Jelezko, M. Trupke, and M. Nesladek. **Pulsed Photoelectric Coherent Manipulation and Detection of N-V Center Spins in Diamond**. *Physical Review Applied*, 7(4), apr 2017. https://doi.org/10.1103/physrevapplied.7.044032.

[43] A. N. Tait, S. M. Buckley, J. Chiles, A. N. McCaughan, S. Olson, S. Papa Rao, S. W. Nam, R. P. Mirin, and J. M. Shainline. **Microring resonator-coupled photoluminescence from silicon W centers**. *Journal of Physics: Photonics*, 2(4):045001, jul 2020. https://doi.org/10.1088/2515-7647/ab95f2.

[44] B. Lefaucher. **Optical Study of Micro Resonators with G-centers as an Active Medium**. Master's thesis, School of Engineering Physics - KTH Royal Institute of Technology, Stockholm, Schweden, 2021. https://www.diva-portal.org/smash/get/diva2:1544409/FULLTEXT01.pdf.

[45] Anton Balazh. **Earth**. Licence free imgur image hosting service from 19.08.2021. https://i.imgur.com/lCRbrLG.jpg.

[46] S. Ossicini, L. Pavesi, and F. Priolo. *Light Emitting Silicon for Microphotonics*. Springer Berlin Heidelberg, 2003. https://link.springer.com/book/10.1007/b13588#about.

[47] R. Gross and A. Marx. *Festkörperphysik*. OLDENBOURG WISSENSCHAFTSVERLAG, jan 2014. https://www.degruyter.com/document/doi/10.1515/9783110566130/html.

[48] S. Kasap and P. Capper. *Springer handbook of electronic and photonic materials*. Springer, New York, 2006.

[49] W. Weber. **Adiabatic bond charge model for the phonons in diamond, Si, Ge, and α-Sn**. *Physical Review B*, 15(10):4789–4803, may 1977. https://doi.org/10.1103/physrevb.15.4789.

[50] C. Beaufils, W. Redjem, E. Rousseau, V. Jacques, A. Yu. Kuznetsov, C. Raynaud, C. Voisin, A. Benali, T. Herzig, S. Pezzagna, J. Meijer, M. Abbarchi, and G. Cassabois. **Optical properties of an ensemble of G-centers in silicon**. *Physical Review B*, 97(3), (2018). https://doi.org/10.1103/physrevb.97.035303.

[51] S. Saikan, A. Imaoka, Y. Kanematsu, K. Sakoda, K. Kominami, and M. Iwamoto. **Temperature dependence of Debye-Waller factor in dye-doped polymers**. *Physical Review B*, 41(5):3185–3189, feb 1990. https://doi.org/10.1103/physrevb.41.3185.

[52] E. Dornberger. **Prediction of OSF Ring Dynamics and Grown-in Voids in Czochralski Silicon Crystals**. PhD, 1997. https://doi.org/10.13140/RG.2.1.3112.9209.

[53] Jr. J. W. Morris. *"Defects in Crystals." Chapter 4 in Materials Science and Engineering: An Introduction.*, volume pp. 76-107. Wiley, Hoboken, NJ, 2013.

[54] E. Rosencher and B. Vinter. *Optoelectronics*. Cambridge University Press, 2011. https://www.ebook.de/de/product/5823850/emmanuel_rosencher_borge_vinter_optoelectronics.html.

[55] Jacques Pankove. *Optical processes in semiconductors*. Dover, New York, 1975.

[56] N. Daldosso and L. Pavesi. **Nanosilicon photonics**. *Laser & Photonics Review*, 3(6):508–534, nov 2009. https://doi.org/10.1002/lpor.200810045.

[57] L. Pavesi. **Silicon-Based Light Sources for Silicon Integrated Circuits**. *Advances in Optical Technologies*, 2008:1–12, (2008). https://doi.org/10.1155/2008/416926.

[58] Jr. R. M. Osgood, N. C. Panoiu, J. I. Dadap, X. Liu, X. Chen, I-W. Hsieh, E. Dulkeith, W. M. Green, and Y. A. Vlasov. **Engineering nonlinearities in nanoscale optical systems: physics and applications in dispersion-engineered silicon nanophotonic wires**. *Advances in Optics and Photonics*, 1(1):162, jan 2009. https://doi.org/10.1364/aop.1.000162.

[59] R. S. Jacobsen, K. N. Andersen, P. I. Borel, J. Fage-Pedersen, L. H. Frandsen, O. Hansen, M. Kristensen, A. V. Lavrinenko, G. Moulin, H. Ou, C. Peucheret, B. Zsigri, and A. Bjarklev. **Strained silicon as a new electro-optic material**. *Nature*, 441(7090):199–202, may 2006. https://doi.org/10.1038/nature04706.

[60] T. Baehr-Jones, B. Penkov, J. Huang, P. Sullivan, J. Davies, J. Takayesu, J. Luo, T.-D. Kim, L. Dalton, A. Jen, M. Hochberg, and A. Scherer. **Nonlinear polymer-clad silicon slot waveguide modulator with a half wave voltage of 0.25V**. *Applied Physics Letters*, 92(16):163303, apr 2008. https://doi.org/10.1063/1.2909656.

[61] M. Borghi, C. Castellan, S. Signorini, A. Trenti, and L. Pavesi. **Nonlinear silicon photonics**. *Journal of Optics*, 19(9):093002, aug 2017. https://doi.org/10.1088/2040-8986/aa7a6d.

[62] H. Fukuda, K. Yamada, T. Shoji, M. Takahashi, T. Tsuchizawa, T. Watanabe, J. i. Takahashi, and S. i. Itabashi. **Four-wave mixing in silicon wire waveguides**. *Optics Express*, 13(12):4629, 2005. https://doi.org/10.1364/opex.13.004629.

[63] Y.-H. Kuo, H. Rong, V. Sih, S. Xu, M. Paniccia, and O. Cohen. **Demonstration of wavelength conversion at 40 Gb/s data rate in silicon waveguides**. *Optics Express*, 14(24):11721, 2006. https://doi.org/10.1364/oe.14.011721.

[64] M. A. Foster, A. C. Turner, R. Salem, M. Lipson, and A. L. Gaeta. **Broad-band continuous-wave parametric wavelength conversion in silicon nanowaveguides**. *Optics Express*, 15(20):12949, 2007. https://doi.org/10.1364/oe.15.012949.

[65] A. Liu, H. Rong, M. Paniccia, O. Cohen, and D. Hak. **Net optical gain in a low loss silicon-on-insulator waveguide by stimulated Raman scattering**. *Optics Express*, 12(18):4261, 2004. https://doi.org/10.1364/opex.12.004261.

[66] Q. Xu, V. R. Almeida, and M. Lipson. **Time-resolved study of Raman gain in highly confined silicon-on-insulator waveguides**. *Optics Express*, 12(19):4437, 2004. https://doi.org/10.1364/opex.12.004437.

[67] T. K. Liang and H. K. Tsang. **Efficient Raman amplification in silicon-on-insulator waveguides**. *Applied Physics Letters*, 85(16):3343–3345, oct 2004. https://doi.org/10.1063/1.1807960.

[68] O. Boyraz and B. Jalali. **Demonstration of 11dB fiber-to-fiber gain in a silicon Raman amplifier**. *IEICE Electronics Express*, 1(14):429–434, 2004. https://doi.org/10.1587/elex.1.429.

[69] O. Boyraz and B. Jalali. **Demonstration of a silicon Raman laser**. *Optics Express*, 12(21):5269, 2004. https://doi.org/10.1364/opex.12.005269.

[70] H. Rong, R. Jones, A. Liu, O. Cohen, D. Hak, A. Fang, and M. Paniccia. **A continuous-wave Raman silicon laser**. *Nature*, 433(7027):725–728, feb 2005. https://doi.org/10.1038/nature03346.

[71] H. Rong, A. Liu, R. Jones, O. Cohen, D. Hak, R. Nicolaescu, A. Fang, and M. Paniccia. **An all-silicon Raman laser**. *Nature*, 433(7023):292–294, jan 2005. https://doi.org/10.1038/nature03273.

[72] M. Milosavljević, G. Shao, M. A. Lourenco, R. M. Gwilliam, and K. P. Homewood. **Engineering of boron-induced dislocation loops for efficient room-temperature silicon light-emitting diodes**. *Journal of Applied Physics*, 97(7):073512, apr 2005. https://doi.org/10.1063/1.1866492.

[73] M. Milosavljević, M. A. Lourenço, R. M. Gwilliam, and K. P. Homewood. **Role of heavy ion co-implantation and thermal spikes on the development of dislocation loops in nanoengineered silicon light emitting diodes**. *Journal of Applied Physics*, 110(3):033508, aug 2011. https://doi.org/10.1063/1.3614036.

[74] M. A. Lourenço, M. Milosavljević, R. M. Gwilliam, K. P. Homewood, and G. Shao. **On the role of dislocation loops in silicon light emitting diodes**. *Applied Physics Letters*, 87(20):201105, nov 2005. https://doi.org/10.1063/1.2130533.

[75] M. A. Lourenço, M. S. A. Siddiqui, R. M. Gwilliam, G. Shao, and K. P. Homewood. **Efficient silicon light emitting diodes made by dislocation engineering**. *Physica E: Low-dimensional Systems and Nanostructures*, 16(3-4):376–381, mar 2003. https://doi.org/10.1016/s1386-9477(02)00690-2.

[76] J. P. Hirth, J. Lothe, and T. Mura. **Theory of Dislocations (2nd ed.)**. *Journal of Applied Mechanics*, 50(2):476–477, jun 1983. https://doi.org/10.1115/1.3167075.

[77] W. L. Ng, M. A. Lourenço, R. M. Gwilliam, S. Ledain, G. Shao, and K. P. Homewood. **An efficient room-temperature silicon-based light-emitting diode**. *Nature*, 410(6825):192–194, mar 2001. https://doi.org/10.1038/35065571.

[78] B. Welber, C. K. Kim, M. Cardona, and S. Rodriguez. **Dependence of the indirect energy gap of silicon on hydrostatic pressure**. *Solid State Communications*, 17(8):1021–1024, oct 1975. https://doi.org/10.1016/0038-1098(75)90245-8.

[79] K. P. Homewood and M. A. Lourenço. **Light from Si via dislocation loops**. *Materials Today*, 8(1):34–39, jan 2005. https://doi.org/10.1016/s1369-7021(04)00677-7.

[80] A. Sacchetti. **Electrical current in nanoelectronic devices**. *Physics Letters A*, 374(39):4057–4060, aug 2010. https://doi.org/10.1016/j.physleta.2010.08.001.

[81] J. H. Davies. ***The Physics of Low-Dimensional Semiconductors***. Cambridge University Press, 1998.

[82] T. Edvinsson. **Optical quantum confinement and photocatalytic properties in two-, one- and zero-dimensional nanostructures**. *Royal Society Open Science*, 5(9):180387, sep 2018. http://dx.doi.org/10.1098/rsos.180387.

[83] L. T. Canham. **Silicon quantum wire array fabrication by electrochemical and chemical dissolution of wafers**. *Applied Physics Letters*, 57(10):1046–1048, sep 1990. https://doi.org/10.1063/1.103561.

[84] A. G. Cullis and L. T. Canham. **Visible light emission due to quantum size effects in highly porous crystalline silicon**. *Nature*, 353(6342):335–338, sep 1991. https://doi.org/10.1038/353335a0.

[85] P. Bettotti, M. Cazzanelli, L. Dal Negro, B. Danese, Z. Gaburro, C. J. Oton, G. Vijaya Prakash, and L. Pavesi. **Silicon nanostructures for photonics**. *Journal of Physics: Condensed Matter*, 14(35):8253–8281, aug 2002. https://doi.org/10.1088/0953-8984/14/35/305.

[86] J. M. Shainline and J. Xu. **Silicon as an emissive optical medium**. *Laser & Photonics Review*, 1(4):334–348, dec 2007. https://doi.org/10.1002/lpor.200710021.

[87] L. Pavesi. **Porous silicon dielectric multilayers and microcavities**. *La Rivista del Nuovo Cimento*, 20(10):1–76, oct 1997. https://doi.org/10.1007/bf02877374.

[88] M. Krüger, S. Hilbrich, M. Thönissen, D. Scheyen, W. Theiß, and H. Lüth. **Suppression of ageing effects in porous silicon interference filters**. *Optics Communications*, 146(1-6):309–315, jan 1998. https://doi.org/10.1016/s0030-4018(97)00513-0.

[89] L. Pavesi, C. Mazzoleni, A. Tredicucci, and V. Pellegrini. **Controlled photon emission in porous silicon microcavities**. *Applied Physics Letters*, 67(22):3280–3282, nov 1995. https://doi.org/10.1063/1.115220.

[90] L. Pavesi and P. Dubos. **Random porous silicon multilayers: application to distributed Bragg reflectors and interferential Fabry - Pérot filters**. *Semiconductor Science and Technology*, 12(5):570–575, may 1997. https://doi.org/10.1088/0268-1242/12/5/009.

[91] V. Mulloni and L. Pavesi. **Porous silicon microcavities as optical chemical sensors**. *Applied Physics Letters*, 76(18):2523–2525, may 2000. https://doi.org/10.1063/1.126396.

[92] S. Chan, P. M. Fauchet, Y. Li, L. J. Rothberg, and B. L. Miller. **Porous Silicon Microcavities for Biosensing Applications**. *physica status solidi (a)*, 182(1):541–546, nov 2000. https://doi.org/10.1002/1521-396x(200011)182:1<541::aid-pssa541>3.0.co;2-#.

[93] A. Richter, P. Steiner, F. Kozlowski, and W. Lang. **Current-induced light emission from a porous silicon device**. *IEEE Electron Device Letters*, 12(12):691–692, dec 1991. https://doi.org/10.1109/55.116957.

[94] E. Bassous, M. Freeman, J.-M. Halbout, S. S. lyer, V. P. Kesan, P. Munguia, S. F. Pesarcik, and B. L. Williams. **Characterization of Microporous Silicon Fabricated by Immersion Scanning**. *MRS Proceedings*, 256, 1991. https://doi.org/10.1557/proc-256-23.

[95] K. D. Hirschman, L. Tsybeskov, S. P. Duttagupta, and P. M. Fauchet. **Silicon-based visible light-emitting devices integrated into microelectronic circuits**. *Nature*, 384(6607):338–341, nov 1996. https://doi.org/10.1038/384338a0.

[96] B. Gelloz and N. Koshida. **Electroluminescence with high and stable quantum efficiency and low threshold voltage from anodically oxidized thin porous silicon diode**. *Journal of Applied Physics*, 88(7):4319, 2000. https://doi.org/10.1063/1.1290458.

[97] Y. Kanzawa, T. Kageyama, S. Takeoka, M. Fujii, S. Hayashi, and K. Yamamoto. **Size-dependent near-infrared photoluminescence spectra of Si nanocrystals embedded in SiO2 matrices**. *Solid State Communications*, 102(7):533–537, may 1997. https://doi.org/10.1016/s0038-1098(96)00774-0.

[98] L. Pavesi, L. Dal Negro, C. Mazzoleni, G. Franzò, and F. Priolo. **Optical gain in silicon nanocrystals**. *Nature*, 408(6811):440–444, nov 2000. https://doi.org/10.1038/35044012.

[99] F. Iacona, C. Bongiorno, C. Spinella, S. Boninelli, and F. Priolo. **Formation and evolution of luminescent Si nanoclusters produced by thermal annealing of SiOx films**. *Journal of Applied Physics*, 95(7):3723–3732, apr 2004. https://doi.org/10.1063/1.1664026.

[100] H. Seifarth, R. Grötzschel, A. Markwitz, W. Matz, P. Nitzsche, and L. Rebohle. **Preparation of SiO2 films with embedded Si nanocrystals by reactive r.f. magnetron sputtering**. *Thin Solid Films*, 330(2):202–205, sep 1998. https://doi.org/10.1016/s0040-6090(98)00609-9.

[101] Z. x. Ma, X. b. Liao, J. He, W. c. Cheng, G. z. Yue, Y. q. Wang, and G. l. Kong. **Annealing behaviors of photoluminescence from SiOx:H**. *Journal of Applied Physics*, 83(12):7934–7939, jun 1998. https://doi.org/10.1063/1.367973.

[102] U. Kahler. *Darstellung, Charakterisierung und Oberflachenmodifizierung von Siliziumnanopartikeln in SiO₂*. PhD thesis, Martin-Luther-Universität Halle-Wittenberg, 2001.

[103] M. Zacharias, J. Heitmann, R. Scholz, U. Kahler, M. Schmidt, and J. Bläsing. **Size-controlled highly luminescent silicon nanocrystals: A SiO/SiO₂ superlattice approach**. *Applied Physics Letters*, 80(4):661–663, jan 2002. https://doi.org/10.1063/1.1433906.

[104] J. Heitmann. *Größenkontrollierte Herstellung von Silizium-Nanokristallen und ihre Charakterisierung*. PhD thesis, Martin-Luther-Universität Halle-Wittenberg, 2003. https://sundoc.bibliothek.uni-halle.de/diss-online/03/03H199/of_index.htm.

[105] M. Jafarzadeh, I. A. Rahman, and C. S. Sipaut. **Synthesis of silica nanoparticles by modified sol–gel process: the effect of mixing modes of the reactants and drying techniques**. *Journal of Sol-Gel Science and Technology*, 50(3):328–336, apr 2009. https://doi.org/10.1007/s10971-009-1958-6.

[106] G. Belomoin, J. Therrien, and M. Nayfeh. **Oxide and hydrogen capped ultrasmall blue luminescent Si nanoparticles**. *Applied Physics Letters*, 77(6):779–781, aug 2000. https://doi.org/10.1063/1.1306659.

[107] J. Valenta, P. Janda, K. Dohnalová, D. Nižňansky, F. Vácha, and J. Linnros. **Colloidal suspensions of silicon nanocrystals: from single nanocrystals to photonic structures**. *Optical Materials*, 27(5):1046–1049, feb 2005. https://doi.org/10.1016/j.optmat.2004.08.060.

[108] M. Fujii, K. Toshikiyo, Y. Takase, Y. Yamaguchi, and S. Hayashi. **Below bulk-band-gap photoluminescence at room temperature from heavily P- and B-doped Si nanocrystals**. *Journal of Applied Physics*, 94(3):1990–1995, aug 2003. https://doi.org/10.1063/1.1590409.

[109] H. Takagi, H. Ogawa, Y. Yamazaki, A. Ishizaki, and T. Nakagiri. **Quantum size effects on photoluminescence in ultrafine Si particles**. *Applied Physics Letters*, 56(24):2379–2380, jun 1990. https://doi.org/10.1063/1.102921.

[110] W. D. A. M. de Boer, D. Timmerman, K. Dohnalová, I. N. Yassievich, H. Zhang, W. J. Buma, and T. Gregorkiewicz. **Red spectral shift and enhanced quantum efficiency in phonon-free photoluminescence from silicon nanocrystals**. *Nature Nanotechnology*, 5(12):878–884, nov 2010. https://doi.org/10.1038/nnano.2010.236.

[111] T. F. Krauss, R. M. De La Rue, and S. Brand. **Two-dimensional photonic-bandgap structures operating at near-infrared wavelengths**. *Nature*, 383(6602):699–702, oct 1996. https://doi.org/10.1038/383699a0.

[112] M. Notomi. **Manipulating light with strongly modulated photonic crystals**. *Reports on Progress in Physics*, 73(9):096501, aug 2010. https://doi.org/10.1088/0034-4885/73/9/096501.

[113] A. Shakoor, R. Lo Savio, P. Cardile, S. L. Portalupi, D. Gerace, K. Welna, S. Boninelli, G. Franzò, F. Priolo, T. F. Krauss, M. Galli, and L. O'Faolain. **Room temperature all-silicon photonic crystal nanocavity light emitting diode at sub-bandgap wavelengths**. *Laser & Photonics Reviews*, 7(1):114–121, sep 2012. https://doi.org/10.1002/lpor.201200043.

[114] K.-Y. Cheng, R. Anthony, U. R. Kortshagen, and R. J. Holmes. **High-Efficiency Silicon Nanocrystal Light-Emitting Devices**. *Nano Letters*, 11(5):1952–1956, may 2011. https://doi.org/10.1021/nl2001692.

[115] O. Bisi, S. Ossicini, and L. Pavesi. **Porous silicon: a quantum sponge structure for silicon based optoelectronics**. *Surface Science Reports*, 38(1-3):1–126, apr 2000. https://doi.org/10.1016/s0167-5729(99)00012-6.

[116] Y. Taguchi, Y. Takahashi, Y. Sato, T. Asano, and S. Noda. **Statistical studies of photonic heterostructure nanocavities with an average Q factor of three million**. *Optics Express*, 19(12):11916, jun 2011. https://doi.org/10.1364/oe.19.011916.

[117] S. Ferretti and D. Gerace. **Single-photon nonlinear optics with Kerr-type nanostructured materials**. *Physical Review B*, 85(3), jan 2012. https://doi.org/10.1103/physrevb.85.033303.

[118] S. Coffa, G. Franzò, F. Priolo, A. Polman, and R. Serna. **Temperature dependence and quenching processes of the intra-4f luminescence of Er in crystalline Si**.

Physical Review B, 49(23):16313–16320, jun 1994. https://doi.org/10.1103/physrevb.49.16313.

[119] B. Zheng, J. Michel, F. Y. G. Ren, L. C. Kimerling, D. C. Jacobson, and J. M. Poate. **Room-temperature sharp line electroluminescence at** $\lambda = 1.54m$ **from an erbium-doped, silicon light-emitting diode**. *Applied Physics Letters*, 64(21):2842–2844, may 1994. https://doi.org/10.1063/1.111977.

[120] A. Polman. **Erbium implanted thin film photonic materials**. *Journal of Applied Physics*, 82(1):1–39, jul 1997. https://doi.org/10.1063/1.366265.

[121] H. Ennen, G. Pomrenke, A. Axmann, K. Eisele, W. Haydl, and J. Schneider. **1.54-μm electroluminescence of erbium-doped silicon grown by molecular beam epitaxy**. *Applied Physics Letters*, 46(4):381–383, feb 1985. https://doi.org/10.1063/1.95639.

[122] J. Stimmer, A. Reittinger, J. F. Nützel, G. Abstreiter, H. Holzbrecher, and C. Buchal. **Electroluminescence of erbium-oxygen-doped silicon diodes grown by molecular beam epitaxy**. *Applied Physics Letters*, 68(23):3290–3292, jun 1996. https://doi.org/10.1063/1.116577.

[123] S. Cueff. **Cathodoluminescence and photoluminescence comparative study of erbium-doped silicon-rich silicon oxide**. *Journal of Nanophotonics*, 5(1):051504, jan 2011. https://doi.org/10.1117/1.3549701.

[124] L. Pavesi. **Routes toward silicon-based lasers**. *Materials Today*, 8(1):18–25, jan 2005. https://doi.org/10.1016/s1369-7021(04)00675-3.

[125] G. Franzò, S. Coffa, F. Priolo, and C. Spinella. **Mechanism and performance of forward and reverse bias electroluminescence at 1.54 μm from Er-doped Si diodes**. *Journal of Applied Physics*, 81(6):2784–2793, mar 1997. https://doi.org/10.1063/1.363935.

[126] A. Polman. **Teaching silicon new tricks**. *Nature Materials*, 1(1):10–12, sep 2002. https://doi.org/10.1038/nmat705.

[127] A. Polman, B. Min, J. Kalkman, T. J. Kippenberg, and K. J. Vahala. **Ultralow-threshold erbium-implanted toroidal microlaser on silicon**. *Applied Physics Letters*, 84(7):1037–1039, feb 2004. https://doi.org/10.1063/1.1646748.

[128] B. Min, T. J. Kippenberg, L. Yang, K. J. Vahala, J. Kalkman, and A. Polman. **Erbium-implanted high-Qsilica toroidal microcavity laser on a silicon chip**. *Physical Review A*, 70(3), sep 2004. https://doi.org/10.1103/physreva.70.033803.

[129] T. J. Kippenberg, J. Kalkman, A. Polman, and K. J. Vahala. **Demonstration of an erbium-doped microdisk laser on a silicon chip**. *Physical Review A*, 74(5), nov 2006. https://doi.org/10.1103/physreva.74.051802.

[130] C. Yin, M. Rancic, G. G. de Boo, N. Stavrias, J. C. McCallum, M. J. Sellars, and S. Rogge. **Optical addressing of an individual erbium ion in silicon**. *Nature*, 497(7447):91–94, may 2013. https://doi.org/10.1038/nature12081.

[131] A. J. Kenyon. **Erbium in silicon**. *Semiconductor Science and Technology*, 20(12):R65–R84, nov 2005. https://doi.org/10.1088/0268-1242/20/12/r02.

[132] G. D. Watkins, J. W. Corbett, and R. M. Walker. **Spin Resonance in Electron Irradiated Silicon**. *Journal of Applied Physics*, 30(8):1198–1203, aug 1959. https://doi.org/10.1063/1.1735293.

[133] J. W. Corbett and G. D. Watkins. **Silicon Divacancy and its Direct Production by Electron Irradiation**. *Physical Review Letters*, 7(8):314–316, oct 1961. https://doi.org/10.1103/physrevlett.7.314.

[134] G. D. Watkins and J. W. Corbett. **Defects in Irradiated Silicon. I. Electron Spin Resonance of the Si-ACenter**. *Physical Review*, 121(4):1001–1014, feb 1961. https://doi.org/10.1103/physrev.121.1001.

[135] J. W. Corbett, G. D. Watkins, R. M. Chrenko, and R. S. McDonald. **Defects in Irradiated Silicon. II. Infrared Absorption of the Si-ACenter**. *Physical Review*, 121(4):1015–1022, feb 1961. https://doi.org/10.1103/physrev.121.1015.

[136] G. D. Watkins and J. W. Corbett. **Electron paramagnetic resonance of defects in irradiated silicon**. *Discuss. Faraday Soc.*, 31:86–95, 1961. https://doi.org/10.1039/DF9613100086.

[137] G. D. Watkins and J. W. Corbett. **Defects in Irradiated Silicon: Electron Paramagnetic Resonance and Electron-Nuclear Double Resonance of the Si-ECenter**. *Physical Review*, 134(5A):A1359–A1377, jun 1964. https://doi.org/10.1103/physrev.134.a1359.

[138] J. W. Corbett and G. D. Watkins. **Production of Divacancies and Vacancies by Electron Irradiation of Silicon**. *Physical Review*, 138(2A):A555–A560, apr 1965. https://doi.org/10.1103/physrev.138.a555.

[139] C. E. Jones and W. D. Compton. **Recombination luminescence in irradiated silicon-effects of uniaxial stress and temperature variations**. *Radiation Effects*, 9(1-2):83–88, may 1971. https://doi.org/10.1080/00337577108242037.

[140] C. E. Jones, E. S. Johnson, W. D. Compton, J. R. Noonan, and B. G. Streetman. **Temperature, stress, and annealing effects on the luminescence from electron-irradiated silicon**. *Journal of Applied Physics*, 44(12):5402–5410, dec 1973. https://doi.org/10.1063/1.1662165.

[141] G. Bohnert, K. Weronek, and A. Hangleiter. **Transient characteristics of isoelectronic bound excitons at hole-attractive defects in silicon: The C(0.79 eV), P(0.767 eV), and H(0.926 eV) lines**. *Physical Review B*, 48(20):14973–14981, nov 1993. https://doi.org/10.1103/physrevb.48.14973.

[142] G. Davies. **The optical properties of luminescence centres in silicon**. *Physics Reports*, 176(3-4):83–188, may 1989. https://doi.org/10.1016/0370-1573(89)90064-1.

[143] G. Davies, S. Hayama, L. Murin, R. Krause-Rehberg, V. Bondarenko, A. Sengupta, C. Davia, and A. Karpenko. **Radiation damage in silicon exposed to high-energy protons**. *Physical Review B*, 73(16), apr 2006. https://doi.org/10.1103/physrevb.73.165202.

[144] Y. Yang, J. Bao, C. Wang, and M. J. Aziz. **Sub-bandgap luminescence centers in silicon created by self-ion implantation and thermal annealing**. *Journal of Applied Physics*, 107(12):123109, jun 2010. https://doi.org/10.1063/1.3436572.

[145] G. Davies, E. C. Lightowlers, and Z. E. Ciechanowska. **The 1018 meV (W or I1) vibronic band in silicon**. *Journal of Physics C: Solid State Physics*, 20(2):191–205, jan 1987. https://doi.org/10.1088/0022-3719/20/2/003.

[146] S. M. Buckley, A. N. Tait, G. Moody, B. Primavera, S. Olson, J. Herman, K. L. Silverman, S. P. Rao, S. W. Nam, R. P. Mirin, and J. M. Shainline. **Optimization of photoluminescence from W centers in silicon-on-insulator**. *Optics Express*, 28(11):16057, may 2020. https://doi.org/10.1364/oe.386450.

[147] A. Carvalho, R. Jones, J. Coutinho, and P. R. Briddon. **Density-functional study of small interstitial clusters in Si: Comparison with experiments**. *Physical Review B*, 72(15), oct 2005. https://doi.org/10.1103/physrevb.72.155208.

[148] I. Santos, M. Aboy, P. López, L. A. Marqués, and L. Pelaz. **Insights on the atomistic origin of X and W photoluminescence lines inc-Si fromab initiosimulations**. *Journal of Physics D: Applied Physics*, 49(7):075109, jan 2016. https://doi.org/10.1088/0022-3727/49/7/075109.

[149] M. Aboy, I. Santos, P. López, L. A. Marqués, and L. Pelaz. **W and X Photoluminescence Centers in Crystalline Si: Chasing Candidates at Atomic Level Through Multiscale Simulations**. *Journal of Electronic Materials*, 47(9):5045–5049, apr 2018. https://doi.org/10.1007/s11664-018-6300-z.

[150] C. G. Kirkpatrick, J. R. Noonan, and B. G. Streetman. **Recombination luminescence from ion implanted silicon**. *Radiation Effects*, 30(2):97–106, jan 1976. https://doi.org/10.1080/00337577608233525.

[151] W. Redjem. ***Spectroscopie optique des centres G dans le silicium: des ensembles au centre unique. Physique [physics]***. PhD thesis, Laboratoire Charles Coulomb, Université Montpellier, Français, NNT : 2019MONTS081. tel-02491663, 2019. https://tel.archives-ouvertes.fr/tel-02491663/document.

[152] J. Bao, M. Tabbal, T. Kim, S. Charnvanichborikarn, J. S. Williams, M. J. Aziz, and F. Capasso. **Point defect engineered Si sub-bandgap light-emitting diode**. *Optics Express*, 15(11):6727, 2007. https://doi.org/10.1364/oe.15.006727.

[153] S. Buckley, J. Chiles, A. N. McCaughan, G. Moody, K. L. Silverman, M. J. Stevens, R. P. Mirin, S. W. Nam, and J. M. Shainline. **All-silicon light-emitting diodes waveguide-integrated with superconducting single-photon detectors**. *Applied Physics Letters*, 111(14):141101, oct 2017. https://doi.org/10.1063/1.4994692.

[154] G. Davies, E. C. Lightowlers, D. Griffiths, and J. G. Wilkes. **Room-temperature irradiation of silicon doped with carbon**. *Semiconductor Science and Technology*, 2(8):554–557, aug 1987. https://doi.org/10.1088/0268-1242/2/8/015.

[155] M. L. W. Thewalt, A. G. Steele, S. P. Watkins, and E. C. Lightowlers. **Thermal-Donor-Related Isoelectronic Center in Silicon Which Can Bind up to Four Excitons**. *Physical Review Letters*, 57(15):1939–1942, oct 1986. https://doi.org/10.1103/physrevlett.57.1939.

[156] L. Jeyanathan, G. Davies, and E. C. Lightowlers. **Characterization of the 1117-meV and 1052-meV optical transitions in heat-treated Si**. *Physical Review B*, 52(15):10923–10931, oct 1995. https://doi.org/10.1103/physrevb.52.10923.

[157] F. Rodríguez, G. Davies, and E. C. Lightowlers. **Study of the 1096.9 meV photoluminescent oxygen-related centre in neutron-irradiated CZ-Si: Formation and structure**. *Radiation Effects and Defects in Solids*, 149(1-4):141–148, nov 1999. https://doi.org/10.1080/10420159908230147.

[158] Y. Baron, A. Durand, P. Udvarhelyi, T. Herzig, M. Khoury, S. Pezzagna, J. Meijer, I. Robert-Philip, M. Abbarchi, J.-M. Hartmann, V. Mazzocchi, J.-M. Gérard, A. Gali, V. Jacques, G. Cassabois, and A. Dréau. **Detection of single W-centers in silicon**. *arXiv*, 2021. https://arxiv.org/abs/2108.04283.

[159] V. D. Tkachev, A. V. Mudryi, and N. S. Minaev. **Noble Gas Atoms as Chemical Impurities in Silicon**. *Physica Status Solidi (a)*, 81(1):313–321, jan 1984. https://doi.org/10.1002/pssa.2210810135.

[160] N. S. Minaev and A. V. Mudryi. **Thermally-induced defects in silicon containing oxygen and carbon**. *Physica Status Solidi (a)*, 68(2):561–565, dec 1981. https://doi.org/10.1002/pssa.2210680227.

[161] A. N. Safonov, E. C. Lightowlers, G. Davies, P. Leary, R. Jones, and S. Öberg. **Interstitial-Carbon Hydrogen Interaction in Silicon**. *Physical Review Letters*, 77(23):4812–4815, dec 1996. https://doi.org/10.1103/physrevlett.77.4812.

[162] L. Bergeron, C. Chartrand, A. T. K. Kurkjian, K. J. Morse, H. Riemann, N. V. Abrosimov, P. Becker, H.-J. Pohl, M. L. W. Thewalt, and S. Simmons. **Silicon-Integrated Telecommunications Photon-Spin Interface**. *PRX Quantum*, 1(2), oct 2020. https://doi.org/10.1103/prxquantum.1.020301.

[163] D. Timerkaeva, C. Attaccalite, G. Brenet, D. Caliste, and P. Pochet. **What is thenature of the C-C complex in silicon? Insights from electronic structure calculations.** *arXiv:1702.02334v1*, 2017. https://hal.archives-ouvertes.fr/hal-01635491/document.

[164] D. Timerkaeva, C. Attaccalite, G. Brenet, D. Caliste, and P. Pochet. **Structural, electronic, and optical properties of the C-C complex in bulk silicon from first principles**. *Journal of Applied Physics*, 123(16):161421, (2018). https://doi.org/10.1063/1.5010269.

[165] G. D. Watkins and K. L. Brower. **EPR Observation of the Isolated Interstitial Carbon Atom in Silicon**. *Physical Review Letters*, 36(22):1329–1332, may 1976. https://doi.org/10.1103/physrevlett.36.1329.

[166] E. V. Lavrov and M. Fanciulli. **Interstitial carbon-substitutional tin center in silicon (?)**. *Physica B: Condensed Matter*, 302-303:263–267, jan 2001. https://doi.org/10.1016/s0921-4526(01)00439-2.

[167] L. I. Khirunenko, O. A. Kobzar', Yu. V. Pomozov, M. G. Sosnin, and N. A. Tripachko. **The role of tin in reactions involving carbon interstitial atoms in irradiated silicon**. *Semiconductors*, 37(3):288–293, mar 2003. https://doi.org/10.1134/1.1561520.

[168] E. Rotem, J. M. Shainline, and J. M. Xu. **Stimulated emission and emission efficiency enhancement in nanopatterned silicon**. In Achyut K. Dutta, Yasu-take Ohishi, Niloy K. Dutta, and Andrei V. Lavrinenko, editors, *Active and Passive Optical Components for Communications VII*. SPIE, sep 2007. https://doi.org/10.1117/12.733312.

[169] S. G. Cloutier, P. A. Kossyrev, and J. Xu. **Optical gain and stimulated emission in periodic nanopatterned crystalline silicon**. *Nature Materials*, 4(12):887–891, nov 2005. https://doi.org/10.1038/nmat1530.

[170] E. Rotem, J. M. Shainline, and J. M. Xu. **Electroluminescence of nanopatterned silicon with carbon implantation and solid phase epitaxial regrowth**. *Optics Express*, 15(21):14099, 2007. https://doi.org/10.1364/oe.15.014099.

[171] E. Rotem, J. M. Shainline, and J. M. Xu. **Enhanced photoluminescence from nanopatterned carbon-rich silicon grown by solid-phase epitaxy**. *Applied Physics Letters*, 91(5):051127, jul 2007. https://doi.org/10.1063/1.2766843.

[172] L. Zhu, S. Yuan, C. Zeng, and J. Xia. **Manipulating Photoluminescence of Carbon G-center in Silicon Metasurface with Optical Bound States in the Continuum**. *Advanced Optical Materials*, 8(8):1901830, feb 2020. https://doi.org/10.1002/adom.201901830.

[173] K. Murata, Y. Yasutake, K. i. Nittoh, S. Fukatsu, and K. Miki. **High-density G-centers, light-emitting point defects in silicon crystal**. *AIP Advances*, 1(3):032125, sep 2011. https://doi.org/10.1063/1.3624905.

[174] H. Wang, A. Chroneos, C. A. Londos, E. N. Sgourou, and U. Schwingenschlögl. **G-centers in irradiated silicon revisited: A screened hybrid density functional theory approach**. *Journal of Applied Physics*, 115(18):183509, may 2014. https://doi.org/10.1063/1.4875658.

[175] L. T. Canham, K. G. Barraclough, and D. J. Robbins. **1.3-μm light-emitting diode from silicon electron irradiated at its damage threshold**. *Applied Physics Letters*, 51(19):1509–1511, nov 1987. https://doi.org/10.1063/1.98618.

[176] R. Pinacho, P. Castrillo, M. Jaraiz, I. Martin-Bragado, J. Barbolla, H.-J. Gossmann, G.-H. Gilmer, and J.-L. Benton. **Carbon in silicon: Modeling of diffusion and clustering mechanisms**. *Journal of Applied Physics*, 92(3):1582–1587, aug 2002. https://doi.org/10.1063/1.1489715.

[177] C. Chartrand, L. Bergeron, K. J. Morse, H. Riemann, N. V. Abrosimov, P. Becker, H.-J. Pohl, S. Simmons, and M. L. W. Thewalt. **Highly enriched Si^{28} reveals remarkable optical linewidths and fine structure for well-known damage centers**. *Physical Review B*, 98(19), nov 2018. https://doi.org/10.1103/physrevb.98.195201.

[178] W. L. Wilson, P. F. Szajowski, and L. E. Brus. **Quantum Confinement in Size-Selected, Surface-Oxidized Silicon Nanocrystals**. *Science*, 262(5137):1242–1244, nov 1993. https://doi.org/10.1126/science.262.5137.1242.

[179] Z. H. Lu, D. J. Lockwood, and J.-M. Baribeau. **Quantum confinement and light emission in SiO₂/Si superlattices**. *Nature*, 378(6554):258–260, nov 1995. https://doi.org/10.1038/378258a0.

[180] D. J. W. Mous, R. G. Haitsma, T. Butz, R.-H. Flagmeyer, D. Lehmann, and J. Vogt. **The novel ultrastable HVEE 3.5 MV Singletron™ accelerator for nanoprobe applications**. *Nuclear Instruments and Methods in Physics Research Section B: Beam Interactions with Materials and Atoms*, 130(1-4):31–36, jul 1997. https://doi.org/10.1016/s0168-583x(97)00186-9.

[181] D. Spemann. *Quantitative Ionenstrahlanalyse von optoelektronischen Halbleitermaterialien und Graphit sowie Erzeugung magnetischer Ordnung in Kohlenstoff mittels Ionenbeschuss*. PhD thesis, Universität Leipzig, 2007.

[182] S. Jankuhn. **Fortgeschrittene Festkörperphysik - Ionenbeschleuniger**. *Anleitung Ionenstrahlpraktikum Universität Leipzig*, 2014.

[183] D. Spemann, T. Reinert, J. Vogt, J. Wassermann, and T. Butz. **Active compensation of stray magnetic fields at LIPSION**. *Nuclear Instruments and Methods in Physics Research Section B: Beam Interactions with Materials and Atoms*, 210:79–84, sep 2003. https://doi.org/10.1016/s0168-583x(03)01027-9.

[184] National Electrostatics Corp. **Source of Negative Ions by Cesium Sputtering - SNICS II**, 2019. https://www.pelletron.com/products/snics/.

[185] M. Fox. *Quantum Optics*. Oxford University Press, 2006.

[186] A. Beveratos, S. Kühn, R. Brouri, T. Gacoin, J.-P. Poizat, and P. Grangier. **Room temperature stable single-photon source**. *The European Physical Journal D - Atomic, Molecular and Optical Physics*, 18(2):191–196, feb 2002. https://doi.org/10.1140/epjd/e20020023.

[187] M. D. Eisaman, J. Fan, A. Migdall, and S. V. Polyakov. **Invited Review Article: Single-photon sources and detectors**. *Review of Scientific Instruments*, 82(7):071101, jul 2011. https://doi.org/10.1063/1.3610677.

[188] M. Nothaft, S. Höhla, F. Jelezko, N. Frühauf, J. Pflaum, and J. Wrachtrup. **Electrically driven photon antibunching from a single molecule at room temperature**. *Nature Communications*, 3(1), January 2012. https://doi.org/10.1038/ncomms1637.

[189] I. Aharonovich, D. Englund, and M. Toth. **Solid-state single-photon emitters**. *Nature Photonics*, 10(10):631–641, sep 2016. https://doi.org/10.1038/nphoton.2016.186.

[190] J. L. O'Brien. **Optical Quantum Computing**. *Science*, 318(5856):1567–1570, dec 2007. https://doi.org/10.1126/science.1142892.

[191] K. Takemoto, Y. Nambu, T. Miyazawa, Y. Sakuma, T. Yamamoto, S. Yorozu, and Y. Arakawa. **Quantum key distribution over 120 km using ultrahigh purity single-photon source and superconducting single-photon detectors**. *Scientific Reports*, 5(1), sep 2015. https://doi.org/10.1038/srep14383.

[192] C. H. Bennett and G. Brassard. **Quantum cryptography: Public key distribution and coin tossing**. *Theoretical Computer Science*, 560:7–11, dec 2014. https://doi.org/10.1016/j.tcs.2014.05.025.

[193] German Wikipedia article "No-Cloning-Theorem" from 19.08.2021. https://de.wikipedia.org/wiki/No-Cloning-Theorem.

[194] T. D. Ladd, F. Jelezko, R. Laflamme, Y. Nakamura, C. Monroe, and J. L. O'Brien. **Quantum computers**. *Nature*, 464(7285):45–53, mar 2010. https://doi.org/10.1038/nature08812.

[195] M. Homeister. *Quantum Computing verstehen*. Springer Fachmedien Wiesbaden, 2018. https://www.doi.org/10.1007/978-3-658-22884-2.

[196] Youtube video "A Beginners Guide to Quantum Computing" from IBM Research from 19.08.2021. https://www.youtube.com/watch?v=S52rxZG-zi0.

[197] Wikipedia article "Quantum logic gate" from 19.08.2021. https://en.wikipedia.org/wiki/Quantum__logic__gate.

[198] Wikipedia article "Quantum entanglement" from 19.08.2021. https://en.wikipedia.org/wiki/Quantum__entanglement.

[199] P. Walther, K. J. Resch, T. Rudolph, E. Schenck, H. Weinfurter, V. Vedral, M. Aspelmeyer, and A. Zeilinger. **Experimental one-way quantum computing**. *Nature*, 434(7030):169–176, mar 2005. https://doi.org/10.1038/nature03347.

[200] O. Mandel, M. Greiner, A. Widera, T. Rom, T. W. Hänsch, and I. Bloch. **Controlled collisions for multi-particle entanglement of optically trapped atoms**. *Nature*, 425(6961):937–940, oct 2003. https://doi.org/10.1038/nature02008.

[201] H. J. Briegel and R. Raussendorf. **Persistent Entanglement in Arrays of Interacting Particles**. *Physical Review Letters*, 86(5):910–913, jan 2001. https://doi.org/10.1103/PhysRevLett.86.910.

[202] Wikipedia article "Cluster state" from 09.09.2021. https://en.wikipedia.org/wiki/Cluster_state#cite_note-1.

[203] Wikipedia article "Quantenparallelismus" from 19.08.2021. https://de.wikipedia.org/wiki/Quantenparallelismus.

[204] D. Suter J. Stolze. *Quantum Computing*. Wiley-VCH GmbH, 2008.

[205] Y. L. Lim, S. D. Barrett, A. Beige, P. Kok, and L. C. Kwek. **Repeat-until-success quantum computing using stationary and flying qubits**. *Physical Review A*, 73(1), jan 2006. https://doi.org/10.1103/physreva.73.012304.

[206] H. Wang, J. Qin, X. Ding, M.-C. Chen, S. Chen, X. You, Y.-M. He, X. Jiang, L. You, Z. Wang, C. Schneider, J. J. Renema, S. Höfling, C.-Y. Lu, and J.-W. Pan. **Boson Sampling with 20 Input Photons and a 60-Mode Interferometer in a 1014 -Dimensional Hilbert Space**. *Physical Review Letters*, 123(25), dec 2019. https://doi.org/10.1103/PhysRevLett.123.250503.

[207] S. D. Barrett and P. Kok. **Efficient high-fidelity quantum computation using matter qubits and linear optics**. *Physical Review A*, 71(6), jun 2005. https://doi.org/10.1103/physreva.71.060310.

[208] A. Beige, Y. L. Lim, and L. C. Kwek. **A repeat-until-success quantum computing scheme**. *New Journal of Physics*, 9(6):197–197, jun 2007. https://doi.org/10.1088/1367-2630/9/6/197.

[209] S. Mancini and S. Bose. **Engineering an interaction and entanglement between distant atoms**. *Physical Review A*, 70(2), aug 2004. https://doi.org/10.1103/PhysRevA.70.022307.

[210] L.-M. Duan, B. Wang, and H. J. Kimble. **Robust quantum gates on neutral atoms with cavity-assisted photon scattering**. *Physical Review A*, 72(3), sep 2005. https://doi.org/10.1103/PhysRevA.72.032333.

[211] B. Kraus and J. I. Cirac. **Discrete Entanglement Distribution with Squeezed Light**. *Physical Review Letters*, 92(1), jan 2004. https://doi.org/10.1103/PhysRevLett.92.013602.

[212] X.-F. Zhou, Y.-S. Zhang, and G.-C. Guo. **Nonlocal gate of quantum network via cavity quantum electrodynamics**. *Physical Review A*, 71(6), jun 2005. https://doi.org/10.1103/PhysRevA.71.064302.

[213] Y. L. Lim, A. Beige, and L. C. Kwek. **Repeat-Until-Success Linear Optics Distributed Quantum Computing**. *Physical Review Letters*, 95(3), jul 2005. https://doi.org/10.1103/PhysRevLett.95.030505.

[214] L. Vaidman and N. Yoran. **Methods for reliable teleportation**. *Physical Review A*, 59(1):116–125, jan 1999. https://doi.org/10.1103/PhysRevA.59.116.

[215] N. Lütkenhaus, J. Calsamiglia, and K.-A. Suominen. **Bell measurements for teleportation**. *Physical Review A*, 59(5):3295–3300, may 1999. https://doi.org/10.1103/PhysRevA.59.3295.

[216] A. J. Brash, L. M. P. P. Martins, F. Liu, J. H. Quilter, A. J. Ramsay, M. S. Skolnick, and A. M. Fox. **High-fidelity initialization of long-lived quantum dot hole spin qubits by reduced fine-structure splitting**. *Physical Review B*, 92(12), sep 2015. https://doi.org/10.1103/PhysRevB.92.121301.

[217] P. C. Maurer, G. Kucsko, C. Latta, L. Jiang, N. Y. Yao, S. D. Bennett, F. Pastawski, D. Hunger, N. Chisholm, M. Markham, D. J. Twitchen, J. I. Cirac, and M. D. Lukin. **Room-Temperature Quantum Bit Memory Exceeding One Second**. *Science*, 336(6086):1283–1286, jun 2012. https://doi.org/10.1126/science.1220513.

[218] S. Yang, Y. Wang, D. D. B. Rao, T. H. Tran, A. S. Momenzadeh, M. Markham, D. J. Twitchen, P. Wang, W. Yang, R. Stöhr, P. Neumann, H. Kosaka, and J. Wrachtrup. **High-fidelity transfer and storage of photon states in a single nuclear spin**. *Nature Photonics*, 10(8):507–511, jun 2016. https://doi.org/10.1038/nphoton.2016.103.

[219] D. Loss and D. P. DiVincenzo. **Quantum computation with quantum dots**. *Physical Review A*, 57(1):120–126, jan 1998. https://doi.org/10.1103/physreva.57.120.

[220] L. M. K. Vandersypen and M. A. Eriksson. **Quantum computing with semiconductor spins**. *Physics Today*, 72(8):38–45, aug 2019. https://doi.org/10.1063/PT.3.4270.

[221] B. E. Kane. **A silicon-based nuclear spin quantum computer**. *Nature*, 393(6681):133–137, may 1998. https://doi.org/10.1038/30156.

[222] G. Zhang, Y. Cheng, J.-P. Chou, and A. Gali. **Material platforms for defect qubits and single-photon emitters**. *Applied Physics Reviews*, 7(3):031308, sep 2020. https://doi.org/10.1063/5.0006075.

[223] Wikipedia article "Kane quantum computer" from 27.08.2021. https://en.wikipedia.org/wiki/Kane_quantum_computer.

[224] J. T. Muhonen, J. P. Dehollain, A. Laucht, F. E. Hudson, R. Kalra, T. Sekiguchi, K. M. Itoh, D. N. Jamieson, J. C. McCallum, A. S. Dzurak, and A. Morello. **Storing quantum information for 30 seconds in a nanoelectronic device**. *Nature Nanotechnology*, 9(12):986–991, oct 2014. https://doi.org/10.1038/nnano.2014.211.

[225] J. J. Pla, K. Y. Tan, J. P. Dehollain, W. H. Lim, J. J. L. Morton, F. A. Zwanenburg, D. N. Jamieson, A. S. Dzurak, and A. Morello. **High-fidelity readout and control of a nuclear spin qubit in silicon**. *Nature*, 496(7445):334–338, apr 2013. https://doi.org/10.1038/nature12011.

[226] K. Saeedi, S. Simmons, J. Z. Salvail, P. Dluhy, H. Riemann, N. V. Abrosimov, P. Becker, H.-J. Pohl, J. J. L. Morton, and M. L. W. Thewalt. **Room-Temperature Quantum Bit Storage Exceeding 39 Minutes Using Ionized Donors in Silicon-28**. *Science*, 342(6160):830–833, nov 2013. https://doi.org/10.1126/science.1239584.

[227] A. Morello, J. J. Pla, P. Bertet, and D. N. Jamieson. **Donor Spins in Silicon for Quantum Technologies**. *Advanced Quantum Technologies*, 3(11):2000005, jul 2020. https://doi.org/10.1002/qute.202000005.

[228] S. Asaad, V. Mourik, B. Joecker, M. A. I. Johnson, A. D. Baczewski, H. R. Firgau, M. T. Mądzik, V. Schmitt, J. J. Pla, F. E. Hudson, K. M. Itoh, J. C. McCallum, A. S. Dzurak, A. Laucht, and A. Morello. **Coherent electrical control of a single high-spin nucleus in silicon**. *Nature*, 579(7798):205–209, mar 2020. https://doi.org/10.1038/s41586-020-2057-7.

[229] A. Gali, M. Fyta, and E. Kaxiras. **Ab initiosupercell calculations on nitrogen-vacancy center in diamond: Electronic structure and hyperfine tensors**. *Physical Review B*, 77(15), apr 2008. https://doi.org/10.1103/physrevb.77.155206.

[230] E. Bourgeois, M. Gulka, and M. Nesladek. **Photoelectric Detection and Quantum Readout of Nitrogen-Vacancy Center Spin States in Diamond**. *Advanced Optical Materials*, 8(12):1902132, apr 2020. https://doi.org/10.1002/adom.201902132.

[231] L. J. Rogers, S. Armstrong, M. J. Sellars, and N. B. Manson. **Infrared emission of the NV centre in diamond: Zeeman and uniaxial stress studies**. *New Journal of Physics*, 10(10):103024, oct 2008. https://doi.org/10.1088/1367-2630/10/10/103024.

[232] F. Dolde, I. Jakobi, B. Naydenov, N. Zhao, S. Pezzagna, C. Trautmann, J. Meijer, P. Neumann, F. Jelezko, and J. Wrachtrup. **Room-temperature entanglement between single defect spins in diamond**. *Nature Physics*, 9(3):139–143, feb 2013. https://doi.org/10.1038/nphys2545.

[233] G. Waldherr, Y. Wang, S. Zaiser, M. Jamali, T. Schulte-Herbrüggen, H. Abe, T. Ohshima, J. Isoya, J. F. Du, P. Neumann, and J. Wrachtrup. **Quantum error correction in a solid-state hybrid spin register**. *Nature*, 506(7487):204–207, feb 2014. https://doi.org/10.1038/nature12919.

[234] V. M. Acosta, A. Jarmola, E. Bauch, and D. Budker. **Optical properties of the nitrogen-vacancy singlet levels in diamond**. *Physical Review B*, 82(20), nov 2010. https://doi.org/10.1103/physrevb.82.201202.

[235] I. P. Radko, M. Boll, N. M. Israelsen, N. Raatz, J. Meijer, F. Jelezko, U. L. Andersen, and A. Huck. **Determining the internal quantum efficiency of shallow-implanted nitrogen-vacancy defects in bulk diamond**. *Optics Express*, 24(24):27715, nov 2016. http://dx.doi.org/10.1364/OE.24.027715.

[236] T. Lühmann, R. John, R. Wunderlich, J. Meijer, and S. Pezzagna. **Coulomb-driven single defect engineering for scalable qubits and spin sensors in diamond**. *Nature Communications*, 10(1), oct 2019. https://doi.org/10.1038/s41467-019-12556-0.

[237] C. E. Bradley, J. Randall, M. H. Abobeih, R. C. Berrevoets, M. J. Degen, M. A. Bakker, M. Markham, D. J. Twitchen, and T. H. Taminiau. **A Ten-Qubit Solid-State Spin Register with Quantum Memory up to One Minute**. *Physical Review X*, 9(3), sep 2019. https://doi.org/10.1103/PhysRevX.9.031045.

[238] M. Bruel. *Patent* **Process for the production of thin semiconductor material films**, December 1994.

[239] L. Wang, M. T. Wilson, and N. M. Haegel. **Interpretation of photoluminescence excitation spectroscopy of porous Si layers**. *Applied Physics Letters*, 62(10):1113–1115, mar 1993. https://doi.org/10.1063/1.108759.

[240] J. Noffsinger, E. Kioupakis, C. G. Van de Walle, S. G. Louie, and M. L. Cohen. **Phonon-Assisted Optical Absorption in Silicon from First Principles**. *Physical Review Letters*, 108(16), apr 2012. https://doi.org/10.1103/PhysRevLett.108.167402.

[241] M. Grundmann and D. Bimberg. **Theory of random population for quantum dots**. *Physical Review B*, 55(15):9740–9745, apr 1997. https://doi.org/10.1103/physrevb.55.9740.

[242] M. Abbarchi, C. Mastrandrea, T. Kuroda, T. Mano, A. Vinattieri, K. Sakoda, and M. Gurioli. **Poissonian statistics of excitonic complexes in quantum dots**.

Journal of Applied Physics, 106(5):053504, sep 2009. https://doi.org/10.1063/1.3197848.

[243] N. Dotti, F. Sarti, S. Bietti, A. Azarov, A. Y. Kuznetsov, F. Biccari, A. Vinattieri, S. Sanguinetti, M. Abbarchi, and M. Gurioli. **Germanium-based quantum emitters towards a time-reordering entanglement scheme with degenerate exciton and biexciton states**. *Physical Review B*, 91(20), may 2015. https://doi.org/10.1103/physrevb.91.205316.

[244] M. Abbarchi, F. Troiani, C. Mastrandrea, G. Goldoni, T. Kuroda, T. Mano, K. Sakoda, N. Koguchi, S. Sanguinetti, A. Vinattieri, and M. Gurioli. **Spectral diffusion and line broadening in single self-assembled GaAs-AlGaAs quantum dot photoluminescence**. *Applied Physics Letters*, 93(16):162101, oct 2008. https://doi.org/10.1063/1.3003578.

[245] V. Alex, S. Finkbeiner, and J. Weber. **Temperature dependence of the indirect energy gap in crystalline silicon**. *Journal of Applied Physics*, 79(9):6943–6946, may 1996. https://doi.org/10.1063/1.362447.

[246] M. Cardona and M. L. W. Thewalt. **Isotope effects on the optical spectra of semiconductors**. *Reviews of Modern Physics*, 77(4):1173–1224, nov 2005. https://doi.org/10.1103/revmodphys.77.1173.

[247] S. Rudin, T. L. Reinecke, and B. Segall. **Temperature-dependent exciton linewidths in semiconductors**. *Physical Review B*, 42(17):11218–11231, dec 1990. https://doi.org/10.1103/physrevb.42.11218.

[248] A. Berthelot, I. Favero, G. Cassabois, C. Voisin, C. Delalande, Ph. Roussignol, R. Ferreira, and J. M. Gérard. **Unconventional motional narrowing in the optical spectrum of a semiconductor quantum dot**. *Nature Physics*, 2(11):759–764, oct 2006. https://doi.org/10.1038/nphys433.

[249] A. Alkauskas, B. B. Buckley, D. D. Awschalom, and C. G. Van de Walle. **First-principles theory of the luminescence lineshape for the triplet transition in diamond NV centres**. *New Journal of Physics*, 16(7):073026, jul 2014. https://doi.org/10.1088/1367-2630/16/7/073026.

[250] T. Q. P. Vuong, G. Cassabois, P. Valvin, A. Ouerghi, Y. Chassagneux, C. Voisin, and B. Gil. **Phonon-Photon Mapping in a Color Center in Hexagonal Boron Nitride**. *Physical Review Letters*, 117(9), aug 2016. https://doi.org/10.1103/physrevlett.117.097402.

[251] L. C. Andreani. **Optical Transitions, Excitons, and Polaritons in Bulk and Low-Dimensional Semiconductor Structures**. In *Confined Electrons and Photons*, pages 57–112. Springer US, 1995. https://doi.org/10.1007/978-1-4615-1963-8_3.

[252] D. Rosales, T. Bretagnon, B. Gil, A. Kahouli, J. Brault, B. Damilano, J. Massies, M. V. Durnev, and A. V. Kavokin. **Excitons in nitride heterostructures: From zero- to one-dimensional behavior**. *Physical Review B*, 88(12), September 2013. https://doi.org/10.1103/physrevb.88.125437.

[253] S. Berger, C. Voisin, G. Cassabois, C. Delalande, P. Roussignol, and X. Marie. **Temperature Dependence of Exciton Recombination in Semiconducting Single-Wall Carbon Nanotubes**. *Nano Letters*, 7(2):398–402, feb 2007. https://doi.org/10.1021/nl062609p.

[254] M. Abbarchi, M. Gurioli, A. Vinattieri, S. Sanguinetti, M. Bonfanti, T. Mano, K. Watanabe, T. Kuroda, and N. Koguchi. **Phonon sideband recombination kinetics in single quantum dots**. *Journal of Applied Physics*, 104(2):023504, jul 2008. https://doi.org/10.1063/1.2948932.

[255] G. Cassabois, P. Valvin, and B. Gil. **Intervalley scattering in hexagonal boron nitride**. *Physical Review B*, 93(3), jan 2016. https://doi.org/10.1103/physrevb.93.035207.

[256] J. M. Gérard, B. Sermage, B. Gayral, B. Legrand, E. Costard, and V. Thierry-Mieg. **Enhanced Spontaneous Emission by Quantum Boxes in a Monolithic Optical Microcavity**. *Physical Review Letters*, 81(5):1110–1113, aug 1998. https://doi.org/10.1103/physrevlett.81.1110.

[257] A. Dousse, J. Suffczyński, A. Beveratos, O. Krebs, A. Lemaître, I. Sagnes, J. Bloch, P. Voisin, and P. Senellart. **Ultrabright source of entangled photon pairs**. *Nature*, 466(7303):217–220, jul 2010. https://doi.org/10.1038/nature09148.

[258] B. Krummheuer, V. M. Axt, and T. Kuhn. **Theory of pure dephasing and the resulting absorption line shape in semiconductor quantum dots**. *Physical Review B*, 65(19), may 2002. https://doi.org/10.1103/physrevb.65.195313.

[259] F. Vialla, Y. Chassagneux, R. Ferreira, C. Roquelet, C. Diederichs, G. Cassabois, P. Roussignol, J. S. Lauret, and C. Voisin. **Unifying the Low-Temperature Photoluminescence Spectra of Carbon Nanotubes: The Role of Acoustic Phonon Confinement**. *Physical Review Letters*, 113(5), jul 2014. https://doi.org/10.1103/physrevlett.113.057402.

[260] P. Y. Yu and M. Cardona. *Fundamentals of Semiconductors*. Springer Berlin Heidelberg, 2010. https://doi.org/10.1007/978-3-642-00710-1.

[261] C. de Tomas, A. Cantarero, A. F. Lopeandia, and F. X. Alvarez. **Thermal conductivity of group-IV semiconductors from a kinetic-collective model**. *Proceedings of the Royal Society A: Mathematical, Physical and Engineering Sciences*, 470(2169):20140371, sep 2014. https://doi.org/10.1098/rspa.2014.0371.

[262] A. K. Buin, A. Verma, and M. P. Anantram. **Carrier-phonon interaction in small cross-sectional silicon nanowires**. *Journal of Applied Physics*, 104(5):053716, sep 2008. https://doi.org/10.1063/1.2974088.

[263] R. B. Capaz, A. Dal Pino, and J. D. Joannopoulos. **Identification of the migration path of interstitial carbon in silicon**. *Physical Review B*, 50(11):7439–7442, sep 1994. https://doi.org/10.1103/physrevb.50.7439.

[264] R. B. Capaz, A. Dal Pino, and J. D. Joannopoulos. **Theory of carbon-carbon pairs in silicon**. *Physical Review B*, 58(15):9845–9850, oct 1998. https://doi.org/10.1103/physrevb.58.9845.

[265] H. Wang, A. Chroneos, C. A. Londos, E. N. Sgourou, and U. Schwingenschlögl. **Carbon related defects in irradiated silicon revisited**. *Scientific Reports*, 4(1), may 2014. https://doi.org/10.1038/srep04909.

[266] J. M. Binder, A. Stark, N. Tomek, J. Scheuer, F. Frank, K. D. Jahnke, C. Müller, S. Schmitt, M. H. Metsch, T. Unden, T. Gehring, A. Huck, U. L. Andersen, L. J. Rogers, and F. Jelezko. **Qudi: A modular python suite for experiment control and data processing**. *SoftwareX*, 6:85–90, 2017. https://doi.org/10.1016/j.softx.2017.02.001.

[267] X. Chen, J. N. Greiner, J. Wrachtrup, and I. Gerhardt. **Single Photon Randomness based on a Defect Center in Diamond**. *Scientific Reports*, 9(1), dec 2019. https://doi.org/10.1038/s41598-019-54594-0.

[268] P. Grünwald. **Effective second-order correlation function and single-photon detection**. *New Journal of Physics*, 21(9):093003, sep 2019. https://doi.org/10.1088/1367-2630/ab3ae0.

[269] S. C. Kitson, P. Jonsson, J. G. Rarity, and P. R. Tapster. **Intensity fluctuation spectroscopy of small numbers of dye molecules in a microcavity**. *Physical Review A*, 58(1):620–627, jul 1998. https://doi.org/10.1103/physreva.58.620.

[270] A. Beveratos, R. Brouri, J.-P. Poizat, and P. Grangier. *Quantum Communication, Computing, and Measurement 3*, volume pp. 261-267. Springer US, 2002. https://doi.org/10.1007/b114701.

[271] V. D. Tkachev and A. V. Mudryi. **Piezospectroscopic effect on zero-phonon luminescence lines of silicon**. *Journal of Applied Spectroscopy*, 29(6):1485–1491, dec 1978. https://doi.org/10.1007/bf00613548.

[272] S. W. Schmitt, G. Sarau, and S. Christiansen. **Observation of strongly enhanced photoluminescence from inverted cone-shaped silicon nanostructures**. *Scientific Reports*, 5(1), nov 2015. https://doi.org/10.1038/srep17089.

[273] S. Cueff, F. Dubois, M. S. R. Huang, D. Li, R. Zia, X. Letartre, P. Viktorovitch, and H. S. Nguyen. **Tailoring the Local Density of Optical States and Directionality of Light Emission by Symmetry Breaking**. *IEEE Journal of Selected Topics in Quantum Electronics*, 25(3):1–7, may 2019. https://doi.org/10.1109/jstqe.2019.2902915.

[274] L. W. Song, X. D. Zhan, B. W. Benson, and G. D. Watkins. **Bistable defect in silicon: The interstitial-carbon–substitutional-carbon pair**. *Physical Review Letters*, 60(5):460–463, feb 1988. https://doi.org/10.1103/physrevlett.60.460.

[275] N. B. Manson, M. Hedges, M. S. J. Barson, R. Ahlefeldt, M. W. Doherty, H. Abe, T. Ohshima, and M. J. Sellars. **NV⁻-N⁺ pair centre in 1b diamond**. *New Journal of Physics*, 20(11):113037, nov 2018. https://doi.org/10.1088/1367-2630/aaec58.

[276] G. Brassard, N. Lütkenhaus, T. Mor, and B. C. Sanders. **Limitations on Practical Quantum Cryptography**. *Physical Review Letters*, 85(6):1330–1333, aug 2000. https://doi.org/10.1103/physrevlett.85.1330.

[277] G. Cui and M. G. Raymer. **Quantum efficiency of single-photon sources in the cavity-QED strong-coupling regime**. *Optics Express*, 13(24):9660, 2005. https://doi.org/10.1364/opex.13.009660.

[278] J. N. Becker and C. Becher. **Coherence Properties and Quantum Control of Silicon Vacancy Color Centers in Diamond**. *physica status solidi (a)*, 214(11):1700586, sep 2017. https://doi.org/10.1002/pssa.201700586.

[279] T. Iwasaki, Y. Miyamoto, T. Taniguchi, P. Siyushev, M. H. Metsch, F. Jelezko, and M. Hatano. **Tin-Vacancy Quantum Emitters in Diamond**. *Physical Review Letters*, 119(25), dec 2017. https://doi.org/10.1103/physrevlett.119.253601.

[280] A. Szenes, B. Bánhelyi, L. Zs. Szabó, G. Szabó, T. Csendes, and M. Csete. **Improved emission of SiV diamond color centers embedded into concave plasmonic core-shell nanoresonators**. *Scientific Reports*, 7(1), oct 2017. https://doi.org/10.1038/s41598-017-14227-w.

[281] T. Gaebel, M. Domhan, C. Wittmann, I. Popa, F. Jelezko, J. Rabeau, A. Greentree, S. Prawer, E. Trajkov, P.R. Hemmer, and J. Wrachtrup. **Photochromism in single nitrogen-vacancy defect in diamond**. *Applied Physics B*, 82(2):243–246, nov 2005. https://doi.org/10.1007/s00340-005-2056-2.

[282] V. Mazzocchi, P.G. Sennikov, A.D. Bulanov, M.F. Churbanov, B. Bertrand, L. Hutin, J.P. Barnes, M.N. Drozdov, J.M. Hartmann, and M. Sanquer. **99.992% 28Si CVD-grown epilayer on 300mm substrates for large scale integration of silicon spin qubits**. *Journal of Crystal Growth*, 509:1–7, mar 2019. https://doi.org/10.1016/j.jcrysgro.2018.12.010.

[283] E. Krüger. **Optische Eigenschaften von CuI-Dünnschichten und -Mikrodrähten**. Master's thesis, Universität Leipzig, 2018.

[284] M. A. Green and M. J. Keevers. **Optical properties of intrinsic silicon at 300 K**. *Progress in Photovoltaics: Research and Applications*, 3(3):189–192, 1995. https://doi.org/10.1002/pip.4670030303.

[285] K. L. Brower. **EPR of a Jahn-Teller distorted (111) carbon interstitialcy in irradiated silicon**. *Physical Review B*, 9(6):2607–2617, mar 1974. https://doi.org/10.1103/physrevb.9.2607.

[286] M. X. Yan, K. P. Homewood, and B. C. Cavenett. **PDMR and ODMR crystalline p^+-i-n^+ silicon diodes**. *Journal of Physics C: Solid State Physics*, 19(8):L189–L193, mar 1986. https://doi.org/10.1088/0022-3719/19/8/006.

[287] A. H. Zewail. **Are the homogeneous linewidths of spin resonance (ODMR) and optical transitions related?** *The Journal of Chemical Physics*, 70(12):5759–5766, jun 1979. https://doi.org/10.1063/1.437404.

[288] A. Dréau, M. Lesik, L. Rondin, P. Spinicelli, O. Arcizet, J.-F. Roch, and V. Jacques. **Avoiding power broadening in optically detected magnetic resonance of single NV defects for enhanced dc magnetic field sensitivity**. *Physical Review B*, 84(19), nov 2011. https://doi.org/10.1103/physrevb.84.195204.

[289] T. Plakhotnik, M. W. Doherty, and N. B. Manson. **Electron-phonon processes of the nitrogen-vacancy center in diamond**. *Physical Review B*, 92(8), aug 2015. https://doi.org/10.1103/physrevb.92.081203.

[290] K. Jensen, V. M. Acosta, A. Jarmola, and D. Budker. **Light narrowing of magnetic resonances in ensembles of nitrogen-vacancy centers in diamond**. *Physical Review B*, 87(1), jan 2013. https://doi.org/10.1103/physrevb.87.014115.

[291] M. Niethammer, M. Widmann, T. Rendler, N. Morioka, Y.-C. Chen, R. Stöhr, J. U. Hassan, S. Onoda, T. Ohshima, S.-Y. Lee, A. Mukherjee, J. Isoya, N. T. Son, and J. Wrachtrup. **Coherent electrical readout of defect spins in silicon carbide by photo-ionization at ambient conditions**. *Nature Communications*, 10(1), dec 2019. https://doi.org/10.1038/s41467-019-13545-z.

[292] R. R. Mishra and A. K. Sharma. **Microwave–material interaction phenomena: Heating mechanisms, challenges and opportunities in material processing**. *Composites Part A: Applied Science and Manufacturing*, 81:78–97, feb 2016. https://doi.org/10.1016/j.compositesa.2015.10.035.

[293] C. Saltiel and A. K. Datta. **Heat and Mass Transfer in Microwave Processing**. In *Advances in Heat Transfer*, pages 1–94. Elsevier, 1999. https://doi.org/10.1016/s0065-2717(08)70303-4.

[294] S. Chandrasekaran, S. Ramanathan, and T. Basak. **Microwave material processing-a review**. *AIChE Journal*, 58(2):330–363, oct 2011. https://doi.org/10.1002/aic.12766.

[295] J. Krupka, P. Kamiński, R. Kozłowski, B. Surma, A. Dierlamm, and M. Kwestarz. **Dielectric properties of semi-insulating silicon at microwave frequencies**. *Applied Physics Letters*, 107(8):082105, aug 2015. https://doi.org/10.1063/1.4929503.

[296] D. J. Lepine. **Spin-Dependent Recombination on Silicon Surface**. *Physical Review B*, 6(2):436–441, jul 1972. https://doi.org/10.1103/physrevb.6.436.

[297] C. Böhme. ***Dynamics of spindependent charge carrier recombination***. PhD thesis, PhilippsUniversität Marburg, 2002.

[298] D. Kaplan, I. Solomon, and N.F. Mott. **Explanation of the large spin-dependent recombination effect in semiconductors**. *Journal de Physique Lettres*, 39(4):51–54, 1978. https://doi.org/10.1051/jphyslet:0197800390405100.

[299] I. Solomon, D. Biegelsen, and J. C. Knights. **Spin-dependent photoconductivity in n-type and p-type amorphous silicon**. *Solid State Communications*, 22(8):505–508, may 1977. https://doi.org/10.1016/0038-1098(77)91402-8.

[300] I. Solomon. **Spin-dependent recombination in a silicon p-n junction**. *Solid State Communications*, 20(3):215–217, oct 1976. https://doi.org/10.1016/0038-1098(76)90179-4.

[301] B. Movaghar, B. Ries, and L. Schweitzer. **Theory of the resonant and non-resonant photoconductivity changes in amorphous silicon**. *Philosophical Magazine B*, 41(2):159–167, feb 1980. https://doi.org/10.1080/13642818008245377.

[302] L. S. Vlasenko, Y. V. Martynov, T. Gregorkiewicz, and C. A. J. Ammerlaan. **Electron paramagnetic resonance versus spin-dependent recombination: Excited triplet states of structural defects in irradiated silicon**. *Physical Review B*, 52(2):1144–1151, jul 1995. https://doi.org/10.1103/physrevb.52.1144.

[303] K. Fukui, T. Sato, H. Yokoyama, H. Ohya, and H. Kamada. **Resonance-Field Dependence in Electrically Detected Magnetic Resonance: Effects of Exchange Interaction**. *Journal of Magnetic Resonance*, 149(1):13–21, mar 2001. https://doi.org/10.1006/jmre.2000.2277.

[304] T. Eickelkamp, S. Roth, and M. Mehring. **Electrically detected magnetic resonance in photoexcited fullerenes**. *Molecular Physics*, 95(5):967–972, dec 1998. https://doi.org/10.1080/00268979809483230.

[305] A. V. Barabanov, O. V. Tretiak, and V. A. L'vov. **Complete theoretical analysis of the Kaplan-Solomon-Mott mechanism of spin-dependent recombination in semiconductors**. *Physical Review B*, 54(4):2571–2577, jul 1996. https://doi.org/10.1103/physrevb.54.2571.

[306] A. Schnegg, J. Behrends, M. Fehr, and K. Lips. **Pulsed electrically detected magnetic resonance for thin film silicon and organic solar cells**. *Physical Chemistry Chemical Physics*, 14(42):14418, 2012. https://doi.org/10.1039/c2cp41258f.

[307] J. Behrends. *Spin-dependent Transport and Recombination in Solar Cells studied by Pulsed Electrically Detected Magnetic Resonance*. PhD thesis, Institut für Experimentalphysik der Freien Universität Berlin, 2009.

[308] C. Boehme and K. Lips. **Theory of time-domain measurement of spin-dependent recombination with pulsed electrically detected magnetic resonance**. *Physical Review B*, 68(24), dec 2003. https://doi.org/10.1103/physrevb.68.245105.

[309] C. Boehme and K. Lips. **The Investigation of Charge Carrier Recombination and Hopping Transport with Pulsed Electrically Detected Magnetic Resonance Techniques**. In *Charge Transport in Disordered Solids with Applications in Electronics*, pages 179–219. John Wiley & Sons, Ltd, nov 2006. https://doi.org/10.1002/0470095067.ch5.

[310] D. Ephron, M. R. Beasley, H. Bahlouli, and K. A. Matveev. **Correlated hopping through thin disordered insulators**. *Physical Review B*, 49(4):2989–2992, jan 1994. https://doi.org/10.1103/physrevb.49.2989.

[311] M. Eckardt, J. Behrends, D. Münter, and W. Harneit. **Compact electrically detected magnetic resonance setup**. *AIP Advances*, 5(4):047139, apr 2015. https://doi.org/10.1063/1.4919247.

[312] A. Kurobe and H. Kamimura. **Correlation Effects on Variable Range Hopping Conduction and the Magnetoresistance**. *Journal of the Physical Society of Japan*, 51(6):1904–1913, jun 1982. https://doi.org/10.1143/jpsj.51.1904.

[313] R. L. Vranch, B. Henderson, and M. Pepper. **Spin-dependent pair generation at Si/SiO_2 interfaces**. *Applied Physics Letters*, 53(14):1299–1301, oct 1988. https://doi.org/10.1063/1.100450.

[314] R. L. Vranch, B. Henderson, and M. Pepper. **Spin-dependent recombination in irradiated Si/SiO₂ device structures**. *Applied Physics Letters*, 52(14):1161–1163, apr 1988. https://doi.org/10.1063/1.99192.

[315] K. Morigaki. **Recombination mechanisms in amorphous semiconductors deduced from resonance measurements**. *Journal of Non-Crystalline Solids*, 77-78:583–592, dec 1985. https://doi.org/10.1016/0022-3093(85)90728-8.

[316] M. Yoshida and K. Morigaki. **Triplet exciton recombination in a-Si: H as elucidated by optically detected magnetic resonance experiments**. *Philosophical Magazine B*, 54(2):L63–L66, aug 1986. https://doi.org/10.1080/13642818608239004.

[317] W. Schmid. **Auger lifetimes for excitons bound to neutral donors and acceptors in Si**. *Physica Status Solidi (b)*, 84(2):529–540, dec 1977. https://doi.org/10.1002/pssb.2220840216.

[318] H. Morishita, L. S. Vlasenko, H. Tanaka, K. Semba, K. Sawano, Y. Shiraki, M. Eto, and K. M. Itoh. **Electrical detection and magnetic-field control of spin states in phosphorus-doped silicon**. *Physical Review B*, 80(20), nov 2009. https://doi.org/10.1103/physrevb.80.205206.

[319] T. Itahashi, H. Hayashi, M. R. Rahman, K. M. Itoh, L. S. Vlasenko, M. P. Vlasenko, and D. S. Poloskin. **Optical and dynamic nuclear polarization of ²⁹Si nuclei via photoexcited triplet states of oxygen-vacancy complexes in isotopically controlled silicon**. *Physical Review B*, 87(7), feb 2013. https://doi.org/10.1103/physrevb.87.075201.

[320] W. Akhtar, T. Sekiguchi, T. Itahashi, V. Filidou, J. J. L. Morton, L. Vlasenko, and K. M. Itoh. **Rabi oscillation and electron-spin-echo envelope modulation of the photoexcited triplet spin system in silicon**. *Physical Review B*, 86(11), sep 2012. https://doi.org/10.1103/physrevb.86.115206.

[321] D. P. Franke, F. Hoehne, L. S. Vlasenko, K. M. Itoh, and M. S. Brandt. **Spin-dependent recombination involving oxygen-vacancy complexes in silicon**. *Physical Review B*, 89(19), may 2014. https://doi.org/10.1103/physrevb.89.195207.

[322] W. Akhtar, V. Filidou, T. Sekiguchi, E. Kawakami, T. Itahashi, L. Vlasenko, J. J. L. Morton, and K. M. Itoh. **Coherent Storage of Photoexcited Triplet States Using ²⁹Si Nuclear Spins in Silicon**. *Physical Review Letters*, 108(9), feb 2012. https://doi.org/10.1103/physrevlett.108.097601.

[323] K. L. Brower. **Electron Paramagnetic Resonance of the Neutral (S=1) One- Vacancy-Oxygen Center in Irradiated Silicon**. *Physical Review B*, 4(6):1968–1982, sep 1971. https://doi.org/10.1103/physrevb.4.1968.

[324] W. Akhtar, H. Morishita, L.S. Vlasenko, D.S. Poloskin, and K.M. Itoh. **Electrically detected magnetic resonance of phosphorous due to spin dependent recombination with triplet centers in γ-irradiated silicon**. *Physica B: Condensed Matter*, 404(23-24):4583–4585, dec 2009. https://doi.org/10.1016/j.physb.2009.08.116.

[325] W. Akhtar, H. Morishita, K. Sawano, Y. Shiraki, L. S. Vlasenko, and K. M. Itoh. **Electrical detection of cross relaxation between electron spins of phosphorus and oxygen-vacancy centers in silicon**. *Physical Review B*, 84(4), jul 2011. https://doi.org/10.1103/physrevb.84.045204.

[326] H. Saito, S. Hayashi, Y. Kusano, K. M. Itoh, M. P. Vlasenko, and L. S. Vlasenko. **Electron spin resonance study of surface and oxide interface spin-triplet centers on (100) silicon wafers**. *Journal of Applied Physics*, 123(16):161582, jan 2018. https://doi.org/10.1063/1.5010816.

[327] E. H. Poindexter, P. J. Caplan, B. E. Deal, and R. R. Razouk. **Interface states and electron spin resonance centers in thermally oxidized (111) and (100) silicon wafers**. *Journal of Applied Physics*, 52(2):879–884, feb 1981. https://doi.org/10.1063/1.328771.

[328] K. Kato, T. Yamasaki, and T. Uda. **Origin of P_{b1} center at $SiO_2Si(100)$ interface: First-principles calculations**. *Physical Review B*, 73(7), feb 2006. https://doi.org/10.1103/physrevb.73.073302.

[329] A. Stesmans and V. V. Afanas'ev. **Electron spin resonance features of interface defects in thermal $(100)Si/SiO_2$**. *Journal of Applied Physics*, 83(5):2449–2457, mar 1998. https://doi.org/10.1063/1.367005.

[330] A. Stirling, A. Pasquarello, J.-C. Charlier, and R. Car. **Dangling Bond Defects at Si-SiO_2 Interfaces: Atomic Structure of the P_{b1} Center**. *Physical Review Letters*, 85(13):2773–2776, sep 2000. https://doi.org/10.1103/physrevlett.85.2773.

[331] K. Keunen, A. Stesmans, and V. V. Afanas'ev. **Inherent Si dangling bond defects at the thermal $(110)Si/SiO_2$ interface**. *Physical Review B*, 84(8), aug 2011. https://doi.org/10.1103/physrevb.84.085329.

[332] T. Matsuoka, L. S. Vlasenko, M. P. Vlasenko, T. Sekiguchi, and K. M. Itoh. **Identification of a paramagnetic recombination center in silicon/silicon-dioxide interface**. *Applied Physics Letters*, 100(15):152107, apr 2012. https://doi.org/10.1063/1.3702785.

[333] L. S. Vlasenko. **Photoelectrically detected magnetic resonance spectroscopy of the excited triplet states of point defects in silicon**. *Physics of the Solid State*, 41(5):697–700, may 1999. https://doi.org/10.1134/1.1130851.

[334] R. Laiho, M. M. Afanasjev, M. P. Vlasenko, and L. S. Vlasenko. **Electron Exchange Interaction $S = 1$ Defects Observed by Level Crossing Spin Dependent Microwave Photoconductivity in Irradiated Silicon**. *Physical Review Letters*, 80(7):1489–1492, feb 1998. https://doi.org/10.1103/physrevlett.80.1489.

[335] S. Hayashi, H. Saito, K. M. Itoh, M. P. Vlasenko, and L. S. Vlasenko. **Electron spin resonance identification di-carbon-related centers in irradiated silicon**. *Journal of Applied Physics*, 123(16):161592, feb 2018. https://doi.org/10.1063/1.5010234.

[336] T. Itahashi, H. Hayashi, K.M. Itoh, D.S. Poloskin, L.S. Vlasenko, and M.P. Vlasenko. **Dynamic nuclear polarization of ^{29}Si via spin S=1 centers in isotopically**

controlled silicon. *Physica B: Condensed Matter*, 404(23-24):5054–5056, dec 2009. https://doi.org/10.1016/j.physb.2009.08.241.

[337] M. Hollenbach, Y. Berencén, U. Kentsch, M. Helm, and G. V. Astakhov. **Engineering telecom single-photon emitters in silicon for scalable quantum photonics**. *Optics Express*, 28(18):26111, aug 2020. https://doi.org/10.1364/oe.397377.

[338] F. M. Hrubesch, G. Braunbeck, M. Stutzmann, F. Reinhard, and M. S. Brandt. **Efficient Electrical Spin Readout of NV⁻ Centers in Diamond**. *Physical Review Letters*, 118(3), jan 2017. https://doi.org/10.1103/physrevlett.118.037601.

[339] P. Siyushev, M. Nesladek, E. Bourgeois, M. Gulka, J. Hruby, T. Yamamoto, M. Trupke, T. Teraji, J. Isoya, and F. Jelezko. **Photoelectrical imaging and coherent spin-state readout of single nitrogen-vacancy centers in diamond**. *Science*, 363(6428):728–731, feb 2019. https://doi.org/10.1126/science.aav2789.

[340] S. Depinna, B. C. Cavenett, I. G. Austin, T. M. Searle, M. J. Thompson, J. Allison, and P. G. Le Comber. **Characterization of radiative recombination in amorphous silicon by optically detected magnetic resonance: Part I**. *Philosophical Magazine B*, 46(5):473–500, nov 1982. https://doi.org/10.1080/01418638208224023.

[341] S. P. Depinna, K. Homewood, B. C. Cavenett, I. G. Austin, T. M. Searle, G. Willeke, and S. Kinmond. **O.D.M.R. investigation of recombination in μc-Si:H**. *Philosophical Magazine B*, 47(5):L57–L62, jan 1983. https://doi.org/10.1080/13642812.1983.11643266.

[342] K. P. Homewood, B. C. Cavenett, W. E. Spear, and P. G. LeComber. **Spin effects in p$^+$-i-n$^+$ a-Si:H cells; photovoltaic detected magnetic resonance (PDMR)**. *Journal of Physics C: Solid State Physics*, 16(13):L427–L431, may 1983. https://doi.org/10.1088/0022-3719/16/13/006.

[343] K. P. Homewood, B. C. Cavenett, I. G. Austin, T. M. Searle, W. E. Spear, and P. G. LeComber. **ODMR detected via the electroluminescence in p$^+$-i-n$^+$ a-Si:H cells**. *Journal of Physics C: Solid State Physics*, 17(3):L103–L106, jan 1984. https://doi.org/10.1088/0022-3719/17/3/008.

[344] B. C. Cavenett and M.-X. Yan. **Capacitance detected magnetic resonance in γ-irradiated p$^+$-i-n$^+$ silicon diodes**. *Semiconductor Science and Technology*, 1(3):180–183, sep 1986. https://doi.org/10.1088/0268-1242/1/3/004.

[345] A. Durand, Y. Baron, W. Redjem, T. Herzig, A. Benali, S. Pezzagna, J. Meijer, A. Y. Kuznetsov, J.-M. Gérard, I. Robert-Philip, M. Abbarchi, V. Jacques, G. Cassabois, and A. Dréau. **Broad Diversity of Near-Infrared Single-Photon Emitters in Silicon**. *Physical Review Letters*, 126(8), feb 2021. https://doi.org/10.1103/physrevlett.126.083602.

Danksagung

Hätte man mir zu Beginn meines Studiums gesagt, welchen Weg ich beschreiten werde und was bis zum heutigen Tag alles passieren wird, ich hätte es wohl kaum geglaubt. Die Erfüllung so vieler Hoffnungen und Träume, welche heute mit der Einreichung dieser Arbeit durch einen weiteren ergänzt werden, wäre jedoch ohne die Unterstützung vieler wundervoller Menschen nicht möglich gewesen.

Deshalb möchte ich zunächst meinem Doktorvater, Prof. Dr. Jan Meijer, für die herzliche Aufnahme in seine Arbeitsgruppe, die sowohl wissenschaftliche als auch persönliche Unterstützung und das entgegengebrachte Vertrauen danken. Durch seinen Enthusiasmus schafft er es, seine Studenten für die eigene Arbeit und die Physik im Allgemeinen zu begeistern!

Ebenso danke ich meinem Betreuer, Dr. Sébastien Pezzagna, der für das vorgestellte internationale Projekt mitverantwortlich war und somit die vorliegende Arbeit überhaupt erst ermöglicht hat. Die damit verbundenen Kooperationen haben dazu geführt, dass ich viele neue, schöne Orte und Menschen kennenlernen durfte. Entsprechend danke ich auch allen weiteren Projektpartnern, allen voran Prof. Dr. Marco Abbarchi, Prof. Dr. Guillaume Cassabois und Dr. Anaïs Dréau, für die sehr angenehme Zusammenarbeit und die fruchtbaren und schönen Projektmeetings.

Ohne die Hilfe meiner Mitstreiter aus der Abteilung AQS hätte ich diese Arbeit nicht vollenden können, weshalb ich mich hiermit auch bei all meinen lieben Kollegen bedanken möchte. Besonderen Dank gebührt dabei zunächst Dr. Tobias Lühmann, der mich bei einem Hopfentee dazu aufgefordert hat, Prof. Meijer nach einem Projekt für meine Promotion zu fragen und somit den Grundstein für diese Arbeit gelegt hat. Ohne Johannes Küpper, der sich viel Zeit genommen hat, um mir sowohl den Umgang mit dem 100 kV Beschleuniger beizubringen als auch bei der Elektronenstrahllithografie und Kontaktierung zu helfen, wäre ich wohl gerade zu Beginn der Arbeit etwas verloren gewesen. Auch meinen Kollegen Clemens Scheuner und Sascha Becker möchte ich sowohl für die fachlichen Gespräche als auch für die experimentelle Unterstützung, zum Beispiel bei der Bedienung der FIB, danken. Für die Hilfe beim Aufbau des ODMR/PDMR-Experimentes danke ich Robert Staacke, der sich die Zeit genommen hat, mit mir die Platine zu entwerfen und auch bei der Programmierung der Steuerung geholfen hat. Ebenfalls sei Dr. Michael Kieschnick und Carsten Pahnke gedankt, die mich in die Bedienung des Lipsions eingewiesen haben und dabei auch stets für Fragen erreichbar waren. Zuguterletzt seien ebenfalls Steffen Jankuhn und Birgit Wendisch gedankt, die bei organisatorischen Fragen immer zur Stelle sind und so dafür sorgen, dass alles reibungslos läuft.

Neben der wissenschaftlichen Arbeit möchte ich mich bei meinen Kollegen auch für die vielen, schönen Erfahrungen und Erlebnisse außerhalb der Universität bedanken! Ob beim Schreinern mit Tobi, beim Schmieden und Geocashen mit Johannes, Bogenschießen mit Ralf, den Whisky-Tastings mit Nicole und Paul, Nintendo spielen mit Robert oder den vie-

Wissenschaftlicher Werdegang

Tabellarischer Lebenslauf

Geboren	am 30. Januar 1987 in Weißenfels
1993 − 2003	Grund- und Sekundarschule in Hohenmölsen
2003 − 2006	Abitur am Agricolagymnasium in Hohenmölsen
2007	Grundwehrdienst an der Marineunteroffizierschule in Plön und der General-von-Seidel-Kaserne in Trier
2007 − 2011	Studium der Physik (Bachelor of Science) an der Universität Leipzig Abschlussarbeit "Aufbau und Test eines Messplatzes für magnetooptische Ellipsometrie" in der Abteilung Halbleiterphysik (HLP)
2011 − 2013	Studium der Physik (Master of Science) an der Universität Leipzig Abschlussarbeit "Temperaturabhängige Hochdruck-NMR" in der Abteilung Magnetische Resonanz komplexer Quantenfestkörper (MQF)
2014 − 2016	Prozessingenieur Inline Inspection bei der X-FAB Semiconductor Foundries AG in Erfurt
seit 2016	Promotion an der Universität Leipzig zum Thema "Extrinsische Quantenzentren in Silizium für Nanophotonik und Quantenanwendungen" in der Abteilung Angewandte Quantensysteme (AQS)
2018	Forschungsaufenthalt (1 Monat) am Laboratoire Charles Coulomb (L2C) an der Université de Montpellier

Präsentationen

2018   Vortrag "Optical Properties of an Ensemble of G-Centers in Silicon", 16th International Conference on Nuclear Microprobe Technology and Applications, Guildford/Surrey (GB), 08. - 13.07.2018

Poster "Creation of quantum light sources in silicon using spatial selective ion implantation of high lateral resolution", 22nd International Conference on Ion Implantation Technology, Würzburg (DE), 16. - 21.09.2018
Posterpreis "Best Student Poster Award"

2019   Vortrag "Creation of quantum centers in silicon using spatial selective ion implantation of high lateral resolution", 60. Treffen der Nutzergruppe Ionenimplantation, Erlangen (DE), 04.04.2019

Vortrag "Creation of quantum and classical light emitters in silicon using spatial selective ion implantation", 13th European Conference on Accelerators in Applied Research and Technology, Split (HR), 05. - 10.05.2019

Akquirierte Projekte

2021   EXIST - Gründerstipendium "InQ - Herstellung und Verkauf von Festkörper-Qubits für Anwendungen in Quantentechnologien"

SAB Validierungsförderung "Ions & Quantum (Quantum Enabling Solutions), Validierung von Quantentechnologien auf Festkörper-Basis"

Lehrtätigkeit

2011 − 2013   Kontrolleur der Übungsaufgaben Experimentalphysik I - IV

2016/17   Anfängerpraktikum Elektrodynamik

2017/18   Übungsseminar Experimentalphysik I (Mechanik und Wärmelehre)

2018   Übungsseminar Experimentalphysik II (Elektrodynamik und Optik)

2018/19   Übungsseminar Experimentalphysik I (Mechanik und Wärmelehre)

2019   Übungsseminar Experimentalphysik II (Elektrodynamik und Optik)

Liste der Publikationen inkl. Eigenanteil

2014 **(1)** T. Meier, **T. Herzig** and J. Haase. **Moissanite anvil cell design for giga-pascal nuclear magnetic resonance.** *Review of Scientific Instruments* 85(4): 043903

- Unterstützung bei der Herstellung der Diamantstempelzelle, Diskussion der Ergebnisse und Kommentierung des Manuskripts

2017 **(2)** S. Ditalia Tchernij, **T. Herzig**, J. Forneris, J. Küpper, S. Pezzagna, P. Traina, E. Moreva, I. P. Degiovanni, G. Brida, N. Skukan, M. Genovese, M. Jakšić, J. Meijer and P. Olivero. **Single-Photon-Emitting Optical Centers in Diamond Fabricated upon Sn Implantation.** *ACS Photonics* 4(10):2580-2586

- Herstellung der Mica-Masken, Herstellung der SnPb-Kathoden für die Implantation, Graphitisierung der Diamantprobe, Fotolithografie, Herstellung der Einzelphotonenemitter durch Zinn-Implantation in Diamant, Kommentierung des Manuskripts

2018 **(3)** C. Beaufils, W. Redjem, E. Rousseau, V. Jacques, A. Yu. Kuznetsov, C. Raynaud, C. Voisin, A. Benali, **T. Herzig**, S. Pezzagna, J. Meijer, M. Abbarchi and G. Cassabois. **Optical properties of an ensemble of G-centers in silicon.** *Physical Review B* 97(3)

- 2 MeV Protonenbestrahlung, Literaturrecherche, SRIM-Simulation, Diskussion der Ergebnisse und Kommentierung des Manuskripts

(4) M. Alkahtani, I. Cojocaru, X. Liu, **T. Herzig**, J. Meijer, J. Küpper, T. Lühmann, A. V. Akimov and P. R. Hemmer. **Tin-vacancy in diamonds for luminescent thermometry.** *Applied Physics Letters* 112(24): 241902

- Herstellung der Kathoden für die Implantation, Germanium-Implantation in verschiedene Diamant-Proben, Kommentierung des Manuskripts

(5) S. Ditalia Tchernij, T. Lühmann, **T. Herzig**, J. Küpper, A. Damin, S. Santonocito, M. Signorile, P. Traina, E. Moreva, F. Celegato, S. Pezzagna, I. P. Degiovanni, P. Olivero, M. Jakšić, J. Meijer, P. M. Genovese and J. Forneris. **Single-Photon Emitters in Lead-Implanted Single-Crystal Diamond.** *ACS Photonics* 5(12): 4864-4871

- Herstellung der Kathoden für die Implantation, SRIM-Simulation, Ionenimplantation von Blei, Germanium und Zinn in Diamant, Kommentierung des Manuskripts

2019 **(6) T. Herzig**, P. Räcke, N. Raatz, D. Spemann, W. Redjem, J. W. Gerlach, J. Meijer, G. Cassabois, M. Abbarchi and S. Pezzagna. **Creation of Quantum Centers in Silicon using Spatial Selective Ion Implantation of high Lateral Resolution.** *IEEE Xplore, 2018 22nd International Conference on Ion Implantation Technology (IIT), Würzburg, Germany, 2018, pp. 136-139*

- Literaturrecherche, Massenspektrometrie, Herstellung der Mica-Maske, hochenergetische Protonenbestrahlung, Anfertigung und Diskussion des Manuskripts und der Graphiken

(7) A. Tallaire, O. Brinza, M. De Feudis, A. Ferrier, N. Touati, L. Binet, L. Nicolas, T. Delord, G. Hétet, **T. Herzig**, S. Pezzagna, P. Goldner and J. Achard. **Synthesis of Loose Nanodiamonds Containing Nitrogen-Vacancy Centers for Magnetic and Thermal Sensing.** *ACS Appl. Nano Mater.* 2,9: 5952-5962

- 80 keV Protonenbestrahlung, Kommentierung des Manuskripts

2020 **(8)** W. Redjem, A. Durand, **T. Herzig**, A. Benali, S. Pezzagna, J. Meijer, A. Yu. Kuznetsov, H. S. Nguyen, S. Cueff, J.-M. Gérard, I. Robert-Philip, B. Gil, D. Caliste, P. Pochet, M. Abbarchi, V. Jacques, A. Dréau and G. Cassabois. **Single artificial atoms in silicon emitting at telecom wavelengths.** *Nat. Electron. 3*, 738743

- Kohlenstoff-Implantationen in diverse Si-Proben, Unterstützung bei der Photolumineszenz-Messung im Rahmen der Veröffentlichung, Literaturrecherche, Diskussion der Ergebnisse und Kommentierung des Manuskripts

2021 **(9) T. Herzig**, T. Lühmann, P. Räcke, C. Scheuner, S. Pezzagna, J. Meijer. **Chapter One - Color center formation by deterministic single ion implantation.** In: **Semiconductors and Semimetals**, Elsevier, Volume 104 (2021), pp. 1-30, ISSN 0080-8784, ISBN 9780323850247

- Literaturrecherche, Anfertigung und Diskussion des Manuskripts und einzelner Graphiken

(10) A. Durand, Y. Baron, W. Redjem, **T. Herzig**, A. Benali, S. Pezzagna, J. Meijer, A. Yu. Kuznetsov, J.-M. Gérard, I. Robert-Philip, M. Abbarchi, V. Jacques, G. Cassabois and A. Dréau. **Broad Diversity of Near-Infrared Single-Photon Emitters in Silicon.** *Phys. Rev. Lett 126*, 083602

- Kohlenstoff-Implantationen in diverse Siliziumproben im Rahmen der Veröffentlichung, Literaturrecherche, Diskussion der Ergebnisse und Kommentierung des Manuskripts

(11) Y. Baron, A. Durand, P. Udvarhelyi, **T. Herzig**, M. Khoury, S. Pezzagna, J. Meijer, I. Robert-Philip, M. Abbarchi, J.-M. Hartmann, Vincent Mazzocchi, J.-M. Gérard, A. Gali, V. Jacques, G. Cassabois and A. Dréau. **Detection of single W-centers in silicon.** *arXiv:2108.04283v1*

- Ionen-Implantation von Kohlenstoff, Silizium und Wasserstoff in SOI-Proben, Diskussion der Ergebnisse und Kommentierung des Manuskripts

Selbstständigkeitserklärung

Hiermit erkenne ich die Promotionsordnung vom 24. August 2016 der Fakultät für Physik und Geowissenschaften der Universität Leipzig an und versichere, dass

- die vorliegende Arbeit ohne unzulässige Hilfe und ohne Benutzung anderer als der angegebenen Hilfsmittel angefertigt und dass die aus fremden Quellen direkt oder indirekt übernommenen Gedanken in der Arbeit als solche kenntlich gemacht wurden;

- alle Personen genannt wurden, von denen ich bei der Auswahl des Materials sowie bei der Herstellung des Manuskripts Unterstützungsleistung erhalten habe;

- keine weiteren Personen bei der geistigen Herstellung der vorliegenden Arbeit beteiligt waren oder Hilfe eines Promotionsberaters in Anspruch genommen wurde. Dritte erhielten weder von mir noch in meinem Auftrag unmittelbar noch mittelbar geldwerte Leistungen für Arbeiten, welche im Zusammenhang mit dem Inhalt der vorgelegten Dissertation stehen;

- die vorgelegte Arbeit oder Teile daraus weder im Inland noch im Ausland in gleicher oder ähnlicher Form einer anderen Prüfungsbehörde zum Zwecke einer Promotion oder eines anderen Prüfungsverfahrens vorgelegt wurde;

- keine früheren erfolglosen Promotionsversuche stattgefunden haben.

Leipzig, 09. November 2021   Tobias Herzig

Erklärung für die Bibliothek

Ich bin einverstanden, dass ein Exemplar dieser Arbeit nach positiver Begutachtung in den Bestand der Zweigstelle Physik der Universitätsbibliothek der Universität Leipzig aufgenommen wird.

Leipzig, 09. November 2021   Tobias Herzig